An Anatomical Model of the Cerebral Vasculature and Blood Flow

Claire Lucas

St Cross College

Supervisor: Dr. S. J. Payne

PUMMA research group

Department of Engineering Science

University of Oxford

A thesis submitted for the degree of

Doctor of Philosophy

Trinity Term 2012

An Anatomical Model of the Cerebral Vasculature and Blood Flow

Claire Lucas, St Cross College, University of Oxford

A thesis submitted for the degree of Doctor of Philosophy, Trinity Term 2012

The brain accounts for around 2 % of human adult bodyweight but consumes 20 % of the resting oxygen available to the whole body. The brain is dependent on a constant supply of oxygen to tissue, transported from the heart via the vasculature and carried in blood. An interruption to flow can lead to ischaemia (a reduced oxygen supply) and prolonged interruption may result in tissue death, and permanent brain damage.

The cerebral vasculature consists of many, densely packed, micro-vessels with a very large total surface area. Oxygen dissolved in blood enters tissue by passive diffusion through the micro-vessel walls. Imaging shows bursts of metabolic activity and flow in localised brain areas coordinated with brain activity (such as raising a hand). An appropriate level of oxygenation, according to physiological demand, is maintained via autoregulation; a set of response pathways in the brain which cause upstream or downstream vessels to expand or contract in diameter as necessary to provide sufficient oxygen to every region of the brain. Further, autoregulation is also evident in the response to pressure changes in the vasculature: the perfusing pressure can vary over a wide range from the basal-state with only a small effect on flow due to the constriction or dilation of vessels.

Presented here is a new anatomical model of the cerebral vasculature with experimentally verified geometry, flow and oxygen concentration which is able to autoregulate over a perfusing pressure range of ±40% of the basal level. The dynamics of flow and tissue concentration in the capillary following a demand increase are replicated along with the pathway diameter response in surrounding vessels. The response is governed by a set of physiological signals which determine the proportion of activated muscle cells in the vessel wall.

”O Lord, you have searched me and known me! You know when I sit down and when I rise up; you discern my thoughts from afar. You search out my path and my lying down and you are acquainted with all my ways. Even before a word is on my tongue behold, O Lord, you know it altogether. For you formed my inward parts; you knitted me together in my mother’s womb. I praise you, for I am fearfully and wonderfully made. Wonderful are your works; my soul knows it very well. Your eyes saw my unformed substance; in your book were written, every one of them, the days that were formed for me, when as yet there was none of them. Search me, O God, and know my heart! Try my and know my thoughts! And see if there be any grievous way in me, and lead me in the way everlasting!”

Psalm 139

Acknowledgements

Thankyou to my supervisor, Dr Stephen Payne. It was his lectures as an undergraduate which sparked an interest in mathematical modelling. Stephen had the initial idea for this project and has been invaluable for ideas, knowledge of potential data sources and, more recently, in guidance of writing this thesis and in preparing it for submission. I do not know how many times he's read it and made suggestions for improvement but it is more than I could have hoped for.

This is in contrast to my husband Michael Lucas who fell asleep after 5 pages and has since refused to read anymore. However, his support has been elsewhere: a listening ear and the ability to ask a question which sparks an idea. Lately he has cooked my meals, tidied our house and told me gently when it was time to come home. This PhD is my baby, I look forward to one we can nurture together.

Finally, I must acknowledge my creator and sustainer, the almighty God. To the original engineer who established the beauty it has been such a delight to uncover. "It is the glory of God to conceal a thing, but the glory of kings is to search it out". I can only begin to approximate His genius by this model and I can only begin to imagine His greatness and power.

Abstract

The brain accounts for around 2 % of human adult bodyweight but consumes 20 % of the resting oxygen available to the whole body. The brain is dependent on a constant supply of oxygen to tissue, transported from the heart via the vasculature and carried in blood. An interruption to flow can lead to ischaemia (a reduced oxygen supply) and prolonged interruption may result in tissue death, and permanent brain damage.

The cerebral vasculature consists of many, densely packed, micro-vessels with a very large total surface area. Oxygen dissolved in blood enters tissue by passive diffusion through the micro-vessel walls. Imaging shows bursts of metabolic activity and flow in localised brain areas coordinated with brain activity (such as raising a hand). An appropriate level of oxygenation, according to physiological demand, is maintained via autoregulation; a set of response pathways in the brain which cause upstream or downstream vessels to expand or contract in diameter as necessary to provide sufficient oxygen to every region of the brain. Further, autoregulation is also evident in the response to pressure changes in the vasculature: the perfusing pressure can vary over a wide range from the basal-state with only a small effect on flow due to the constriction or dilation of vessels.

Presented here is a new vasculature model where diameter and length are calculated in order to match the data available for flow velocity and blood pressure in different sized vessels. These vessels are arranged in a network of 6 generations each of bifurcating arterioles and venules, and a set of capillary beds. The input pressure and number of generations are the only specifications required to

describe the network. The number of vessels, and therefore vessel geometry, is governed by how many generations are chosen and this can be altered in order to create more simple or complex networks. The flow, geometry and oxygen concentrations are calculated based on the vessel resistance due to flow from geometry based on Kirchoff circuit laws.

The passive and active length-tension characteristics of the vasculature are established using an approximation of the network at upper and lower autoregulation limits. An activation model is described with an activation factor which governs the contributions of elastic and muscle tension to the total vessel tension. This tension balances with the circumferential tension due to pressure and diameter and the change in activation sets the vessel diameter.

The mass transport equation for oxygen is used to calculate the concentration of oxygen at every point in the network using data for oxygen saturation to establish a relationship between the permeability of the vessel wall to oxygen and the geometry and flow in individual vessels. A tissue compartment is introduced which enables the modelling of metabolic control. There is evidence for a coordinated response by surrounding vessels to local changes. A signal is proposed based on oxygen demand which can be conducted upstream. This signal decays exponentially with vessel length but also accumulates with the signal added from other vessels.

The activation factor is therefore set by weighted signals proportional to changes in tissue concentration, circumferential tension, shear stress and conducted oxygen demand. The model is able to reproduce the autoregulation curve whereby a change in pressure has only a small effect on flow. The model is also able to replicate experimental results of diameter and tissue concentration following an increase in oxygen demand.

Contents

Nomenclature

β $(\mu M/mm^2/\mu m)$ Transmural oxygen gradient

μ $(mmHg\,s)$ Viscosity

τ_d (s) myogenic/diameter time constant

τ_o (s) oxygen time constant

τ_w $(mmHg)$ Shear

a Equivalence between L_0 and D_0

A Activation

A_0 Basal activation

A_c (mm^2) Cross-sectional area

C_{a1}, C_{a2} $(mmHg\,mm)$ Active tension parameter

C_{in} $(\mu M/mm^3)$ Inlet oxygen concentration

C_{da1}, C_{da2} Active tension parameter

C_{dp1} Passive tension parameter

C_{ea1}, C_{ea2} Active tension parameter

C_n $(\mu M/mm^3)$ Node oxygen concentration

CO_2 Carbon dioxide

C_{out} $(\mu M/mm^3)$ Outlet oxygen concentration

c_p $(mmHg\,mm)$ Passive tension parameter

C_{p1} $(mmHg\,mm)$ Passive tension parameter

C_{t1} $(mmHg\,mm)$ Active tension parameter

C_T $(\mu M/mm^3)$ Tissue oxygen concentration

C_v $(\mu M/mm^3)$ Vessel oxygen concentration

ΔC_v $(\mu M/mm^3)$ $C_{in} - C_{out}$

d Diameter ratio $\frac{D}{D_0}$

D (mm) Diameter

D_0 (mm) Basal diameter

D_w (mm^2/s) Diffusion coefficient in the wall

f Fraction of passive to total basal tension

G $(mm^3/mmHg\,s)$ Conductance

J_{O_2} $(\mu M/s)$ Flux

K_h $(mm^3\,mmHg/\mu M)$ Henry coefficient

k_o $(mm^3/\mu M)$ Oxygen signal weight

k_p $(/mm\,mmHg)$ Hoop stress signal weight

k_s $(s/\mu m)$ Conducted signal weight

k_w $(/mmHg)$ shear stress signal weight

K_w (mm/s) Permeability

l Length ratio $\frac{L}{L_0}$

L (mm) Length

L_0 (mm) Davis and Gore reference length

M $(\mu M/mm^3)$ Demand

m_p $(mmHg\,mm)$ Passive tension parameter

O_2 Oxygen

P $(mmHg)$ Pressure

P_a $(mmHg)$ Arterial pressure

P_n $(mmHg)$ Node pressure

P_o $(mmHg)$ Venous pressure

P_v $(mmHg)$ Mid-vessel Pressure

ΔP $(mmHg)$ Difference between inlet and outlet pressure

ΔP_{tot} $(mmHg)$ Network pressure difference $P_a - P_v$

PO_2 $(mmHg)$ Partial pressure of oxygen

Q (mm^3/s) Flow

Q_0 (mm^3/s) Basal flow

$RMSE$ Root mean squared error

R $(mmHg\,s/mm^3)$ Vessel resistance

R_g $(mmHg\,s/mm^3)$ Generation resistance

R_{tot} $(mmHg\,s/mm^3)$ Total network resistance

R_V (mm) Vessel radius

R_T (mm) Tissue radius

S Activation signal

SO_2 (%) Oxygen saturation

S_w (mm/s) Wall permeability

T_a^* Active tension divided by total basal tension

T_h $(mmHg\,mm)$ Hoop tension

$T_{act} = T_a$ $(mmHg\,mm)$ Active tension

$T_{pass} = T_p$ $(mmHg\,mm)$ Passive tension

T_p^* Passive tension divided by total basal tension

$T_{tot} = T_t$ $(mmHg\,mm)$ Total tension

v (mm/s) Velocity

V (mm^3) Volume

V_T (mm^3) Tissue volume

V_w (mm^3) Vessel wall volume

w (mm) Wall thickness

w_0 (mm) Reference wall thickness

CHAPTER 1

INTRODUCTION

The purpose of chapter 1 is to introduce the thesis by giving an overview of background information and the gaps in current models and physiological questions presented in the literature so that the motivation and contribution of the project is clear. Section 1.3 also provides a synopsis of the thesis containing a brief outline of the methods and results contained in each chapter.

SECTION 1:1 BACKGROUND

Oxygen is required by the body for cell respiration. Molecular oxygen, O_2, is used to generate chemical energy as part of metabolism, the chemical reactions in the body. Oxygen is delivered dissolved in the blood and released to cells by diffusion due to an oxygen concentration gradient between blood and the tissue surrounding blood vessels. The cardiovascular system is the network of blood vessels (the vasculature) which delivers oxygen from the lungs to tissue throughout the body, matching supply to demand. The blood vessels also transport waste products (such as carbon dioxide, CO_2) from organs. This movement of blood is driven by the heart which pumps to drive blood against gravity and friction.

Blood vessels are essentially hollow tubes, grouped functionally into ar-

teries, capillaries and veins. Arteries carry blood away from the lungs towards the capillaries which form the main site of diffusion to the tissue. Blood is transported back towards the lungs by veins. Organs are served by sub-systems of vessels, for example the cerebral vasculature carries blood in the brain. Further, there are micro-vessels (arterioles, capillaries and venules) which are smaller vessels delivering blood to local regions of tissue.

The brain has a particularly high metabolic rate and requires a constant supply of oxygen in order for cells to function. The demand for oxygen increases when the neurons in the brain are more active. Prolonged cessation of flow will lead to brain damage and eventually death. In order to increase the delivery of oxygen, arterioles dilate to increase flow in specific areas of the circulation. To reinforce this pathway, surrounding vessels constrict so that blood flows preferentially in vessels with greater volume. Similarly, if a vessel becomes blocked, feeding vessels can dilate in order to increase volume and maintain blood flow and oxygen supply. The ability of the vessels to regulate diameter is called autoregulation. This is also evident in the response of vessels to changes in pressure whereby the diameter alters in order to maintain flow.

Arterioles and venules are able to dilate passively due to the elastic fibres in the vessel wall. They are therefore able to accommodate increases in flow. Arterioles also actively dilate and constrict in order to redirect flow by contracting or relaxing the vascular smooth muscle in the walls. The smooth muscle surrounds the vessel circumference and contraction or dilation is triggered by mechanical, chemical and electrical stimuli. Relaxed vessels have some cells activated, providing the ability to dilate if necessary, this is called the basal tone. The varying contraction of smooth muscle is due to an activation signal which

sets the proportion of active muscle cells. This signal comprises of several individual signals which have varying contributions. Potential signals are, for example, due to the oxygen concentration or demand, or the pressure on the vessel wall.

Blood flows due to a difference in pressure along a vessel, and is proportional to the geometrical resistance of the vessel. An increase in diameter reduces the resistance so that flow increases. This is analogous with electrical circuits with an electrical potential difference (voltage) and flow of electrons (current). The elasticity of a vessel is similar conceptually to capacitor storage. These similarities have been widely used to develop models of the vasculature. Equivalent circuits are created by grouping parallel vessels together into a resistor and connecting an arteriolar, capillary and venular resistor together in series.

A wide variety of experiments have been carried out in the brain in order to identify blood flow, vessel geometry and oxygen concentration behaviour. The relationship between muscle tone and vessel diameter (the length-tension characteristics) has also been investigated in single vessels. Autoregulation has been confirmed by experiments whereby pressure is altered and flow recorded. Similarly, the vessel diameter and blood flow has been recorded following increased oxygen demand.

1.1.1 Current Gaps and Questions

Dynamic models of the vasculature often reproduce the results of experiments using non-physiological parameters. For clinical applications and biological insight, relevant physiological parameters should be calculated from the data. For example, there is much data available relating to oxygen concentration, as collated in section 2.3, but the data vary with tissue prepara-

tion, species and experimental method. These data and the differences need to be examined more closely in order to evaluate the application to verification of a cerebral oxygen model. This will enable the exploration of the value of the diffusion coefficient which governs oxygen transport in the brain and whether oxygen consumption in the vessel wall should be considered. Oxygen concentration and vessel geometry data have not previously been co-ordinated into a model which has experimentally validated characteristics.

The effect of vessel geometry on resistance to flow is well understood, but individual vessels are often grouped in models as equivalent resistors. Similarly, the variation of parameters in vessels of different sizes has begun to be incorporated into compartment models, but these compartments are not specifically related to the branching order, or vessel size. Where individual vessels are considered, the parameters (such as the permeability of the wall to oxygen) are assumed to be uniform which is not verified by data. On the other hand, completely physiologically relevant models which require parameters to be calculated for individual patients would not be time-efficient; detailed models are computationally costly to run. What is required is a way to derive parameters for different vessels in different-sized networks, potentially by non-dimensionalisation of reference data.

Compartmental and equivalent circuit models are useful for establishing the global (overall) response of the brain but a vascular model with individual vessels is required to learn more about the localised co-ordination of vessels in regions of the brain, especially for vessels at the smallest scale. The approximation of vessels with compartments is less physiologically relevant than an anatomical model and so a better incorporation of haemodynamics would improve the usefulness across disciplines. A cerebral model would be especially use-

ful because of the prevalence of vascular disease such as stroke and Alzheimer's amongst the population and the lack of understanding of aspects of these diseases.

The relationship between strain and tension in the vessel wall has been investigated experimentally for large vessels but without reference to the autoregulation state of the vessel. The current models therefore do not incorporate the physiological effect of oxygen demand and pressure on the level of contraction and it is difficult to relate these expressions to small vessels. Understanding the construction of the vessel wall and the mechanics of the vessel in more detail will help with the development of a more physiologically relevant wall model which incorporates current length-tension data.

Myogenic and metabolic autoregulation have been modelled separately but not in compatible models, and not dynamically within a network of vessels. Therefore the interaction of these responses cannot be investigated with current models. Further, there are several proposed hypotheses for the simulation of autoregulation which need to be considered in order to better understand the mechanism of diameter regulation. Current models require knowledge of the new steady-state network following autoregulation in order to calculate the associated signals which is not predictive. Available data could be used to validate a model which is able to simulate both myogenic and metabolic autoregulation.

Section 1:2 Motivation

The motivation for this project is therefore to develop a model which is anatomical in geometry and which accurately replicates experimental flow and oxygen concentration behaviour. This model will be a network of individual vessels with length-tension characteristics which accurately simulate the passive diameter response of vessels to changes in pressure and oxygen demand. The vessels should also display an active diameter response which is co-ordinated by pathways of feeding and surrounding vessels and therefore incorporates feedback signals which communicate physical conditions to individual vessels, and along vessel pathways. By validating against all available data, the model will be an original contribution to the understanding of autoregulation in cerebral blood vessels due to having individual vessels with appropriate geometry which display a co-ordinated active diameter response to both pressure changes and oxygen demand.

With an MRI voxel size (spatial resolution) of the order of mm rather than μm, improved understanding of microvascular networks is imperative to aid analysis of MRI data for small vessels. In particular, the ability to recreate a full vascular network from conditions in which only the larger vessels can be imaged would allow more detailed and accurate information about the cerebral vasculature to be obtained. Further, information related to the interaction of complex networks could then be inferred by using a model to simulate the dynamic behaviour of vessels, both passive and active, which can then potentially be directly linked to images in order to interpret such data.

Section 1:3 Synopsis

The literature review (chapter 2) contains a more detailed description of relevant physiology and concepts as well as an overview of experimental data. The current approaches to modelling of cerebral vascular physiology, and of autoregulation are then described. In particular, the modelling approaches to oxygen exchange are investigated in order to make sense of the varying conclusions present in the literature about oxygen consumption in the vessel wall.

Chapter 3 is a description of the creation of a geometrical vascular model based on the assumption of a bifurcating network with conserved flow at junctions. The size of the network is specified by the number of capillaries and available pressure and velocity data are used to define vessel geometry which replicates experimentally determined flow. Vessels are represented as individual resistors, whereby resistance is determined from the vessel geometry. Pressure is then calculated at the nodes between vessels with flow evaluated by the relationship between pressure, flow and resistance.

In chapter 4, data for oxygen concentration in tissue and in vessels are interpolated in order to estimate the equivalent concentrations in the new network. The oxygen concentration in blood vessels is governed by the flux of oxygen across the vessel wall, which is proportional to the concentration gradient between the blood and surrounding tissue. The effect of oxygen consumption in the vessel wall on flux is investigated in order to calculate an applicable diffusion coefficient so that oxygen concentration can be calculated at nodes only by specifying an overall inlet concentration. The result is an equivalent wall permeability which incorporates consumption in the vessel wall and is proportional to wall thickness and vessel type. A basal tissue concentration is established and the calculated oxygen concentrations are close to the original estimation from the data.

The data relating circumferential strain and tension in a single vessel are used in chapter 5 to find a mathematical relationship between diameter and passive (elastic) and active (muscle) tension. Passive tension is modelled as gaussian at low-strain becoming linear with increased diameter. Active tension is approximated with a base-level tension shift added to separate exponential functions to replicate the non-symmetrical nature of the data for negative and positive strain. The data are related to the new model by specifying basal tension calculated using the upper and lower autoregulation limits. It is shown that the new model has a higher basal proportion of activated cells than previously assumed. Finally the data and equations are non-dimensionalised for use in all vessels in the new network, regardless of diameter.

The passive and active diameter responses to pressure are then simulated in chapter 6. Signals due to shear and hoop stress are proposed which are summed to a sigmoidal activation signal which determines the fraction of activated smooth muscle cells. The contributions of the individual signals are weighted, and determined by calculating the required signal for autoregulation over the pressure range and minimising the error between the summed, and desired signals. The resulting autoregulation curve mimics the experimental curve accurately for a perfusing pressure change of ±40%.

A similar error minimisation is used in chapter 7 to calculate the weights of a local and a conducted metabolic signal due to tissue concentration and oxygen demand. The dynamic response is investigated so that the time constant of oxygen concentration and diameter change can be set in order to replicate experimental results. The dilating pathway, and surround constriction responses are thus recreated so that, together with the myogenic response in chapter 6, the model is able to autoregulate in response to global pressure changes, and local oxygen demand.

Finally, chapter 8 concludes the findings and contribution of the research. The

results are discussed in light of the limitations of the model. Possible future work is then described by which the model could be used to help to investigate vascular diseases which occur in the brain.

Summary

The thesis thus aims to describe the development of a model which is able to replicate autoregulation. The creation of a vascular anatomical model with experimentally validated geometry, flow and oxygen concentration is described in chapters 3 and 4. The length-tension characteristics of each vessel are approximated by a mathematical function as determined in chapter 5. The contribution of active tension to total tension is set by the activation signal with contributions from hoop tension, shear stress, oxygen demand and tissue concentration as described in chapters 6 and 7 so that the myogenic and metabolic diameter responses are replicated by the model. Chapter 8 provides the conclusion of the thesis; a discussion of the model and its limitations, and of potential future usefulness and improvements.

CHAPTER 2

Literature Review

To develop an improved model of the cerebral vasculature requires background knowledge about the function of the cardiovascular system as a whole and the specific details about the brain. This literature review covers a wide range of physiological background detail including blood circulation within the brain and the structure of blood vessels. In order to assess reference data for model validation, experimental data related to the geometry of the cerebral vasculature and oxygen dynamics are introduced along with a description of the experimental methods used. With reference to available data as evidence, the hypotheses of oxygen exchange are then discussed as a foundation for investigation of parameters. The chapter goes on to introduce the phenomenon of autoregulation; the ability of blood vessels to dilate and constrict in response to global network pressure and local tissue demand. Potential mechanisms of autoregulation are reviewed in light of the physiology of muscle contraction. Also included is an outline of available mathematical relationships and equations which describe the physiology of blood flow, oxygen exchange, tension and autoregulation which are a basis for further development in the thesis. Finally, some existing vasculature and autoregulating models are described which form a useful starting point for further development. The limitations of these models are presented as motivation for the work in the rest of the thesis.

Section 2:1 Blood Circulation

This section provides background physiological information related to the cerebral vasculature. First, there is a general introduction to the cardiovascular system and blood vessels with a subsequent focus on the cerebral circulation and vessel construction. The contraction of the smooth muscle in the vessel wall is described since it provides necessary detail for the understanding of the literature relating to autoregulation.

2.1.1 The Cardiovascular System

The cardiovascular circulatory system delivers oxygen to tissue cells and removes carbon dioxide through the transport of blood. As well as oxygen, nutrients are transported to cells from the gastrointestinal tract and metabolic waste from cells to the kidneys. The system comprises the pulmonary and systemic circulation. The former is a loop through the heart and lungs, carrying oxygen-depleted blood away from the heart, through the lungs where it is oxygenated and back to the heart [258]. The systemic circulation takes the oxygenated blood from the heart to organs of the body and back to the heart. Together, these form a closed system of pump, distribution, exchange and collection. The nutrients, waste and gases are transported around the circulation by blood through a network of blood vessels. The heart is the pump and periodic contractions generate blood pressure which causes movement of blood, pumping it against gravity [133].

2.1.2 Blood Vessels

Blood vessels are hollow tubes which form a network known as the vasculature. The space inside a vessel is the lumen and the diameter of a blood vessel denotes this internal lumen diameter. There are three broad types of vessel: arteries, capillaries and veins. The 'distribution' vessels are arteries taking blood containing oxygen and nutrients to the capillaries through the arterioles (smaller arteries). The capillaries are the exchange vessels exchanging oxygen for carbon dioxide,

and nutrients for metabolic waste. Blood is then collected by venules and taken back to the lungs and kidneys through the veins [133]. The arterioles and venules form the micro-circulation serving specific organs and areas of tissue [246]. Arterioles are also the primary regulators of blood flow to the tissue they supply via contraction and dilation [133]. A single arteriole gives rise to a capillary bed which empties into a venule (Figure 2.1).

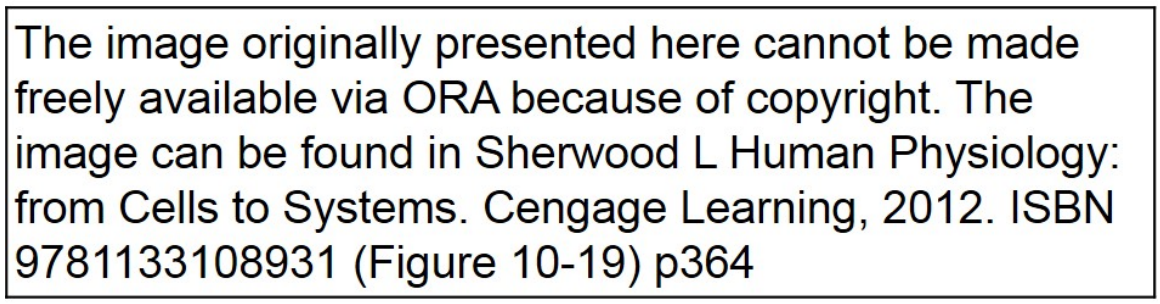

Figure 2.1: *Showing two capillary beds connecting an arteriole and venule [223].*

Blood exerts pressure against vessel walls (blood pressure) which is normally expressed in mmHg (millimetres of mercury where 1 $mmHg = 133Pa$, see Table C.1) and the difference in pressure between inlet and outlet causes flow. Blood is a two-phase fluid containing red and white blood cells and platelets, all suspended in a liquid medium (plasma). Plasma carries proteins, electrolytes and hormones and accounts for 55 % of blood volume. The volume percentage of red blood cells is known as the haematocrit and is typically about 40 %. The red blood cells (erythrocytes) transport the dissolved oxygen which is attached to haemoglobin [45]. Platelets are a very small proportion of blood volume (1 %) and are primarily responsible for coagulation (clotting) of blood after injury. The remainder (white blood cells or leukocytes) are part of the immune system [258].

2.1.3 Cerebral Oxygen Supply

The brain has a high metabolic rate: even though it accounts for only 2 % of body weight, it uses 20 % of resting oxygen consumption [48]. Also, since brain

tissue is unable to store the oxygen and glucose it requires, it is critically dependent on a constant blood supply of between 45 and 65 $ml/100gbrain/min$ or 15 – 20 % of blood flow from the heart [274] . This equates to an oxygen supply of 3.5 $ml/100gbrain/min$ [164] or a metabolism of between 1.3 and 1.8 $\mu mol/g/min$ [274]. Cerebral tissue is thus the most vulnerable of all tissues to ischaemia [227] such that cessation of flow, even for a few minutes, leads to permanent brain damage [164] with five seconds of hypoxia leading to a loss of consciousness [22] and prolonged flow lower than 8 $ml/100g$brain/min rapidly resulting in tissue death [181]. To ensure adequate supply, the vessels are able to regulate flow by dilating or constricting in order to direct oxygen to local tissue. This diameter adjustment is called autoregulation.

2.1.4 The Cerebral Circulation

Oxygen is distributed to tissue in the brain through the cerebral vasculature; the arterial distribution of vessels. The main arteries entering the brain are the two internal carotid arteries at the front, and the two vertebral arteries at the back [2]. Between these, a ring of arteries encircles the under-surface of the brain (called the Circle of Willis) which need not be a complete circle and shows individual variation [21]. From the Circle of Willis, anterior cerebral arteries sprout as well as the anterior communicating artery, middle cerebral arteries, posterior communicating arteries, carotid termini, posterior cerebral arteries and basilar artery apex. From the larger arteries at the base of the brain arise pial arteries which spread over the surface of the brain and dip downwards. From these arteries emerge the arterioles at right angles which perforate into the brain substance and end in capillaries, which drain into venules and back up to veins [69].

2.1.4.1 Vessel Construction

Different vessel types have different wall compositions depending on their function but arterial and venous vessels have three layers in different proportions:

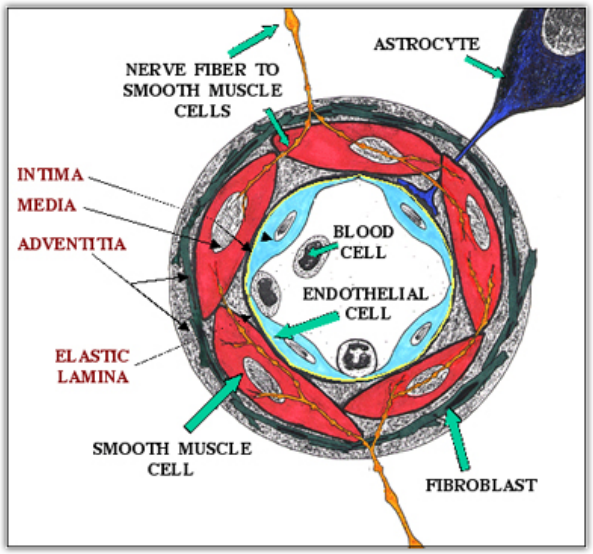

Figure 2.2: *Showing a cross-section of a brain artery with the hollow lumen. The intima (with endothelial cells coloured in light blue) lying on their basal laminar (the black circle). The elastic laminer under the basal laminer. The media (smooth muscle cells) and the adventitia (containing fibroblasts in green, collagen fibres and orange nerve fibres linking to the smooth muscle cells). The dark blue cell outside is an astrocye which surround endothelial cells in the cerebral capillaries. http://www.brain-aneurysm.com/ba1.html*

the inner intima, the thicker media and the outer adventitia [203]. Figure 2.2 shows a section across a brain artery. Between the intima and media is a thin layer of elastic protein tissue (the elastic lamina). In most non-cerebral vessels there is a further elastic layer between the media and adventitia [24]. There are also different components of the blood vessel wall. The intima (which is also found in capillaries) consists of a thin layer of endothelial cells (and is called the endothelium) [125]. The media is comprised of smooth muscle cells and elastin fibres. In the adventitia are fibroblast cells which produce fibrous collagen protein. This fibrous connective tissue has high tensile strength, especially in larger vessels so that a vessel can expand to accommodate a pressure wave of blood flow and then contract to squeeze the blood downstream. As vessels get further from the heart, blood flow becomes less pulsatile since it has been damped by the storage effect of the upstream vessels [133].

The endothelial cells line the interior surfaces of blood vessels. These cells

reduce turbulence of flow by reducing friction and therefore reducing the shear stress of fluid against the vessel wall [218]. They also form a selective barrier for the transport of molecules between blood and tissue [8]. Since they are in direct contact with flowing blood, they are exposed to shear stress which causes cellular deformation [199]. It is thought (as reviewed by Burnstock [37]) that these cells release extra-cellular chemicals when exposed to shear stress which are involved in signalling to the smooth muscles. The smooth muscle enables active contraction of the wall when necessary to either squeeze blood along (closer to the heart), or to restrict and to control blood flow. The smooth muscle comprises vascular smooth muscle cells (VSMCs) which have adrenergic receptors (adrenoceptors) that bind with adrenaline and affect muscle tone by specifically recepting the vasodilating and constricting factors released by the endothelium [261].

Both arteries and veins have layers of smooth muscle surrounding them but arteries have thicker layers of muscle and more elastic fibres and have more pulsatile flow. In the micro-circulation, arterioles are thinner than arteries with very little elastic connective tissue and one or two layers of smooth muscle (and therefore a higher contractile but lower stretch capability) [223]. Post-capillary venules (sometimes described as meta-venules [223]), however, have no smooth muscle [246] since they are functionally more similar to capillaries than venules. Veins and venules have a higher capacity for blood than corresponding arteries and arterioles due to their thin walls and this allows veins to have increased flow when necessary. It also reduces the friction on the vessel wall. The venous pressure difference is not great enough to drive blood flow against gravity (for example from the legs back to the heart) and so the veins also have valves to stop flow moving backwards [258]. Capillaries have small diameter and thin walls through which diffusion occurs [258]. The wall of the capillary comprises of a single layer of endothelial cells so that the diffusion distance from blood to tissue is minimal [223].

2.1.4.2 Smooth Muscle

At rest, the smooth muscle in the vessel wall is not completely relaxed, since in order to regulate flow, vessels must be able to both constrict and to dilate. The vessel diameter is therefore held slightly constricted. This low-level active tension is called the basal condition [15]. The resulting tone (continuous contraction) of smooth muscle is based on the interaction of thin and thick filaments: actin and myosin. These filaments slide over each other using energy from hydrolysis of ATP (Adenosine-5'-triphosphate). The heads of the myosin filament interact with the actin to 'pick up' and move a few nanometres (similar to a treadmill). This is repeated along the actin filament. Physiologically, it is the changes in ion flux, membrane potential and intracellular calcium concentration which control contraction via calcium-calmodulin-dependent phosphorylation of the regulatory myosin light chains and subsequent myosin cross-bridge cycling [150].

Unlike skeletal muscle, the smooth muscle contraction is not triggered by an action potential [223] . VSM contraction can be initiated by mechanical, electrical and chemical stimuli which lead to an increase in intracellular Ca^{2+} concentration. An increase in calcium promotes binding of calcium to the cytoplasmic regulatory protein calmodulin. This forms a calcium-calmodulin complex $CaCM$ which activates myosin light chain kinase (an enzyme that assists in the phosphorylation of myosin light chains). Myosin cross-bridges then repetitively bind and unbind to actin filaments which generates the active force for contraction, and reducing cell length [133].

Chemical stimuli (such as angiotensin) can cause contraction by binding to specific receptors on the muscle cell or to the adjacent endothelium. The amount of force produced is proportional to the number of active acting/myosin binding sites. The process of contraction is initiated by an electrical stimulation. This is induced by an increase in intracellular calcium (either due to opening of cal-

cium gates, or release of internal calcium) [3]. Intracellular calcium concentration is a balance between calcium entering the cell through calcium gates, the calcium released by intracellular storage and the removal of calcium by calcium pumps. Calcium pumps are ATP dependent and so the energy for contraction comes from hydrolysis of ATP which requires oxygen [133]. Dilation is initiated by removing the stimulus for contraction, blocking calcium uptake or by specific dilating agents.

Section Summary

This section described how blood vessels are arranged in the brain so that the requirements for oxygen are met. The ability of the blood vessels to dilate and to constrict in order to maintain supply has been introduced as the physiological mechanism of autoregulation. In order to dilate or constrict, the smooth muscles in the vessel wall must be activated and this mechanism (via the interaction of myosin and actin) has been described in detail along with the chemical initiation of smooth muscle contraction. In section 2.2, the relationship between blood flow and vessel geometry is now explored.

Section 2:2 Haemodynamics

The aim of this section is to present the equations used to determine the resistance of vessels due to their geometry, since it is by diameter adjustment that autoregulation occurs. The equations which relate geometry, blood pressure and flow (along with the assumptions necessary to derive them) are described along with the parameters. This section also presents the results of experiments carried out to identify vessel geometry and blood flow which can be used to verify the geometry of vessels in a model.

2.2.1 Poiseuille's Law

The dynamics of blood flow in vessels are governed by haemodynamic laws, for individual vessels and over the entire network. They are subject to the same principles as the flow of electrons in a circuit; movement due to a potential difference which faces resistance to flow. Blood flows due to a longitudinal pressure gradient ΔP. For the whole cerebral vasculature, this driving pressure (the cerebral perfusion pressure) is the difference between the mean arterial pressure and cerebral venous pressure. For an individual vessel, it is the difference between the inlet and outlet pressure of each vessel $\Delta P = P_{in} - P_{out}$ [258].

Resistance in a network R is defined by the ratio of driving pressure ΔP and flow Q:

$$R = \frac{\Delta P}{Q}. \tag{2.1}$$

This is comparable with Ohm's law for electric circuits and the ratio of electromotive force and current [133]. The hydraulic resistance of an individual vessel can be given by the Hagen-Poiseuille relationship for flow in a tube and is dependent on the diameter of the vessel, D, the viscosity of the fluid, μ, and the length of the vessel, L [258]:

$$R = \frac{128 L \mu}{\pi D^4}. \tag{2.2}$$

Flow is thus especially sensitive to the diameter of the vessel (note the fourth power of diameter) so that small changes have a large effect on resistance. When groups of parallel vessels are connected in series, blood flows preferentially through those pathways with least resistance offering greater local control.

Poiseuille's relationship is valid only with the following assumptions:

- Blood is incompressible
- The vessel is straight, rigid, cylindrical and has constant radius
- The velocity of blood at the wall is zero (the no-slip condition)

- The blood flow is laminar (concentric cylinders) and steady

In tubes where the internal diameter is large compared with red blood cell diameter, blood behaves essentially as a Newtonian (incompressible) fluid. The elastic fibres in vessel walls makes the vessels distensible rather than rigid. Although vessels taper, they are sufficiently short to assume that they are cylindrical in shape. However, a blocked vessel can induce turbulent flow [40, 90] which would invalidate Poiseuille's relationship. Due to the endothelial lining of the vessel wall, it is reasonable to assume no-slip so that the velocity at the wall is zero. For flow to become non-laminar, the Reynolds number has to be greater than 3000 [133]. Moore et al. [169] found that flow in the brain can be assumed to be laminar (since the maximum Reynolds number is approximately 200).

2.2.2 Viscosity

One important further consideration is viscosity, which is non-constant. Viscosity is a property of fluids that indicates the resistance to flow, being the proportionality constant between the stress on the vessel wall due to flow and the velocity gradient. The viscosity of blood depends on both the vessel diameter (because of both wall separation and wall surface area) and varies non-linearly haematocrit H (volume percentage of red blood cells) Figure 2.3 [258]. The latter is due to cell deformation (at high haematocrit) and cell stickiness (at low haematocrit). Viscosity is monotonically dependent on radius for small vessels (the Fåhræus–Lindqvist phenomenon): vessels smaller than 1 mm show decreased viscosity down to $5-7$ μm before increasing again [60]. Figure 2.3 shows this effect for small radius.

A relative viscosity, μ_{rel} in centipoise cP, can be used as determined by Pries et al. [194] accounting for diameter (D μm) and discharge haematocrit (H_D %), the

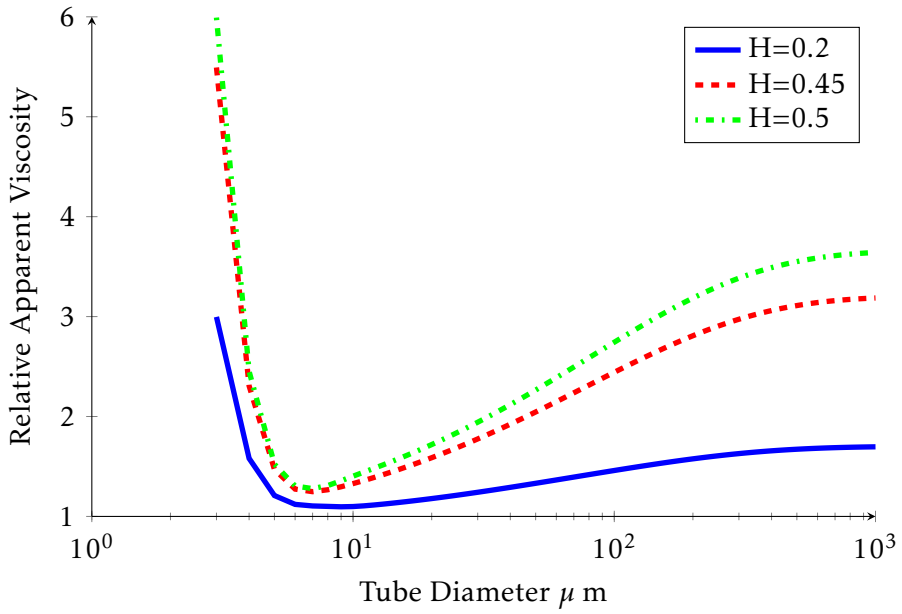

Figure 2.3: *Showing how blood viscosity is affected by haematocrit and diameter*

haematocrit at the outlet of the tube, for diameters between $9\mu m$ and $40\mu m$:

$$\mu_{rel} = 1 + (\mu_{rel0.45} - 1)\frac{(1 - H_D)^C - 1}{(1 - 0.45)^C - 1} \tag{2.3}$$

$$\text{where } \mu_{rel0.45} = 220e^{-1.3D} + 3.2 - 2.44e^{-0.06D^{0.645}} \tag{2.4}$$

$$\text{and } C = (0.8 + e^{-0.075D})\left(-1 + \frac{1}{1 + 10^{-11}D^{12}}\right) + \frac{1}{1 + 10^{-11}D^{12}}. \tag{2.5}$$

2.2.3 Transmural Pressure

A vessel is subject to two pressure gradients, the first is the longitudinal gradient which causes the flow of blood, and the other is across the vessel wall ($\Delta P = P_{internal} - P_{tissue}$). This is called transmural pressure P_t and since the interstitial (tissue) pressure is normally assumed to be zero, intravascular pressure at each point along the vessel is often used as the transmural value [223]. For a short vessel with steady flow, transmural pressure is given as the mean pressure in the vessel:

$$P_t = \frac{P_a + P_v}{2}. \tag{2.6}$$

2.2.4 Compliance

The cerebral circulation is confined within a closed space (the skull and craniospinal axis) which limits the capacity to buffer blood volume change. Therefore, a change in vessel diameter affects intracranial pressure through a change in cerebral blood volume [253]. This is described by the Monro-Kellie doctrine, a biochemical law which means that any volume variation is accompanied by an alteration in intracranial pressure [166] [123]. There is therefore a non-linear elastic relationship between transmural pressure and radius.

Compliance C is defined as the change in volume ΔV following a change in transmural pressure ΔP_t and is similar to electrical capacitance:

$$C = \frac{\Delta V}{\Delta P_t}. \tag{2.7}$$

This analogy with electrical capacitance models the storage of blood in the elastic vessels. In the cerebral micro-vasculature, the arterioles have a high proportion of smooth muscle compared with elastic fibres and so their elasticity is often ignored [182].

2.2.5 Wall Thickness

The vessel wall is normally considered to be incompressible so that wall tissue volume is conserved [35]. With external radius, R_e, equal to internal radius plus wall thickness, $R_e = R_i + w$, assuming constant length:

$$(R_{i,0} + w_0)^2 - R_{i,0}^2 = (R_i + w_0)^2 - R_i^2, \tag{2.8}$$

where subscript 0 denotes reference values of radius and wall thickness.

2.2.6 Measurement of Blood Flow

Flow can be quantified based on the Fick principle, using the concentration of a radioactive substance as a tracer [126]. The difference between arterial and

cerebral tracer concentration is a measure of flow. Similarly, the injection of labelled micro-spheres can be used to calculate flow [104]. Flow can also be measured invasively using electromagnetic flow-meters [159] where a vessel is placed in a magnetic field and flow calculated proportional to voltage induced when the magnetic blood flows. An alternative method is the ultrasound flow-meter (Transcranial Doppler Insonation) [97, 26] where a pair of probes are placed on the vessel and flow calculated from the Doppler shift, the difference between emitted and reflected frequencies induced by moving fluid. Both these methods determine velocity; if the vessel cross-section area is assumed constant, this gives a measure of flow rate [127]. Transcranial doppler ultrasound facilitates continuous measurement of flow velocity enabling monitoring of dynamics, as long as the cross-sectional area is indeed constant.

Magnetic resonance imaging can be used with angiography to visualise blood vessels. The addition of phase-contrast allows encoding of flow velocity in vessels [88]. Recent developments in MRI perfusion imaging have made vascular territories mapping possible [100]. This uses vessel encoded arterial spin labelling (VEASL) of water in arterial blood to show flow in specific vessels. It acts as a tracer for perfusion MRI so that the arterial blood water is magnetised differently from tissue. This magnetisation of water does not decay radioactively (as with injected contrast agents), it decays much more quickly but the temporal resolution is correspondingly higher. Vessels are encoded in sequence, and the difference in images acquired with and without ASL shows the perfusion at each voxel.

2.2.7 Flow in individual vessels

There have been only a few investigations of individual vessel flow in the vasculature which are now described in more detail.

Zweifach and Lipowsky [281] adapted methods used to calculate impedance in circuits to determine resistance for successive segments of terminal vascular

bed. Flow through individual branches was interrupted by a needle and upstream-downstream pressure recorded until zero-flow reached. This was treated as a short-circuit in an analogous electronic circuit. Zweifach and Lipowsky presented a graph of 200 data points describing arterial to venous distribution of intravascular pressure and velocity in cat mesentery (where each data point is the average of 3-5 measurements at that diameter). This is reproduced here (Figure 2.4) and is an invaluable resource since it is indexed by vessel diameter, found by extraction of the mesentery vessels.

The image originally presented here cannot be made freely available via ORA because of copyright. The image source is http://circres.ahajournals.org/content/41/3/380.full.pdf (Figure 5)

Figure 2.4: *The arterial to venous distribution of intravascular pressure and velocity in mesentery. Diameter is representative of the position of the vessel within the network. Each data point represents the average value of three to five measurements at that diameter. The curves are a piece-wise cubic spline fit of the data. Reproduced directly from [281]*

Torres et al. [239] measured red blood cell velocity in hamster skinfold using photodiodes. Results are given in Table 2.1. The velocities of the smaller vessels are comparable with those measured at equivalent diameter in Figure 2.4, although the venules here have much lower velocity.

Vessel Order	D (μm)	v (mm/s)
1A	64.3 ± 20	5.8 ± 3.5
2A	31.6 ± 12.1	3.2 ± 2.1
3A	13.4 ± 5.5	2.2 ± 1.1
4A	7.7 ± 2.4	1.4 ± 0.9
V	65.5 ± 38.0	0.7 ± 0.5

Table 2.1: *Results taken from [239] giving vessel diameter and velocity of flow.*

2.2.8 Measurement of Vessel Geometry

Table 2.2 collates vessel dimension values from various experimental results. Where possible, these are characterised by branching order which reduce in diam-

eter towards the capillaries. For example, $3A$ is the third generation of arteriole. Of these experiments, Harper and Bohlen [93] and Vovenko [265] both investigated the rat cerebral vasculature. Harper extracted the geometry from images of both hypertensive(*) and control rats and investigated the passive diameter when intravascular pressure was increased. The cerebral capillary is larger than that found in the retractor muscle. Zweifach also found capillaries around 8 μm as shown in Figure 2.4. However, the arterioles in the brain are smaller than those at equivalent branching order in the retractor muscle (for example, compare the diameter of second-order arterioles $A2$: 34.3 and 33 μm in the rat brain with 45 μm in the hamster retractor). The size of the capillary is limited by the size of red blood cells, the diameters of the vessels moving away from capillaries is based on the density of vessels in the vascular bed and this affects the total flow, a more important consideration than branching order.

Vessel Order	D (μm)	w (μm)	Preparation	Reference
Arteriole	9.5	6.5	Rat liver	Seiyama [216]
Arteriole	23.2	6.5	Rat mesentery	Tsai [242]
Arteriole	24	2.4	Rat mesentery	Tsai [242]
Arteriole	29.9	2.2	Hamster cheek	Davis and Gore [57]
1A	51.2	6.02	Rat cerebral	Harper [93]
1A	42.5*	7.74	Rat cerebral	Harper [93]
2A	34.3	5.69	Rat cerebral	Harper [93]
2A	27.1*	5.81	Rat cerebral	Harper [93]
3A	21.6	4.08	Rat cerebral	Harper [93]
3A	21.1*	4.43	Rat cerebral	Harper [93]
4A	12.5	3.80	Rat cerebral	Harper [93]
4A	9.4*	4.32	Rat cerebral	Harper [93]
1A	64	15.8	Hamster retractor muscle	Kuo [139]
2A	45	11.2	Hamster retractor muscle	Kuo [139]
3A	35	8.8	Hamster retractor muscle	Kuo [139]
4A	19.5	6.5	Hamster retractor muscle	Kuo [139]
1A	62	15.3	Hamster retractor muscle	Kuo [140]
2A	50	12.4	Hamster retractor muscle	Kuo [140]
3A	40	10.0	Hamster retractor muscle	Kuo [140]
4A	23.9	6.5	Hamster retractor muscle	Kuo [140]
1A	55	13.6	Hamster retractor muscle	Swain [234]
2A	45	11.2	Hamster retractor muscle	Swain [234]
3A	34	8.6	Hamster retractor muscle	Swain [234]
4A	22	6.5	Hamster retractor muscle	Swain [234]
1A	45		Rat cerebral	Vovenko [265]
2A	33		Rat cerebral	Vovenko [265]
3A	26		Rat cerebral	Vovenko [265]
4A	13		Rat cerebral	Vovenko [265]
5A	8		Rat cerebral	Vovenko [265]
Capillary	8		Rat cerebral	Vovenko [265]
Capillary	3.4	0.5	Hamster retractor muscle	Ellsworth [74]
Capillary	3.6	0.5	Hamster retractor muscle	Stein [231]
Capillary type III	4.4	0.17	Rat cerebral	Shaver [222]
5V	13		Rat cerebral	Vovenko [265]
4V	31		Rat cerebral	Vovenko [265]
3V	71		Rat cerebral	Vovenko [265]
2V	145		Rat cerebral	Vovenko [265]
1V	258		Rat cerebral	Vovenko [265]
Venule	65.5		Hamster skinfold	Torres [239]
Post-cap. venules	8-30	av 10	Cat cerebral	Roggendorf [204]
Collecting Venule	30-50	av 3.33	Cat cerebral	Roggendorf [204]

Table 2.2: *Variation in diameter and wall thickness in various tissue preparations*

Section Summary

Haemodynamics describes the relationship between flow, resistance and pressure in the vessel where resistance is a function of the geometry of the vessel. The Hagen-Poiseuille equation has been given and the parameters and necessary assumptions outlined. The viscosity of blood is non-constant and a relationship between vessel diameter and haematocrit is necessary to calculate the vessel resistance. This section also describes the measurement of both blood flow and vessel geometry with attention paid to those experiments carried out in cerebral preparations. The next section is a discussion of the distribution and consumption of oxygen in the brain, both theoretically and in reference to experimental results.

Section 2:3 Oxygen Concentration

Oxygen and carbon dioxide are exchanged between air and blood in the lungs, and between blood and tissue in vessels. The oxygen transport in the brain is dependent on the availability of oxygen in the blood and the metabolism of oxygen by cells. The current approach to oxygen transport, consumption and exchange differs between models, partially due to the differences in the data sets which are used. This section aims to assess these differences by collating available data and parameter values and comparing in light of these differing hypotheses in order to assess their validity for an improved model and to establish a data source for model validation.

2.3.1 Definitions for Oxygen Content

There are various ways to describe the amount of oxygen present depending on how oxygen is carried in the blood. Concentration, C, is the mass per unit volume, saturation, SO_2, the percentage (or fraction) of bound oxygen by volume and partial pressure, PO_2, the proportion of pressure (or tension) exerted by oxygen in the mixture of total blood pressure.

The concentration of oxygen in blood is the number of moles per unit volume taken by adding the amount dissolved in plasma (typically 2%) and the amount bound to haemoglobin (typically 98 %) [258]. The oxygen content in a vessel is calculated as:

$$C = \alpha PO_2 + \beta[Hb]SO_2(P), \tag{2.9}$$

where the partial pressure PO_2 is measured in $mmHg$. α signifies the solubility of O_2 in plasma (which is 90 % water [256, 161]). The saturation SO_2 is a measurement of oxygen bound to haemoglobin (haematocrit $[Hb]$) with β being the oxygen-carrying capacity per unit volume of red blood cells (which are 70 % water [161]). The capacity of oxygen bound to haemoglobin is greater than the solubility in plasma [161].

Each molecule of haemoglobin can bind four molecules of oxygen [258] and this binding is both rapid and reversible. The oxygen saturation SO_2 is therefore calculated as the percentage of bound haemoglobin HbO_2 to total, including unbound Hb:

$$SO_2 = \frac{HbO_2}{Hb + HbO_2} \times 100. \tag{2.10}$$

Valabrègue et al. [256] use a value of $[Hb] = 2.3\ mM/L$ in their cerebral model. The relationship between blood saturation and partial pressure is shown by the oxyhaemoglobin dissociation curve which is sigmoidal and well approximated by the empirical Hill equation [219] for $SO_2 > 0.3$:

$$PO_2 = \left(\frac{SO_2 \times P_{50}^H}{1 - SO_2} \right)^{1/H} \tag{2.11}$$

where P_{50} is the partial pressure at which 50 % of haemoglobin is bound to O_2 (typically about 26.6 $mmHg$ in a healthy human [263]) and H the hill coefficient for (2.7 – 3.0 for haemoglobin [219]). Arciero et al. [6] use values of $H = 2.8$ and $P_{50} = 26\ mmHg$ for skeletal muscle. Valabrègue et al. [256] give $H = 2.73$.

As oxygen partial pressure increases, more oxygen molecules bind to haemoglobin until a maximum amount is reached (giving an overall sigmoidal relationship between partial pressure and oxygen saturation). Above $PO_2 = 60mmHg$, the saturation does not change significantly with partial pressure and any further increase in oxygen concentration is due to oxygen dissolved in plasma [263].

An increase in temperature, or decrease in pH, shifts this curve to the right, increasing P_{50} (so that there is decreased affinity of haemoglobin for oxygen, making it harder for haemoglobin to bind to oxygen but easier to release). A change in pH can be caused by a change in the concentration of chemicals (e.g. hydrogen or carbon dioxide): an increase in pCO_2 decreases the affinity for O_2. The conversion between oxygen partial pressure and saturation was approximated by Kelman [124] by converting values to standard temperature and pH (see Figure 2.5). The curve fit for $10 < PO_2 \leq 100\ mmHg$ is modelled as:

$$x = Pa_{O_2} 10^{(0.24(37-T)+0.4(pH-7.4)+0.06(log10(40)-log10(Pa_{CO_2}))} \tag{2.12}$$

$$SO_2 = 100(a_1 x + a_2 x^2 + a_3 x^3 + x^4)/(a_4 + a_5 x + a_6 x^2 + a_7 x^3 + x^4) \tag{2.13}$$

with standard values of $PaO_2 = 84\ mmHg$, $pH = 7.4$, $PaCO_2 = 40\ mmHg$, $T = 37^oC$ and coefficients:

a_1	-8.5322289×10^3	a_5	-3.1346258×10^4
a_2	2.1214010×10^3	a_6	2.3961674×10^3
a_3	-6.7073989×10^1	a_7	-6.7104406×10^1.
a_4	9.3596087×10^5		

The image originally presented here cannot be made freely available via ORA because of copyright. The image was sourced at http://jap.physiology.org/content/21/4/1375.full.pdf

Figure 2.5: *The Kelman (Equation 2.13) model approximation of the oxygen dissociation curve reproduced from [124] .*

The relationship between partial pressure and plasma concentration is linear, according to Henry's law [258]:

$$C_P = \alpha P_{O_2} = \frac{1}{K_h} P_{O_2}. \tag{2.14}$$

In Equation 2.14, K_h is the Henry coefficient, the reciprocal of solubility α. The relationship between total blood and plasma concentration is:

$$C_B = C_P + \frac{[Hb]PO}{1 + (\frac{\alpha P_{50}}{C_P})^H}. \tag{2.15}$$

Various values for solubility are found in the literature, some of which are summarised in Table 2.3. The units vary between the volume fraction in the solvent, and the molar concentration. The molar mass of oxygen is 32 g/M, and the density 1.429 g/L (at body temperature and pressure), therefore the molar volume conversion is:

$$1(\mu M)/mm^3 = 22.39(ml O_2)/ml. \tag{2.16}$$

Solubility varies with temperature, pressure and solvent. α refers to the solubility in plasma (3×10^{-5} $ml O_2/ml(plasma)/mmHg$ at $37^o C$ [156, 161]), which is assumed to be the same as in water, $\alpha_{\text{water}} = 1.39 \times 10^{-6}$ $\mu M/mm^3/mmHg$ [256]. Oxygen is also dissolved in red blood cell water and in tissue ($\alpha_{\text{tissue}} = 2.6 \times 10^{-5}$ $ml O_2/ml(\text{tissue})/mmHg$ in brain tissue [46]). Popel et al. [193] calculated solubility in vessel wall tissue from the oxygen gradients. Table 2.3 collates various values from literature and shows that Tsai cites a low value for plasma, which is normally approximated as water. Likewise, blood is approximated as plasma, for oxygen diffusion purposes. Tissue has a lower solubility than blood.

Solvent	$\alpha \times 10^{-5}$ $(mlO_2/mlmmHg)$	$\alpha \times 10^{-6}$ $(\mu M/mm^3mmHg)$	Preparation	Reference
Water	3.11	1.39*	Water	Valabregue [256]
Plasma	2.14*	0.96	Rat mesentery	Tsai [242]
Plasma	3.3*	1.47	Hamster retractor muscle	Vadapali [255]
Plasma	3*	1.34	Human skeletal muscle	McGuire [156]
Blood	3.4*	1.52	Human skeletal muscle	Hyman [108]
Tissue	2.9*	1.30	Human skeletal muscle	Hyman [108]
Tissue	2.6*	1.16	Human brain	Mintun [163]
Tissue	2.84*	1.27	Hamster striated muscle	Kuo and Pittman [139]
Tissue	2.85	1.275*	Hamster retractor muscle	Popel [193]

Table 2.3: *Various solubility values as used by other investigators to convert partial pressure into oxygen concentration. Asterisked* are the original units.*

2.3.2 Oxygen Dynamics

The model of oxygen in the brain has two parts: the amount of oxygen extracted from blood into tissue, and the amount of oxygen in tissue which is consumed. Figure 2.6 is a vessel diagram showing a compartmental model of oxygen exchange between capillary and tissue which will be expanded in the following text.

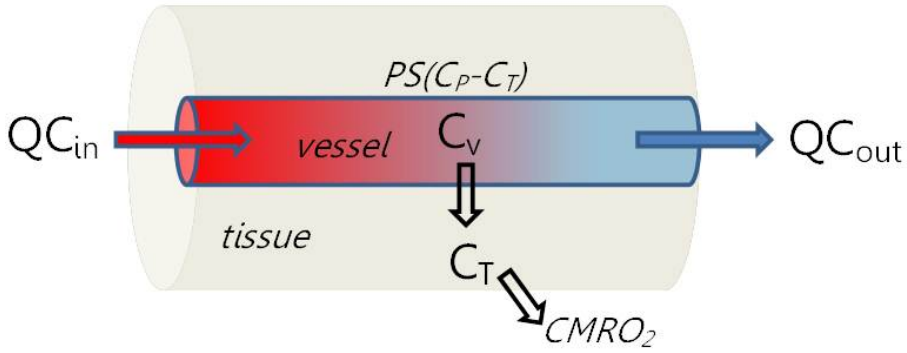

Figure 2.6: *The vessel and model compartments showing oxygen entering and exiting the vessel, and being transferred to tissue and metabolised.*

In Figure 2.6, C_v is the blood vessel oxygen concentration, C_P the plasma concentration and C_T the tissue concentration. At the arterial end of the vessel, C_{in} is the arterial blood concentration and, similarly, C_{out} the concentration at the venous end. Flow is Q so that the total amount of oxygen entering the vessel is QC_{in}.

PS is the wall permeability, P, multiplied by the wall surface area, S, and $CMRO_2$ the rate of consumption of oxygen.

Longitudinal oxygen diffusion can be ignored with comparison to convection if the Péclet number is greater than 1 (so that convection is more significant than longitudinal diffusion). Park and Payne [189] calculate the Péclet number to be of the order of $10-100$. The Péclet number is calculated as:

$$Pe = \frac{LU}{D}, \tag{2.17}$$

where L is the characteristic length ($\sim O(100)\ \mu m$), U the velocity ($\sim O(1)\ mm/s$) and D the mass diffusion coefficient ($\sim O(\times 10^{-5})\ cm^2/s$).

2.3.2.1 Mathematical Model

The flux of oxygen J is the rate of movement of molecules of oxygen across the vessel wall ($moles/m^2/s$) [258]. The flux of oxygen is related to the diffusion coefficient, D_c, of oxygen, and the permeability of the wall, P, and is normally assumed to be proportional to the concentration gradient, ΔC, across the vessel wall.

The diffusion coefficient, D_c, refers to diffusion in space and depends on the substance (oxygen), mass and temperature. The permeability coefficient, P_c, also depends on the material [165] and is substituted for the diffusion coefficient when describing flux through a cell membrane. However, most investigators described here use the diffusion coefficient to refer to the specific diffusion of oxygen in tissue. The overall permeability of the wall depends on the thickness of the membrane, Δx, so that thinner walls have higher permeability. P and D_c are related by the non-dimensional partition coefficient K (the ratio of concentrations in a mixture of two phases at equilibrium).

$$P = \frac{KD_c}{\Delta x}. \tag{2.18}$$

Boas et al. [27] define vessel permeability, K_w, as a function of diffusion coefficient D_c and wall thickness w:

$$K_w = \frac{P}{K} = \frac{D_c}{w}. \tag{2.19}$$

Flux can therefore be described by Fick's law of diffusion, such that oxygen flux across the wall depends on the permeability of the wall to oxygen, K_w, and the diffusion distance, z (which could be wall thickness w) [27] :

$$J_{O_2} = -K_w \frac{\Delta C}{z}. \tag{2.20}$$

The concentration gradient of oxygen between tissue, $C_T(z)$, and blood, C_v, is the driving force of diffusion. In their study of labelled O_2, Kassissia et al. [120] found that most oxygen never leaves the capillary (only that dissolved in plasma C_P). Valabrègue et al. [256] therefore applied this mass balance between plasma C_P and tissue concentration using Henry's law (Equation 2.14) to convert between partial pressure and plasma concentration. The barrier to diffusion can be considered to be either the vessel wall, or inclusive of the tissue surrounding the vessel [256]. Therefore, D_c can be approximated as either D_w or D_T and z as either w (the wall thickness) or d, the diffusion distance into tissue [258].

The concept of mass balance can be applied to the transport of oxygen in blood vessels [243] so that, conserving mass, the amount of oxygen entering a segment, $Q \times C_{in}$, minus the amount exiting, $Q \times C_{out}$, equals the diffusion flux out of the vessel J_{O_2}:

$$J_{O_2} = \frac{Q}{\pi DL}(C_{in} - C_{out}). \tag{2.21}$$

The oxygen extracted in a vessel then is the flux times the surface area of the vessel wall (πDL):

$$OE = \pi DL J_{O_2}. \tag{2.22}$$

Vadapalli et al. [255] define a flux into the vessel wall, J_i, and out into tissue, J_o, assuming that oxygen is consumed in the vessel wall by smooth muscle and

endothelial cells. The flux from blood into the vessel wall is calculated from the saturation gradient, $\Delta SO_2/L$, with Equation 2.9 as:

$$Q[Hb]\beta\Delta SO_2 = \pi DLJ_i. \tag{2.23}$$

Applying a mass balance to Equation 2.22 for vessel concentration C_v results in a solvable ordinary differential equation for the longitudinal oxygen gradient:

$$Q\frac{dC_v}{dz} = -\frac{D_c}{z}\pi D(C_T - C_v(z)). \tag{2.24}$$

For Equation 2.24 to be valid, steady state must be assumed. Vessels are assumed to not taper so that D is constant over the entire length and, similarly, they are assumed straight. The blood is approximated as well mixed, so that concentration is the same over the entire radius. Finally, the oxygen concentration in tissue surrounding the vessel C_T is assumed to be uniform over the entire length of the vessel.

The concept of an oxygen extraction fraction, OEF, has been established to describe how much oxygen is consumed by tissue compared to the blood concentration [39]:

$$OEF = \frac{C_{in} - C_{out}}{C_{in}}. \tag{2.25}$$

The fraction of extracted oxygen which is metabolised is described by the efficiency ϵ. Kassissia et al. [120] found that the fraction of extracted O_2 that returns to the vasculature from tissue is very small. Therefore, Buxton and Frank [39] argue that oxygen extraction must be almost completely efficient ($\epsilon = 1$) so that metabolised oxygen $CMRO_2$ is equal to the flux of oxygen from the vessel in basal conditions.

2.3.3 Tissue Consumption

Oxygen is delivered to tissue to satisfy the metabolic demand; the amount of oxygen necessary for reactions in tissue. The oxygen transport system ensures that the amount of oxygen available to tissue satisfies demand, with a base level of oxygen dissolved in tissue.

The Krogh cylinder model [135] assumes that each vessel (radius R) supplies oxygen to a cylindrical section of surrounding tissue with radius R_T. In the vessel, oxygen is transported through the blood by both convection and diffusion whereas, in tissue, transport is via diffusion. The volume of tissue is:

$$V_T = \pi(R_T^2 - R^2)L. \tag{2.26}$$

Although the Krogh model represents capillary tissue, Duling and Berne [64] showed that oxygen also diffuses in arterioles in the brain. Data from Vovenko [265] show a reduction in oxygen concentration across all vessels and radially through tissue surrounding all three types of vessel (see subsection 2.3.5).

Tsai et al. [242] find a maximum arteriolar diffusion distance of 93.6 ± 11.1 μm in rat mesentery by solving Equation 2.24 with $C_T = 0$. Mintun [163] sets capillary tissue radius R_T to 32 μm (half of human intercapillary distance). Middleman [161] defines the ratio of R_T to R_C as 10. Instead of a cylinder, Hudetz [106] uses a cone model for capillaries with the tissue radius varying from 38 μm at the arteriolar end to 18 μm at the venular end, where less oxygen is available in the vessel. Therefore, the vessel oxygen concentration is likely to determine the diffusing distance with arterioles supplying the largest volume of tissue, and venules the least. There is thus no agreed way of using a Krogh cylinder model.

2.3.4 Wall Consumption

The diffusion coefficient refers to the diffusivity of oxygen in tissue [165]. It is an approximation of the diffusivity of oxygen in the various components of the wall and tissue. If the vessel wall consumes oxygen in smooth muscle and endothelial cells, then the demand must be incorporated into the equation for flux so that, at steady state, M is the steady state oxygen demand of the wall per unit area in $\mu M/mm^2/s$.

Instead of setting a wall permeability, Arciero et al. [6] incorporate this func-

tional demand M of the wall. The model combines mass balance and the Krogh cylinder model to give the change in concentration measurements across the wall as a function of demand, wall volume and flow in arterioles and capillaries (but excluding venules):

$$\frac{dC_T}{dL} = \frac{\pi M(R_T^2 - R^2)}{Q}. \tag{2.27}$$

Similarly, Mintun et al. [163] use a Krogh model and calculate the oxygen tension in radial tissue (at distance r) using PO_i (the concentration at the vessel/tissue interface), and tissue consumption M:

$$PO_T(r) = PO_i - \frac{M \cdot R_T^2}{2D_w \cdot \alpha} \cdot ln(r/R) - \frac{M(R_c^2 - r^2)}{4P_w \cdot \alpha}. \tag{2.28}$$

2.3.5 Measurement and Data

There are very few measurements of oxygen concentration available in the literature. The Clark electrode [47] is a polarographic method where the polarographic electrode is a noble metal membrane-covered cathode with a reference electrode. Current flows in the circuit formed by the electrodes and medium. The electrode consumes oxygen and generates a current proportional to the partial pressure. The Clark electrode is insulated with a gas-permeable membrane. It is used in-vitro to determine dissolved oxygen concentration at different points by converting between partial pressure and oxygen concentration via Henry's law. Electrodes have a tendency to drift which reduces their reliability for long-term observation, but the initial spatial resolution is very fine. Over time, the accuracy of an electrode diminishes because of the consumption of oxygen by the method, and by the contamination of the electrode surface. A thin membrane ($7\mu m$ [10]) allows greater spatial accuracy, and a fast response time, but the degradation of the electrode happens more quickly. The electrode must also be calibrated frequently in order to convert the generated current to partial pressure.

Alternatively, light absorption of haemoglobin can be used to determine the partial pressure of oxygen in blood [240]. Oxygen saturation is determined by measurements of light absorption at different wavelengths of the haemoglobin absorption spectrum and the relative amounts of oxy- and deoxy-haemoglobin quantified. The partial pressure is calculated by the oxygen dissociation curve. The method is indirect and must be corrected for light scattering by the red blood cells. Further, partial pressure cannot be determined in tissue by haemoglobin spectrophotometric methods. Near infrared spectroscopy (NIRS) uses light in the infrared region of the spectrum ($700 - 1000\ nm$) which is able to penetrate tissue up to $8\ cm$ [51]. It is also able to monitor changes in the oxygenation of the brain. Within tissue, there are two compartments of light attenuation: the absorbers (with fixed concentration) and the chromophores (with varying concentration). The chromophores are, for example, oxyhaemoglobin HbO_2 and deoxyhaemoglobin Hb. Changes in concentration can be determined from the change in light attenuation assuming that tissue absorption remains constant but with low spatial resolution.

Blood oxygen level-dependent functional magnetic resonance (BOLD fMRI) measures blood oxygenation based on the fact that HbO_2 is paramagnetic (exhibits magnetisation proportional to the applied magnetic field) and Hb diamagnetic (not attracted into a magnetic field). Therefore if the concentration of HbO_2 increases, there is a change in magnetic susceptibility and alteration of the MR signal. This method is continuous (with temporal resolution of about $1\ s$) with 2 or $3\ mm$ spatial resolution. However, the signal is noisy and so statistical procedures are necessary to establish the underlying signal.

There is also the phosphorescence quenching technique [259] which allows high spatial resolution of oxygen tension. A slow injection of porphyrin dye is phosphoresced by excitation with light and the rate of decay of phosphoresce de-

pends on the amount of oxygen surrounding the dye. The technique allows for simultaneous optical measurement of PO_2 in the vessel and surrounding tissue so that the gradients, and oxygen flux, can be calculated [241]. The calibrations performed in vitro can be applied to in vivo measurements since the rate of decay is independent of material. However, the phosphorescence decays consume oxygen (0.01 $mmHg$/flash [243]) which distorts the signal. This can be avoided by using repeated low intensity light excitation so that diffusion can replenish the consumed oxygen [226, 238]. The spatial resolution is greater than with physical electrodes [245].

$CMRO_2$ can be measured globally using the disappearance rate of a tracer, bound to oxygen. To measure local $CMRO_2$ directly involves arresting perfusion and so it can be done instead by defining a rate factor between flow and tissue oxygen transport in order to determine the time constant of the oxygen response to demand [151].

$CMRO_2$ can also be measured with positron emission tomography (PET). PET combines the principles of CT (computerised tomography) and SPECT (single photon emission computerised tomography) where radioisotopes are incorporated into oxygen to make a radio pharmaceutical. When the labelled atom disintegrates, the emitted positron annihilates with an electron producing two beams of gamma rays in opposite directions. These rays strike the scanner at 2 points and produce energy which can be mapped to show regional increases in metabolism.

Oxygen flux can be measured with photon counting. Photon counting is a non-invasive measurement which uses light. When light enters the photocathode of a photomultiplier tube, photo electrons are emitted. These photoelectrons induce secondary electron emission which is collected as an output pulse by the anode.

Values for flux, metabolism, permeability and oxygen gradients can also all be calculated using the equations described which model oxygen exchange. These

calculated values have been listed alongside experimental values in the following section.

2.3.5.1 Vessel Concentration

Vovenko [265] offers data related to the partial pressure of oxygen in the microvasculature of rat brain measured by needle oxygen micro-electrodes, the results being given in Table 2.4. These can be combined with vessel geometry to show the consumption of oxygen across the vasculature. The values in Table 2.4 are similar to those found by Duling [68]: $PO_2 = 80.1 \pm 3.4$ $mmHg$ in the lumen of 45 ± 3 μm cerebral cat arterioles and 72.6 ± 3.6 $mmHg$ for 22 ± 2 μm arterioles. The results are used by Boas et al. [27] as an approximation of the human cerebral microvasculature. The conversion used by Vovenko between the partial pressure measured and oxygen saturation requires recalculation of the oxygen disassociation curve for $PaCO_2 = 34.2$ $mmHg$, $PaO_2 = 85.6$ $mmHg$ and $pH = 7.37$. However, even with these values the Vovenko results are difficult to replicate. In the brain, the longitudinal capillary gradient is substantial [243] due to a high metabolic rate. Vovenko found a longitudinal capillary gradient of 0.0659 $mmHg/\mu m$ [265] with a drop across the capillaries from 57.9 ± 10.6 $mmHg$ at the arterial side, to 40.9 ± 11.1 $mmHg$ measured at the venous side. The partial pressure at the outlet of the capillary is lower than the average concentration in the next venular generation $5V$ (41.1 ± 10.9 $mmHg$). The rise in oxygen partial pressure in $5V$ compared with the capillary C is attributed to collateral circulation (possible shunts directly between arterioles and venules) by Tsai et al. [243], though it could be due to the variability of the measurements.

Popel et al. [193] calculated lower values of luminal PO_2 in hamster retractor muscle, for example finding a partial pressure of 31.6 $mmHg$ in the lumen of 23.5 μm diameter arterioles. Similarly, Torres et al. [239] investigated hamster skinfold with phosphorence and found lower values of PO_2 (as given in Table 2.5).

Vessel Order	D (μm)	PO_2 (mmHg)	SO_2 (%)	Vessel Order	D (μm)	PO_2 (mmHg)	SO_2 (%)
1A	45 ± 7	81.2 ± 6.2	94 ± 2	1V	258 ± 31	41.3 ± 9.7	59 ± 14
2A	33 ± 7	78.7 ± 8.9	94 ± 2	2V	145 ± 15	39.6 ± 10.1	57 ± 16
3A	26 ± 7	75.8 ± 11.1	93 ± 6	3V	71 ± 24	40.1 ± 9.1	57 ± 14
4A	13 ± 4	68.3 ± 8.3	89 ± 8	4V	31 ± 9	41.1 ± 10.9	59 ± 17
5A	8 ± 2	61.5 ± 12	84 ± 11	5V	13 ± 6	38.2 ± 12.3	54 ± 18
C	8	50	63				

Table 2.4: *Summarising the results in rat brain from [265] giving vessel diameter and partial pressure of oxygen. The partial pressure is converted to oxygen saturation using the equation from [219].*

Vessel Order	D (μm)	PO_2 (mmHg)
1A	64.3 ± 20	51.8 ± 9.8
2A	31.6 ± 12.1	44.1 ± 9.1
3A	13.4 ± 5.5	39.9 ± 9.2
4A	7.7 ± 2.4	34.8 ± 7.9
V	65.5 ± 38.0	30.8 ± 10.8

Table 2.5: *Summarising the results from Torres [239] in hamster skin giving vessel diameter and partial pressure of oxygen.*

A summary of such data was compiled by Tsai et al. [243] and is reproduced in Figure 2.7. It compiles information from various studies in microvessels done by different methods. It shows that the brain study by Vovenko had the highest partial pressures and, since the brain tissue is of interest, these data are preferred as a reference. The brain also has the lowest venular oxygen gradient with a large gradient in pre-capillary arterioles.

Figure 2.7: *The oxygen tension in various experiments reproduced from Tsai et al. [243]*

2.3.5.2 Tissue Concentration

The tissue oxygen pressure is characterised as heterogeneous by Lübbers and Baumgärtl [145] when measured polargraphically, other techniques show tissue pressure of $10 - 40$ $mmHg$ (i.e. slightly lower than venous PO_2) [174]. Johnston

et al. [118] assume that tissue concentration is equal to the concentration in the end-capillary compartment. Masamoto and Tanishita [151] concluded that since P_{T,O_2} is well maintained within a narrow range, it can be considered homogeneous and, likewise, Boas et al. [27] approximate tissue concentration as 15 $mmHg$ for all vessels as an average of the two values proposed by Popel (20 and 10 $mmHg$) [99].

Measuring partial pressure in tissue is difficult due to the drifting of oxygen sensors, and potential consumption of oxygen by the measuring technique [242]. There is therefore much variation in reported tissue concentrations. Metzger and Heuber [158] measured arteriolar tissue oxygen pressure polargraphically and found it to be negligible. In cats and dogs, normal tissue concentration is reported at 28±7 $mmHg$ [147], with 32–36 $mmHg$ reported in patients during brain tumour surgery [7] and 25 – 104 $mmHg$ in patients having surgery on aneurysms [62].

2.3.5.3 Tissue Oxygen Gradient

The radial oxygen gradient can be used to normalise the tissue concentration. Vovenko measured oxygen tension in rat cerebral tissue at points up to 40 μm from 10 – 30 μm diameter arterioles, 5 – 7 μm capillaries and 10 – 40 μm venules and showed a non-linear decrease in tension. There is a ±10 % experimental error associated with the results, and some vessels have obviously differing radial oxygen gradients to the others. Vovenko's results are reproduced in Figure 2.8. The gradient in tissue surrounding arterioles is normally quoted at about 1 $mmHg/\mu m$ [243] as an average of the 1.5 $mmHg\mu m$ close to the vessel wall established by Vovenko and 0.5 $mmHg/\mu m$ at 40 μm from the arteriole wall [265] .Tsai et al. [242] found an oxygen gradient of around 0.7 $mmHg/\mu m$ in the tissue surrounding rat mesentery arterioles, up to 40 μm; the results are reproduced in Figure 2.9.

For capillary tissue, Vovenko [265] determined a gradient of 0.25 – 0.5 $mmHg/\mu m$ in the more distal 40 μm surrounding tissue to cerebral capillaries in rats. Between the capillary wall, and the distal site of tissue supplied by the capil-

The image originally presented here cannot be made freely available via ORA because of copyright. The image was sourced at http://link.springer.com/article/10.1007%2Fs004240050825 (figure 3)

Figure 2.8: *The radial tissue oxygen gradient reproduced from [265] for rat cerebral microvasculature*

The image originally presented here cannot be made freely available via ORA because of copyright. The image was sourced at http://physrev.physiology.org/content/83/3/933.long (figure 5)

Figure 2.9: *The radial tissue oxygen gradient for rat mesentery reproduced from [243] for different individual vessels measured. The shaded portion is the distance occupied by the vessel wall and the upper line gives the gradient if the wall and tissue are assumed to have the same rate of oxygen consumption.*

lary there was a $10-20$ $mmHg$ difference in partial pressure of oxygen. Integlietta et al. [111] found a higher value of 1.5 $mmHg/\mu m$ in capillaries using the phospherescence method in experiments close to the wall of skinfold capillaries. This implies that most of the diffusion occurs close to the vessel in arteriolar and capillary tissue.

Integlietta et al. [111] also investigated the gradient around the venules, finding a value of 3 $mmHg/\mu m$ in skeletal muscle of hamster. Again, this was higher than the $0.1-0.4$ $mmHg/\mu m$ found by Vovenko in rat pial microcirculation. Tsai compares these results and proposed that, in venules, the supply of tissue is very much dependent on the vascular bed and organ [243] with the brain having lower tissue oxygen gradients, despite the higher intra-vascular PO_2.

2.3.5.4 Tissue Consumption

The amount of oxygen metabolised by tissue is the cerebral metabolic rate, $CMRO_2$, or M_T. The oxygen consumption rate of vascular tissue is reported to be in the range $1.1-4.5$ $\times 10^{-3} ml O_2/\text{min}/g$ [241]. For 24 μm arterioles, Swain and Pittman [233] found a tissue consumption rate of 1.57 $\times 10^{-4} ml O_2/ml/s$ in the hamster retractor muscle, approximately the same as 1.6 $\times 10^{-4} ml O_2/ml/s$ de-

clared for human cerebral by Middleman [161]. Tsai et al. [243] calculated a tissue consumption rate of 1.4 $\times 10^{-2} ml O_2/(g\text{tissue})/min$ for tissue in the rat mesentery, using the partial pressure oxygen profile in tissue and converted with cerebral tissue density 1.05 g/ml [209]. Hudetz [106] proposed a mathematical model of the cerebral capillary with consumption 8.34 $\times 10^{-4} ml O_2/(cm^3 s)$ and Mintun et al. [163] calculated a tissue oxygen consumption of 8.2 $\times 10^{-4}$ $cm^3 O_2/cm^3/s$ from the diffusion coefficient in the human brain. Therefore, the tissue consumption calculated from the diffusion rate and flux is much higher than that calculated from the partial pressure oxygen gradient.

Consumption M_T ($\times 10^{-4} ml O_2/ml/s$)	Preparation	Reference
1.57	Hamster retractor arterioles	Swain and Pittman [233]
1.6	Human cerebral	Middleman [161]
2.4	Rat mesentery	Tsai [243]
8.20	Cerebral capillary model	Hudetz [106]
8.34	Cerebral diffusion model	Mintun [163]

Table 2.6: *Summarising tissue consumption values from a variety of sources.*

2.3.5.5 Tissue Diffusion Coefficient

Mintun et al. [163] set baseline tissue consumption to 8.2 $\times 10^{-4} ml O_2/cm^3/s$ starting from a diffusion coefficient D_T equal to 1.8 $\times 10^{-5}$ cm^2/s . Middleman quotes $D_T = 1.5 \times 10^{-5} cm^2/s$ in human cerebral tissue. Popel uses a smaller value of $D_T = 1.39 \times 10^{-5} cm^2/s$ [99] taken from Kuo and Pittman in hamster striated muscle [139] and Ursino et al. [250] sets $D_T = 1.6 \times 10^{-5} cm^2/s$ for a human cerebral model. These values have less spread than the tissue consumption values with a higher value from Mintun compared with Middleman.

Diffusion Coefficient $\times 10^{-5} cm^2/s$	Preparation	Reference
1.39	Hamster striated muscle	Kuo and Pittman [139]
1.5	Human cerebral	Middleman [161]
1.6	Human cerebral model	Ursino [250]
1.8	Human cerebral model	Mintun [163]

Table 2.7: *Summarising tissue diffusion coefficient values from a variety of sources.*

2.3.5.6 Flux

Vadapalli et al. [255] neatly summarised various values of flux calculated from values for $\Delta S/L$ (saturation gradient) in the literature. These are reproduced here in Table 2.8 with some other experimental values added.

However, Vadapalli also uses Equation 2.23 to show that flux is of the order of $3-4 \times 10^{-6} ml O_2/(cm^2 s)$ for all vessels, which is smaller than the values reported in Table 2.8, reinforcing the idea that the diffusion coefficient in tissue and over the vessel wall cannot be considered the same (as discussed in subsubsection 2.3.5.8).

Vessel Order	D (μm)	J ($\times 10^{-6}$ $ml O_2/(cm^2 s)$)	Preparation	Reference
Capillary	3.4	0.8	Hamster retractor muscle	[74]
Capillary	3.6	1.2	Hamster retractor muscle	[231]
Terminal Arteriole	8.5	63	Rat pancreas	[217]
Arteriole	9.5	11 – 32	Rat liver	[216]
Arteriole	23.2	27	Rat mesentery	[242]
Arteriole	23	24	Rat mesentery	[244]
1A	64	51	Hamster retractor muscle	[139]
2A	45	50	Hamster retractor muscle	[139]
3A	35	58	Hamster retractor muscle	[139]
4A	19.5	42	Hamster retractor muscle	[139]
1A	62	49	Hamster retractor muscle	[140]
2A	50	82	Hamster retractor muscle	[140]
3A	40	84	Hamster retractor muscle	[140]
4A	23.9	65	Hamster retractor muscle	[140]
1A	55	40	Hamster retractor muscle	[234]
2A	45	42	Hamster retractor muscle	[234]
3A	34	65	Hamster retractor muscle	[234]
4A	22	48	Hamster retractor muscle	[234]
1A	64.3	41	Hamster skinfold	[239]
2A	31.6	21	Hamster skinfold	[239]
3A	13.4	6.7	Hamster skinfold	[239]
4A	7.7	1.5	Hamster skinfold	[239]

Table 2.8: *Collating the results of experiments to show variations in intravascular flux.*

2.3.5.7 Transmural Oxygen Gradient

Transmural oxygen gradients have been measured on cat pial arterioles [68], rat mesenteric arterioles [242], [243], rat cremaster muscle [224], and dog carotid arteries [210]. These data vary significantly, from ≤ 1 to 20 $mmHg/mm$. The largest gradient is in the first few micrometres, the endothelial layer [243]. Sharan, however, found a gradient in the range of $1 - 2$ $mmHg/\mu m$ in rat pial microvessels [221] and ascribed higher values to misuse of the mass transport equation when calculating values.

Santilli et al. [210] determined the profile of the partial pressure of oxygen within the vessel wall of dog with a microelectrode, finding a steep gradient, espe-

cially in the endothelial layer, of 20 $mmHg/\mu m$. Tsai et al. [243] found an overall gradient between 4 and 11 $mmHg/\mu m$ over the rat mesentery vessel wall with values of blood PO_2 of 23 and 49 $mmHg$ respectively (see Figure 2.9). This was for arteriole vessels with walls 2.5 to 3.5 μm thick. For a 23.2 ± 2.9 μm diameter vessel with wall 2.3 μm thick, the transmural oxygen difference was 18.1 ± 1.7 $mmHg$ with an absolute partial pressure in the vessel of 43.3 ± 3.7 $mmHg$ [242]. In the hamster skeletal muscle venule, Intaglietta et al. [111] found a transmural gradient of 4.17 $\mu M/mm^3/\mu m$.

Of these studies, only Duling et al. [68] investigated cerebral vessels (in cat) but the experimental method has been criticised by Tsai [243]. Duling found a transmural difference of 6.5 $mmHg$ and 11.9 $mmHg$ in 45 ± 3 μm and 22 ± 2 μm lumen vessels respectively (corresponding to gradients of approximately 0.81 $mmHg/\mu m$ and 1.98 $mmHg/\mu m$). Vovenko found drops in PO_2 in the cerebral cortex of rat comparable to those in pial arterioles, of $1 - 2$ $mmHg/\mu m$ at control and 0.7 $mmHg/\mu m$ for dilated vessels [266]. Duling found a relationship between transmural tissue gradient ΔP_{O_2} $mmHg$ and wall thickness w in μm:

$$\frac{\Delta P_{O_2}}{w} = 0.91 + 0.87/w. \tag{2.29}$$

The high regression coefficient (0.98) implies a uniform wall tissue consumption proportional to wall thickness.

There are therefore two conflicting conclusions found in the literature: that the oxygen gradient in the arteriole wall is similar to the surrounding tissue (in which case the diffusion barrier of the wall can be incorporated into tissue); or that it is much higher due to the endothelial layer.

2.3.5.8 Consumption in the wall

Swain and Pittman [234] state that "flux of oxygen from the arterioles is greater than would be expected by passive diffusion". They calculated oxygen consumption compared to oxygen extraction of 10 % for larger hamster retractor arterioles

and 35 % for the 4th generation arteriole vessels. This implied a further compartment which consumes oxygen, or another reason for high oxygen gradient longitudinally along the vessel. One possibility is the shunt vessels which link arterioles to venules [220]. Other hypotheses are a different wall permeability, and consumption in the vessel wall compared with surrounding tissue.

Using the value of flux determined by Kuo and Pittman in hamster striated muscle [139], Popel [99] calculated the oxygen gradient in the wall required to give the experimentally determined flux as being 15 $mmHg/\mu m$ for a Krogh diffusion coefficient ($K_w = P_w\alpha$) of 4.2 - 6.8 $\times 10^{-10} ml O_2/cm/mmHg/s$ and, with reference to the value found by Sharan in the rat brain, concluded that the the diffusion coefficient must be an order of magnitude higher than previously thought. The chosen value was $D_w = 1.39 \times 10^{-5} cm^2/s$ and Ursino et al. [250] used a similar value of $D_w = 1.3 \times 10^{-5} cm^2/s$. Ursino's value is smaller than the one used in the surrounding tissue ($1.6 \times 10^{-5} cm^2/s$ see Table 2.7). As an approximation for the whole wall, Tsai et al. [242] set the diffusion constant to be $1.7 \times 10^{-5} cm^2/s$ based on experiments by Baumgartl and Lubbers [12].

A change in wall permeability affects the longitudinal gradient of oxygen since increased wall resistance to diffusion would also decrease the flux of oxygen out of the vessel. Endothelial cells studied in cell cultures have an oxygen consumption rate in the range of $2 - 8 \times 10^{-2}$ $ml O_2/min/g$ [241] measured using the phosphorence technique. Consumption by the endothelial and smooth muscle cells of the wall was therefore deemed a possibility by Tsai et al. [242]. Endothelial cells are involved in the synthesis and production of wall material (collagen and elastin) and in chemicals which affect muscle tone (e.g. nitric oxide) in which it was pointed out that the large transmural gradients indicated consumption in the vessel wall. Figure 2.9 shows that the wall PO_2 profile is significantly different to that in surrounding tissue and so two rates of oxygen consumption are implied. Whereas

other studies suggest a consumption rate closer to that of the surrounding tissue [85], [192], Tsai proposed a consumption rate, $M_w = 3.9\ mlO_2/g\text{tissue}/min$, two orders of magnitude higher than surrounding tissue (on average 277.8 ±45.0 times higher) with a related diffusive flux of $2.2 \pm 0.2 \times 10^{-5} mlO_2/(cm^2 s)$. This is of the same order as the hamster retractor arterioles seen in Table 2.8. The resulting consumption in the wall is $6.5 \times 10^{-2} \pm 0.5 mlO_2/cm^3\text{tissue}/s$ [243]. Duling et al. [68] estimated the consumption of the cat pial vessel wall to be $1.7\ mlO_2/min/g\text{tissue}$ ($2.97 \times 10^{-2} mlO_2/ml/s$) in order to match gradients found by microelectrode study [255] .

Vadapalli et al. [255] investigated a theoretical model of flux as a function of demand (see Equation 2.23) and found that it remains constant over four orders of magnitude of M. This equation assumes flux into the wall to be a function of both diffusion coefficient and oxygen demand, and uses the transmural oxygen gradient as $PO_v - PO_T$. The resting hamster retractor muscle consumption is around $5 \times 10^{-3} mlO_2/ml/s$, and demand increases with muscle contraction. Vadapalli calculated that J is of order $10^{-6}\ mlO_2/cm^2/s$, and that the consumption is likely to be the same as for resting muscle. This flux is an order of magnitude smaller than found from the longitudinal gradients in Table 2.8. He concluded that the values of flux found as a function of longitudinal gradient are over-estimates and so diffusion coefficients are likely to be too high.

In endothelial cells in vitro, D_c has been found to vary between $1.4 - 8.7 \times 10^{-6}\ cm^2/s$. Vadapalli sets the overall Krogh constant for the wall to $K_w = \alpha D_w = 3.17 \times 10^{-10}\ mlO_2/cm/mmHg/s$ ($D_w = 9.61 \times 10^{-6} cm^2/s$) with 4.45×10^{-10} $mlO_2/cm/mmHg/s$ for the endothelial cell layer, and $4.5 \times 10^{-10} mlO_2/cm/mmHg/s$ for smooth muscle. This value for D_c is 1.77 times smaller than that proposed by Tsai. The findings of Vadapalli on flux are therefore of interest. Flux calculated from longitudinal gradients and constant tissue concentration are higher than cal-

culated as a function of demand. This has an impact on reported values for diffusion coefficient calculated from flux.

Instead of the diffusion coefficient, Valebrègue et al. [256] use PS to represent permeability P multiplied by the surface area S of capillary exchange with a value of 7020 or 3000 $ml/min/100g$ depending on metabolic demand. This is based on experiments carried out by Kassissia et al. [120] who calculated a value of tracer oxygen permeability $P_c = D_c/z$ as 5.3 $\times 10^{-3} mm/s$ across the capillary wall in dog brain. Boas [27] used an approximate extraction coefficient over the vessel wall of $k_w = 7 \times 10^{-15} M/mmHg/s$ for all vessels regardless of length or diameter for the control state (where tissue partial pressure is 15 $mmHg$). However, Boas models the vasculature as a network of vessels with constant length which is unrealistic. The approximation of wall permeability as a function of diffusing distance implies that wall volume may effect resistance to oxygen. If the amount of smooth muscle, for example, is proportional to the wall volume; this is a way to normalise permeability and demand for the dimension of the vessel.

Section Summary

The experimental literature considered here shows that the reported oxygen concentration in vessel and tissue varies with the vasculature and species considered and with experimental method. Blood and tissue can be considered to be the same in differing species, the main difference is in the oxygen demand across species and vasculature. As well as oxygen demand (and therefore flux), the geometry has an effect on the vessel concentration because of the longitudinal gradient and surface area. Where possible, it is important to use cerebral references and to relate these to vessel diameter in order to extrapolate from different species. Vovenko and Duling agree on vessel concentration in the brains of rat and cat and so these form a useful reference for any model. Similarly, Duling and Vovenko agree on the transmural gradients as being similar to surrounding tissue gradients.

There are also differing hypotheses for fitting Fick's law to data for oxygen concentration. These depend on whether the wall and tissue are considered as separate barriers to diffusion, and therefore if there are two compartments or three (including the vessel). The diffusion coefficient for the wall may or may not be different to the surrounding tissue. It depends on whether the transmural gradient is assumed to be larger than in tissue. The wall comprises of tissue, endothelial, and smooth muscle cells with resultantly different resistance to oxygen (permeability). Higher transmural gradients imply higher consumption in these vessels than for surrounding tissue. If the consumption of oxygen by these cells is incorporated into the model, the demand affects the diffusion coefficient. However, Figure 2.9 shows that this is necessary to replicate the wall and tissue gradient in cerebral vessels.

Section 2:4 Vessel Mechanics

Although vessel strain is included in current models, the expressions are not explicitly linked to physiological parameters and the application to small vessels has not been investigated. The mechanics of the blood vessel wall are therefore introduced in this section beginning with an overview of the terminology of stress and strain and continuing with a discussion of the mechanical properties of the components of the vessel wall. The experimental relationship between diameter stretch and tension is included and the resulting models of muscle and elastic component tension described.

2.4.1 Background: Stress and Strain

The difference between internal and external pressure P results in a net force F which is balanced by wall tension T. For a thin-walled vessel and small section δx, this area of the wall in cross section (two sides of lumen) is approximately $\delta A = 2w\delta x$. The circumferential (or hoop) tension is a function of both transmural pressure (P_t which is equal to intravascular pressure P, see subsection 2.2.3) and

vessel diameter by Laplace's law:

$$T = \frac{PD}{2}. \tag{2.30}$$

Laplace's law holds for thin-walled vessels, where the wall thickness is less than 10 % of the vessel radius. However, Pries and Secomb use a thin-wall assumption for cerebral vessels [198] where the wall thickness is up to 30 % of the diameter. A thin-walled vessel can be considered a surface where tension is consistent throughout the wall thickness. There is a relationship with diameter because pressure must stay the same over an entire shape (due to Pascal's principle of pressure equilibrium) and therefore a higher radius (with higher surface area) must have a higher tension.

The force acts to dilate the vessel with a resulting circumference extension ΔL modified by the wall stiffness k:

$$F = \Delta L k. \tag{2.31}$$

The inverse of stiffness is the vessel compliance C which is calculated for an elastic vessel as:

$$C = \frac{\Delta V}{\Delta P}. \tag{2.32}$$

The circumferential extension can be normalised as strain ϵ

$$\epsilon = \frac{\Delta L}{L_0} = \frac{\Delta D}{D_0}. \tag{2.33}$$

Under strain, the vessel wall generates a circumferential balancing stress σ [16], where stress and strain (dilation) are related by the elastic [Young's] modulus E of the vessel wall such that:

$$E = \frac{\sigma}{\epsilon}. \tag{2.34}$$

Many investigators (see example [38, 142, 152]) describe an incremental modulus to fit the pressure-radius curve which varies widely for differing vessel types. Bergel [18] defined an incremental elastic modules for Hooke-type deformation.

2.4.2 Mechanical Properties of Blood Vessels

The stress-strain relationships of blood vessels are strongly nonlinear and so there is no definitive Young's modulus for the stiffness of the vessel wall [270]. The difficulty with ascribing a mathematical description of the vessel lies in the three components of blood vessel walls having different mechanical characteristics. The stiffness of the vessel and elasticity modulus of the constituent materials are related by the dimensions of the vessel where A_0 is the reference area.

$$k = \frac{EA_0}{D_0}. \tag{2.35}$$

This expression implies that large vessels must have stiffer (less elastic) walls since they have larger radius and therefore greater stress [42]. Monson et al. [167] investigated the stiffness of vessels of different size, and from different locations. Monson compared properties of available cadaver vessels to a few fresh vessels in order to investigate whether the more widely available cadaver data can be used. He investigated the mechanical properties of fresh cerebral arteries and veins of around 0.052 mm diameter [168] from the brain surface and demonstrated both that arteries are dramatically stiffer than veins, and also that they fail at twice the stress. Furthermore, cadaver vessels behaved similarly to fresh vessels but with less extensibility.

2.4.2.1 Elastin and Collagen

Elastin is an elastomeric protein which behaves linearly (Hookean) up to large strains with a Young's modulus in the range $0.1 - 1$ MPa (for example, cited as 0.6 MPa by Middleman [161]). Elastin is a soft nonlinearly elastic material and is assumed isotropic. It is extensible up to about 140 % before failure [270]. Collagen is stiffer than elastin and smooth muscle with values of Young's modulus ranging from $5 - 9$ GPa [53] with a maximum extension of 10 % [270]. Collagen fibre mesh is stiff, nonlinear and anisotropic.

2.4.2.2 Smooth Muscle

The active vascular smooth muscle in the vessel wall generates a contractile force, or an active tension which opposes the direction of stretch by contraction or dilation and contributes to the overall tension acting on the vessel wall. Smooth muscle is a combination of contractile and elastic components and can take different contractile states. A contracted smooth muscle cell can generate a stress (force per unit area) of $240 - 400\ kPa$ [173] with an elastic modulus 10 times larger than relaxed state [270] between 51 kPa [260] and 1.38 MPa, calculated by Brozovich and Morgan [36] from stress-strain relationships. Smooth muscle present in the vessel wall can be modelled as something which modifies the stiffness parameter of the vessel wall. There is therefore a non-linear dependence of total compliance on muscular compliance [16].

2.4.2.3 Total Stress

There is variation in elasticity between vessels due to the differing proportions of elastin, collagen and smooth muscle and the total stress σ_T (calculated as force over the total area) is the sum of elastic σ_e and active stress σ_a.

$$\sigma_T = \sigma_e + \sigma_a. \tag{2.36}$$

2.4.3 Length-Tension Relationships

The isometric length-tension curve represents the maximum potential force that a muscle is capable of generating at varying strain. The length-tension relationship states that isometric tension generation is a function of the magnitude of overlap between actin and myosin filaments. There is also a passive force due to stretching of elastin which increases non-linearly with strain [42, 57]. The length-tension curve illustrates the two components of the potential maximum force with the active tension from the interaction between myosin and actin, and the passive from connective tissue. At low stretch (below the resting radius), muscle stress de-

termines the overall tension. As the radius saturates towards the maximum value (1.3 times the resting radius according to Hathaway et al. [95]), muscle stress decreases and passive increases exponentially so that the compliance is determined by the passive component [57].

2.4.3.1 Experimental Data

The passive and maximally active length-tension characteristics of vascular smooth muscle (VSM) have been explored in several studies [57, 172, 179] based on techniques established by Bevan and Osher [23] and Duling et al. [66]. Vessels are perfused with, or bathed in, activating or relaxing salt solutions to determine the minimal circumferential tension (passive component) and maximally active tension (maximally active component) present in the vessel wall at a given circumferential length.The force is measured by a force transducer in the solution. Active tension is obtained by subtracting the tension in relaxing solution (Ca^{2+} – free salt solution) from the tension in activating solution (with norepinephrine). Thus the operating range of wall tension can be defined for a given vessel [41] and also the variation with pressure.

Passive and maximally active length-tension characteristics of rat mesenteric arteries have been investigated with in-vitro wire [172, 179, 180]. Table 2.9 summarises the experimental findings of Mulvany [172] and Nyborg [179, 180].

Mulvany conducted 8 experiments measuring active and passive tension over a range of circumferences ($0.5L_0 - 1.6L_0$, where L_0 is the circumference πD_0 at which maximum active tension $T_{a,0}$ is developed). Mulvany determined that the maximum active tension of $\approx 100 - 200\mu m$ diameter arteries was at $L_0 = 0.96L_{100}$, where L_{100} was the passive circumference at a pressure of $100mmHg$. Mulvany found a plateau of active tension between $0.9L_0$ and $1.3L_0$ where active tension was $0.8T_{T,0}$ ($T_{T,0}$ being the total tension). Active tension fell to $0.3T_{T,0}$ at $1.6L_0$ (with zero-tension at $1.92L_0$) and $0.2T_{T,0}$ at $0.5L_0$ (with zero tension at $0.38L_0$).

For the 6 arteries investigated by Nyborg [179] : $D_0 = 0.83 \pm 0.02 D_{100} = 225 \pm 12$ μm; $T_{a,0} = 3.68 \pm 0.18$ N/m and $T_{p,0} = 0.74 \pm 0.1$ N/m. Below $0.8L_0$ and above $1.2L_0$, the active tension fell linearly with maximum tone at $1.18L_0$ and zero tension intercepts (the length at which extrapolated tension equals zero) at $0.4 \pm 0.01 L_0$ and $1.72 \pm 0.04 L_0$.

Nyborg also studied in-vitro wall tension in bovine retinal small arteries using a pressure-myograph system [180]. At $D_0 = 1.1 D_{100} = 215 \pm 8$ μm, the active tension was maximum at $T_{a,0} = 0.94 \pm 0.1$ N/m and passive tension $T_{p,0} = 0.89 \pm 0.21$ N/m. The zero-tension intercepts for active tension were at $0.48 \pm 0.02 L_0$ and $1.61 \pm 0.04 L_0$ and passive tension at $1.4L_0$ was 42.91 ± 12.87 N/m or $43 T_{p,0}$.

Table 2.9 collects these values and shows that the magnitude of basal tension is not proportional to diameter.

L	Passive (N/m)	Active (N/m)
Mulvany [172] $D_0 = 208 \pm 9$ μm		
0.38 L_0	0	0
0.5 L_0		$0.2 T_{T0}$
0.9 L_0		0.8 $T_{T,0}$
1 L_0	$T_{p,0} = 0.62$ N/m	$T_{a,0} = 2.46$ N/m
1.3 L_0		0.8 $T_{T,0}$
1.4 L_0	2.4 $T_{T,0} = 12 T_{p,0}$	0.6 $T_{T,0}$
1.6 L_0	4.4 $T_{T,0}$	$0.3 T_{T,0}$
1.92 L_0	0	0
Nyborg [179] $D_0 = 225 \pm 12$ μm		
0.4 L_0		0
1 L_0	$T_{p,0} = 0.74 \pm 0.1$ N/m	$T_{a,0} = 3.68 \pm 0.18$ N/m
1.5 L_0	$2 T_{T,0} = 12 T_{p,0}$	
1.72 L_0		0
Nyborg [180] $D_0 = 215 \pm 8$ μm		
0.48 L_0		0
1 L_0	$T_{p,0} = 0.89 \pm 0.21$ N/m	$T_{a,0} = 0.94 \pm 0.1$ N/m
1.4 L_0	$20 T_{T,0} = 43 T_{p,0}$	
1.61 L_0		0

Table 2.9: *The experimental length-tension findings of Mulvany [172] and Nyborg [179, 180] for arteries where $L_0 = \pi D_0$ is the circumference with maximum active tension T_0.*

Davis and Gore [57] dissected single arterioles from hamster cheek pouch. The ends of the vessel were held with micro-pipettes which were pressurised to inflate the vessel. The internal vessel diameter was measured from images taken of the procedure. Vessels were activated with a solution of potassium and norepinephrine at varying relative concentrations. Measurements of tension were calculated for passive (activation = 0) and fully active (activation = 1) vessels using Laplace's relationship between pressure and diameter, Equation 2.30. The results are especially useful because it is rare to find a set of data for both active and passive tension; these are reproduced in Figure 2.10 for a 50 μm arteriole (diameter in vivo) where $L_0 = 80.8\ \mu m$ is the circumference at 60 $mmHg$ in Ca^{2+}, when active tension is maximum. At shortened lengths, active contraction dominates the force generation. Just beyond resting length, the active tension is reduced and passive tension increases. Therefore the active curve is triangular, but non-symmetrical, [170].

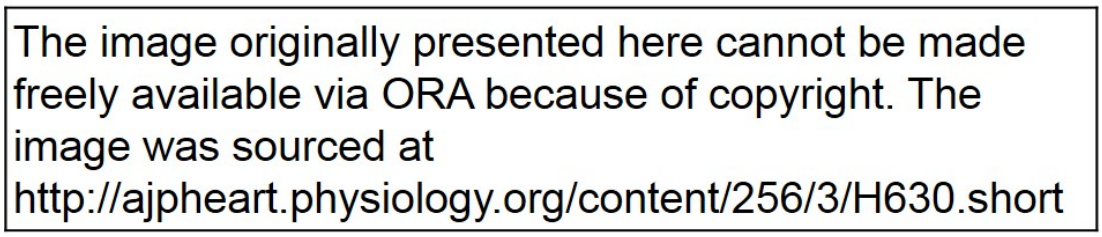

Figure 2.10: *(adapted from [57]) Length-tension characteristics of an arteriole.*

2.4.3.2 Passive Tension Models

Nyborg [179, 180] described the relative passive tension with an exponential function (with characteristic $b = 4.7 \pm 0.2$ in retinal arteries and $b = 10.1 \pm 0.4$ in mesenteric arteries):

$$\frac{T_p}{T_{p,100}} = e^{b(\frac{L}{L_{100}}-1)} \tag{2.37}$$

where $L_{100} = \pi D_{100}$, the passive circumference at an intra-luminal pressure of $100 mmHg$.

Carlson and Secomb [42] re-labelled this function for absolute passive tension T_{pass}, introducing constants: C_{pass} ($T_{p,100}$) and C'_{pass} (b).

$$T_{\text{pass}} = C_{\text{pass}} e^{C'_{\text{pass}}(\frac{L}{L_0}-1)}. \tag{2.38}$$

Pries and Secomb [197] developed an expression, Equation 2.39 from Fung [78], for elastic stress which has two components of elasticity (for elastin and collagen) and where ϵ is the strain, $(D-D_0)/D_0 = (L-L_0)/L_0$, assumed to be the same for both elastin and collagen.

$$\sigma_e = C_1(e^{\alpha_1 \epsilon} - 1) + C_2(e^{\alpha_2 \epsilon} - 1) \tag{2.39}$$

This common strain model is analogous to two springs acting in parallel with different stiffness parameters α [78] where individual stresses can be added. ϵ, α_1, α_2, C_1 and C_2 are estimated from stress-strain experiments.

2.4.3.3 Active Tension Models

In skeletal muscle, maximal tension is observed at a specific length. Vascular smooth muscle is mechanically similar to this skeletal muscle [94]. Since contractile filaments of the muscle cell overlap, the maximum tension is generated when the overlap between myosin and actin filaments is maximal. Active tension decreases non-symmetrically around this maximum point [102].

Feldberg et al. [76] and Paul [190] both approximate active stress as a triangular stress-strain function:

$$\sigma_a = \begin{cases} A\sigma_{max}\left(1 - \left|\frac{\epsilon-\epsilon_{max}}{\epsilon_w}\right|\right), & \text{for } |\epsilon - \epsilon_{max}| < \epsilon_w \\ 0, & \text{otherwise .} \end{cases} \tag{2.40}$$

where ϵ_w is the working (in-vitro) range of strain L/L_0. At $\epsilon = \epsilon_{max}$, the overlap between myosin and actin filaments is maximal so that the maximum stress is $\sigma_a = A\sigma_{max}$. At maximum stress, the degree of contraction also depends on A, the degree

of activation of muscles. A takes a value between 0 and 1 where 0 is complete relaxation and the basal level is 0.5.

This triangular function can be approximated by a Gaussian function:

$$\sigma_a = be^{-[(\epsilon-m)/s]^2}. \tag{2.41}$$

where b is the maximum active stress the wall can develop and m and s are the position and width of the active stress-distension curves. Carlson and Secomb [42] described active tension in this way with a Gaussian curve:

$$T_{\text{act}} = C_{\text{act}} e^{-\left(\frac{\frac{L}{L_0}-C'_{\text{act}}}{C''_{\text{act}}}\right)^2}, \tag{2.42}$$

where C_{act} is the peak active tension, C'_{act} is the location of maximum active tension as a function of L_0, and C''_{act} determines the width of the active curve.

Otten [185] suggested an exponential expression which incorporates a parameter β to determine the gradient skew (since the active curve is non-symmetrical):

$$\hat{F} = e^{\left[-\left(\frac{(L/L0+1)^{\beta}-1}{w}\right)^{\rho}\right]}, \tag{2.43}$$

where $\hat{F}$ is normalised muscle force (F/F_{max}), ϵ is muscle strain $(L - L_0)/L_0$ with optimum length L_0 and ρ, β and w control the roundness, skew and width of the curve. Increasing ρ increases the gradient of the curve; a negative β has a steeper contracted gradient whereas a positive β gives a steeper dilated gradient. w correlates with the width of the curve . Kaufman et al. [122] set $\rho = 2$.

There is therefore no universal expression for use in calculating the active tension. Feldberg and Carlson and Secomb use symmetrical functions with only Otten including the skew for active tension.

Section Summary

The transmural pressure leads to strain in the vessel wall which is related to stress by the elasticity of the components of the wall: principally elastin, collagen

and smooth muscle. The stress due to pressure is therefore balanced by a function of passive elastic, and active muscle stress. The active tension is a non-symmetrical triangular function of strain, with a basal condition near maximum. The passive tension is a non-linear function of strain as shown by experimental data. The contribution of muscle tension is determined by the activation; the proportion of muscle cells contracted. The next section describes how the activation enables autoregulation in the vasculature.

Section 2:5 Autoregulation

This section details the current knowledge about the autoregulation process. The responses to pressure and to metabolic demand are described with reference to existing models and experimental evidence.

2.5.1 The Myogenic Response

Blood flow in the brain is regulated by the activation of smooth muscle in the walls of arteriole vessels. Greater pressure leads to greater stretch and, conversely, greater contraction, which is held for as long as the vessel is stretched. This is called the myogenic response and has been well documented in cerebral arterioles [28, 54, 235].

The elasticity of the vessel wall constituent material allows for some passive dilation to accommodate an increase in global perfusion pressure (the difference between inlet and outlet pressure). However, within the autoregulation range (approximately 50 to 150 mmHg) changes in blood pressure result in a much smaller proportional change in blood flow [178]. This is the phenomenon known as autoregulation, first described in the kidney in 1931 [201] after being predicted by Baylis based on changes in dog hind limb volume during alteration in arterial pressure [13].

If vessels are maximally dilated (which can also be done artificially with drugs),

then increases in pressure lead to large changes in cerebral blood flow (shown as the 'dilated' path in Figure 2.11). If vessels are maximally constricted, the 'constricted' pathway is followed. When allowed to adapt, the net result is the 'autoregulating' path in which flow changes are relatively small despite large changes in pressure.

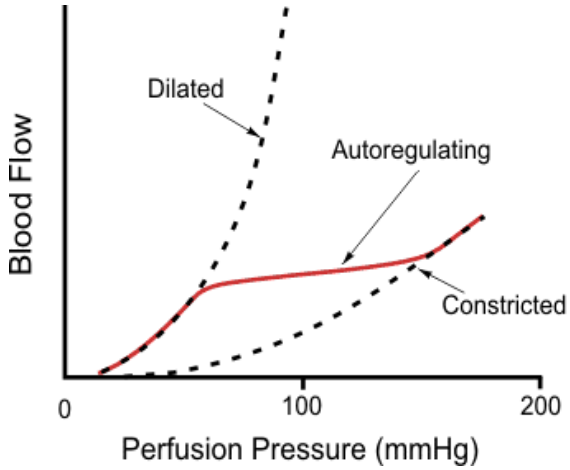

Figure 2.11: *The relationship between cerebral blood flow and perfusion pressure [128] showing the range of autoregulation* $(50-150 mmHg)$ *and changes outside this range*

Where the paths meet signify the upper limit of autoregulation through constriction at around 150 $mmHg$ perfusion pressure, at maximum dilation which occurs at around 50 $mmHg$, the lower limit. The autoregulation curve is therefore made up of three phases: dilation at low pressure, constriction at high pressure and then elastic dilation beyond the limit of autoregulation. The plateau of the curve does not necessarily have zero slope [252].

2.5.1.1 Experimental Studies

Biochemical and experimental methods have both been developed which permit the study of vasodilation and thus the analysis of autoregulation. Hughes and Bund [107] found that a rat mesenteric artery dilated between 1 and 50 $mmHg$ before contracting (with minimum diameter at 120 $mmHg$) before dilating again, becoming passive in nature. For a 35 μm radius arteriole, the maximum radius was

1.3 times the resting radius [57, 95]. Hayashi et al. [96] applied pressure changes at 3 $mmHg/s$ to extracted human cerebral arteries and found a (non-linear) higher distensibility below 80 $mmHg$ than above 150 $mmHg$. Hayashi also found that the radius remained unchanged below 40 $mmHg$ and there is therefore a basal (unstretched) diameter which ensures that vessels do not collapse at low pressure. Hayashi describes the autoregulation curve with Equation 2.44:

$$ln(P/P_s) = \beta(R/R_s - 1), \tag{2.44}$$

where $P_s = 100\ mmHg$ and R_s is the vessel radius at 100 $mmHg$. The log-log graph is linear between 60 and 160 $mmHg$ with β between 10 and 20. However, this curve simply replicates an experimental study and does not provide physiological insight.

This reaction to pressure can also be observed in isolated, pressurised blood vessels indicating that it is an independent mechanism. Kontos et al. [134] discovered that, in cats, the response was diameter dependent. Dropping the pressure from 200 to 40 $mmHg$, it was noticed that the larger vessels dilated first (at higher pressure) but that the maximum response of vessels with diameter between 150 and 170 μm was less than that for smaller vessels. Different vascular segments therefore contribute differently to overall network control. Large pial vessels play a major role during moderate pressure change whereas smaller ones undergo large vasodilation in response to large pressure drops [253] with intermediate diameter vessels having the strongest response [162]. The vessel location also affects the response, with a weak response in small rat mesenteric vessels and a strong response in similarly sized cerebral vessels [184]. The strength of response can even vary within the same vessel bed, for vessels of the same size [137].

2.5.1.2 Clinical Studies

Patients with impaired autoregulation are vulnerable to pressure changes with a resulting risk of hyperperfusion (high blood flow) or ischaemia (decreased oxy-

gen due to low blood flow). Studies have attempted to assess the static autoregulation limits with reference to other physiological parameters. The most common experimental approach is to induce changes in the mean arterial blood pressure (ABP) via the infusion of drugs which do not affect metabolism [141, 191]. ABP can be increased by the infusion of phenylephrine, angiotensin or noradrenaline and decreased by the infusion of sodium nitropusside or thrimethapan [187]. However, each of these chemicals has its own temporal dynamics which means that the dynamic response is difficult to obtain.

Jørgensen et al. used a head-up tilting method [119] to induce a pressure change, Bondar et al. used an external decompression applied to the lower body [29] and Birch et al. extended this to sinusoidal changes in lower body pressure [25]. A concern with these static approaches however, is that physiological variables are also affected [187]. Further, these methods are not suitable for many patients which inhibits their usefulness.

Dynamic autoregulation is the ongoing alteration of vessel diameter in small vessels. It can be monitored directly and continuously by Transcranial Doppler Ultrasound (see discussion in subsection 2.2.6). Aaslid et al. [1] used a thigh-cuff (which is inflated to cut off flow) to induce a step change in ABP finding a 2 second lag between pressure drop and CBF response, and a $10-15$ second recovery time. This short time-scale minimises the influence of other variables (CO_2 for example) which impair static measurements, but the painful procedure of cuff inflation may also induce other responses [187].

2.5.2 The Flow Response

The autoregulation curve is evidence that, within a certain perfusion pressure range, there is a constant flow in the cerebral network. Increased flow of blood in a vessel results in a linear increase in pressure-stretch on the vessel wall which initiates the myogenic response of contraction. Despite this, there is a local dilation

response to low flow which maintains functional and metabolic oxygen needs and prevents collapse. This dilation response was demonstrated in arteries by Bevan in collaboration with Garcia-Roldan and Gaw [80, 82].

Any diameter response has further effects on flow, and therefore on shear stress. It is possible that vessels respond to low flow directly, or to the shear stress caused by flow [116]. Shear stress is the frictional drag exerted tangentially on a vessel wall by the flow of blood. Steady state wall shear τ_w is found by Equation 2.46 and so is dependent on viscosity, μ, flow, Q, and diameter, D:

$$\tau_w = \frac{32\mu Q}{\pi D^3}. \tag{2.45}$$

Viscosity is also a function of diameter due to the Fåhræus–Lindqvist effect (see subsection 2.2.2). To prevent a shear increase when flow increases, the diameter must also increase.

Ursino et al. [253, 249] assumed that high flow is related to high pressure, and is therefore not an independent signal but instead part of the myogenic response. Similarly, Ursino assumed that low flow is instead regulated by metabolic requirements. Since flow is related to both the pressure gradient along the vessel (ΔP), and the resistance of the vessel, shear stress can be calculated at steady state as:

$$\tau_w = \frac{32\Delta PD}{128L}. \tag{2.46}$$

2.5.3 The Metabolic Response

2.5.3.1 Response to Demand

Although total blood flow remains relatively constant in response to changes in pressure, local blood flow is continuously readjusted to satisfy the metabolic demand of brain cells. In order to meet the oxygen demand of tissue, adequate flow must be provided. The result of raising a hand, for instance, is an increase in flow in the relevant motor area of the brain [98] and a reduced flow in surrounding

vessels [27]. Terminal vascular beds continually adapt to both demand and circumstance [150]. This is local, acute autoregulation [3] which works dynamically to constantly meet the demands of tissue in the brain by altering resistance to flow [6].

Donegan et al. [61] showed that a reduction of O_2 consumption by 50% led to a reduction in cerebral blood flow by 50% without impairing autoregulation. A coupling between flow and dilation is important for the adaption of the network to demand for oxygen. Functional activity is accompanied by an increase in oxygen extraction [129], followed by decreased venous oxygen content and then local and upstream dilation which increases flow [228, 84, 75]. It has been suggested that there also exists collateral flow through networks of 'dormant' capillaries [176] which become active when required [129]. Sokoloff et al. [229] suggested that 10% of capillaries are subject to recruitment in response to need but this is dismissed by other researchers [17, 105].

The metabolic demand for oxygen increases when local brain areas increase in functional activity [262]. Lin et al. [144] found that task-induced increases in oxygen demand were small (12 – 17 %) with associated small change in tissue concentration (< 10 $mmHg$ in rat [151]) but were accompanied by a disproportionately large flow increase (Lin found that a 52 – 65 % increase in flow accompanied a 12 – 17 % increase in demand). Similarly, Masamoto and Tanishita [151] described how a 10 % increase in $CMRO_2$ results in a 54 % increase in CBF . Therefore metabolism and flow are coupled systems [34, 229] where flow is increased by dilation of vessels. However, the extent of overcompensation of flow is not yet understood, nor why there is such an overcompensation.

2.5.3.2 Response to Supply

A change in supply also affects the tissue oxygen level. Rolett et al. [205] measured the tissue oxygen partial pressure P_T in rat brain by electron paramagnetic

resonance oximetry and found that it changed depending on arterial oxygen levels (i.e. with oxygen supply). The arterial oxygen partial pressure P_{a,O_2} values were 145.1 ± 11.7, 56.5 ± 4.4 and 40.7 ± 2.3 $mmHg$ with corresponding P_T values of 15.1 ± 1.8, 8.8 ± 0.4 and 6.8 ± 0.3 $mmHg$. Johnston et al. [118] found that, similar to the autoregulation curve, there is little change in flow within the normal range of arterial oxygen partial pressures ($52-97$ $mmHg$) but that decreasing Pa_{O_2} from 50 to 25 mmHg doubled the cerebral blood flow. The haemoglobin-oxygen dissociation curve means that the range of oxygen concentration is narrow over these values of partial pressure. Kontos et al. [134] found that elevating O_2 levels typically causes vasoconstriction of arterioles and reduced flow through the network [65].

2.5.3.3 The Dynamic Metabolic Response

The dynamic response to a demand increase is a rapid P_T decrease and slow recovery taking up to 25 seconds [4]. The lag results in an overall increase in tissue oxygen concentration [264]. In experiments, Vazquez et al. [264] found that 10 seconds of rat forepaw stimulation induced a 48.8 % increase in flow and 27.7 % increase in tissue oxygen tension peaking 9.8 seconds after stimulation onset with an initial tissue oxygen partial pressure measured to be 32.8 $mmHg$.

Ances et al. [4] conducted similar stimulations of rat forepaw over 4 seconds and 1 minute finding an initial tissue oxygen decrease of 0.42 ± 0.24 $mmHg$ (from a baseline of 23.1 ± 3.2 $mmHg$) followed by a rapid initial peak in flow (1 second later peaking at 55.8 ± 5.9 % of baseline flow, 4 seconds after stimulus onset). Tissue oxygen increased by 4.6 ± 0.7 $mmHg$, or 20.7 ± 5.9 %, peaking 5.6 ± 0.2 s after stimulus onset. At the end of the stimulation period (steady state), blood flow returned to 110 ± 2% of baseline with tissue 102 ± 1 % above baseline. Following stimulation offset, there was a tissue oxygen decrease -0.71 ± 0.31 $mmHg$. Ances therefore found a quicker peak response than that found by Vazquez with a lower

tissue oxygen increase.

Stefanovic et al. [230] also conducted a fore-paw stimulation experiment and found a $10.9 \pm 1.2\%$ dilation of vessels with diameter smaller than $10\ \mu m$ (labelled by Stefanovic as capillaries), a decrease in transit time from $1.6 \pm 0.2\ s$ to $1.2 \pm 0.2\ s$ (corresponding to a 64 % increase in flow calculated from volume and transit time) and a 19.5 ± 6.2 % flux increase (corresponding to a 32.5 % oxygen extraction increase calculated from flux and surface area, or a 19.2% decrease in the longitudinal oxygen gradient if this was steady state). The medium vessels ($10 - 30\ \mu m$) dilated, on average, by 6.4 ± 1 % with a corresponding 51 % flow increase and 27.15 % increase in oxygen extraction with a 15.8 % decrease in longitudinal oxygen gradient.

Mandeville et al. [149] previously performed a fore-paw stimulation experiment finding a capillary volume increase ratio of 1.09 ± 0.03 accompanying a flow ratio increase of 1.6 ± 0.25. This volume increase corresponds with a diameter ratio increase of 1.02 ± 0.009. Capillaries do not have smooth muscle and so any dilation is due to a very small amount of elastic material in the wall. Therefore, the vessels labelled as capillaries by Stefanovic are more likely to be terminal arterioles.

Any imbalance between metabolic demand and supply leads to an initially reduced tissue-oxygen level P_T. Reduced tissue oxygen might therefore also induce a flow response. The critical tissue concentration for hypoxia is associated with a threshold of around 10 $mmHg$ by Johnston et al. [118] and $6.8 - 8.8\ mmHg$ (with flow at 10 % of baseline) by Rolett et al. [205]. However Masamoto and Tanishita [151] discovered that a decrease in tissue tension due to metabolic increase does not ever cause hypoxia implying that the blood flow increase is unnecessary. In fact, the tissue oxygen concentration increases during demand because the evoked CBF response exceeds requirements, the reason why is as yet undetermined.

Optical imaging shows that the metabolism of oxygen ($CMRO_2$) increases be-

fore flow [225] and so the increased flow does not supply the increased oxygen. Lin extends this to argue that a flow increase is not, in fact, required to maintain tissue oxygen concentration, or to stimulate oxygen delivery. Furthermore, suppressing the vasodilatory response which allows a flow increase does not affect the ability to match demand. Instead, the increase in flow is thought to supply oxygen for tissue concentration recovery. Under suppressed flow conditions (Figure 2.12) with 10 seconds of increased demand, the tissue oxygen decreased by 11.7 % over the course of the stimulation from a baseline of 42 $mmHg$, with a minimum at 10.8 seconds, 0.8 seconds after stimulation offset (where the demand returned to baseline).

The image originally presented here cannot be made freely available via ORA because of copyright. The image was sourced at http://www.sciencedirect.com/science/article/pii/S1053811908004916?np=y (Figure 2)

Figure 2.12: *Oxygen concentration in the tissue following a* 10 *second demand increase of* 12.5 %. *Tissue concentration reduces to* 88 % *of baseline in* 10 *seconds and over* 10 *seconds of recovery, tissue concentration recovers to* 96 % *of baseline [264]*

2.5.3.4 Simulations of Tissue Dynamics

For $CMRO_2$ to be an independent parameter, there needs to be a two-compartment scenario in which tissue concentration C_T can vary dynamically. The relationship between $CMRO_2$ and CBF is affected by the vessel wall permeability to oxygen, P, and the surface area S. A lower C_T allows for more $CMRO_2$ variation, similarly a higher S. A two compartment model of tissue dynamics was derived by Valabrègue et al. [256] to represent the change in tissue concentration with supply and demand:

$$V_c \cdot \frac{\partial C(x,t)}{\partial t} = -Q(t) \cdot \frac{\partial C(x,t)}{\partial x} - PS \cdot \Big(C_p(x,t) - C_T(t)\Big) \tag{2.47}$$

$$V_T \cdot \frac{\partial C_T(t)}{\partial t} = PS \cdot \Big(C_{p,avg}(t) - C_T(t)\Big) - CMRO_2(t), \tag{2.48}$$

where V_c is the capillary volume, V_T the tissue volume and $C_{p,avg}$ is the plasma concentration averaged over the vessel. The capillary inlet boundary condition is $C(0,t) = C_a$, the initial capillary concentration $C(x,0) = C_{initial}(x)$ and the initial tissue concentration $C_T(0) = C_{T,initial}$

Valabrègue solved for steady state to calculate the transmural gradient of oxygen concentration for a given flow and consumption, reducing the equation for steady state to:

$$\frac{dC_T(x)}{dx} = -\frac{PS}{Q}(C_p(x) - C_T) \tag{2.49}$$

$$CMRO_2 = PS(C_{p,avg} - C_T). \tag{2.50}$$

PS was set to either 7020 or 3000 ($ml/min.100g$) resulting in a high resting OEF of 60 % in capillaries, with a P_T of 15 and 5 $mmHg$ respectively. Valabrègue found that an increased tissue oxygen pressure decreased the oxygen gradient and therefore the extraction fraction and $CMRO_2$. An uncoupling between flow and consumption was proposed since, otherwise, high consumption leads to a negative tissue concentration in the equation or an increase in tissue concentration is only found with a decrease in metabolism.

A very similar 2 compartment model of capillary C_c and tissue C_T concentration averaged over space was proposed by Vazquez et al. [264]:

$$V_c\frac{dC_c(t)}{dt} = 2q(t)(C_a - C_c(t)) - PS_v\Big(C_p(t) - C_T(t)\Big) \tag{2.51}$$

$$V_T\frac{dC_T(t)}{dt} = PS_c\Big(C_p(t) - C_T(t)\Big) - CMRO_2(t) \tag{2.52}$$

$$C_c = C_p(t) + \frac{4[Hb]}{1 + \left(\frac{\alpha P_50}{C_p}\right)^h}. \tag{2.53}$$

The variable q is the dynamic ratio change in blood flow ($Q(t)/Q_0$, where Q_0 is the baseline blood flow) and V_c and V_T are the capillary and tissue volumes. The experimental tissue concentration corresponds to $C_T(t)$. The partial pressure of

oxygen was converted to concentration using the oxygen solubility constant so that $C_T = \alpha P_{o2}$.

In Vazquez's simulation, the flow response peaked 6.8 seconds after stimulation and returned to baseline 20 seconds after the stimulation was removed. P_T increased from baseline 32.8 $mmHg$ to 41.9 $mmHg$ (a 27.7 % increase). Tissue PO_2 began to increase 2 seconds after stimulation, peaking at 9.8 seconds. There was a resulting undershoot to 32 $mmHg$ 30 seconds after stimulus offset with a return to baseline by 54 seconds after offset. If the flow change was suppressed (to match the experimental method), the tissue signal decreased from baseline 42.5 $mmHg$ to 37.7 $mmHg$ (a 12.7 % decrease) with no lag, reaching a minimum at 10.8 seconds after stimulation and returning to baseline by 22 seconds after the stimulation was removed.

In order to match simulations with experimental results, Vazquez had to allow the capillary volume to change by 82 % (equating to a 35 % increase in vessel diameter). This dilation is far higher than found experimentally by Stefanovic. Dilation of the capillary would cause both a larger surface area, and thinner walls - both of which would increase PS but the 82 % increase in capillary volume by dilation is highly unlikely due to the limits of elasticity in the capillary wall. Capillary recruitment is a possibility (and would also increase flow). Similarly, a larger wall permeability (an increase of 36.7% delayed by 1.7 s) enabled the simulation to match the data. An independent increase in diffusivity due to neural activity was proposed by Mayhew et al. [153].A further possibility is that the oxygen tension at the vessel inlet increases by 27 % which relies on the reduction of oxygen extraction within other vessels in the network.

2.5.3.5 Metabolic Control

It has been proposed that either oxygen acts as a direct vasoconstrictor, or that oxygen inhibits a vasodilatory mechanism. A reduction of inflow causes a buildup

of vasodilatory metabolites such as CO_2 as well as increased production of these anaerobic dilators [114]. Increased flow potentially increases the washout of these substances restoring basal dilation. However, under conditions of elevated flow, when oxygen is applied to tissue the dilation of pial arterioles is reduced implying that the signal comes from production (rather than washout) of vasodilatory metabolites [267].

Demand is communicated to other vessels in the network. Groebe [87] assumed that the venules sense oxygen and carbon dioxide levels and that arteriolar constriction and dilation occurs only by the myogenic and shear-dependent response with a non-local oxygen signal conducted from the venules. Granger et al. [86] suggested that terminal arterioles could be more sensitive to oxygen than larger vessels since this would reduce oxygen tension allowing greater perfusion and oxygen extraction without altering vascular resistance. It is thought that red blood cells may act as oxygen sensors and communicators of metabolic demand [72]. Winn et al. [268] found that adenosine levels in the rat brain also increased as systemic arterial pressure was reduced below the autoregulatory range.

Red blood cells release ATP at a rate depending on their oxyhaemoglobin saturation level with an increased amount of ATP when exposed to low PO_2 (as documented by Bergdeld and Forrester [20]). Ellsworth et al. [73] defined vessel hypoxia as $PO_2 < 35\ mmHg$ and found that ATP was also released when exposed to low pH levels. McCullough et al. [155] applied ATP extra-luminally and intraluminally to hamster cheek retractor muscle and noted upstream constriction and dilation respectively. At an ATP concentration of $10^{-6}M$ applied intra-luminally, there was an 8 % increase in vessel diameter corresponding to a 17 % increase in flow. Collins et al. [49] applied 400 pL ($4 \times 10^{-4}\ mm^3$) of $10^{-6}\ M$ ATP (i.e. with a concentration of $25,000\ \mu M/mm^3$) to the hamster cheek retractor venule which increased second order and terminal arteriole diameters (450 μm upstream) by

10 – 12 % with a resulting 60 – 50% increase in red blood cell flux and 90% flux increase in the capillaries.

The concentration of ATP, then, is able to initiate vessel diameter change. Since ATP is released by the red blood cells in response to vessel hypoxia, it is potentially an underlying mechanism for the reaction. ATP is released in blood vessels, whereas a change in tissue oxygen concentration can also cause vasodilation which precedes the concentration change in the blood vessels. It is therefore likely that the tissue is the initial instigator of the flow response to demand.

Section Summary

There is a non-linear relationship between blood pressure and perfusion (flow) because of the dilation and constriction of blood vessels [150]. Vessels are able to regulate diameter which enables control of resistance to flow [6]. This vasoconstriction and vasodilation is active and described as autoregulation [150]. Acting alone, vessels can compensate for local conditions and, collectively, the network of vessels can ensure that functional demands for oxygen are met and that pressure changes are accounted for.

There are many hypotheses as to how autoregulation occurs but little argument that there is both a myogenic and a metabolic response governing the diameter of blood vessels. Contradictions in the literature have been highlighted here such as whether there is a flow response, or whether the metabolic response incorporates low flow. Relevant experimental results have been described which give the dynamics of the flow response to oxygen demand and the tissue concentration dynamics. Many potential controllers of vessel diameter have been confirmed experimentally leading to several hypotheses for what governs autoregulation. These activation factors are discussed in the next section.

Section 2:6 Activation of Smooth Muscle

It is the activation of the smooth muscles which forms the basis of the autoregulatory response since these control the vessel diameter. The proportion of muscle cells activated is called the activation. This section is an overview of possible physiological instigators of muscle activation which are used in current models. As well as pressure, studies have suggested that there is a sigmoidal dependence of muscle tone on wall tension, wall stress, shear, oxygen and strain and these are outlined here. Also described is the need for a feedback signal to communicate with upstream vessels and the current modelling approach to the coordination of vessels.

2.6.1 Activation Model

Over the range of the autoregulation curve (see section 2.5), the total tension varies substantially due to the change in contributions of active and passive components. At low stretch (below the resting radius), muscle stress determines the overall tension. As the radius saturates towards maximum value (1.3 times resting radius from [95]), muscle stress decreases and the passive component increases exponentially so that the compliance is determined largely by the passive component [57].

The total compliance of a muscle and passive material in parallel is analogous with resistance in a circuit:

$$C_{tot} = \frac{C_M C_P}{C_M + C_P}, \tag{2.54}$$

where C_{tot} is the total compliance, C_M the active muscle compliance and C_P the passive compliance. At high strain, muscle tension is reduced. It was previously assumed that the reduction in active tension at large circumferences was due to damage but Mulvany and Warshaw [172] showed that this was actually due to the vascular smooth muscle contractile apparatus and variation in the proportions of

smooth muscle cells activated.

Carlson and Secomb [42] developed a model of the steady-state diameter pressure response considering variable smooth muscle tone. The wall is represented as a non-linear spring and contractile unit in parallel and the maximum tone that can be generated is the sum of a passive (non-linear) spring with tension T_{pass} and maximally active (contractile) components of tension (total maximally active tension T_{act}) [112]:

$$T_{total} = T_{pass} + AT_{act}. \tag{2.55}$$

The amount of activation of smooth muscle A determines the level of active contribution to tension ranging between 0 and 1 [42] and the total tension is in equilibrium with the circumferential wall tension experienced due to pressure, determined by Laplace's law Equation 2.30. The maximum tension at any muscle fibre length is the sum of the spring (passive) and active vascular smooth muscle unit and, below normal operating pressure, there is a basal level of tension which prevents collapse of the vessels, the dominant contribution being active. The tension is a function of strain, and the level of activation A is determined by other factors.

Feldberg et al. [76] also models the wall as a passive elastic and active muscular compartment arranged in parallel. Using data from Hass et al. [89] and Casellas and Moore [43] the relationship between pressure and activation A is shown to be almost linear in the interval of pressure 1.2 to 16 kPa. Feldberg establishes the following function with $P_{min} = 1.2\ kPa$ and $P_{max} = 16\ kPa$, where $A = 0$ is no cell activation so that the vessel is completely passive, $A = 1$ is complete activation so that beyond this level no further contraction can occur. In between, the relationship between pressure and radius is nearly linear.

$$A_{MYO}(P) = \begin{cases} 0 & \text{for } P < P_{min} \\ \frac{P-P_{min}}{P_{max}-P_{min}} & \text{for } P_{min} \leq P \leq P_{max} \\ 1 & \text{for } P > P_{max} \end{cases} \tag{2.56}$$

Jacobsen's expression (Equation 2.57) depends on the level of cell activation between 0 and 1 [112]. Relaxed microvessels are not strain free due to a basal muscle tension, modelled as residual strain by Jacobsen, or as a basal activation of 0.5 by Carlson and Secomb [42]:

$$R \approx R_{max}\left(1 - a_1 exp\left(-a_2 C_M\right)\right), \tag{2.57}$$

where R is the vessel radius, and a_1 and a_2 are constants to be found. Both models lack physiological relevance because they model the curve and not the underlying processes.

2.6.2 Stimulation of activation

Physiologically, following an increase in pressure, there is an influx of sodium and calcium through ion channels in the membrane which leads to membrane depolarisation of smooth muscle cells accompanied by contraction of the vessel [91, 93, 130, 131]. Activation of smooth muscle cells is therefore linked to the flux of calcium across the cell membrane [213]. The influx of calcium initiates the release of stored calcium. The free calcium binds to the thin filaments which induces actin binding to myosin. The myosin light chain phosphorylation leads, ultimately, to the contraction of the actin-myosin complex via the hydrolysis of ATP which supplies energy to the actin-myosin complex so that the filaments slide past each other [42].

Muscles are activated both by local conditions, and also upstream and downstream conditions. The latter has been determined experimentally by Duling et al. [67] since application of acetylcholine to arterioles leads to both local and ascend-

ing vasodilation. Conducted responses are transmitted both upstream and downstream along vessel walls [14] as well as downstream by the condition of the blood flowing and the chemicals contained within. There are many proposed triggers for autoregulation. Namely these are: the pressure response (which might be strain or wall tension and is called myogenic), the response to flow (which may be a shear response) and the low oxygen metabolic response (as discussed in section 2.5).

2.6.2.1 Stretch Activation

Since calcium channels in the muscle cell can be activated by stretch [213], it is possible that the muscle could be responding directly to the strain experienced under elastic deformation. The model of Iida [110] assumes that the wall elastic modulus is a function of pressure. This accurately portrays the first two phases of the autoregulation curve but not the high-pressure passive response. Similarly, Cornelissen et al. [52] set tone to depend on intravascular pressure whereas Lee and Schmid-Schönbein [143] set the elasticity to be modulated by a pressure-dependent reference diameter. Borgström and Grände [31, 32] used a force-equilibrium balance within the vessel wall, so that the myogenic reaction is triggered by the wall tension and the rate of change of wall tension.

For a stretch-model, there must be a transducing mechanism to sense either wall tension or stretch and to stimulate VSM contraction. There is disagreement over possible sensors for this stretch, or wall tension. Davis proposes stretch-activated cation channels [56] whereas McCarron proposes voltage-dependent calcium channels [154]. Bulbring [247] observed depolarisation and contraction following stretch of guinea pig vascular smooth muscle. Harder blocked the nerve endings in the adventitia and recorded no alteration in the myogenic response of cat cerebral arteries [91].

Johnson rejects the possibility that diameter, or pressure induced stretch, regulate the myogenic response [115]. Multiple activation levels can exist at given

strain, and the level of calcium is not proportional to strain [279]. Further, the vessels can constrict to less than the steady state diameter [279].

2.6.2.2 Tension Activation

Johnson suggests the alteration of wall tension as the principal factor of activation since intracellular calcium concentration, and the level of myosin light chain phosphorylation correlates with wall tension rather than diameter [279]. Wall tension, as a mechanical load, could be transmitted to cells via the cytoskeleton leading to muscle contraction [59]. Johansson and Mellander [113] studied the activation of resistance vessels by dynamic stress and the depolarisation of muscle cells was found to better correlate with tension than muscle length [208, 33, 132, 117]. Therefore, Vanbavel and Mulvany [257] and Yang and Clark [273, 272] set the muscle tone to depend on wall tension in their models.

2.6.2.3 Flow Activation

Experimental data from Kuo et al. [136, 138] show that there is a definite independent response to low and high flow. At low flow, this can be reduced to a low-oxygen response. However, the response to increased shear stress is not the myogenic response of vascular smooth muscle, since it is endothelial cells which experience shear force [176]. Malek and Izumo [148] found that increased flow reorientates and elongates the endothelial cells decreasing the effective resistance to flow, by reducing drag.

Shear stress also stimulates the endothelium to release chemicals. Endothelial factors have been identified which influence vessel tone by inducing dilation or constriction of smooth muscles both locally, and in upstream feeding arterioles [71, 171, 41]. Michiels found evidence of nitric oxide [NO] being released by the endothelium in response to shear stress [160], an increase in flow also stimulated the release of PGI_2 and NO which induce vasodilation. NO and PGI_2 are thus known as endothelium-derived relaxing factors (EDRFs) [186, 79].

Reinhart found that this NO response to shear was effectively instantaneous [202] and Cornelissen et al. [52] assumed the level of tone generated by VSM was dependent on the concentration of NO, which gave a sigmoidal function of wall shear stress. NO also plays an important role in maintenance of basal tone. Flemming et al. demonstrated this [11] by infusing an NOS inhibitor which increased resting blood pressure.

There are also endothelial released vasoconstricting factors. Peptide endothelin is one of these factors [271] which is released in hypoxic conditions. Endothelial factors in the bloodstream are transported to other vessels via the blood causing a continued downstream response. Although endothelial factors can be transported by the blood stream, ischaemia damages the endothelium which leads to a disruption in the release of chemical constrictors and dilators. The endothelium also acts as a barrier (the blood brain barrier) to the cerebral spinal fluid: due to cell damage, ischaemia causes the barrier to break down.

Investigators have found both validation and counter-validation of the effects of preventing endothelium response, as reviewed by Meininger and Davis [157]. For example, in cat cerebral arteries the endothelium derived factors were found to restore the response in vessels without endothelium [92] but not in rat cerebral vessels [278]. The conclusion drawn by Meininger and Davis is that the former could be due to a separate mechanism of autoregulation and that, in almost all vessels, the endothelium is not necessary for a response so that the reaction depends only on the smooth muscle cells in the walls of arteries and arterioles. The myogenic response in the absence of shear stress has been tested with low perfusion rate experiments using pressure myograph systems. Small arterioles between 25 and 250 μm diameter have been examined in this way [183]. The three phases of the autoregulation curve are reproduced implying that the endothelium aids the response but is not essential.

2.6.2.4 Metabolic Activation

The metabolic hypothesis describes how the levels of carbon dioxide, hydrogen, lactate and oxygen affect flow [98]. Borgström and Gestrelius [30] coupled oxygen availability with the activation of vascular smooth muscle assuming that the concentration of vasodilatory substances affects the dependence of activation on calcium concentration. Since the result of activity is increased tissue metabolism (utilisation of oxygen) in specific areas of the brain, the response may also be due to reduced oxygen concentration and the metabolic pathway. Arciero et al. [6] proposed that low oxygen concentration could instead affect the concentration of ATP which would induce an upstream vasodilatory response. Adenosine, formed by the breakdown of ATP, is a potent vasodilator [275]

The effects of chemicals on vessels can be investigated experimentally. It has been shown that ischaemia leads to co-ordinated upstream and downstream muscle activity in many vessels [121]. Independent reduction of O_2, or increases in adenosine or potassium (for example), causes vasodilation upstream as well as locally, but in a proactive rather than a responsive manner [109].

Mishra [164] showed that above a CO_2 partial pressure of 40 $mmHg$, flow increases by $1-2$ $ml/100g/min$ for every 1 $mmHg$ change in $PaCO_2$. Carbon dioxide is a product of metabolism, as are hydrogen and lactate. Increased hydrogen and lactate alter the pH of tissue which causes vasodilation. Figure 2.13 shows the effect of oxygen and carbon dioxide on cerebral blood flow; the independent reduction of oxygen below $50mmHg$ causes an increase in flow which brings increased oxygen supply.

The image originally presented here cannot be made freely available via ORA because of copyright. The image was sourced at http://web.squ.edu.om/med-Lib/MED_CD/E_CDs/anesthesia/site/content/v04/040118r00.htm (Figure 19-4)

Figure 2.13: *The relationship between partial pressure of carbon dioxide and oxygen in tissue and cerebral blood flow. http://web.squ.edu.om/med-Lib/MED_CD/E_CDs/anesthesia/site/content/v04/040118r00.htm*

2.6.2.5 Neural Activation

Behzadi and Liu suggested that the compliance of muscle (in parallel with the compliance of the elastic vessels) is modulated by neural activity [16]. The overall compliance is then modulated by local factors, whether by elasticity or muscle tone or both, in order to regulate diameter. The response to brain function may be due to the release of vasodilatory substances from active neural cells which diffuse to the vessel walls, or from mediated signals which are transferred from active neurons to local vessels.

2.6.2.6 Strain-rate activation

There is a further hypothesis that strain rate has an influence on active stress. Borgström and Grände [31] calculated active tension as the sum of two terms: one proportional to circumferential stress and one proportional to the rate of change of circumferential stress with time.

2.6.3 Activation Signal

Zulliger et al. [280] postulated that wall adaption aims to restore an optimal biomechanical set point implying that there is an absolute equilibrium and that deviation from this set point can be sensed by the cells. Jacobsen et al. [112] instead proposed a myogenic response modelled explicitly, with the rest of the signals lumped into a constant, which modifies smooth muscle cell activation, requiring activation to be chemically dependent on absolute vessel parameters. Carlson and Secomb [42] assumed that activation depends sigmoidally on a sum of varying factors S_{tone} (comprising of wall tension, strain, pressure for example):

$$A = \frac{1}{1 + exp(-S_{\text{tone}})}, \tag{2.58}$$

where S_{tone} is the signal derived from a combination of local and conducted conditions compared with basal conditions. At control (basal) state, S_{tone} is zero so

that activation A is 0.5. Carlson noted that the dependence of activation on wall tension shows a negative feedback mechanism whereby an increase in tension increases activation which contracts the vessel and reduces wall tension.

In-vivo, arterioles have a basal activation level due to this control signal [58]. Each individual component of the signal has a gain (or weight) C_{signal} so that, for instance, the myogenic signal is $C_{\text{myo}} \times$ tension. The myogenic, metabolic and conducted responses were combined to one response signal for activation by Pries and Secomb [196]. They weighted these responses separately and the values for the weighting were proposed to be dependent on vessel size. There is evidence of different weightings in different sized vessels, with some positive and some negative values [112]. For example, since increased shear stress leads to vasodilation, the weighting of shear would be negative whereas the vasoconstriction caused by increased pressure means that the weighting of pressure is positive. Larger arterioles are mostly under myogenic control whereas smaller arterioles respond predominantly to metabolic conditions [134]. Ursino et al. [253], for example, thus neglected the shear response in smaller vessels

2.6.3.1 Feedback Signal

Secomb reviewed the mechanisms of signal transfer [195] and found that a response is conducted from cell to cell along the walls via gap junctions (involving changes in membrane potential and ionic concentrations). Since these occur via both endothelial and smooth muscle cells, capillaries and venules also participate in this conducted response [14].

2.6.4 Passive Vessels

Venules lack smooth muscle and therefore do not have an active response (though they are elastic). With reference to experimental data [83, 175], Ursino also assumed that the largest basal arteries in the circle of Willis are not directly involved in response and are therefore passive [253]. Passive vessels are subject to

the elastic properties described in subsubsection 2.4.3.2.

Section Summary

Autoregulation is possible because of the activation of smooth muscle which alters the total tension of the vessel. The physiology of muscle contraction is linked to the availability of calcium, which can depend on various physiological parameters. The hoop stress, shear stress and tissue concentration are likely contenders, along with a signal which is conducted upstream to communicate oxygen availability. A sigmoidal feedback signal enables a saturation of the number of muscle cells activated due to a combined signal based on other parameters, which have to be determined individually for each vessel.

Section 2:7 Stroke

A potential clinical application of a cerebral autoregulation model is to improve the understanding and diagnosis of vascular disease. This chapter contains information related to brain injury which are related to the disrupted supply of blood to brain tissue. Vascular dementia occurs when blood vessels are damaged so that cells become oxygen deprived and die in small localised areas. Stroke is either the result of a burst blood vessel (haemorrhage) or a blood clot (ischaemic). The physiology of ischaemic and haemorrhagic stroke is described and current diagnosis methods and treatment options outlined.

2.7.1 Physiology

Dementia is characterised by a loss of cognitive ability beyond what is expected due to normal ageing [63]. Dementia describes a set of symptoms including memory loss, disorientation, language problems and difficulty with problem solving which can be progressive or sudden [206]. Alzheimer's disease is the most common cause of dementia and causes a gradual deterioration [212]. Vascular demen-

tia is also known as multi-infarct dementia and can be caused suddenly by stroke, or small vessel disease (for example, thickening of the vessel wall), or a mixture [232].

A stroke is a type of brain injury which leads to a disruption of oxygen supply to brain tissue. A stroke can be ischaemic, originating from an occlusion (blockage) of a vessel, or be caused by a burst vessel (haemorrhagic stroke). Strokes occur most commonly in arterioles rather than venules and 85 % of strokes are ischaemic [55]. Haemorrhagic strokes are the most fatal with about half of patients dying compared with 20 % of those who have had an ischaemic stroke [5]. There also exist transient ischaemic attacks; a series of mini-strokes due to a temporary decrease in blood supply to the brain. These are indicative of partially blocked or narrowed vessels and can be predictors of more severe strokes later on if left untreated [269].

The main disease pathways which cause ischaemic stroke are thrombotic or embolic. The thrombotic pathway is due to plaque in the vessels; these fatty deposits build up and narrow the vessel wall whilst also increasing wall stiffness. An embolic pathway describes a clot breaking, from as far away as the heart, and travelling downstream, blocking smaller vessels. Reduced vessel diameter can cause flow to become turbulent which can rupture the plaque and damage the vessel wall [19]. This damage causes clotting (platelets sticking to the wound) which further narrows the vessel wall.

Figure 2.14: *The mechanisms of embolism, thrombosis and haemorrhage. Reproduced from [50]*

Haemorrhagic strokes due to the rupture of a blood vessel can be caused by high blood pressure or aneurysms. Over time, high blood pressure weakens blood vessels and makes them susceptible to breakage. An aneurysm is a particularly

dilated blood vessel (like a balloon) caused by a weakened wall. Aneurysms can eventually burst, filling the space between the surface of the brain and skull with blood. This increases the pressure on brain tissue.

As an occlusion develops, the available collateral circulation and autoregulatory mechanisms can cope to a certain extent. The flow to affected areas reduces and adjacent areas have increased flow as a consequence [27]. The resulting death of brain cells due to reduced oxygen supply affects related functions such as movement, speech and memory potentially causing severe disability [211].

2.7.2 Treatment

The treatment for each type of stroke is different. Ischaemic strokes can be treated with blood thinners (such as Tissue Plasminogen Activator) to dissolve the clot, or antiplatelet medicine to stop clots forming [277]. Angioplasty may also be necessary to remove a blockage by inflating a balloon in a vessel. Surgery can be used to remove a clot. However, treating a burst vessel in the same way would be catastrophic. Haemorrhages can be treated with surgery: blocking off an aneurysm by clamping or bypassing a vessel. Also, leaked fluid must be drained to relieve swelling [248]. Since the treatment for ischaemic strokes and haemorrhage are different, and time critical, the development of fast and accurate techniques for diagnosis is very important. A scan can tell whether a stroke has been due to an infarct (ischaemia) or haemorrhage but finding the location of a stroke and quantifying the extent of the damage is harder. Subsection 2.7.3 details the imaging options available.

2.7.3 Imaging Modalities

Conventional computerised tomography (CT) is an X-ray image reconstructed to show three-dimensional anatomy. It can be contrast or non-contrast depending on whether or not dye is injected. CT is able to detect haemorrhage immediately

following a stroke as a high-contrast area [81]. It is therefore the first modality for fast decision making due to the availability of CT machines in hospitals. However, after ischaemic stroke a contrast-CT can be negative for the first 36 hours [103]. A CT can also be used during therapeutic intervention such as thrombolysis [101].

X-ray angiography procedure is to inject a contrast material into the blood-stream and radio-graphically visualise the blood vessels from a time-series of images showing the flow patterns. The vessels themselves are seen by subtracting an image containing dye from one without and so narrowed or bulging vessels can be identified. This is useful following another test which has detected an abnormality [236].

A magnetic resonance image (MRI) creates a three-dimensional picture of the brain using magnetic fields. An MRI detects changes in brain tissue and is therefore useful for detecting strokes in small blood vessels. However, it is slower than a CT image to acquire.

Ultrasound can be used to investigate blood flow into the carotid arteries in the neck with trans-cranial Doppler [236]. This reveals the speed of blood-flow and thus identifies reduced blood flow into the brain. A trans-cranial Doppler can detect cerebral emboli [70]. An echocardiogram (heart ultrasound) can check the heart for clots which may have led to embolic strokes [207]. PET (positron emission tomography) also uses radioactive material to look at metabolic activity in the brain. It can be used to determine the extent of damage [236].

Although imaging gives a wide range of information, clinicians must rely on a combination of imaging and symptoms to make decisions [101]. The symptomatic effects of a stroke are due to the reduced blood flow to specific areas [237]. Prolonged reduced flow impairs oxygen supply to tissue and causes tissue death. Specific brain regions are responsible for different brain functions and so the resulting disability can indicate the broad location of a stroke. A right-hemisphere stroke

can result in left-side paralysis of the body or difficulty in reasoning. A stroke in the left side can result in right-side paralysis and inhibited speech. A brain-stem stroke is the most devastating since it reduces blood flow going into the whole brain.

Section Summary

A stroke leads to a disruption of oxygen supply to the tissue and an ischaemic stroke is caused by an alteration of vessel geometry which cannot be overcome by vessel dilation. The diagnosis of stroke relies on imaging modalities and knowledge of symptoms. The success of treatment depends on the time taken to diagnose the type of stroke and so improved understanding of how blood flows around the brain under pathological conditions would improve the current outlook for stroke patients. In the following section, existing models of the vasculature, flow and autoregulation are described.

Section 2:8 Models of the Vasculature

Since the vascular network is highly complex and active, mathematical models play a key role in understanding its behaviour [214]. This section details the development of models representing the vasculature found in the literature as well as models of oxygen transport and autoregulation. The models described here are those considered to be the foundations for the creation of an improved model.

2.8.1 Advantages of Models

Compared with experimental study, modelling has many advantages for analysing biological systems. Often, investigations using in vivo animal studies are limited by the availability of animals and by the differences between animals and humans. The complexity of procedure also hinders experiments and modelling can provide fresh insight into biological problems.

In creating a physiological model, a human system is translated into a set of ordinary differential equations and data points which can be run as computer simulations. Data may be introduced into these models in order to check a hypothesis or to investigate situations and to predict outcome. Data points from experiments can be used to validate models in order to prove their predictive powers. This can be used in personalised modelling for investigating the potential effects of medication, procedures or the time-course of disease. These would be impossible to replicate experimentally, especially individual models.

A further advantage of models is that they can be coupled together such that, for example, a model of flow in the brain could be linked to a model of oxygen consumption, or pharmacological intervention developed elsewhere in order to build an extended system. This also means that models can be broken down into smaller components for further investigation. This is a concept of 'lumped' models in which a system component is represented as an input, output and process which approximates the output from available data. These approximate internal complex processes as a more simple equation which can be solved for a variety of inputs. Certain assumptions are made in order to find an equation for the discrete entities, and many entities can be put together to mimic larger systems.

2.8.2 Lumped parameter models

For the cerebral vasculature, lumped models can be derived from electrical circuit analogies with current representing flow, voltage instead of pressure and resistance calculated for the vessel resistance. The first models which represented the adaptive cerebro-vasculature in this way were two or three-compartment Windkessel models with a serial pipe, dilating arteriole and passive venule [276]. The dilation is represented by a capacitor. Inductors may be used to represent the inertia of the blood in the venous section.

In successive models, [252, 253, 254] Ursino et al. represented the circulation in

rat brain with a circuit of compliances and resistances. Ursino's model is a detailed lumped parameter model. The driving voltage is the arterial pressure with input current Q equivalent to input flow. The arteriolar ability to store blood is represented by a capacitor C_a, and resistance R_a is used to mimic the necessary pressure drop to capillary pressure P_c. There are sections for proximal cerebral arteries, distal cerebral arteries, capillaries, veins and venous sinuses. The model incorporates arterial mechanics (allowing changes in vessel elasticity) and feedback of autoregulation. Since Ursino's model is a first-order system which reproduces autoregulation data, it is difficult to connect the first-order parameters (gain, time-constant) to physiological parameters.

Banaji et al. [9] created a model which considered the physiological systems involved with autoregulation. The model incorporates intracellular calcium and nitric oxide and the effect on vascular smooth muscle tone. It also takes into account the extracellular pH and CO_2 levels. This model is extremely detailed, with 80 differential equations. Although physiologically representative, it is difficult to translate as a useful clinical model because parameter values for individual patients are difficult to establish from data.

Lately, multi-compartment models have been proposed. Carlson et al. [41] and Arciero et al. [6] represent the vascular system as a series of 7 representative compartments: the upstream artery (A), large arteriole (LA), small arteriole (SA), capillary (C), small venule (SV), large venule (LV) and downstream vein (V). The arterioles are divided into large and small based on diameter and are assumed to be vasoactive with other compartments being passive. The compartments are connected in series with each containing n vessels. Vessels within a compartment are assumed to be identical with uniform length and diameter. The system is also symmetric (so that the length of the small arteriole compartment is the same as the small venule) although this is not confirmed by the data where venules are larger

than arterioles found at the same branching order (see subsection 2.2.8).

The resistance of a compartment depends on the number of vessels n and the resistance of individual vessels in the compartment R_i:

$$\frac{1}{R} = \frac{n}{R_i}. \tag{2.59}$$

The total resistance, R_t, for m compartments in series from is the sum of these:

$$R_t = R_1 + R_2 + ...R_m. \tag{2.60}$$

Since flow is conserved in these compartment models, total flow is the same in every compartment and flow in individual vessels is dependent on the number of vessels in the compartment:

$$Q_{vessel} = Q_{tot}/n. \tag{2.61}$$

Existing compartmental models are very simple. However, they are unable to model the effect of local changes. What is required for a greater understanding of individual vessel flow is a model which enables the vessels within a compartment to adapt individually to investigate network interaction.

2.8.3 Vascular Models

A representative segment model has been developed by Boas et al. [27] based on an earlier geometric model by Quick et al. [200]. The basis for the model is a set of vessels with length and diameter arranged in such a way as to distribute flow with vessels modelled by resistors (Figure 2.15). Boas uses a two-dimensional branching model with each parent vessel branching into two identical vessels (for arterioles) or the reverse for venules.

Figure 2.15: *Branching resistor showing conservation of flow as voltage and resistors representing vessels from [27]*

The geometry of the Boas model is based on experimental data from Zweifach and Lipowsky [281] with a 20% diameter decrease in arterioles per branch. The venule diameter increases by 20% per branch with larger venules than arterioles, representative of the vasculature. The length of capillary vessels is $250\mu m$ and of all other vessels $100\mu m$. However, the resulting velocity is higher than found in-vitro.

Figure 2.16: *Boas model of a vascular network where dashed lines represent microvascular groups. Reproduced from [200]*

Boas models oxygen partial pressure with a uniform tissue oxygen partial pressure of 15 $mmHg$ based on oxygen distribution data gathered by Vovenko [265]. The wall permeability is defined as the multiple of oxygen solubility α_w and the diffusion coefficient D_w [193]:

$$K_w = \alpha_w D_w = 5 \times 10^{-8} \mu l/mm/s/mmHg. \tag{2.62}$$

K_w is reduced by geometry (diameter D, length L and wall thickness w) so that:

$$k_w = \pi DL \frac{K_w}{w} = 7 \times 10^{-15} Mol/mmHg/s \tag{2.63}$$

for all vessels. The average oxygen saturation of vessel inlet and outlet is found with lower arteriolar saturation than in-vitro The results are reproduced (at determined diameters) in Table 2.10.

Boas is able to view the effect on the network of reducing diameter of specific vessels, or increasing oxygen consumption (initially equal to extracted oxygen calculated by Fick's law Equation 2.22). Boas establishes that there is 'surround negativity', a reduction in flow (−2%), volume and oxygen saturation in vessels sur-

Type	Diameter D (μm)	Saturation SO_2 (%)
A1	30.5	94
A2	24.4	93
A3	19.5	92
A4	15.6	89
A5	12.5	84
A6	10	77
C	8	66
V6	12	61
V5	15	59
V4	18.7	58
V3	23.4	58
V2	29.3	58
V1	36.6	58

Table 2.10: *Table collating oxygen saturation as calculated by Boas et al. [27]*

rounding the perturbed vessel. However, the model does not include any diameter autoregulation and does not model any collateral circulation.

2.8.4 Models Incorporating Autoregulation

In models of autoregulation, the exact chemical or mechanical pathways are inevitably approximated. Through successive models, Ursino et al. [250, 251, 252, 253, 254] modelled the interaction between different control mechanisms based on the hypothesis that control is activated when flow rate deviates from the basal condition. This includes the myogenic model and chemical models. The parameter of maximum active tension $T_{max0,j}$ is set and an activation factor A alters the contribution to tension:

$$T_{max,j} = T_{max0,j}\left(1 + A_j\right) \tag{2.64}$$

An absolute change in perfusion pressure (for large vessels $D \approx 150\mu m$) or flow (for small vessels $D \approx 75\mu m$) is subject to a low pass filter with a time constant $\tau = 10\ s$ with gain $G = 0.02/mmHg$ and this is added to another sigmoidal signal from the logarithmic change in carbon dioxide concentration with gain $G = 1.3$ and time constant $\tau = 20\ s$, together, these signals modify the activation factor through a sigmoidal static relationship :

$$A = \sum \frac{G}{1 + \tau S}. \tag{2.65}$$

A correction factor for CO_2 reactivity at low flow is required to mimic the impeded reactivity found in-vivo. The steady-state autoregulation results of this model (flow and radius) are good in comparison with data but the radius variation is larger than for the data resulting in over-regulation of flow. There are few vessels involved, and the small vessels are much larger than the small arterioles calculated by Boas. Further, the model is compartmental approximating large and small arterioles, capillaries and venules separately.

Pries and Secomb created a network with an initial steady state in agreement

with data from rat mesentery. The adaptive model [196, 197, 215] consists of sensitivity to various parameters (including wall stress and shear) represented by different signals. Individual vessel diameters (D) adapt dynamically according to an information signal S:

$$\frac{dD}{dt} = S \times D. \tag{2.66}$$

The signal resulting from shear stress is termed S_t, from transmural pressure S_p and the metabolic signal S_m. The signals are weighted in order to match the sensitivity for different vessels. The partial pressure of oxygen in the tissue is assumed proportional to flow and the haematocrit. A signal S_c conducted upstream from the capillaries based on oxygen levels is summed at nodes whilst decreasing exponentially along vessels. In order to maintain a minimum vessel diameter (and prevent collapse) a set point k_s is also included in the signal:

$$S = k_t S_t + k_p S_p + k_m[S_m + k_c S_c] - k_s. \tag{2.67}$$

A perturbed network will adapt iteratively to minimise the error with the known final steady state. Pries and Secomb were able to adjust the sensitivity so that different mechanisms could be isolated. They found that the myogenic mechanisms alone would cause the network to collapse to one pathway. Without the conducted signal, the metabolic signal results in capillaries with high flow due to their large pressure gradients and small diameter and flow. These are important results; that the stability of the network depends on the interaction of these signals. Pries and Secomb assign the same signal sensitivity to all vessels. Further, this model relies on knowing the steady state resulting conditions of a perturbed network.

Arciero et al. [6] also used a signal which activates vascular smooth muscle. Arciero proposes that red blood cells may act as oxygen sensors, able to com-

municate metabolic demand by releasing ATP at a rate depending on the oxyhaemoglobin saturation level of the cells. It is inferred that this ATP initiates a conducted response that travels upstream triggering arteriolar vasodilation in the same way as Pries and Secomb. The release rate of ATP, R, is a function of the oxygen saturation, $S(x)$, and based on a linear fit of results of experiments:

$$R = R_0[1 - R_1 S(x)], \tag{2.68}$$

where R_0 and R_1 are constants describing the 'maximum release rate' and 'proportionality constant' respectively. ATP is degraded by cells in the vessel wall and so the change in concentration of ATP ($C_A(x)$) is given by the difference between release rate and degradation rate:

$$\frac{d}{dx}[(1 - H_D)QC_A(x)] = \frac{\pi}{4}D^2 H_T R(S(x)) - k_d \pi D C_A(x), \tag{2.69}$$

where H_T is the tube haematocrit and the degradation is assumed first order with rate constant k_d. This is solved separately for each compartment at several points over the vessel in order to allow for change of ATP concentration and saturation along the length of the vessel.

Similarly to Pries and Secomb, Arciero assumes that the signal decays exponentially with distance travelled, with a length constant L_0. However, there is a signal generated at each point in the network (rather than just in the capillaries) proportional to the local ATP concentration. The signal is summed from the end of the largest venule to the midpoints of the arterioles:

$$S(x_{mp,k}) = \int_{x_{mp,k}}^{x_{end}} e^{\frac{-(y - x_{mp,k})}{L_0}} C(y)dy, \tag{2.70}$$

where $x_{mp,k}$ is the midpoint of vessel k and $C(y)$ is the ATP concentration at distance y from the largest venule with endpoint x_{end}.

Arciero calculates the dynamic diameter response as:

$$\frac{dD}{dt} = \frac{1}{\tau_d}\frac{D_c}{T_c}(T - T_{total}) \tag{2.71}$$

where D_c and T_c are the basal values for diameter and tension, T is the current Laplace tension, and T_{total} the tension calculated from the combination of active and passive tension. Unlike Ursino, the activation is also subject to iteration as:

$$\frac{dA}{dt} = \frac{1}{\tau_a}(A_{total} - A) \tag{2.72}$$

where A_{total} is calculated with sigmoidal dependence on the input signal.

Arciero finds that metabolic regulation is opposed by the myogenic and shear dependent responses, by splitting these responses into large and small vessels, Ursino avoids this opposition. The model is also compartmental but the small arteriolar compartment has a more relevant diameter of 14.8 μm. However, the oxygen demand and ATP release rate values are based on the physiology of skeletal muscle. In muscle, the demand is variable $1 - 25\ cm^3O_2/100cm^3/min$ whereas in cerebral tissue, a 12.5 % demand change gives a range of $8.75 - 11.25$ $cm^3O_2/100cm^3/min$. Further, in cerebral tissue there is a tightly controlled narrow range of oxygen saturation and so the effect on ATP concentration is small.

Section Summary

Several models have been described here in more detail since there are useful aspects in all of them. Boas' model incorporates individual vessels but does not include a diameter response. The conducted metabolic signal based on ATP concentration is an especially interesting possibility which could be incorporated into the Boas model, but there is an issue with the reduced variability of oxygen concentration in the brain. Pries and Secomb have a signal which directly modifies the vessel diameter with components for the myogenic and metabolic responses. The sigmoidal dependence of smooth muscle activation on signal, as used by Ursino

and Arciero, is more physiologically relevant. There is therefore scope to incorporate parts of autoregulation compartmental models into the Boas vascular model in order to model the vascular response to local oxygen demand, diameter variation and overall perfusion pressure.

Summary

In this chapter the physiological and mathematical background information have been described which is relevant to the following work. Experimental data have been collected and data from cerebral preparations identified. Throughout the literature review, different modelling approaches have been discussed with the final section concentrating on some specific models of interest.

By addressing the assumptions of these models, and incorporating different aspects, an improved tool for investigation into the vasculature could be developed which could be useful for clinicians diagnosing stroke based on the flow patterns shown in functional imaging. Most vascular models have compartments representing similar vessels. An improved model would have individual vessels, accurate geometry producing flow and pressure which is validated by the data for flow and pressure and be easy to manipulate to model diameter constriction or dilation.

Data for oxygen saturation indicates a non-uniform oxygen distribution in the vasculature and tissue which has not previously been incorporated (instead demand, or tissue concentration is assumed constant). An existing upstream signal is for a compartmental model with each section containing a number of vessels. The signal is multiplied by the number of vessels, but this doesn't show how signals behave when one vessel in a compartment is damaged which is important for the understanding of local autoregulation found in previous investigations.

The work described in the following chapters is the establishment of a new vascular model which must have experimentally verified geometry, haemodynamics and oxygen concentration and will be validated by the myogenic and metabolic responses outlined in this chapter. The model will be physiologically relevant whilst still simplifying the cellular processes of muscle activation.

CHAPTER 3

An Anatomical Model of the Cerebral Vasculature

The work presented in this chapter is an expansion of ***C. Lucas*** *and S. J. Payne, 'An Anatomical Model of the Cerebral Vasculature and the Autoregulation of Cerebral Blood Flow. In 6th World Congress of Biomechanics (WCB 2010). August 1-6, 2010 Singapore, pages 446–449. Springer, 2010. [146]*

The new vascular anatomical model proposed here is similar to the model of Boas [27] where there are 6 bifurcating arterial generations and a further 6 generations of venous vessels. It is a branching network though with the capillaries connected at the ends by 2 further generations of "cross-link" capillaries which have zero flow at steady state but the ability to take flow if necessary. This is representative of multiple potential pathways in the vasculature and of the redundancy of some vessels.

In this chapter, a method is described which determines the geometry of the vessels and calculates vessel resistance. Available pressure and velocity data are used to optimise geometry so that the flow is conserved in a bifurcating network. The geometry depends only on the capillary diameter chosen, and the number of generations of vessels. The vessels are represented as a linear set of equations so that flow and pressure can be calculated at every point in the system.

Section 3:1 Representation of the Vasculature

The proposed model of the vasculature comprises vessels connected at nodes which branch from a single arteriole over 6 generations into capillaries (see Figure 3.1). These capillaries then converge into 6 generations of venules. The vasculature is modelled as a circuit of resistors with vessels arranged in parallel forming a generation, and generations in series. There are $n = 128$ nodes in the model connected by 220 vessels forming 13 generations in total. The numbers of vessels in each branching generation from arteriole to capillary form a geometric series with common ratio 2 and this is reversed in the converging generations of venules. Successive arteriolar generations (from left to right) are referred to as $A1 : A6$, capillaries C and venules $V6 : V1$. Vessels are then referred to by generation and vessel number within the generation. For example, $A3-4$ is the fourth vessel in the third arteriolar generation.

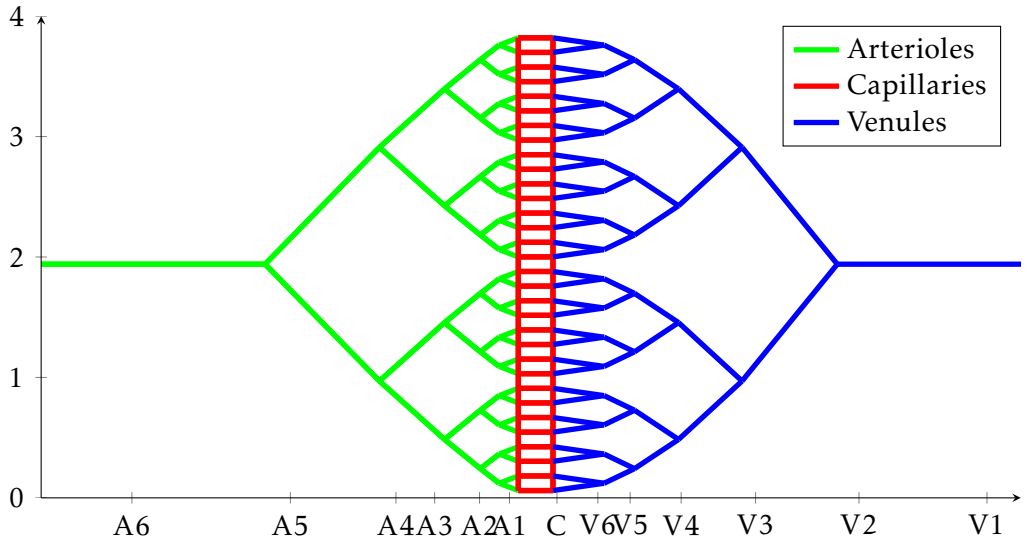

Figure 3.1: *Showing the layout of model including the vertical collateral capillaries.*

The map of vessels is stored in an adjacency matrix A. This is an $n \times n$ matrix where each row i (and column j) corresponds to a node of the vasculature. Any element of the matrix A_{ij} specifies whether or not a connection exists between nodes $n = i$ and $n = j$. A vessel existing is represented by 1, whereas a 0 shows no

vessel connecting the nodes.

Section 3:2 Geometry and Flow

It is an important requirement for any network that flow is conserved, i.e. when a vessel splits into two equal branches, the flow is halved in each branch. Flow $Q(mm^3/s)$ is equal to velocity $v(mm/s)$ times cross sectional area $A_c(mm^2)$:

$$Q = vA_c = v(\pi r^2) = (\frac{\pi}{4} vD^2). \tag{3.1}$$

Multiple pressure and velocity data points (including one for each generation diameter from the Boas model [27]) were extracted from the line of fit of the Zweifach graph Figure 2.4 and are given, together with calculated flow, in Table 3.1.

3.2.1 Velocity

It is possible to find a fit of this data which can be used to find pressure and velocity values which correspond to any diameter. In order to find a polynomial fit of diameter and velocity which is able to solve for all generations, arteriole diameters are set as negative to mirror them being on the negative x-axis on the Zweifach graph and capillary diameter is set to 0. Figs are given in the appendix: Table A.8 gives the results of a third (Equation A.1), fourth (Equation A.2) and fifth (Equation A.3) order fit of this data.

Although a cubic function passes closest to the capillary velocity (+0.55mm/s) see Table A.8), it has greater overall error. The root mean squared error (RMSE) for cubic is 0.9806mm/s and for fourth order is 0.4103mm/s. For a fifth order approximation, the error is 0.4066mm/s, but the error in the smaller vessels is larger for a fifth order approximation than a fourth order (see Figure A.1 and Table A.8). For small vessels (Diameter less than 41μm), the RMSE for a fourth order fit is 0.4240mm/s and for fifth order is 0.4318mm/s.

Vessel Type	Diameter D (μm)	Velocity v (mm/s)	Pressure P ($mmHg$)	Flow Q ($\times 10^{-3} mm^3/s$)
A	54.6	15.0	87.2	35.0
A	50.7	14.7	84.5	29.6
A	47.3	14.4	82.0	25.3
A	43.4	13.8	78.5	20.5
A	40.3	13.3	75.3	13.6
A	36.1	12.7	70.8	13.0
A1	30.5	11.0	63.3	8.0
A	26.2	9.4	58.3	5.1
A2	24.4	8.7	55.8	4.1
A	22.9	8.0	53.7	3.3
A3	19.5	6.7	49.2	2.0
A4	15.6	5.0	43.3	1.0
A5	12.5	3.2	38.3	0.4
A	11.6	3.4	37.9	0.4
A6	10.0	2.8	35.8	0.2
C	8.0	2.3	34.2	0.1
V6	12.0	1.7	31.7	0.2
V5	15.0	1.8	30.0	0.3
V	16.8	1.8	29.7	0.4
V4	18.7	1.9	27.6	0.5
V	21.1	2.3	28.1	0.8
V3	23.4	3.0	26.9	1.3
V	26.0	3.4	26.3	1.9
V2	29.3	4.5	24.6	3.0
V	31.6	5.0	25.7	3.9
V1	36.6	6.3	23.3	6.6
V	41.0	8.5	23.3	9.9
V	46.1	9.3	22.9	14.2
V	51.7	10.2	22.2	19.6

Table 3.1: *Values extracted from Zweifach graph Figure 2.4 [281] with vessel type identified at the diameters used by Boas in his model [27].*

A better fit to these small vessels is achieved with a narrower range of vessel diameter. Equation A.6 is a fifth order fit of velocity for vessels smaller than $41 \mu m$. The RMSE for the small vessels is $0.2908 mm/s$. However, this fit cannot be extrapolated for fifth order beyond the range: the RMSE for all vessels is $3.3040 mm/s$ due to the turning points of the fit (see Figure A.2). A compromise between the fit of the smaller vessels, and ability to extrapolate if necessary (for example, if larger

networks were to be modelled) uses the fourth order fit (Equation A.5) over a narrow range with a RMSE of $0.4143 mm/s$ for vessels $D \leq 41 \mu m$, and $0.4382 mm/s$ for all vessels.

3.2.2 Diameter

The capillary diameter is given by Zweifach as $8 \mu m$ and relates to a velocity of $2.3 mm/s$ (from Figure 2.4) with a flow of $1.17 \times 10^{-4} \mu l/s$ from Equation 3.1. Since the total flow at each node is assumed to be conserved, the flow in each vessel of the 6th arterial and venular generations must be equal to the capillary vessel flow. Conservation of flow at a bifurcation is assumed for each of the other generations and so generally Equation 3.2 holds for adjacent generations of vessel:

$$D_i^2 v_i = 2 D_{i+1}^2 v_{i+1} \, . \tag{3.2}$$

Equation 3.2 is solved over all generations using fzero (a zero solution routine in MATLAB) to find the diameter which satisfies the velocity. The resulting diameter values (starting with a capillary diameter of $8 \mu m$) are given in the results (subsection 3.4.1, Table 3.3, 106). These diameters are smaller than those used by Boas (see Table 3.1). This may be because the correct capillary velocity from the data is above the polynomial fit and so values are shifted. Nevertheless, the values of diameter better satisfy the velocity required for conservation of flow. Similarly to Boas, the venule diameters are found to be bigger than the corresponding arteriole diameters as found in-vitro by Vovenko [265].

3.2.3 Wall Thickness

It is difficult to find consistent values for the ratio of wall thickness to lumen diameter from the literature because of the elasticity of these vessels, which means that they are thinner at high pressure, and the variation between vessel types. In Table 2.2, data from rat brain for capillaries and venules are given. Capillaries have very thin walls, only 1 cell thick. The capillary wall thickness can be set to 3.86%

based on the experiments in rat brain carried out by Shaver [222]. Venules have thinner walls than arterioles since they do not have the layer of smooth muscle found in arterioles. The average value found in cat brain by Roggendorf [204] is 10%.

It can be assumed that wall volume V_w is conserved regardless of vessel diameter change, i.e. if a vessel elastically increases in size, the wall will become thinner (see Equation 2.8).

Vessel wall volume is calculated as

$$V_w = \pi L((R+w)^2 - R^2). \tag{3.3}$$

The conservation of wall volume is expressed in Equation 3.5 where w_0 and D_0 are any reference wall thickness and diameter respectively and vessel length L is assumed constant:

$$2Rw + w^2 = 2R_0 w_0 + w_0^2. \tag{3.4}$$

Since $2R_0 \equiv D_0$, this is equivalent to:

$$w^2 + Dw = w_0^2 + D_0 w_0 = \frac{V_w}{\pi L}. \tag{3.5}$$

Parameter λ is declared:

$$\lambda = \frac{V_w}{\pi L}. \tag{3.6}$$

The rat cerebral arteriole diameter and wall thickness data from Harper [93] (see Table 2.2) can be plotted as the parameter λ from Equation 3.6 (see Figure 3.2). λ is fit as a function of experimental diameter (assumed to be D_0 μm). A second-order fit is chosen since a linear fit produces negative results at low diameter, and a higher-order fit has turning points either side of the range of diameters. For this quadratic fit, the root mean squared error is 17.88 μm^2, which is high, however the resulting error in wall thickness using Equation 3.7 is only 0.5598 μm.

$$\lambda = \frac{V_w}{\pi L} = w_0^2 + D_0 w_0 = 0.16 D_0^2 + 1.4(mm) D_0 + 14(mm^2) \tag{3.7}$$

Wall thickness w can then be found for each vessel at any diameter D with reference to any other diameter D_0 and wall thickness w_0 by solving Equation 3.8.

$$w = \frac{-D \pm \sqrt{(D^2 + 4(w_0^2 + D_0 w_0))}}{2} = \frac{-D \pm \sqrt{(D^2 + 4(\lambda))}}{2} \tag{3.8}$$

The fit shows that the walls of smaller arterioles have less volume as a function of

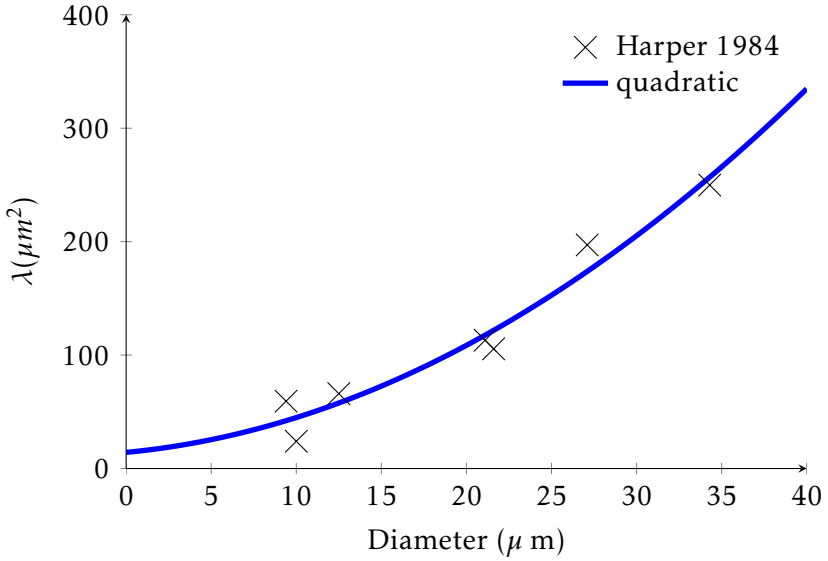

Figure 3.2: *Showing a quadratic fit of arteriolar lumen and tissue volume data from [93].*

diameter whilst having an increase in wall-to-lumen ratio. Results of Equation 3.7 for the model diameters are given in Figure 3.6 and Table 3.3 in subsection 3.4.1.

3.2.4 Pressure

Zweifach also determined the mean intravascular pressure in cerebral vessels. These data can also be approximated by a polynomial fit between diameter D μm and mid-vessel pressure P_v $mmHg$ from Table 3.1.

Similarly to the fit for velocity (as described in subsection 3.2.1), the fifth order fit Equation A.9 has a lower overall root mean squared error (1.3821 $mmHg$) compared with fourth-order Equation A.8 (1.8921 $mmHg$), and cubic (2.6433 $mmHg$) but the error in the small vessels ($\leq 41\mu m$) is large (2.0403 $mmHg$ and 1.4435 $mmHg$ for fourth and fifth order respectively). Fitting to vessels with diameter

less than $41\mu m$, the RMSE is 1.6248 $mmHg$ for fourth (Equation A.11), and 0.9909 $mmHg$ for fifth order approximations (Equation A.12). The model diameters found in subsection 3.2.2 are all smaller than $40\mu m$ (the maximum is the feeding venule with diameter $30.98\mu m$). Extrapolating these fits to the entire diameter range produces large errors (3.8446 $mmHg$ and 10.8244 $mmHg$) and so if large networks with more generations were required, then Equation A.9 is more suitable. The polynomial coefficients for both fits are listed in Table 3.2.

Polynomial Coefficients	Larger Networks	Current Network
$p_1\ (mmHg/\mu m^5)$	6.7915×10^{-8}	2.5706×10^{-7}
$p_2\ (mmHg/\mu m^4)$	-2.2463×10^{-6}	-4.0910×10^{-6}
$p_3\ (mmHg/\mu m^3)$	-2.5166×10^{-4}	-6.3397×10^{-4}
$p_4\ (mmHg/\mu m^2)$	0.0138	0.0168
$p_5\ (mmHg/\mu m)$	-0.4248	-0.2846
$p_6\ (mmHg)$	33.10108	32.4953

Table 3.2: *Comparing the polynomial coefficients for fitting for diameters $\leq 41\mu m$, and for networks with larger diameters*

When fitting for velocity, the diameters are unknown and therefore the fourth-order plot for small vessels is used. Figure A.2 shows that the fourth-order small vessel plot extrapolates well compared with the fifth-order. This ability to extrapolate is not true for the pressure fit, Figure A.4. Since the model diameters are already known from previous calculations, the higher order fit for smaller diameters is used here. In general, the fit can be chosen to best incorporate the diameter range found in the model.

The new model diameters from Table 3.3 are used to calculate pressure at the vessel midpoint, P_m, using Equation A.12. The pressure is interpolated to find the input and output node pressure, P_n, of each vessel (and therefore the pressure drop across each generation ΔP) and over the entire vasculature ΔP_{tot} giving an arterial inlet pressure of $P_a = 57.79 mmHg$ (compared with $60 mmHg$ for Boas) and venous outlet pressure $P_o = 23.61 mmHg$ (compared with Boas $25 mmHg$). The resulting

model mid-vessel pressure is given in Figure 3.7 and Table 3.4 in subsection 3.4.1.

3.2.5 Length

The total flow (the sum of flow in each generation) is $3.7 \times 10^{-3} \mu l/s$. Using the flow and pressure gradient values evaluated from the Zweifach data, and viscosity from subsection 2.2.2; the resistance of each segment is found by Equation 2.1. The length L of each vessel can then be calculated by rearranging Equation 2.2, giving Equation 3.9:

$$L = \frac{RD^4\pi}{\mu 128} \,. \tag{3.9}$$

Length is found to be non-symmetric for corresponding generations (see Table 3.3): the arterial vessels are longer with smaller diameters than equivalent venous vessels. The capillary length $144.97 \mu m$, and venules and large arterioles have values ranging between $867.09 \mu m$ and $91.08 \mu m$.

Section 3:3 Method Summary

This section summarises the method proposed in chapter 3 and describes how it can be used for a network of any size to find geometry which satisfies the conservation of flow requirement, and matches the Zweifach network. A method for calculating flow and pressure in individual vessels in the network is then described.

3.3.1 Geometry

The total flow in the network is set by the Zweifach capillary velocity and diameter, and the number of capillary vessels. The number of capillary vessels depends on how many generations there are in the network. Assuming that total flow is the same for each generation, vessel flow depends only on the number of vessels in that generation.

Starting from this assumption, and the fit of velocity and flow data proposed here, any sized network can be optimised so that the diameter of the vessel is at

the required velocity for conservation of flow, shown in Figure 3.3.

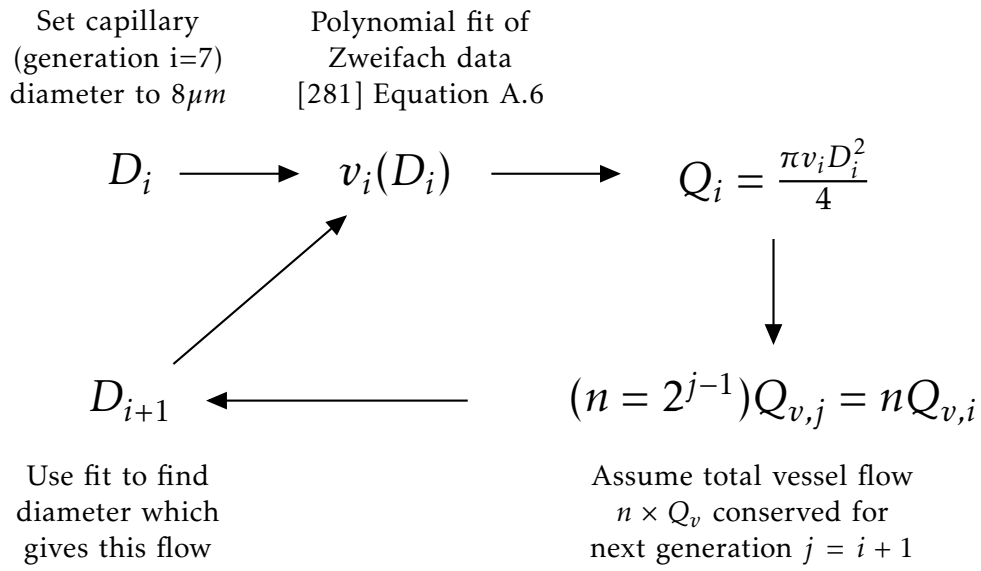

Figure 3.3: *Flowchart describing processes used to establish the diameter using the assumption of conserved flow and data for pressure and velocity as a function of vessel diameter.*

The geometry of the network causes resistance to flow which results in a pressure drop across a vessel. Using the proposed fit of diameter and pressure, the pressure drop and therefore vessel resistance can be found. This can then be used to determine the necessary vessel length to cause such resistance (see Figure 3.4).

The geometry of the network can then be found for each generation, assuming that each vessel within the generation has the same characteristics.

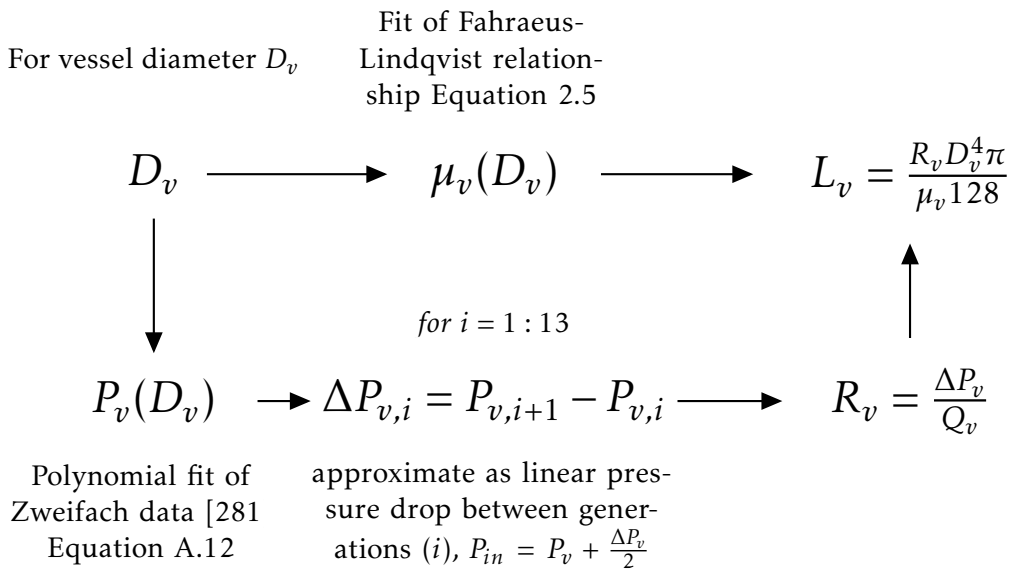

Figure 3.4: *Flowchart describing processes used to establish the vessel length using the initial approximation of linear pressure drop along a vessel, and the Fahraeus-Lindqvist relationship between diameter and viscosity.*

3.3.2 Calculating flow and pressure

For a network of individual vessels, the flow is calculated from diameter and length. This enables re-calculation of flow in the network when vessel parameters are changed. The resulting vessel conductance $G = 1/R$ is used to weight an adjacency matrix of connections using Equation 3.10 so that $G_{i,j}$ gives the conductance of the vessel connecting nodes i and j.

$$G_{i,j} = 1/R_{i,j} \tag{3.10}$$

Kirchoff's circuit laws states that the sum of current into a node is zero. This can be expressed for 3-resistors in terms of node pressure P_n, conductance G and flow Q as Equation 3.12:

$$\sum Q = 0 \tag{3.11}$$

$$Q = G\Delta P \tag{3.12}$$

Equation 3.12 can be represented for every node n as a matrix of linear equations where, if P_a and P_o are known, the node pressures can be calculated. Fig-

ure 3.5 describes how the resulting nodal pressure can be interpolated to find mid-vessel pressure assuming a linear pressure drop across the vessel. This pressure gradient can then be used with vessel resistance to find the flow in each vessel. These are calculated for the model and given in Table 3.4 and graphically in Figure 3.7.

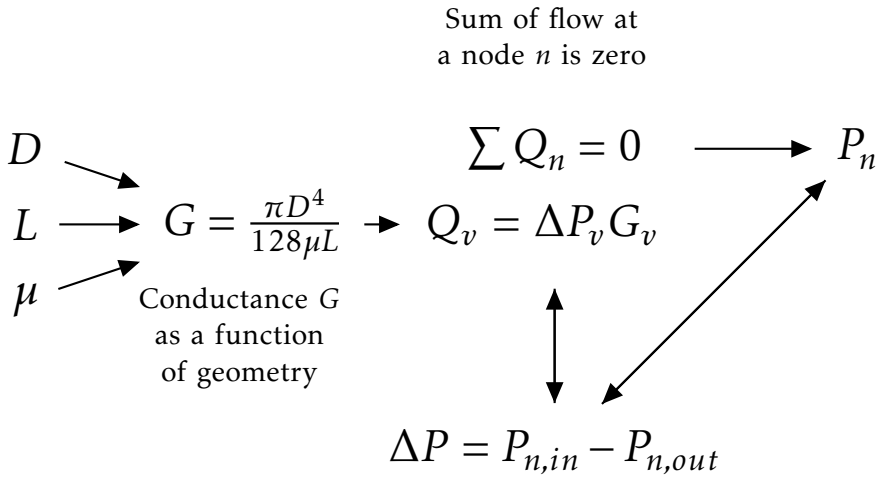

Figure 3.5: *Flowchart describing the process of establishing flow and node-pressure using geometry and Poiseuille's relationship Equation 2.1.*

Section 3:4 Results

This section compiles the results of calculations described in the chapter and presents the geometry of a 13 generation branching network and resultant flow and pressure.

3.4.1 Geometry

Table 3.3 gives the geometrical characteristics of the network which are also presented graphically in Figure 3.6.

In Figure 3.6 (b), vessel $V6$ has longer length than other venules, and the capillary. Length is calculated from derived pressure and so this may be an error, especially with the long capillaries. In comparison, the results for diameter (Figure 3.6 (a)) show a smooth, non-symmetrical decreasing diameter towards the capillaries.

Generation (no. vessels)	Diameter (μm)	Wall /Diameter (%)	Length (μm)
A1(1)	23.97	20.2	867.09
A2(2)	19.17	22.19	626.32
A3(4)	15.28	24.94	354.19
A4(8)	12.08	28.85	189.97
A5(16)	9.46	34.52	97.48
A6(32)	7.32	42.87	91.08
C(94)	8	3.86	144.97
V6(32)	11.51	10	295.3
V5(16)	14.53	10	177.72
V4(8)	17.79	10	284.49
V3(4)	21.45	10	429.1
V2(2)	25.7	10	577.68
V1(1)	30.77	10	631.86

Table 3.3: *Table collating geometrical properties of diameter from equation Equation 3.2, and length from Equation 3.9.*

Arteriole wall thickness (Figure 3.6 (c)) is calculated from the wall volume and shows that the smaller diameter arterioles have larger wall thickness.

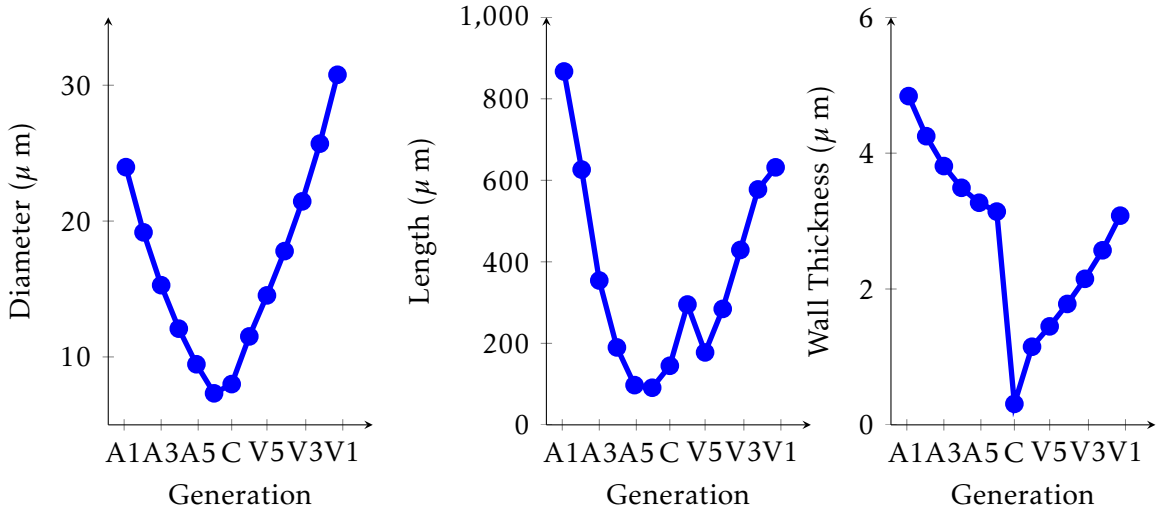

(a) Vessel Diameter (b) Vessel Length (c) Wall Thickness

Figure 3.6: *The model diameter, length and wall thickness are displayed for each generation of vessels, A1:6, C and V6:1 .*

3.4.2 Pressure and Flow

Table 3.4 gives the resulting velocity and flow of blood, and the mean intravascular pressure of vessels in the network. These are also presented graphically in Figure 3.7. The results using the training data show that the method is able to calculate a symmetrical flow using the geometry calculated from the data-fit and calculating pressure, and subsequently flow, from the pressure at the first and last node.

Generation (no. vessels)	Velocity (mm/s)	Flow ($\times 10^{-3} \mu l/s$)	Pressure ($mmHg$)	Viscosity ($\times 10^{-5} mmHg\,s$)
A1(1)	8.2	3.7	54.32	1.75
A2(2)	6.41	1.85	47.92	1.68
A3(4)	5.05	0.92	42.98	1.64
A4(8)	4.03	0.46	39.62	1.61
A5(16)	3.29	0.23	37.36	1.59
A6(32)	2.75	0.12	35.27	1.57
C(64)	2.3	0.12	32.79	1.57
V6(32)	1.11	0.12	30.84	1.61
V5(16)	1.4	0.23	29.9	1.63
V4(8)	1.86	0.46	29.15	1.66
V3(4)	2.56	0.92	28.05	1.71
V2(2)	3.57	1.85	26.51	1.78
V1(1)	4.97	3.7	24.61	1.89

Table 3.4: *Table collating results of velocity, flow and pressure calculated from polynomial relationship based on Figure 2.4 and viscosity calculated from the Boas relationship .*

Flow is conserved so that it is symmetric across corresponding arterioles and venules in the network (see Figure 3.7 (a)) . The velocity distribution in the arterial and venous vessels shows the differing conditions in the arterial and venous sides of the network due to the non-symmetrical lengths. The velocity at the model diameters is displayed along with those calculated using the polynomial fit of the Zweifach graph at the same diameter, and similarly for pressure. The pressure drop shows a large drop over the capillary and post-capillary venule generation despite the low flow here since resistance is very high. This has an effect on the

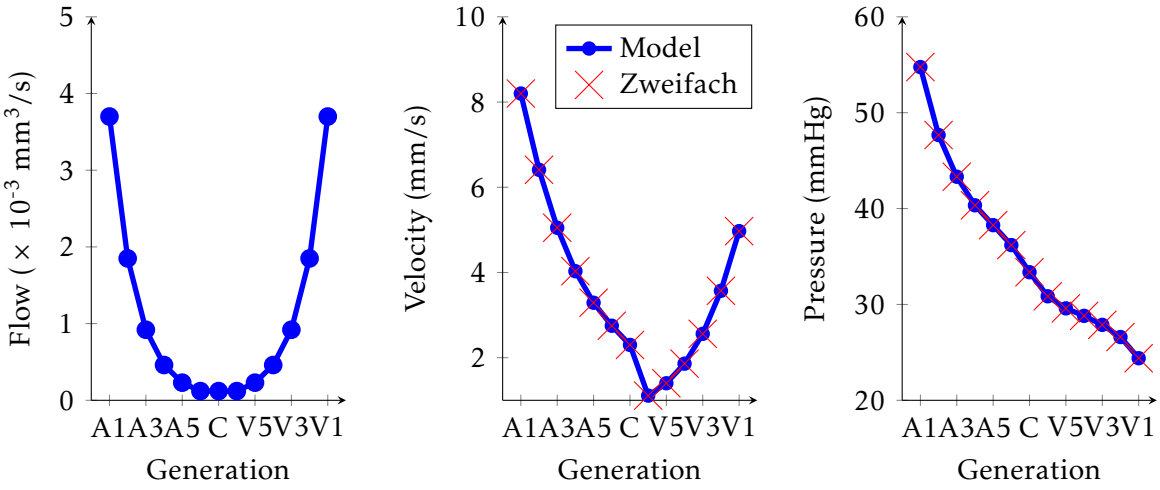

(a) Flow (b) Velocity (c) Pressure

Figure 3.7: *Flow and velocity calculated for model geometry and inlet pressure which more closely matches the data. They are displayed for each generation of vessels, A1:6, C and V6:1 .*

calculated vessel length.

The method described is a generic method which enables model construction of any size by specifying the number of capillaries. Further, with applicable data this method could be extended to other vascular beds.

Summary

The Zweifach network vasculature data [281] is well replicated by the model proposed here. To establish the vessel geometry, a method is described which works backwards from the Zweifach data to find diameter values necessary for velocity, which is related to required flow. The lengths required to create the pressure drop which equates to the same flow are then found. The resulting length and diameter values can be used to calculate resistance, and therefore validate model flow using the input and output pressures of the system. For individual vessels, the pressure drop can be found by using the Poiseuille relationship between flow, pressure and resistance. These processes can be summarised by a flowchart describing the use of data to find the diameter values

Figure 3.3 the length Figure 3.4 and the pressure and flow Figure 3.5. This model moves on from compartmental or lumped parameter models towards more detailed spatial models.

CHAPTER 4

A Model of Oxygen Concentration in the Cerebral Vasculature

Once flow in the network has been calculated, as outlined in chapter 3, the distribution of oxygen concentration can be found by calculating oxygen flux across the vessel wall and consumption from the tissue compartment. The literature review section 2.3 presents a variety of parameter values, both calculated and found experimentally. There are also conflicting hypotheses for these parameters. Therefore, this model starts from the cerebral oxygen concentration data found by Vovenko and the parameters are explored in order to determine a likely set of parameters for cerebral oxygen transport.

Section 4:1 Data

4.1.1 Fick's Law

As described by Popel in [193], the flux J of oxygen out of a vessel (the amount of substance in micromoles μM per unit area mm^2 per unit time s) is driven by the transmural concentration gradient (ΔC_w) across the vessel wall, (width w mm) with C_v the volume mean vessel oxygen concentration ($\mu M/mm^3$) and C_T the oxygen concentration in surrounding tissue (assumed to be the same over the entire vessel length).

The rate of diffusion is determined by the physiology of the vessel wall, parameterised by the diffusion coefficient for oxygen in tissue $D_c(mm^2/s)$. This flux is equal to the oxygen extracted in the vessel (see Equation 2.20 and Equation 2.21).

The resulting longitudinal concentration gradient in the vessel, $\frac{dC_v}{dx}$, is found using Fick's law at steady state and depends on the circumference of the vessel $\pi D(mm)$ and the blood flow $Q(mm^3/s)$, as shown in Equation 2.24.

The solution for this first order ordinary differential equation (with diffusion coefficient for the wall D_w) is :

$$C_v(x) = [C_{in} - C_T]\, e^{-\frac{D_w \pi D}{wQ} x} + C_T, \tag{4.1}$$

where C_{in} is the oxygen concentration in the blood at the inlet of the vessel. The solution is a non-linear oxygen profile along the vessel, assuming constant tissue concentration along the vessel, so that the output concentration C_{out} is found by the solution of Equation 4.1 at $x = L$.

$$C_{out} = [C_{in} - C_T]\, e^{-\frac{D_w \pi D L}{wQ}} + C_T \tag{4.2}$$

Equation 4.2 can be solved sequentially from a known node concentration but requires the parameters D_w and C_T to be known for each vessel.

4.1.2 Data and Previous Model

Vovenko determined the partial pressure of oxygen on the inner surface of vessels in rat brain [265]; the findings given in Table 2.4. The conversion between partial pressure and oxygen saturation used by Vovenko does not fit the standard oxygen dissociation curve (as described in subsubsection 2.3.5.1). Duling measured the partial pressure in the lumen of cerebral arterioles in cat [68]. Boas [27] modelled the oxygen saturation in the cerebral vasculature with tissue concentration and a diffusion coefficient based on physiological considerations. Some of the resulting oxygen saturation values from Table 4.1 can be converted into partial pressure by comparing with the values given by Vovenko.

Type	Diameter D (μm)	Saturation SO_2 (%)	Partial Pressure PO_2 ($mmHg$)
A1	30.5	94	78.7
A2	24.4	93	75.8
A3	19.5	92	-
A4	15.6	89	68.3
A5	12.5	84	61.5
A6	10	77	-
C	8	66	-
V6	12	61	-
V5	15	59	41.3
V4	18.7	58	-
V3	23.4	58	-
V2	29.3	58	-
V1	36.6	58	-

Table 4.1: *Table collating tissue partial pressure determined from oxygen saturation as calculated by Boas in [27]*

4.1.3 Concentration Data

Oxygen concentration, C_v ($\mu M/mm^3$) is converted from average partial pressure via Equation 2.14 with $K_h = 0.72\ mmHg\ mm^3/\mu M$ taken from [256]. These are given in Table 4.2 :

Vessel	Diameter D (μm)	Partial Pressure (mean) P_{O2} ($mmHg$)	Concentration C_v ($\mu M/mm^3$)
A1	45	81.2	112.8
	45	80.1	111.3
A2	33	78.7	109.3
A3	26	75.8	105.3
	22	72.6	100.83
A4	13	68.3	94.9
A5	8	61.5	85.4
C	8	49.4	68.6
V5	13	38.2	53.1
V4	31	41.1	57.1

Table 4.2: *Conversion of partial pressure into oxygen concentration from Vovenko data [265] and Duling data [68].*

Values from Table 4.2 are plotted in Figure 4.1, with the axis labelled at the diameter. Arterioles are given negative diameter to distinguish them from venules; capillary diameter is set to 0 (see Table 4.3). The results of the Boas model from Table 4.1 are also plotted.

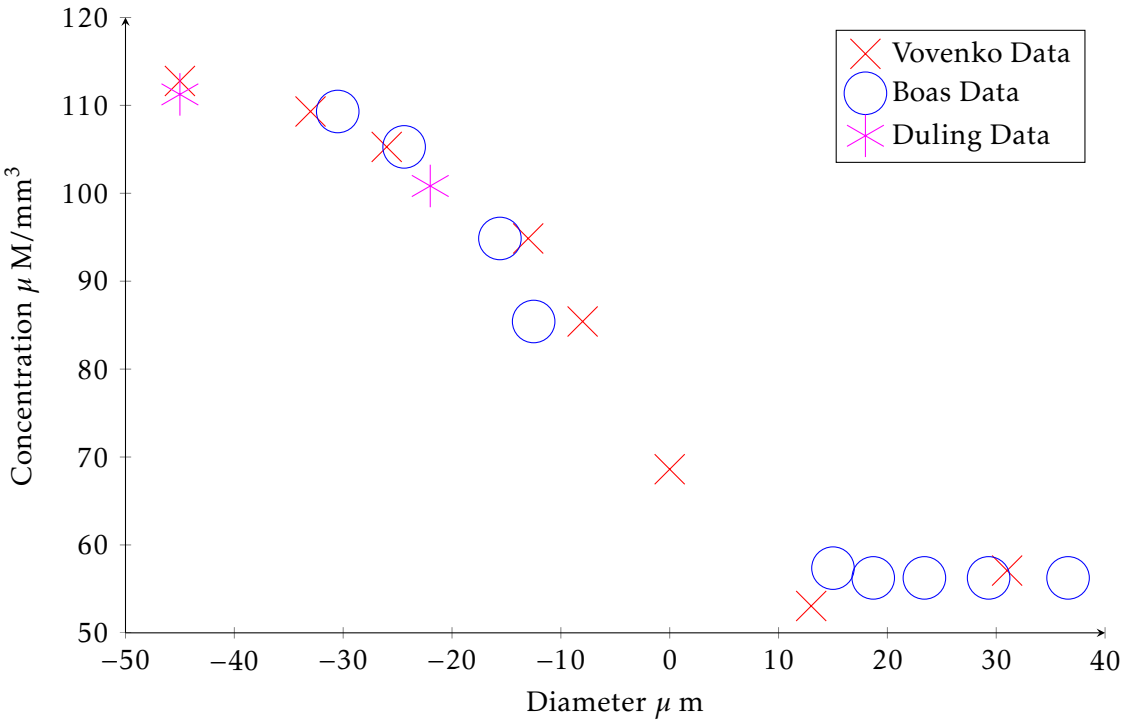

Figure 4.1: *Showing the collated oxygen concentration from measured partial pressure from Table 4.2 and Table 4.1*

The Vovenko and Duling data fit well together with Boas removing the anomaly of the post-capillary venule concentration $V5$.

Section Summary

The data described in this section are for cerebral vessels but can be fit against vessel diameter in order to provide an estimate of the Lucas model oxygen concentration. Any fit of the data assumes that diameter (D μm) is indicative of vessel branching order.

Section 4:2 Data Fitting

4.2.1 Data Manipulation

There are a few issues to consider. Firstly, the partial pressure found by Vovenko decreases in vessel $V5$ compared to the capillaries, potentially because of shunting. The Lucas model does not include shunting and so the Boas value for $V5$ can be included for the fit and the Vovenko $V5$ value ignored. Secondly, the oxygen saturation calculated by Boas decreases slightly in $V6$ and $V5$ and then stays the same over the rest of the venules (58%). There is no direct PO_2 value for 58% in the Vovenko results, but $57\% \approx 40 mmHg$ and $59\% \approx 41$ $mmHg$ so 58% is set as 40.5 $mmHg$. The resulting data set is given in Table 4.3. The longitudinal gradient of oxygen concentration is non-linear and the shape of the diameter-oxygen curve can be described as sigmoidal rather than polynomial: with a flatter initial phase in the larger arterioles (and in the venules), and the steepest gradient through the capillaries. Due to varying geometries and functional demand, the oxygen gradients in different vessels are unlikely to have the same mathematical relationship between diameter and concentration. Furthermore, the Lucas diameter range for vessels $A1$ to $V6$ is small compared with the range of the available data with several vessels falling between two data points.

Diameter D (μm)	Concentration C_v ($\mu M/mm^3$)
−45	112.8
−45	111.3
−33	109.3
−26	105.3
−22	100.8
−13	94.9
−8	85.4
0	68.6
15	57.4
18.7	56.3
23.4	56.3
29.3	56.3
36.6	56.3

Table 4.3: *Data set of diameter and oxygen concentration compiled from Boas [27], Duling [68] and Vovenko [265].*

4.2.2 Cubic-Spline Interpolation

Cubic spline interpolation can be used to find the piecewise polynomial fit of the data in Table 4.3. A piecewise function is a set of multiple sub-functions for the intervals of the data. The two values for $45\mu m$ have to be averaged in order to use them giving 112.02 $\mu M/mm^3$. For 12 data points, there are 11 intervals with cubic polynomial coefficients given in the rows of Table 4.4 which are used in Equation 4.3 to calculate concentration between the data-points.

$$C_v = p1D^3 + p2D^2 + p3D + p4. \tag{4.3}$$

The resulting fit is evaluated at the Lucas diameters and is shown in Figure 4.2 with concentration values given in Table 4.5. Since the fit is an interpolation between points, the standard deviation of the measurement error affects the calculated concentration and causes kinks in the curve (see $A2$ in Figure 4.2).

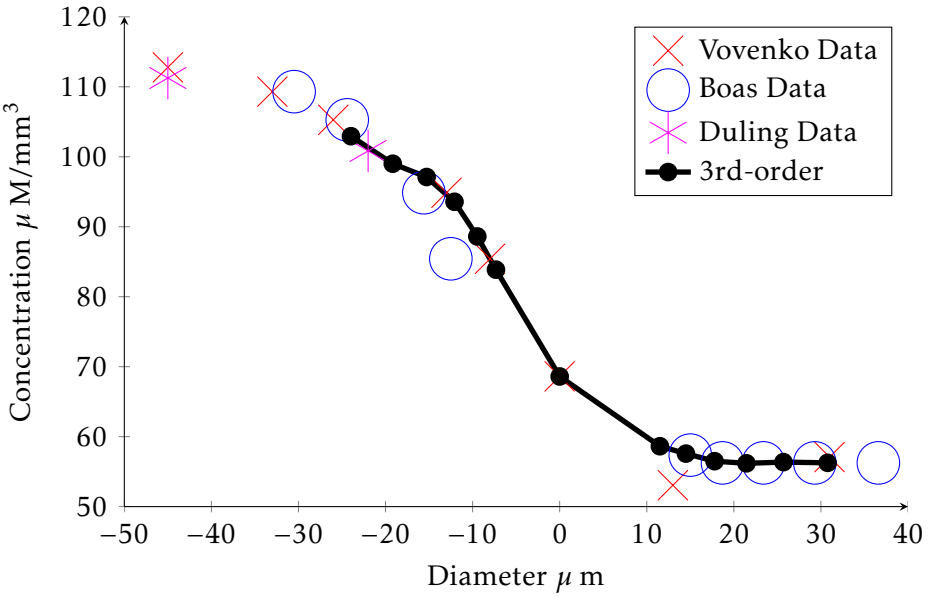

Figure 4.2: *Oxygen concentration data fit to Lucas diameter. Arteriole diameter is negative to distinguish from venules.*

Diameter range (μm)	p1	p2	p3	p4
$-45:-33$	-0.002705	0.06571	-0.62567	112.02
$-33:-26$	-0.002705	-0.03167	-0.21719	109.3
$-26:-22$	0.017945	-0.088476	-1.0582	105.3
$-22:-13$	-0.01102	0.12686	-0.90467	100.8
$-13:-8$	0.0101	-0.17068	-1.2991	94.9
$-8:0$	0.0047167	-0.019182	-2.2484	85.4
$0:15$	-0.0022543	0.094019	-1.6497	68.6
$15:18.7$	0.0059182	-0.0074266	-0.35084	57.4
$18.7:23.4$	-0.0050302	0.058266	-0.16273	56.3
$23.4:29.3$	0.00066279	-0.012659	0.051618	56.3
$29.3:36.6$	0.00066279	-0.0009279	-0.028546	56.3

Table 4.4: *Piecewise polynomial coefficients to fit diameter between data points to oxygen concentration.*

Order	Diameter D (μm)	Concentration C_v (mean) ($\mu M/mm^3$)
A1	23.97	102.94
A2	19.17	99.01
A3	15.28	97.11
A4	12.08	93.57
A5	9.46	88.61
A6	7.32	83.86
C	8	68.61
V6	11.51	58.63
V5	14.50	57.57
V4	17.79	56.49
V3	21.45	56.19
V2	25.70	56.36
V1	30.77	56.26

Table 4.5: *Table showing the mean vessel concentration using a piece-wise fit of data from Vovenko [265], Duling [68] and model results from [27].*

4.2.3 Calculation of the Node Concentrations

The capillaries measured by Vovenko have an average diameter of 8 μm and length of 258 μm long with a longitudinal oxygen gradient of 91.5 $\mu M/mm^3/mm$ and mid-vessel concentration 68.61 $\mu M/mm^3$. The Lucas model capillary has diameter 8 μm and the length is 144.97μm. The inlet C_{in} and outlet C_{out} node concentrations $C_{n,cap}$ can therefore be calculated using the average longitudinal gradient:

$$C_{n,cap} = 68.61 \pm 13.26 \mu M/mm^3, \tag{4.4}$$

so that $C_{in} = 75.24\ \mu M/mm^3$ and $C_{out} = 61.98\ \mu M/mm^3$. These are compared with the average capillary node concentrations measured by Vovenko of $80.42 \mu M/mm^3$ and $56.81 \mu M/mm^3$.

The node concentrations calculated for the capillaries can be used, together with the mean arteriole concentration, to find the node concentrations sequentially in the arterioles where j is the vessel generation ($j = 6$ for $A6$) and $C_{out,A6} = C_{in,C}$:

$$C_{in,j} = 2C_{v,j} - C_{out,j} = 2C_{v,j} - C_{in,j+1}. \tag{4.5}$$

With this method, the inlet vessel concentration for $A6$ is calculated to be 92.49 $\mu M/mm^3$ which is higher than the average concentration of $A5$. If the value for $C_{out,j}$ is greater than the average vessel concentration (as happens in $A5$), the oxygen inlet concentration is taken to be the average of the vessel concentrations as an approximation, enabling the calculation of node concentrations to continue. Table 4.6 gives these updated results where new concentrations are parenthesised in and C_v is updated accordingly.

Order	Concentration C_v (mean) ($\mu M/mm^3$)	Inlet C_{in} ($\mu M/mm^3$)	Outlet C_{out} ($\mu M/mm^3$)	Gradient $\frac{\Delta C}{L}$ ($\mu M/mm^3/mm$)
A1	102.94	104.9	100.97	4.53
A2	(100.36)	100.97	99.75	1.95
A3	97.11	99.75	94.46	14.94
A4	93.57	94.46	92.68	9.37
A5	(92.58)	92.68	92.49	1.98
A6	83.86	92.49	75.24	189.33
C	68.61	75.24	61.98	91.50
V6	(61.25)	61.98	60.52	4.92
V5	(60.04)	60.52	59.56	5.45
V4	(58.32)	59.56	57.08	8.71
V3	(56.85)	57.08	56.62	1.08
V2	(56.54)	56.62	56.46	0.27
V1	56.26	56.46	56.06	0.64

Table 4.6: *The mean vessel concentration with updated values (parenthesised) calculated as described.*

4.2.4 Consideration of the Longitudinal Gradient

The longitudinal gradient of $A6$ is extremely high, although it is expected that longitudinal gradients increase with decreasing diameter [234]; Swain and Pittman measured an 18.6%/mm saturation gradient in 21μm hamster retractor muscle arterioles. The uncertainty in measurement of the smallest arteriole by Vovenko is ±12 $mmHg$. At a minimum, this vessel would have concentration 68.75 $\mu M/mm^3$ (compared with 85.42 $\mu M/mm^3$ as measured). If the longitudinal gradient for the pre-capillary arteriole was set to the same as the capillaries (91.5

$\mu M/mm^3/mm$), the mean concentration of $A6$ calculated from the outlet concentration would be 79.41 $\mu M/mm^3$ (see Table 4.7 for updated values). The consistency of the longitudinal gradient is improved, although $A2$ has a very low oxygen gradient. The data is therefore largely affected by where the concentration measurement is

Order	Concentration C_v (mean) ($\mu M/mm^3$)	Inlet C_{in} ($\mu M/mm^3$)	Outlet C_{out} ($\mu M/mm^3$)	Gradient $\frac{\Delta C}{L}$ ($\mu M/mm^3/mm$)
A1	102.94	106.74	99.14	8.76
A2	99.01	99.14	98.87	0.42
A3	97.11	98.87	95.34	9.99
A4	94.49	95.34	93.64	8.92
A5	88.61	93.64	83.58	103.25
A6	79.41	83.58	75.24	91.50
C	68.61	75.24	61.98	91.50
V6	60.04	61.98	58.1	13.13
V5	57.57	58.1	57.05	5.94
V4	56.78	57.05	56.52	1.85
V3	56.46	56.52	56.4	0.28
V2	56.36	56.4	56.32	0.13
V1	56.26	56.32	56.19	0.2

Table 4.7: *The mean vessel concentration with updated values considering the oxygen gradient of A6.*

taken along the vessel length. Assuming that the data points are mid-vessel causes problems when interpolating nodal concentration. Further, the standard deviation of the concentration measurements affects nodal concentrations. The final set of reference concentrations in Table 4.7 has been altered by considering the relationship between longitudinal gradient and vessel diameter in order to establish nodal concentrations which decrease along the vessel length.

Section Summary

In section 4.2, available data are interpolated to calculate estimates for Lucas vessel concentration based on the Lucas vessel diameters. A resulting set of reference vessel concentration and diameters is presented in Table 4.3. A method to calculate capillary inlet and outlet node-concentration is then described, based

on averaged capillary longitudinal oxygen gradient from the data. These values are then used, together with the calculated vessel concentration, to calculate the nodal concentration for other vessels. The estimated vessel concentrations calculated from the piece-wise fit are revised due to the necessity for $C_{in} \geq C_{out}$ and then again due to considerations of longitudinal oxygen gradient. The vessel and node-concentrations are updated and presented in Table 4.7.

These concentration values are a starting point for exploration of the parameters in Fick's equation: the tissue concentration, and the diffusion coefficient, as described in section 4.3.

Section 4:3 Fick's Law Parameters

In this section, the parameters used in Fick's law are explored using the reference oxygen concentration calculated in the previous section. As well as vessel geometry and blood flow, the flux of oxygen from blood into tissue is proportional to the transmural oxygen gradient (across the vessel wall) and the diffusion coefficient of oxygen in tissue. Transmural oxygen gradient is the difference between vessel and tissue concentration and therefore tissue concentration also affects the rate of oxygen transfer.

Initially, the diffusion coefficient is calculated assuming uniform tissue concentration at 40 μm into the tissue for all vessels. The radial tissue concentration is then considered both in the tissue and in the vessel wall. Finally the diffusion distance (the distance into the tissue over which diffusion is calculated) is explored so that both vessel wall consumption and tissue consumption are examined.

4.3.1 Diffusion Coefficient: Uniform Tissue Concentration

Tsai calculates a value for the diffusion coefficient of the vessel wall in [243] as $D_w = 1.7 \times 10^{-3} mm^2/s$ but Vadapalli measures a smaller value of $D_w = 9.61 \times 10^{-4} mm^2/s$ [255] in human arteries. Both are calculated from the transmural oxygen gradient which requires knowledge of the tissue concentration. Boas assumes

a constant tissue partial pressure of $15mmHg$ in the brain, which converts to $20.83\mu M/mm^3$ by Henry's law (Equation 2.14). Assuming a tissue concentration of $20.83\mu M/mm^3$, the capillary wall diffusion coefficient can be calculated by re-arranging Equation 4.2 for D_w and the capillary node concentrations taken from Table 4.7:

$$D_w = -\frac{wQ}{\pi DL} ln\left(\frac{C_{out} - C_T}{C_{in} - C_T}\right). \tag{4.6}$$

This gives $D_w = 2.74\times10^{-6}mm^2/s$, which is much smaller than the values for the wall calculated by Tsai and Vadapalli. The capillary flow is low ($0.12\times10^{-3}mm^3/s$) and the walls are very thin ($3.088\times10^{-4}mm$ from Table 3.3) which results in a very low value for diffusion coefficient. However, the associated permeability (from Equation 2.19) is 0.0089 mm/s, which is higher than 0.0053 mm/s calculated by Kassissia [120], the thin wall increasing permeability. Ursino [252] models the capillaries as supplying tissue up to $40\mu m$ away (rather than over just the wall) and assumes that the wall is not a separate barrier to diffusion. Using this distance instead of w, the value for D_w becomes $3.55\times10^{-4}mm^2/s$ (permeability still 0.0089 mm/s), which is much larger but is still an order of magnitude smaller than given by Tsai and less than half of the Vadapalli value.

For other vessels, with $C_T = 20.83\mu M/mm^3$ using $w = 40\mu m$, the diffusion coefficient has a range over two orders of magnitude (see Table 4.8) but still smaller than Vadapalli. The capillary and pre-capillary arteriole have similar diffusion coefficients. Vessel $A5$ offers least resistance to oxygen diffusion (hence the large longitudinal oxygen gradient Table 4.7) and vessel $A1$ has permeability close to the value proposed by Kassissia.

A larger value of D_w requires a larger diffusion distance instead of w (which would also decrease permeability), or a smaller tissue gradient $C_v - C_T$. It is therefore likely that vessels supply a larger tissue volume, or that the tissue concentration is lower at 40 μM distance than assumed by Boas. The assumption of uniform

tissue concentration is thus explored in the next part.

Order	Diffusion Coefficient $D_w(\times 10^{-4} mm^2/s)$	Permeability K_w $(\times 10^{-3} mm/s)$
A1	2.10	5.25
A2	0.07	0.18
A3	1.01	2.53
A4	0.59	1.48
A5	4.75	11.88
A6	3.15	7.88
C	3.55	8.89
V6	0.43	1.08
V5	0.33	0.83
V4	0.17	0.43
V3	0.04	0.10
V2	0.03	0.08
V1	0.09	0.23

Table 4.8: *Calculation of the diffusion coefficient using Boas' uniform tissue concentration assumption [27] of* $C_T = 20.83 \mu M/mm^3$.

4.3.2 Radial Tissue Concentration Gradient

It is clear from experiments carried out in the rat brain by Vovenko [265] (reproduced in Figure 2.8) that tissue oxygen concentration is non-constant throughout the vasculature and non-linear radially throughout the tissue. Values given in Table 4.9 are at external vessel wall oxygen tension $PO_{2,0}$ (at the interface between vessel wall and surrounding tissue) and at points throughout the tissue. $\Delta PO_2/30$ is the gradient between $PO_{2,0}$ and $PO_{2,30}$, likewise for $\Delta PO_2/40$. $\Delta PO_2/10$ is the gradient between $PO_{2,30}$ and $PO_{2,40}$, i.e. further from the vessel wall. These values agree with the gradients described in subsubsection 2.3.5.3.

If the tissue tension at $40 \mu m$ is calculated as a function of wall tension, the ratios are consistent (Table 4.10). Since C relates linearly to PO_2, equations 4.7 - 4.9 are proposed with C_0 the concentration at the interface between the vessel wall and tissue, and $C_{T,A}$, $C_{T,C}$ and $C_{T,V}$ the tissue concentration at 40 μm. The relationships found in Table 4.10 can be used to find tissue concentration as a

Type	$PO_{2,0}$ $mmHg$	$PO_{2,30}$ $mmHg$	$PO_{2,40}$ $mmHg$	$\Delta PO_2/30$ $mmHg/\mu m$	$\Delta PO_2/40$ $mmHg\mu m$	$\Delta PO_2/10$ $mmHg\mu m$
A	73	50	40	0.83	0.88	1
A	68	45	40	0.77	0.7	0.5
A	61	36	-	0.87	-	-
A	53	35	32	0.60	0.53	0.3
A	50	31	28	0.63	0.55	0.3
average A	-	-	-	0.74	0.64	0.53
C	47	37	-	0.33	-	-
C	43	30	28	0.43	0.38	0.2
C	40	31	-	0.30	-	-
average C	-	-	-	0.35	0.38	0.2
V	43	34	32	0.30	0.28	0.20
V	34	27	26	0.23	0.20	0.10
V	33	25	24	0.27	0.23	0.10
average V	-	-	-	0.27	0.24	0.13

Table 4.9: *Table extracting approximate tissue partial pressure at 30μm and 40μm depth, extracted from Figure 2.8 [265]*

function of wall concentration, if the concentration immediately next to the wall is known, using equations 4.7 - 4.9. Therefore the transmural oxygen concentration gradient $(C_v - C_0)$ is required.

Type	$PO_{2,0}$ $mmHg$	$PO_{2,40}$ $mmHg$	$PO_{2,40}/PO_{2,0}$
A	73	40	0.53
A	68	40	0.59
A	53	32	0.60
A	50	28	0.56
average A	-	-	0.57
C	43	28	0.65
V	43	32	0.74
V	34	26	0.76
V	33	24	0.73
average V	-	-	0.74

Table 4.10: *Table of tissue partial pressure at 40μm depth, extracted from Figure 2.8 [265] as a function of vessel partial pressure*

$$C_{T,A} = 0.57C_0 \tag{4.7}$$

$$C_{T,C} = 0.65C_0 \tag{4.8}$$

$$C_{T,V} = 0.74C_0. \tag{4.9}$$

4.3.3 Transmural Concentration Gradient

There is a concentration gradient across the vessel wall which may be similar to that in surrounding tissue, or higher due to consumption in the wall (see discussion in subsubsection 2.3.5.7). The consumption in the capillary wall is lower than for other vessels due to the lack of smooth muscle. This has an effect on the calculated diffusion coefficient. Vovenko measured a value of capillary tissue concentration of $59.72\mu M/mm^3$ close to the vessel (gradient 2.88×10^4 $\mu M/mm^3/mm$) through to $38.89\mu M/mm^3$ $40\mu m$ into the tissue (gradient 743 $\mu M/mm^3/mm$). This correlates to a diffusion coefficient (calculated using Equation 4.6) of $5.76 \times 10^{-4} mm^2/s$ for distal tissue (permeability 0.0144 mm/s by Equation 2.19), or $4.45 \times 10^{-6} mm^2/s$ for the wall (with the same permeability 0.0144 mm/s). These permeabilities are an order of magnitude higher than calculated in subsection 4.3.1. The transmural gradient is extremely high. Due to the very thin capillary wall, however, this measurement is unlikely to have been taken at the wall/tissue interface and so it is more useful to assume a constant radial gradient for capillary wall and tissue.

4.3.4 Diffusion Distance (Tissue Radius)

Duling [64] and Boas [27] both state diffusion coefficient to be proportional to wall thickness. Tsai [243] also proposes consumption in the vessel wall, which is proportional to the amount of smooth muscle present (and therefore to the tissue volume). Kassissia [120] calculates a value for permeability $K_w = D_w/w$ of $5.3 \times 10^{-3} mm/s$. Over a $40\mu m$ tissue distance, D_w would be $2.12 \times 10^{-4} mm^2/s$, less than half the value calculated for capillary vessels in subsection 4.3.3 with $C_T = 38.89$. For other vessels, setting $D_w = K_w \times w = 2.12 \times 10^{-4} mm^2/s$, the tissue concentration

is calculated for each vessel using Equation 4.10 (rearranged from Equation 4.2).

$$C_T = \frac{C_0 - C_i e^{\frac{-D_w \pi D L}{wQ}}}{1 - e^{\frac{-D_w \pi D L}{wQ}}} \tag{4.10}$$

The resulting values, Table 4.11, show very little consumption in venule tissue since the oxygen gradient is very low. The negative values in $A5, A6$ and C are due to a very high oxygen gradient; D_w in these vessels is therefore higher than 2.12×10^{-4} mm^2/s. Since there is a transmural gradient, the ratio $\frac{C_{T,40}}{C_v}$ should be greater than those values used in equations 4.7 - 4.9. If w is considered to

Vessel Concentration $C_v(\mu M/mm^3)$	Distal Tissue Concentration $C_{T,40}(\mu M/mm^3)$	Ratio $\frac{C_{T,40}}{C_v}$ $(\mu M/mm^3 \mu m)$
102.94	21.64	0.21
99.01	96.56	0.98
97.11	60.77	0.63
94.49	73.99	0.78
88.61	-62.97	-0.71
79.41	-7.47	-0.09
68.61	-10.98	-0.16
60.04	51.97	0.87
57.57	51.88	0.9
56.78	53.88	0.95
56.46	55.73	0.99
56.36	55.79	0.99
56.26	54.8	0.97

Table 4.11: *Calculation of the tissue concentration in the* $40\mu m$ *region and associated relationship with vessel concentration.*

be the actual vessel wall distance, and the diffusion coefficient $D_w = 5.3 \times w \times 10^{-3}$ mm^2/s, the equation would yield the same concentrations but at the vessel wall with the resulting wall gradients shown in Table 4.12. The transmural gradient for the arterioles is larger than evaluated in the brain by Duling and Vovenko (see subsubsection 2.3.5.7). The value for $A6$ is close to that found by Santilli ($27.78\mu M/mm^3/\mu m$). $A3$ (diameter 15.28 μm) is similar to the $23.2\mu m$ vessel evaluated by Tsai ($10.93\mu M/mm^3/\mu m$). $V6$ has a gradient larger than the $4.17\mu M/mm^3/\mu m$ value calculated in venules by Intaglietta [111] but $V3$, $V2$ and

$V1$ have low gradients. The high gradient for C over the thin wall implies large amounts of consumption in the capillary wall since oxygen loss is large.

Order	D_w $\times 10^{-5} mm^2/s$	Wall Gradient $\frac{dC}{dw}$ $(\mu M/mm^3 \mu m)$
A1	2.57	16.79
A2	2.25	0.58
A3	2.02	9.54
A4	1.85	5.88
A5	1.73	46.41
A6	1.66	27.68
C	0.16	257.75
V6	0.61	7.01
V5	0.77	3.92
V4	0.94	1.63
V3	1.14	0.34
V2	1.36	0.22
V1	1.63	0.47

Table 4.12: *Presenting the results of the assumption of wall permeability as a function of wall thickness.*

Section Summary

In section 4.3 the tissue concentration is shown to be non-uniform. The transmural oxygen concentration gradient is found to be important in calculating an appropriate diffusion coefficient for the vessel wall. This diffusion coefficient is not a constant for oxygen in tissue, but is variable, perhaps with tissue volume. Consumption in the vessel wall results in a higher transmural gradient than in surrounding tissue, this could also be due to a lower diffusion coefficient. Wall permeability is probably higher than in surrounding tissue though, due to the small wall thicknesses, since setting permeability to 5.3×10^{-3} mm/s results in transmural gradients which are too high. Therefore it is the consumption of oxygen which affects the values for diffusion coefficient calculated previously, as discussed in subsubsection 2.3.5.8. In subsection 4.4.1, the resulting model parameters of permeability and transmural concentration gradient are described.

Section 4:4 Lucas Oxygen Transport Model

This section describes the parameters used in the Lucas model to calculate tissue oxygen concentration and flux. There is also a description of the method used to solve sequentially from the arterial inlet concentration.

4.4.1 Model: Tissue Concentration

In light of the results above, the model of exchange with wall permeability cannot be assumed to apply over the capillary wall since the gradients calculated are too high. Capillary oxygen exchange is approximated by assuming that the vessel supplies $40\mu m$ tissue with no capillary wall (so that the diffusion distance is $w = 40\mu m$). The distal tissue concentration is set to $31.11\mu M/mm^3$ so that over the first $10\mu M$ the gradient is $2.07\mu M/mm^2/\mu m$ (as found by Intaglietta) dropping to $0.52\mu M/mm^2/\mu m$ over $35\mu m$ as found by Vovenko. The resulting diffusion coefficient value is $D_T = 4.54 \times 10^{-4} mm^2/s$ (permeability 0.0113 mm/s.) This value is twice as much as was calculated using the permeability for tissue proposed by Kassissia, although the experimental value proposed by Kassissia was based on the diffusion of tracer oxygen in water in capillaries.

Arterioles have oxygen consumption in the wall as well due to smooth muscle and endothelial cells. The venules also have oxygen consumption in the wall due to the endothelial layer. In these vessels ($A1 : A6$ and $V6 : V1$), the amount of oxygen consumption is proportional to the volume of the cell wall and so can be standardised by the transmural gradient. Therefore, in arterioles and venules, the diffusion distance is better approximated as the vessel wall thickness than the tissue radius. To incorporate the transmural wall gradient, β, a function is proposed

for tissue concentration for arterioles and venules:

$$C_{T,A} = C_{v,A} - w\beta_A \mu M/mm^3 \tag{4.11}$$

$$C_{T,C} = 31.11 \mu M/mm^3 \tag{4.12}$$

$$C_{T,V} = C_{v,V} - w\beta_V \mu M/mm^3 \tag{4.13}$$

For arterioles, the concentration gradient over the wall can be approximated as $\beta_A = 3.30 \mu M/mm^3 \mu m$ [243]. Since Duling showed that smaller vessels have higher gradients, the upper bound of the range is chosen. For venules, the gradient over the wall is set to $\beta_V = 4.17 \mu M/mm^3/\mu m$ [111] .

4.4.2 Model: Wall Permeability

The diffusion coefficient, D_w, is calculated using Equation 4.6 with tissue concentration from Equation 4.13. The wall permeability $S_w = D_w/w$ is then evaluated. Since the transmural gradient is the same for each type of vessel, the difference in value is due to the longitudinal oxygen gradient and differences in permeability. The permeability is not consistent due to the varying amount of smooth muscle and endothelial cells in the wall. The permeability of the thinner-walled arterioles $A5$ and $A6$ is higher than $A1 : A4$. Similarly $V6 : V5$ have higher permeability values than $V3 : V1$ but lower values than the arterioles. The values are calculated based on the estimated reference node concentration from Table 4.7, these values are affected by the fit of the data. A model based on physiological parameters uses S_w to calculate the flux. S_w is estimated by taking average values for the small and large arterioles and venules (vessels $A1 : A4$, $A5 : A6$, $V6 : V5$ and $V4 : V1$).

Order	D_w $1\times10^{-4}\ mm^2/s$	S_w $1\times10^{-3}\ mm/s$	S_w (average) $1\times10^{-3}\ mm/s$
A1	1.33	27.48	13.32
A2	0.04	0.92	13.32
A3	0.59	15.41	13.32
A4	0.33	9.46	13.32
A5	2.64	80.77	63.93
A6	1.48	47.09	63.93
C	4.54	11.34	11.34
V6	0.11	9.26	7.12
V5	0.07	4.98	7.12
V4	0.04	2.07	0.85
V3	0.01	0.43	0.85
V2	0.01	0.28	0.85
V1	0.02	0.60	0.85

Table 4.13: *Wall permeability calculated from diffusion coefficient.*

4.4.3 Model: Node Concentration

Equation 4.2 can be solved sequentially from the inlet of $A1$ to give node concentrations with Equation 4.13 substituted for C_T at basal state:

$$C_{out} = C_{in} - 2\beta w \frac{1 - e^{-\frac{S_w \pi D L}{Q}}}{1 + e^{-\frac{S_w \pi D L}{Q}}}. \tag{4.14}$$

The inlet concentration is calculated by solving Equation 4.14 in reverse from the known capillary inlet concentration with S_w from Table 4.13 giving $C_{in,A1} = 107.23$ $\mu M/mm^3$.

Section Summary

The parameters which describe oxygen transport in the Lucas model are given in Table 4.14. Arterioles, capillaries and venules are considered to be physiologically different with resultant different values of wall permeability. The transmural oxygen gradient across the wall is considered in order to calculate a non-uniform, steady-state tissue concentration for all vessels. Since the capillary wall is very thin with no smooth muscle, the wall and tissue are grouped together with tissue radius 40 μm.

Parameter	Symbol	Value	Units	Reference
Large Arterioles $A1 : A4$				
Inlet Concentration	$C_{in,A1}$	107.23	$\mu M/mm^3$	subsection 4.4.3
Permeability	$S_w = D_w/w$	1.33×10^{-2}	mm/s	subsection 4.4.2
Transmural Gradient	β_A	3.30	$\mu M/mm^2/\mu m$	[243] subsection 4.4.1
Small Arterioles $A5 : A6$				
Permeability	$S_w = D_w/w$	6.39×10^{-2}	mm/s	subsection 4.4.2
Transmural Gradient	β_A	3.30	$\mu M/mm^2/\mu m$	[243] subsection 4.4.1
Small Venules $V6 : V5$				
Permeability	$S_w = D_w/w$	7.12×10^{-3}	mm/s	subsection 4.4.2
Transmural Gradient	β_V	4.17	$\mu M/mm^2/\mu m$	[111] subsection 4.4.1
Large Venules $V4 : V1$				
Permeability	$S_w = D_w/w$	8.46×10^{-4}	mm/s	subsection 4.4.2
Transmural Gradient	β_V	4.17	$\mu M/mm^2/\mu m$	[111] subsection 4.4.1
Capillaries				
Permeability	$S_w = D_w/0.04$	1.13×10^{-2}	mm/s	subsection 4.4.2
Tissue Gradient	β_C	0.94	$\mu M/mm^3/\mu m$	subsection 4.4.1

Table 4.14: *The parameters required for calculating node and tissue concentration. The permeability for capillaries is averaged over a 40 µm tissue radius rather than wall thickness, as described above.*

Section 4:5 Model Results

Final results calculated using Equation 4.14 with $A1$ inlet concentration 107.23 $\mu M/mm^3$ and parameters listed in Table 4.14 are given in Table 4.15. The tissue concentration is calculated with Equation 4.13 with vessel concentration C_v from Table 4.15 and is given in Table 4.16. Figure 4.3 shows the vessel concentration with negative arteriole diameter to distinguish from venules, capillary diameter being displayed at 0. The large arteriole ($A1 : A4$) concentrations are higher than calculated with interpolation, similarly with the small venules ($V6 : V3$). The overall shape passes close to the data values.

	Vessel C_v ($\mu M/mm^3$)	Inlet C_{in} ($\mu M/mm^3$)	Outlet C_{out} ($\mu M/mm^3$)	Gradient $\frac{\Delta C}{L}$ ($\mu M/mm^3/mm$)
A1	105.36	107.23	103.49	4.31
A2	101.6	103.49	99.7	6.05
A3	98.17	99.7	96.64	8.65
A4	95.45	96.64	94.26	12.54
A5	90.16	94.26	86.05	84.13
A6	80.65	86.05	75.24	118.72
C	68.61	75.24	61.98	91.49
V6	60.45	61.98	58.93	10.33
V5	58.18	58.93	57.42	8.47
V4	57.32	57.42	57.21	0.76
V3	57.09	57.21	56.97	0.55
V2	56.85	56.97	56.74	0.40
V1	56.65	56.74	56.56	0.29

Table 4.15: *The mean vessel and node concentration solved sequentially from the inlet of A1 with Equation 4.14, and parameters from Table 4.14.*

Order	Tissue C_T ($\mu M/mm^3$)
A1	89.39
A2	87.56
A3	85.6
A4	83.94
A5	79.38
A6	70.29
C	31.11*
V6	55.65
V5	52.12
V4	49.9
V3	48.14
V2	46.14
V1	43.82

Table 4.16: *The tissue concentration is calculated using Equation 4.13 over the vessel wall, except for capillaries where it is calculated as described in subsection 4.4.1.*

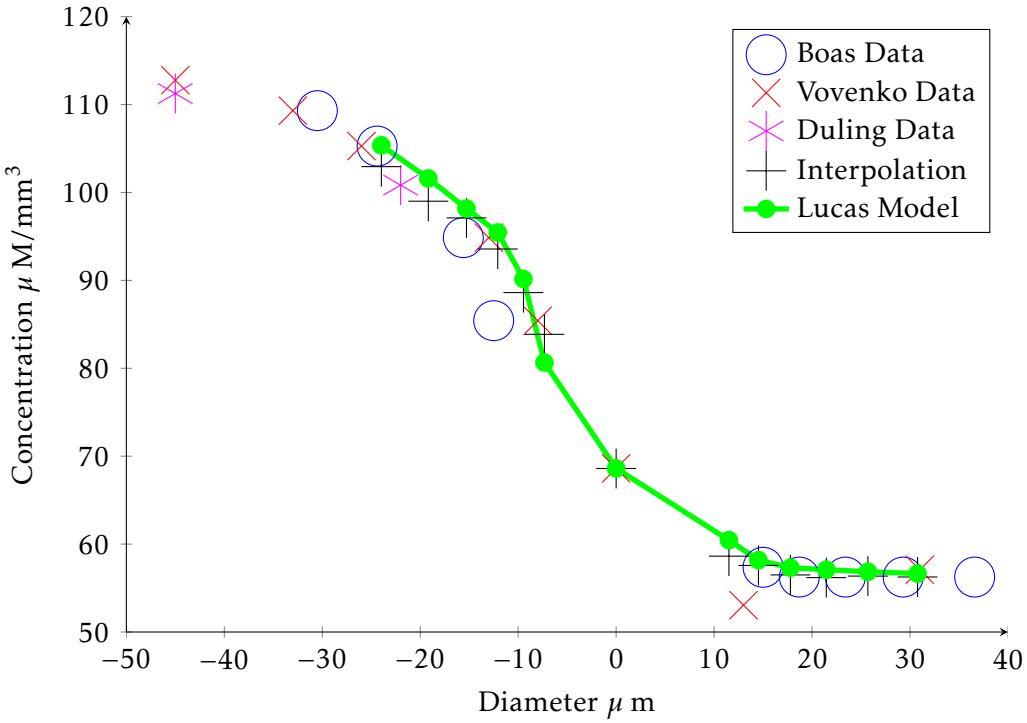

Figure 4.3: *Oxygen concentration in vessels calculated at steady state*

Summary

In this chapter, an oxygen model is established which is based on physiological parameters and closely matches cerebral oxygen data. Oxygen partial pressure data from [265] are modelled in vessel walls and tissue by the mass-transport equations. The diffusion coefficient in tissue is investigated both for diffusion over the wall, and diffusion over a $40\mu m$ radius tissue cylinder. Due to a transmural oxygen gradient found in available data for arterioles and venules, and the presence of smooth muscle and endothelial cells in the wall, consumption is assumed to occur in the arteriole and venule vessel wall and a wall permeability function proposed so that the diffusion coefficient is a function of steady state wall thickness. Difficulty with establishing the capillary transmural oxygen gradient, and the physiology of capillaries being more similar to tissue mean that the capillary wall and tissue are approximated as one compartment and the mass transport equation solved over the tissue radius.

Chapters 3 and 4 have described how a basal state model can be established. In the next chapter, a model of tension as a function of vessel strain is proposed in order to approximate the elasticity of the vessel and the response to pressure.

CHAPTER 5

Length-Tension characteristics

In order to use an activation model of autoregulation (section 2.6), it is necessary to be able to calculate passive and active tension over the diameter range of a vessel. Davis and Gore [57] found length-tension characteristics over a large range of circumferential strain. In chapter 5, an existing fit of this model is improved resulting in a continuous, two-phase function for passive and active tension. The data are related to the Lucas network vessels and a non-dimensional model is therefore proposed which can be used for any reference diameter, and therefore for any vessel in the network.

Section 5:1 Davis and Gore Data

The data of Davis and Gore in hamster cheek pouch are presented for non-dimensional strain in Figure 2.10. Since the graph shows simultaneous passive and active values over a range (compared with those in Table 2.9), values of tension were extracted and converted to $mmHg\,mm$ using $1 \times 10^2\ dyne/cm = 0.75006\ mmHg\ mm$ (see Table C.1). The extracted tension and strain values are given in Table 5.1 where the length ratio $l = \frac{L}{L_0}$.

l	Passive Tension ($mmHg\,mm$)	Maximal Active Tension ($mmHg\,mm$)	Total Tension ($mmHg\,mm$)
0.55	0	1.50	1.50
0.60	0	3.38	3.38
0.65	0.09	4.69	4.78
0.70	0.19	5.50	5.69
0.75	0.25	6.13	6.38
0.80	0.38	6.75	7.13
0.85	0.56	7.50	8.06
0.90	0.62	8.00	8.63
0.95	0.75	8.63	9.38
1.00	1.25	8.87	10.13
1.05	3.00	8.25	11.25
1.10	6.75	6.00	12.75
1.15	10.88	not shown	
1.20	14.87	not shown	

Table 5.1: *The tension curves extracted from Figure 2.10. Passive tension is where activation is zero, total where activation is one, and maximal active found by subtracting passive from total.*

5.1.1 Carlson Fit

Carlson [42] suggested a model of the active length-tension characteristics as described in subsection 2.4.3 (Equation 2.38 and Equation 2.42). For the Davis and Gore data, the model parameters are converted using $1\ N/m = 7.5006\ mmHg\,mm$ where necessary. Carlson cites the diameter D_p extrapolated for a pressure of 100 $mmHg$, this is converted into the equivalent L_0 value (at maximum active tension) by multiplying by C'_{act} (where $\frac{D}{D_p} - C'_{\text{act}} = 0$).

D_p (μm)	L_0 equivalent (μm)	C_{pass} ($mmHg\,mm$)	C'_{pass}	C_{act} ($mmHg\,mm$)	C'_{act}	C''_{act}
85.7	73.02	4.9129	26.7850	7.6800	0.8520	0.2760

Table 5.2: *Parameter values used by Carlson [42] to model the Davis and Gore length-tension data for hamster cheek arterioles.*

When plotted against the data (Figure 5.1), the Carlson model is found not to follow the length-tension characteristics well. Even with the magnitude varied, the symmetrical active model does not accurately mimic the high-strain characteristics. Similarly, the passive strain does not model dilated tension very well.

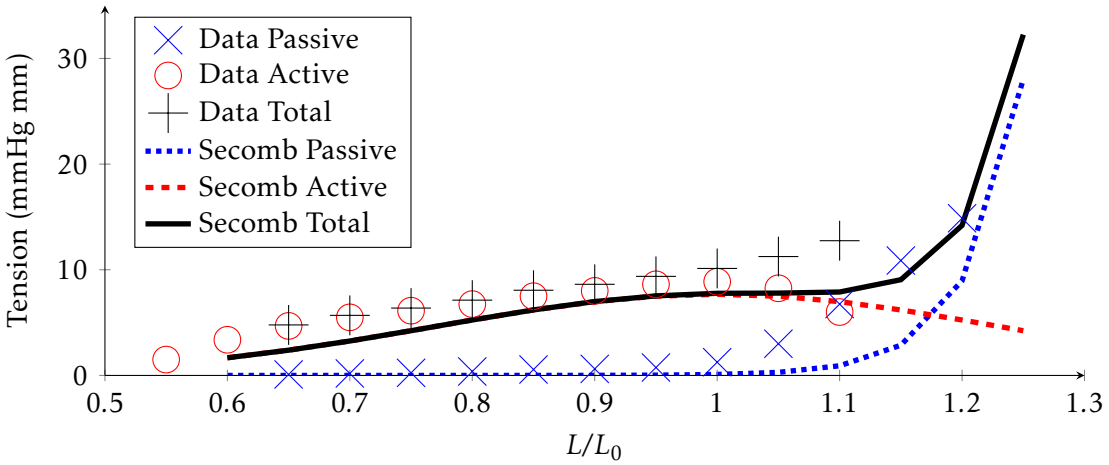

Figure 5.1: *Showing the fit of Davis and Gore data Table 5.1 using the Carlson model (equations 2.38 and 2.42).*

Clearly, the model can be improved so that the passive and active components of the data are replicated, especially in the non-symmetrical nature of the curve.

Section 5:2 Lucas Fit

Although the Carlson fit of the data is not accurate, the gaussian shape is a good starting point for a fit of the passive data. In this section, fits are tested using both single and multiple phases and a combination of linear and non-linear equations.

5.2.1 Passive Model

5.2.1.1 Passive Continuous

For $D/D_0 = L/L_0 = d$, the Davis and Gore data can be fit to the exponential strain model Equation 2.38 or a two-exponential strain model Equation 2.39 by optimising the data fit to Equation 5.1 or Equation 5.2, where T_{pass} values are those for passive tension in Table 5.1. The optimisation is done via an inbuilt trust-region-dogleg algorithm. The dogleg algorithm approximates a non-linear function with a piecewise linear polygon and solves over a trusted step size, reducing the region size until a solution is reached [177]. These equations are modified from Equation 2.38 and Equation 2.39. The calculated parameters are given in Table 5.3 and the resulting values for passive tension calculated and presented in Table 5.4 and shown in Figure 5.3.

$$T_{pass} = C_{p1} e^{C_{d,p1} d} \tag{5.1}$$

$$T_{pass} = C_{p1} e^{C_{d,p1} d} + C_{p2} e^{C_{d,p2} d}. \tag{5.2}$$

Model	C_{p1} ($\times 10^{-4}$ $mmHg\,mm$)	$C_{d,p1}$	C_{p2} ($\times 10^{-4}$ $mmHg\,mm$)	$C_{d,p2}$
One-Exponential	1.45	9.65		
Two-Exponential	0.75	9.65	0.70	9.65

Table 5.3: *The continuous model parameters found to model the passive Davis and Gore length-tension data for both one-exponential and two-exponential functions.*

The two-exponential model is essentially the same as the one-exponential model; the calculated tensions are very similar (see Table 5.4). Therefore, there seems to be no merit in the use of a second exponential. For a single exponential model, the RMSE is 0.9084 $mmHg\,mm$, the shape of the function does not model the strain between 0.9 and 1.1 very well.

d	Passive Data ($mmHg\,mm$)	Two Exponential ($mmHg\,mm$)	Error ($mmHg\,mm$)	One Exponential ($mmHg\,mm$)	Error ($mmHg\,mm$)
0.65	0.09	0.08	-0.01	0.08	-0.01
0.70	0.19	0.13	-0.05	0.13	-0.05
0.75	0.25	0.22	-0.03	0.22	-0.03
0.80	0.38	0.35	-0.02	0.35	-0.02
0.85	0.56	0.58	+0.01	0.58	+0.01
0.90	0.62	0.94	+0.31	0.94	+0.31
0.95	0.75	1.53	+0.77	1.52	+0.77
1.00	1.25	2.48	+1.23	2.48	+1.23
1.05	3.00	4.04	+1.04	4.04	+1.04
1.10	6.75	6.58	-0.17	6.58	-0.17
1.15	10.88	10.71	-0.16	10.71	-0.17
1.20	14.87	17.44	+2.57	17.43	+2.56
RMSE	-	-	0.91	-	0.91

Table 5.4: *The passive tension curve data from Figure 2.10 modelled by one and two exponentials.*

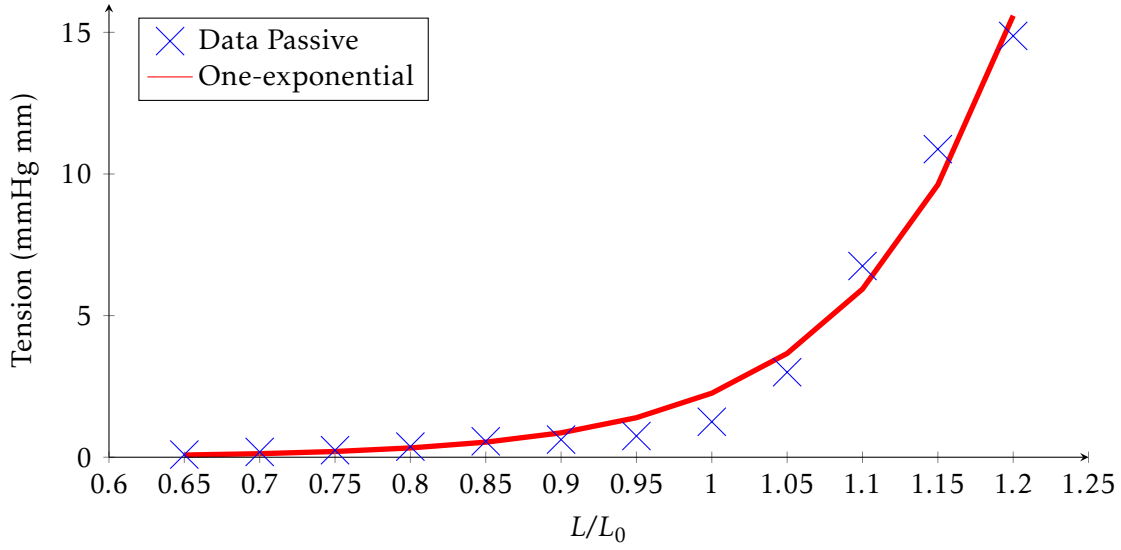

Figure 5.2: *The Davis and Gore data modelled by an exponential function*

5.2.1.2 Passive Two-Phase Exponential

If, instead of a continuous function, the passive tension is modelled in two phases the fit can be improved. It seems logical to split between positive and negative strain (see Equation 5.3). Table 5.5 gives the two-phase parameters.

$$T_{\text{pass}} = \begin{cases} C_{p1}e^{C_{dp1}d} & \text{if } d \leq 1 \\ C_{p2}e^{C_{dp2}d} & \text{otherwise} \end{cases} \tag{5.3}$$

Model	C_{p1} ($\times 10^{-3}$ $mmHg\,mm$)	C_{dp1}	C_{p2} ($\times 10^{-4}$ $mmHg\,mm$)	C_{dp2} $mmHg\,mm$
Two-phase	2.40	6.21	4.27	8.74

Table 5.5: *The two-phase model parameters found best to model the passive Davis and Gore length-tension data.*

The calculations for a two-phase model are compared with the previous function in Table 5.6. The root mean squared tension error is 0.46 $mmHg\,mm$, which is an improvement over the continuous model. However, the discontinuity causes large errors for positive strain $d = 1.05$ (see Figure 5.3).

d	Passive Data ($mmHg\,mm$)	Two-phase Model ($mmHg\,mm$)	Error ($mmHg\,mm$)	Continuous Model ($mmHg\,mm$)	Error ($mmHg\,mm$)
0.65	0.09	0.14	+0.05	0.08	-0.01
0.70	0.19	0.19	0	0.13	-0.05
0.75	0.25	0.25	0	0.22	-0.03
0.80	0.38	0.35	-0.03	0.35	-0.02
0.85	0.56	0.47	-0.09	0.58	+0.01
0.90	0.62	0.64	+0.02	0.94	+0.31
0.95	0.75	0.88	+0.13	1.52	+0.77
1.00	1.25	1.20	-0.05	2.48	+1.23
1.05	3.00	4.13	+1.13	4.04	+1.04
1.10	6.75	6.40	-0.35	6.58	-0.17
1.15	10.88	9.91	-0.97	10.71	-0.17
1.20	14.87	15.34	+0.47	17.43	+2.56
RMSE	-	-	0.46	-	0.91

Table 5.6: *The passive tension curve data from Figure 2.10 modelled by a two-phase model compared with the previously established continuous model.*

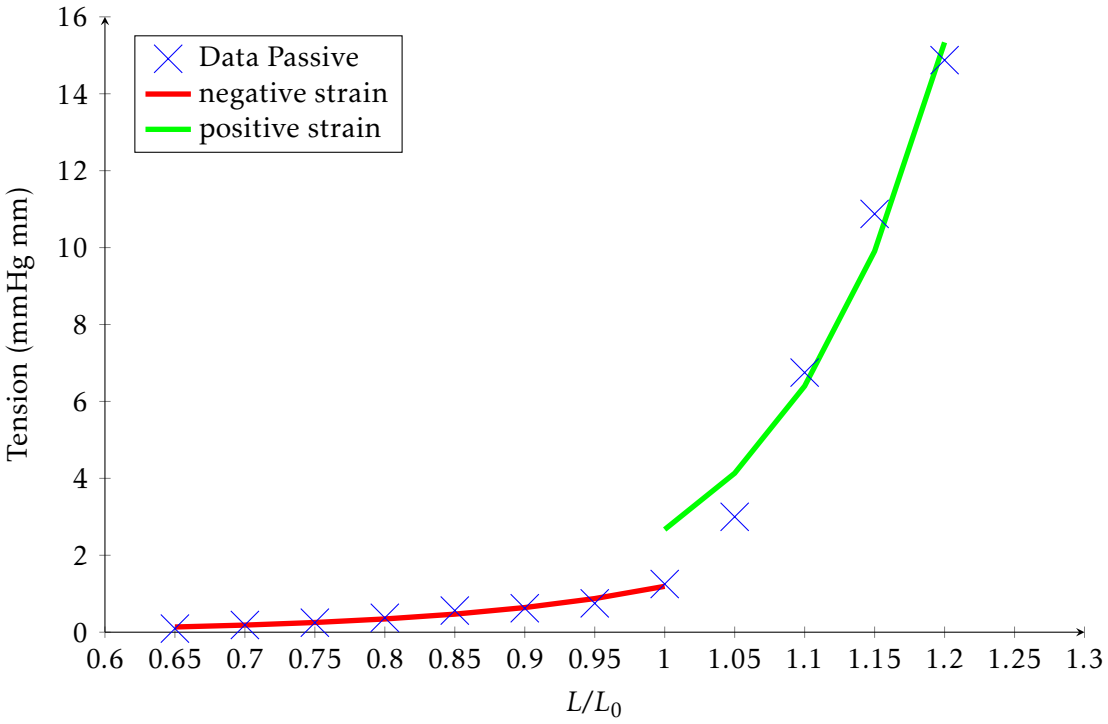

Figure 5.3: *The Davis and Gore data modelled by two-phase exponential function*

5.2.1.3 Passive Two-Phase

Instead of this two phase non-linear model, positive strain can be modelled as linear instead of exponential so that Equation 5.4 is solved with resulting RMSE 0.3350 $mmHg\,mm$. The linear and exponential functions cross at a positive strain of $D/D_0 = 1.0139$ and so Equation 5.4 can be altered so that the condition $d \leq 1.0139$, giving a continuous passive function (with non-continuous gradient) with parameters given in Table 5.7.

$$T_{\text{pass}} = \begin{cases} C_{p1} e^{C_{dp1} d} & \text{if d} \leq 1.0139 \\ m_p d + c_p & \text{otherwise} \end{cases} \tag{5.4}$$

Model	C_{p1} ($\times 10^{-3}$ $mmHg\,mm$)	C_{dp1}	m_p ($mmHg\,mm$)	c_p
Two-phase	2.40	6.21	70.24	-69.91

Table 5.7: *The two-phase model parameters found to model the passive Davis and Gore length-tension data where positive strain has linear tension.*

Table 5.8 gives the results of this function. The errors for positive strain are

reduced up to $d = 1.20$ compared with the two-phase exponential function.

d	Passive Data ($mmHg\,mm$)	Two-phase Linear ($mmHg\,mm$)	Error ($mmHg\,mm$)	Two-phase Exp. ($mmHg\,mm$)	Error ($mmHg\,mm$)
0.65	0.09	0.14	+0.05	0.14	+0.05
0.70	0.19	0.18	-0.01	0.18	-0.01
0.75	0.25	0.25	0	0.25	0
0.80	0.38	0.34	-0.04	0.34	-0.04
0.85	0.56	0.47	-0.09	0.47	-0.09
0.90	0.62	0.64	+0.02	0.64	+0.02
0.95	0.75	0.87	+0.12	0.87	+0.12
1.00	1.25	1.19	-0.06	0.32	-0.06
1.05	3.00	3.84	+0.84	4.13	+1.13
1.10	6.75	7.35	+0.06	6.40	-0.35
1.15	10.88	10.86	-0.02	9.91	-0.97
1.20	14.87	14.37	-0.50	15.34	+0.47
RMSE	-	-	0.34	-	0.46

Table 5.8: *The passive tension curve data from Figure 2.10 modelled by a two-exponential two-phase model compared with the previously established continous model.*

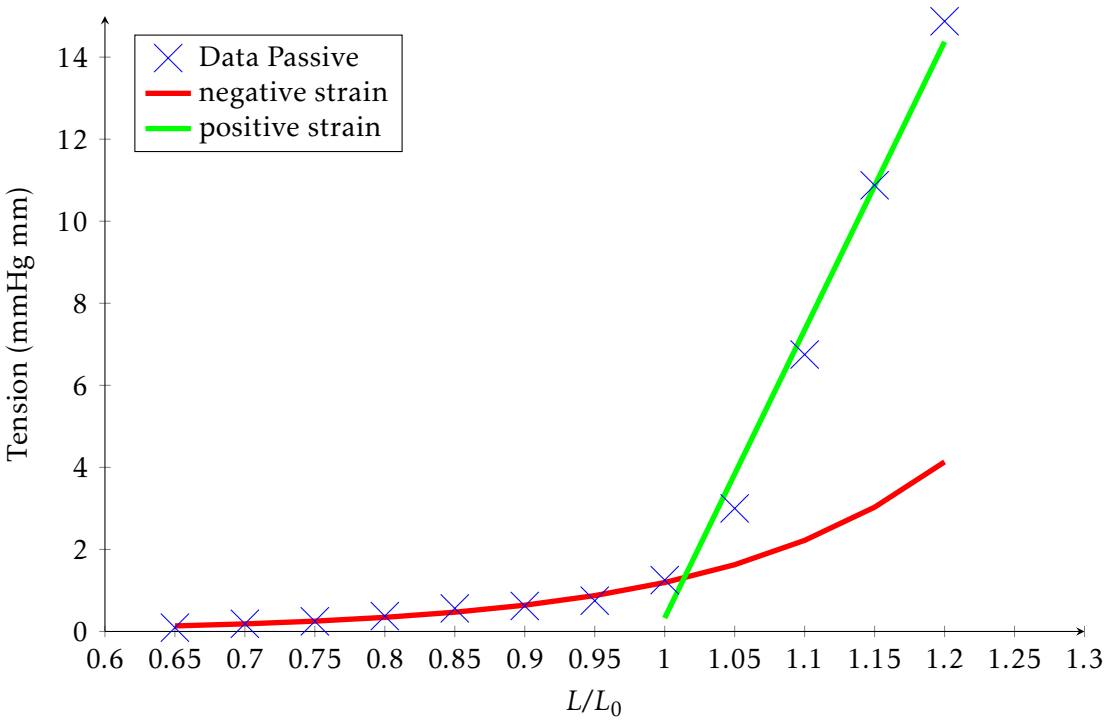

Figure 5.4: *The Davis and Gore data modelled by two-phase function with positive strain having a linear length-tension relationship*

The correlation between the new model and the passive data is good (see Fig-

ure 5.4), and implies that tension is linear at higher strain. The point of transition to the linear relationship is very close to L_0 (the point of maximum active tension).

5.2.2 Active Model

A similar progression is employed to find an improved fit of the active tension, starting with the exponential function proposed by Carlson Equation 2.42 and extending to a two-phase model.

5.2.2.1 Continuous Exponential

Equation 2.42 is redefined at $d = l$ with $\left(\frac{1}{C''_{act}}\right)^2 = C_{da1}$. The value of C_{ea1} shifts the point of maximum tension away from $d = 1$ (see Figure 5.5) and the function produces a symmetrical length-tension curve:

$$T_{act} = C_{a1} e^{-C_{da1}(d-C_{ea1})^2}. \tag{5.5}$$

The function is fit to the data using the same inbuilt trust-region dogleg algorithm with parameters given in Table 5.13.

C_{a1} $(mmHg\,mm)$	C_{da1}	C_{ea1}
8.48	8.68	0.94

Table 5.9: *The continuous model parameters found to model the active Davis and Gore length-tension data for a continuous exponential function.*

The single exponential fit shown in Figure 5.5 is symmetrical and therefore, in order to minimise the overall error, the negative-strain length-tension characteristics are fit more successfully than the positive-strain tension. Since $C_{ea1} = 0.94$, the peak of the curve is shifted from $D = D_0$.

d	Active Data ($mmHg\,mm$)	Exponential ($mmHg\,mm$)	Error ($mmHg\,mm$)
0.55	1.5	2.25	+0.75
0.6	3.38	3.09	-0.29
0.65	4.69	4.07	-0.62
0.7	5.5	5.13	-0.37
0.75	6.13	6.18	+0.05
0.8	6.75	7.14	+0.39
0.85	7.5	7.9	+0.40
0.9	8	8.36	+0.36
0.95	8.63	8.48	-0.15
1	8.87	8.23	-0.64
1.05	8.25	7.65	-0.6
1.1	6	6.81	+0.81
RMSE	-	-	0.51

Table 5.10: *The active tension curve data from Figure 2.10 modelled by one exponential.*

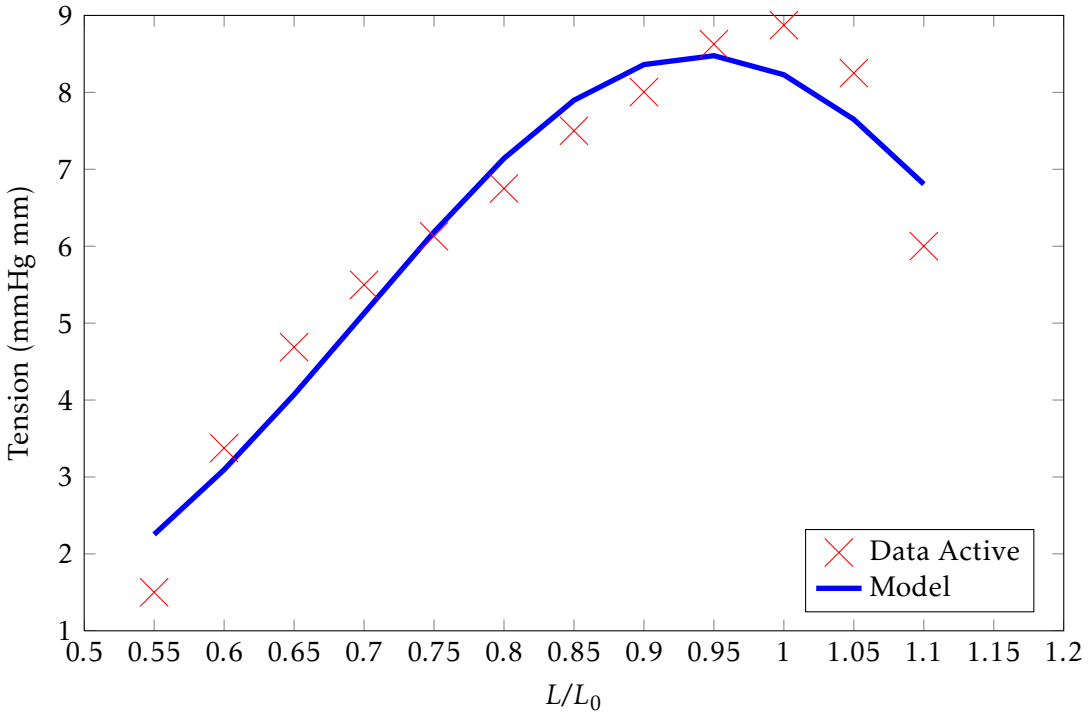

Figure 5.5: *The Davis and Gore active tension data modelled by an exponential function*

5.2.2.2 Discontinuous Exponential

A non-symmetrical curve can be produced by a discontinuous function, like Equation 5.6 with parameters calculated and given in Table 5.11.

$$T_{\text{act}} = \begin{cases} C_{a1} e^{-(C_{da1}(d-C_{ea1})^2)} & \text{if } d < 1 \\ C_{a2} e^{-(C_{da2}(d-C_{ea2})^2)} & \text{otherwise.} \end{cases} \tag{5.6}$$

C_{a1} $(mmHg\,mm)$	C_{da1}	C_{ea1}	C_{a2} $(mmHg\,mm)$	C_{da2}	C_{ea2}
8.67	6.77	0.98	8.92	49.14	1.01

Table 5.11: *The discontinuous model parameters found to model the active Davis and Gore length-tension data.*

The root mean squared error is 0.3681 $mmHg\,mm$ (see Table 5.11) and the positive strain model fits the three values exactly since there are 3 degrees of freedom.

d	Active Data $(mmHg\,mm)$	Exponential $(mmHg\,mm)$	Error $(mmHg\,mm)$
0.55	1.50	2.46	+0.96
0.60	3.38	3.24	-0.14
0.65	4.69	4.12	-0.57
0.70	5.50	5.07	-0.43
0.75	6.13	6.03	-0.10
0.80	6.75	6.94	+0.19
0.85	7.50	7.71	+0.21
0.90	8.00	8.29	+0.29
0.95	8.63	8.61	-0.02
1.00	8.87	8.87	0
1.05	8.25	8.25	0
1.10	6.00	6.00	0
RMSE	-	-	0.37

Table 5.12: *The active tension curve data from Figure 2.10 modelled by two exponentials for negative and positive strain.*

Figure 5.6 shows that although the equations provide a good fit for strain greater than 0.8, the discontinuity around $D = D_0$ is problematic, and the low-strain tension is not well modelled.

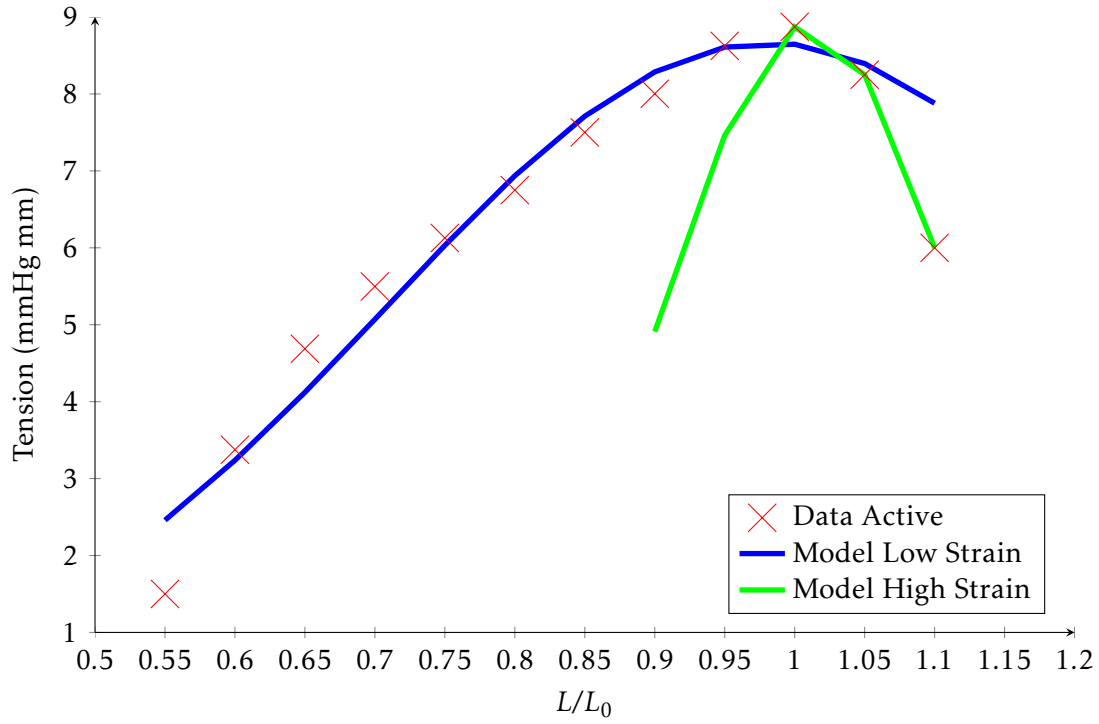

Figure 5.6: *The Davis and Gore active tension data modelled by separate exponential functions for negative and positive strain*

5.2.2.3 Shifted continuous Exponential

The low-strain exponential can be shifted (by adding C_t) so that the active tension is better modelled. This shift models the effect of residual tension in the vessel wall.

$$T_{act} = \begin{cases} C_{t1} + C_{a1} e^{-C_{da1}(d-C_{ea1})^2} & \text{if } d < 0.99 \\ C_{a2} e^{-C_{da2}(d-C_{ea2})^2} & \text{otherwise.} \end{cases} \tag{5.7}$$

The parameters used in these equations are given in Table 5.13, with the calculated tension given in Table 5.14 and displayed in Figure 5.7. The crossover between the two phases is at $d = 0.9889$ so that the function is continuous.

C_{t1} ($mmHg\,mm$)	C_{a1} ($mmHg\,mm$)	C_{da1}	C_{ea1}	C_{a2} ($mmHg\,mm$)	C_{da2}	C_{ea2}
-235.32	244.21	0.11	1.07	8.92	49.14	1.01

Table 5.13: *The shifted continuous model parameters found to model the active Davis and Gore length-tension data.*

The root mean squared error for active tension is 0.2033 $mmHg\,mm$ and Fig-

d	Active Data ($mmHg\,mm$)	Exponential ($mmHg\,mm$)	Error ($mmHg\,mm$)
0.55	1.50	1.88	0.38
0.60	3.38	3.15	-0.23
0.65	4.69	4.3	-0.39
0.70	5.50	5.32	-0.18
0.75	6.13	6.22	0.09
0.80	6.75	6.99	0.24
0.85	7.50	7.63	0.13
0.90	8.00	8.14	0.14
0.95	8.63	8.52	-0.11
1.00	8.87	8.87	0
1.05	8.25	8.25	0
1.10	6.00	6.00	0
RMSE	-	-	0.20

Table 5.14: *The active tension curve data from Figure 2.10 modelled continuously by two separate exponentials where one is shifted.*

ure 5.7 shows an improved overall fit compared with the non-shifted model.

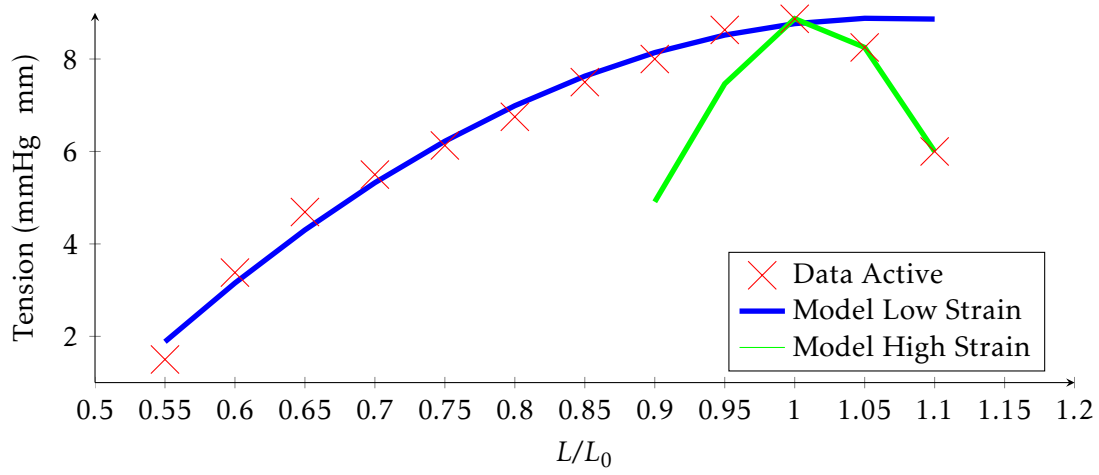

Figure 5.7: *The Davis and Gore active tension data modelled continuously by separate exponential functions for negative and positive strain*

Section Summary

Length-tension characteristics for non-dimensional strain have previously been modelled by single or multiple exponential functions. However, it has been shown here that passive tension can be approximated as a combination of an exponential and linear function of strain giving a continuous function which becomes

linear at $D = 1.01D_0$. A continuous active function can also be created using two-exponentials where the low strain ($D \leq 0.99D_0$) function includes a linear translation by $-235.32\ mmHg\,mm$ in order to more accurately replicate the data. Unfortunately, this also means that the function is invalid for $d \leq 0.48$ since tension becomes negative at this value.

Section 5:3 Lucas Reference Diameter

There is an assumption so-far that the Lucas model geometry and parameters calculated in previous chapters is at the maximum-active state, so that $D_0 = L_0$. A further assumption is that all arterioles are at this basal state so that they will respond with the same length-tension curve. However, each of these assumptions might be incorrect. The first of these, that $D_0 = L_0$, is investigated here using different scenarios of the limits of the auto-regulation pressure-flow curve so that the basal activation is calculated dependent on a value of a, where $D_0 = aL_0$, and L_0 is the length at which maximum active tension occurs. Figure 5.9 gives a summary of the method as a flowchart.

5.3.1 Limits of Autoregulation

At base state, the total network resistance is $R_{tot,0} = 8{,}770.90\ mmHgs/mm^3$. This is split between arterioles, $R_{A,0} = 6401.40\ mmHgs/mm^3$ and capillaries and venules $R_{CV,0} = 2369.50\ mmHgs/mm^3$ calculated using equations 2.2 and 5.8:

$$R_{tot} = \sum_{1}^{13} R_i = \sum_{1}^{13} \frac{R_v}{n_i}, \tag{5.8}$$

where R_{tot} is the sum of generation resistance R_i calculated as the parallel sum of vessel resistance R_v for n vessels in generation i (where there are a total of 13 generations).

The total flow is $Q_0 = 3.7 \times 10^{-3}\ mm^3/s$ (see Table 3.4) and the network driving pressure $\Delta P_{tot,0} = 34.18\ mmHg$ (calculated from Equation 2.1 so that $P_{out,0} = 23.61\ mmHg$ and $P_{in,0} = 57.79\ mmHg$).

The autoregulation curve (Figure 2.11) shows that vessels can regulate up to approximately ±50% of driving pressure. The arteriole diameter stretch required to achieve this is calculated using the new driving pressure gradient:

$$\Delta P_{tot,u} = 1.5(\Delta P_{tot,0}) = 51.27 mmHg, \tag{5.9}$$

where $\Delta P_{tot,u}$ is the upper pressure bound at +50% of baseline. At the upper limit, inlet arterial pressure is calculated as:

$$P_{in,u} = P_{out,0} + 51.27 = 74.88\, mmHg. \tag{5.10}$$

For autoregulation, flow is assumed not to change:

$$Q_u = Q_0 = 0.0037\, mm^3/s. \tag{5.11}$$

Therefore network resistance:

$$R_{T,u} = \Delta P_{tot,u}/Q_0 = 13,858 mmHgs/mm^3. \tag{5.12}$$

Since it is assumed that only arterioles regulate:

$$R_{A,u} = R_{T,u} - R_{CV,0} = 11,487\, mmHgs/mm^3. \tag{5.13}$$

The arteriolar resistance is the series sum of resistance for generations $i = 1$ to 6 (Equation 5.8). For individual arterioles:

$$R_v/R_{v,0} = \frac{\mu/\mu_0}{d^4}, \tag{5.14}$$

and, since the number of vessels n doesn't change, for generation g:

$$R_g/R_{g,0} = \frac{\mu/\mu_0}{d^4}. \tag{5.15}$$

Therefore, the total resistance is the sum of these generations:

$$R_T = \sum_1^6 R_{g,0}\left(\frac{\mu/\mu_0}{d^4}\right). \tag{5.16}$$

If viscosity changes are ignored, and d assumed to be the same for all vessels, this can be approximated as:

$$R_T \approx \frac{R_{T,0}}{d^4}. \tag{5.17}$$

For arterioles, d_u (at the upper limit) and d_l (at the lower limit) are calculated from resistance as:

$$d_u \approx \sqrt[4]{\frac{R_{A,0}}{R_{A,u}}} \approx 0.8640, \text{and } d_l \approx 1.2988. \tag{5.18}$$

By recalculating viscosity at this diameter (using Equation 2.5 and assuming the same haematocrit as at basal state), the resistance and diameter values can be iterated for all arterioles until the total arteriolar resistance is found to be equal to $R_{a,u} = 11,487\ mmHgs/mm^3$ and $R_{a,l} = 2249.40\ mmHgs/mm^3$, when $d_u = 0.8602$ and $d_l = 1.3152$.

5.3.2 Vessel A1 at limits

The mean vessel pressure in the first arteriole $P_{v,A1}$ can be found since, for the first vessel ($A1$), vessel flow is equal to network flow, and vessel inlet pressure is equal to the network inlet pressure. R_{A1} can be calculated from the diameter and viscosity at the autoregulation limits.

$$P_{v,A1} = P_{in} - Q_0 R_{A1} \tag{5.19}$$

At high pressure, $P_{v,A1,u} = 68.47\ mmHg$ and at low pressure $P_{v,A1,l} = 39.43\ mmHg$. Table 5.15 gives the total pressure drop, inlet pressure and network resistance as well as the diameter fraction, resistance and vessel pressure for vessel $A1$ at the upper and lower limits of autoregulation.

	ΔP_{tot}	P_{in}	R_T	d	$R_v(A1)$	$P_v(A1)$
Basal	34.18	57.79	8770.93	1	1874.68	54.32
Upper	51.27	74.88	13858.48	0.8602	3531.28	68.47
Lower	17.09	40.70	4619.49	1.3152	684.26	39.43

Table 5.15: *Parameters calculated to satisfy autoregulated flow at low and high pressure limits of autoregulation.*

5.3.3 Equivalent L_0

Referring back to Figure 2.10, it is clear that the passive tension at $L/L_0 = 1.3152$ will be extremely high. This graph must therefore be shifted so that L_0 is equivalent to the basal state of the Lucas model. At the maximum limit of autoregulation, the diameter is fully constricted against pressure and so activation is assumed to equal 1. At the low pressure limit, activation is assumed to be 0 since the diameter is fully dilated against pressure. The basal activation, A_0, can be anywhere between these two limits.

At the high pressure limit, Laplace tension is equal to the maximum total tension, Equation 5.20. For low pressure, activation is zero and therefore the tension is equal only to passive tension, Equation 5.21. At basal state, the Laplace tension is a combination of passive and active tension depending on basal activation A_0, Equation 5.22:

$$T_{A1,u} = T_{p,A1,u} + T_{a,A1,u} = \frac{P_{v,A1,u} D_{A1,u}}{2} = 0.7046\, mmHg\, mm. \tag{5.20}$$

$$T_{A1,l} = T_{p,A1,l} = \frac{P_{v,A1,l} D_{A1,l}}{2} = 0.6216\, mmHg\, mm, \tag{5.21}$$

$$T_{A1,0} = T_{p,A1,0} + A_0 T_{a,A1,0} = \frac{P_{v,A1,0} D_{A1,0}}{2} = 0.6510\, mmHg\, mm, \tag{5.22}$$

where T_{A1} is the circumferential tension in vessel $A1$ at upper u, lower l and basal 0 state calculated using Equation 2.30 with intravascular pressure P_v and vessel diameter D. T_p is the passive tension and T_a the active with the same subscript notation.

At the upper limit, with activation $A = 1$, the Laplace tension is equal to the passive tension T_p plus the active tension T_a, at the lower limit with $A = 0$ the

Laplace tension is equal only to the passive tension. The ratio, x, of lower to upper limit Laplace tension (calculated from Equation 5.21 and Equation 5.20) is 0.8822. There exists a length $a = L/L_0$ on the Davis and Gore graph where:

$$x = \frac{T_l}{T_u} = \frac{T_{p,l}}{T_{p,u} + T_{a,u}} = 0.8822. \tag{5.23}$$

Table 5.1 gives the values of T_a and T_p for a variety of length ratios l. The constricted and dilated diameter ratios can be calculated as if each point were the basal state by multiplying l by 0.8602 and 1.3152 (see Table 5.16). The passive and active tensions at these length ratios are found by linearly interpolating the data between the existing points and evaluating at the new length ratio.

l	Constricted (0.8602 l)	Passive ($mmHg\,mm$)	Active ($mmHg\,mm$)	Dilated (1.3152 l)	Passive ($mmHg\,mm$)	Active ($mmHg\,mm$)
0.65	0.56	-0.08	3.22	0.85	0.57	7.55
0.70	0.60	0	3.91	0.92	0.68	8.26
0.75	0.65	0.08	4.61	0.99	1.12	8.81
0.80	0.69	0.17	5.31	1.05	3.16	8.15
0.85	0.73	0.22	5.89	1.12	8.09	5.19
0.90	0.77	0.31	6.43	1.18	13.03	2.23
0.95	0.82	0.44	7.01	1.25	17.96	-0.72
1.00	0.86	0.57	7.60	1.32	22.89	-3.68
1.05	0.90	0.63	8.04	1.38	27.82	-6.64
1.10	0.95	0.74	8.58	1.45	32.76	-9.60

Table 5.16: *Values of passive and active tension calculated at lower and upper autoregulation limits if each length were equivalent to the Lucas network basal diameter*

Calculating the ratio, x, of $T_{p,l}$ to $T_{p,u} + T_{a,u}$ at each point and interpolating linearly to find the length ratio $L/L_0 = a$ for which $x = 0.8822$ gives a value of $a = 0.8194$ (where $x = 0.8824$), this value being subject to slight error due to the interpolation. Therefore, the basal Lucas network (with diameter D_0) can be compared with the data of Davis and Gore by shifting so that $D_0 = 0.8194 L_0$ (as shown in Figure 5.8).

Figure 5.8 shows the Davis and Gore data projected onto the Lucas model basal diameter. The calculation of $a = D_0/L_0$ is done by assuming a pressure regulation

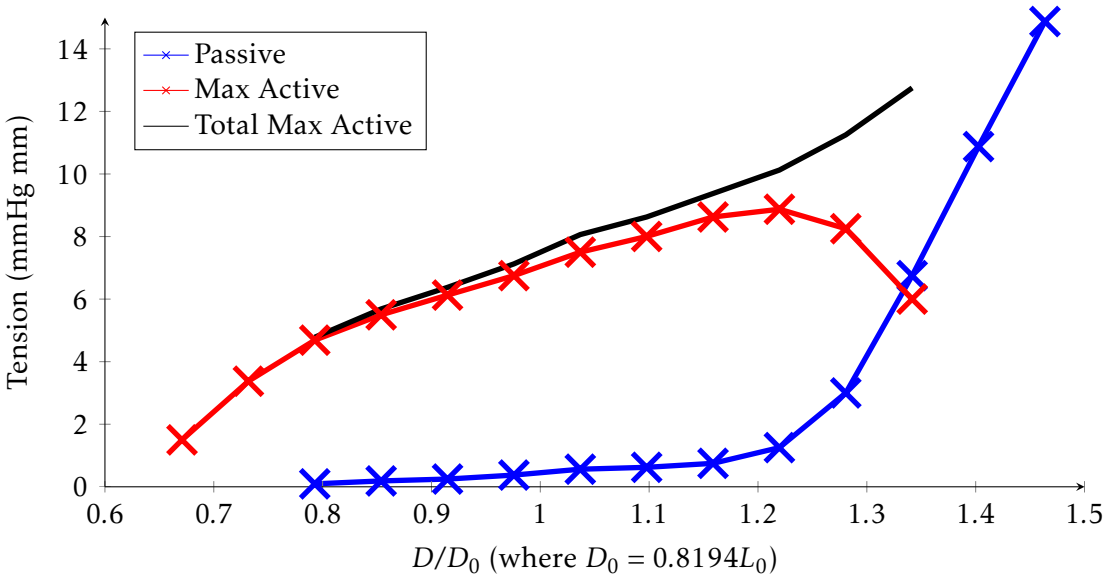

Figure 5.8: *The Davis and Gore data recast to Lucas model D_0, where $D/D_0 = 1$ at $L/L_0 = 0.8194$*

limit of ±50% and calculating the necessary diameter to fulfil the criteria of conserved flow at these pressure limits. The passive and active tensions at these limits are calculated by assuming saturated activation A so that the Laplace tension is equal to the passive, or passive plus fully active tensions. Therefore, a value for the ratio of lower and upper limit Laplace tensions can be calculated (x) and equated to a point on the Davis and Gore graph giving the equivalent basal condition of the Lucas network. The data translated into Lucas diameter fraction $d = D/D_0$ are given in Table 5.17. With the data in this form, the passive tension when $d = 1.3152$ is calculated (by interpolation) to be 5.08 $mmHg\,mm$.

At the limits of autoregulation $d_u = 0.8602$ and $d_l = 1.3152$, the equivalent Davis and Gore diameter fractions l_u and l_l are calculated as (for example):

$$l_u = d_u a, \tag{5.24}$$

so that $l_u = 0.70$ and $l_l = 1.08$.

The Davis and Gore vessel has tension of a different magnitude to the Lucas vessel. The position of maximum active tension in Figure 5.8 is at $L/L_0 = 1$ or

l	d	Passive Tension ($mmHg\,mm$)	Maximal Active Tension ($mmHg\,mm$)	Total Tension ($mmHg\,mm$)
0.55	0.67	0	1.50	1.50
0.60	0.73	0	3.38	3.38
0.65	0.79	0.09	4.69	4.78
0.70	0.85	0.19	5.50	5.69
0.75	0.92	0.25	6.13	6.38
0.80	0.98	0.38	6.75	7.13
0.85	1.04	0.56	7.50	8.06
0.90	1.10	0.62	8.00	8.63
0.95	1.16	0.75	8.63	9.38
1.00	1.22	1.25	8.87	10.13
1.05	1.28	3.00	8.25	11.25
1.10	1.34	6.75	6.00	12.75
1.15	1.40	10.88	not shown	
1.20	1.47	14.87	not shown	

Table 5.17: *The Davis and Gore data recast to Lucas model $D_0 = aL_0$, where $D/D_0 = 1$ at $L/L_0 = 0.8194$.*

$D/D_0 = 1.2204$. The magnitudes of tension at the autoregulation limits are calculated by linear interpolation of the existing data points and given in Table 5.18.

	d	l	T_p ($mmHg\,mm$)	T_a ($mmHg\,mm$)	T_t ($mmHg\,mm$)
Basal	1	0.82	0.45	7.04	7.86
Upper	0.8602	0.70	0.19	5.56	5.75
Lower	1.3152	1.08	5.08	7.01	5.08

Table 5.18: *Passive and action tension at the autoregulation limits of the Davis and Gore vessel.*

5.3.4 Basal Activation

Using the total tension at the limits of autoregulation, the ratio, r, of passive basal tension $T_{p,0}$ to total tension at the upper limit $T_{p,u} + T_{a,u}$ can be calculated for the Davis and Gore values (see Table 5.17 at $d = 1$):

$$r = \frac{T_{p,0}}{T_{p,u} + T_{a,u}} = 0.78. \tag{5.25}$$

This ratio can then be used to find the passive tension of the equivalent Lucas vessel $A1$ (see Equation 5.20):

$$T_{p,A1,0} = r T_{A1,u}, \tag{5.26}$$

so that Lucas $T_{p,A1,0} = 0.0549\ mmHg\,mm$.

The fraction of passive tension to total tension at basal state, f, is interpolated from the data:

$$f = T_{p,0}/T_{T,0}, \tag{5.27}$$

for $a = 0.8194$, f is equal to 0.06. Therefore $T_{T,A1,0} = 0.9172\ mmHg\,mm$ and $T_{a,A1,0} = 0.7519\ mmHg\,mm$.

The contribution of basal active tension $T_{a,A1,0}$ to the Laplace tension $T_{A1,0}$ is set by the activation A_0 which can be found by rearranging Equation 5.22:

$$A_0 = \frac{T_{A1,0} - T_{p,A1,0}}{T_{a,A1,0}}, \tag{5.28}$$

giving $A_0 = 0.6909$.

The vessel is therefore more active than previously assumed by other investigators (see subsection 2.6.3 where Carlson sets $A_0 = 0.5$). This is because the length-tension graph is shifted towards a more constricted basal state where there is a lower proportion of passive tension. It should be noted that the starting point for these calculations is the assumption that the limits of auto-regulation are ±50% driving pressure and so the values, or the assumed pressure limit, may not be correct.

5.3.5 Lucas Tension Parameter Results

This process can of course be repeated for any basal state, or any proposed autoregulation limits. The values of D/D_0 for other pressure limits are given in Table 5.19.

A pressure limit of ±30 % sets D_0 close to L_0 ($a = 0.99$), but activation is high (0.80). For an activation of 0.50, the pressure limit is ±59 % so that the network can regulate more than suggested in the literature. The diameter dilation and constriction does not need to be symmetrical in order to achieve symmetrical pressure limits, due to the non-linearity of the model. For a ±50 % pressure regulation, the

$\pm\Delta P/\Delta P0$	A_0	f	a	D/D_0 (constricted)	D/D_0 (dilated)
0.2	0.7444	0.3439	1.0634	0.9234	1.0651
0.25	0.7876	0.2057	1.0274	0.9112	1.0922
0.3	0.8001	0.1159	0.9904	0.8998	1.1231
0.4	0.7480	0.0741	0.8896	0.8709	1.2009
0.5	0.6909	0.0600	0.8194	0.8602	1.3152
0.55	0.6500	0.0429	0.7609	0.8515	1.3981
0.57	0.5751	0.0370	0.7313	0.8482	1.4394
0.59	0.5026	0.0341	0.7087	0.8449	1.4873
0.60	0.4292	0.0312	0.6924	0.8433	1.5144

Table 5.19: *The parameters calculated for varying pressure limits of autoregulation.*

diameter constricts by 14 % but dilates by 31 %. The diameter is therefore not held at the point of maximum tension but below it.

Section Summary

The data collected by Davis and Gore is displayed using non-dimensional strain with L_0 chosen to be the circumference with maximum active tension. Using a sequence of assumptions and comparisons between the data and the Lucas model, these data can be re-cast in terms of the basal diameter D_0 calculated for the Lucas model where the relationship between L_0 and D_0 is set by the parameter $a = D_0/L_0$. This process relies on interpolation between data points, which is subject to some error. A summary of the calculations is given in Figure 5.9.

The three most plausible cases from Table 5.19 are at driving pressure gradient ±59% (since $A_0 \approx 0.5$), ±50% (the standard autoregulation curve) and ±30% (where $a \approx 1$ so that $D/D_0 = L/L_0$).

Choose autoregulation limits for pressure (e.g. upper u)	e.g $\Delta P_{T,u}$
Calculate network resistance $R_{T,u}$ at this limit *assuming conserved flow*	$R_{T,u} = \frac{\Delta P_{T,u}}{Q0}$
Calculate vessel diameter fraction d_u which sums to correct resistance *assuming arteriole only regulation by the same diameter ratio*	$R_{T,u} = \frac{R_{T,0}}{d_u^4}$
Calculate mean vessel pressure $P_{v,u,A1}$	$P_{v,u,A1} = P_{in,u} - \frac{Q0R_{v,u,A1}}{2}$
Calculate laplace tension T_{A1}	$T_{A1,u} = \frac{T_{A1,u}D_{v,A1,u}}{2}$
Assume that activation $A_l = 0$ at the lower limit and $A_u = 1$ at the upper limit Calculate the ratio x of upper and lower tension	$x = \frac{T_{A1,u}}{T_{A1,l}}$
Calculate the constricted and dilated passive and active tensions at each length fraction in the data	e.g $T_{p,u} = T_p(d_u)$
Find the length ratio a with the same tension ratio x	$a = \frac{T_{p,u}(ad_u)}{T_{p,l}(a)+T_{a,l}(a)} = \frac{D_0}{L_0}$
Find the ratio r of passive and total tension at basal and upper limit	$T = \frac{T_{p,0}(a)}{T_{p,u}(a)+T_{a,u}(a)}$
Therefore calculate the Lucas passive basal tension in $A1$	$T_{p,A1,0} = rT_{A1,u}$
Find the fraction f of passive to total tension	$f = \frac{T_p(a)}{T_T(a)}$
Therefore calculate the Lucas total	$T_{T.A1,0} = \frac{Tp,A1,0}{f}$
and active tension in $A1$	$T_{a,A1,0} = T_{T,A1,0} - T_{p,A1,0}$
Finally calculate the Lucas basal activation A_0 in vessel $A1$	$A_0 = \frac{TA1,0-T_{p,A1,0}}{T_{a,A1,0}}$

Figure 5.9: *Procedure for establishing the Lucas vessel length-tension characteristics.*

Section 5:4 Non-Dimensional Tension Model

Since the basal tension is not uniform across the vessels in the Lucas network, it is important to find a non-dimensional version of equations 5.4 and 5.7 which model the passive and active length-tension characteristics.

5.4.1 Non-dimensionalisation

In order to replicate the length-tension characteristics for any pressure-limit conditions, Equation 5.4 and Equation 5.7 are now non-dimensionalised around T_{T0}, since this can be found from $T_{h,0}$ using the values of f (the ratio between passive and total tension at basal state) and A_0 (the basal activation) calculated previously (Table 5.19).

$$T_{p0} = f\,T_{T0} \tag{5.29}$$

$$T_{a0} = (1-f)T_{T0} \tag{5.30}$$

$$T_0 = T_{p0} + A_0 T_{A_0} \tag{5.31}$$

$$T_0 = T_{T0}(f + A_0(1-f)). \tag{5.32}$$

The parameters C_{p1}, C_{t1}, C_{a1} and C_{a2} are all non-dimensionalised using the basal total tension T_{T0}, where non-dimensional parameters are denoted by an asterisk:

$$\frac{T_{\text{pass}}}{T_{T0}} = \begin{cases} C^*_{p1} e^{C_{dp1} d} & \text{if } d \le d_p \\ m^*_p d + c^*_p & \text{otherwise} \end{cases} \tag{5.33}$$

Similarly,

$$\frac{T_{act}}{T_{T0}} = \begin{cases} C^*_{t1} + C^*_{a1} e^{-C_{da1}(d-C_{ea1})^2} & \text{if } d < d_a \\ C^*_{a2} e^{-C_{da2}(d-C_{ea2})^2} & \text{otherwise.} \end{cases} \tag{5.34}$$

where d_p and d_a are diameter ratios at the cross-over between functions: $d_p = 1.0139$, $d_a = 0.9889$, when $a = 1$.

Table 5.20 gives the non-dimensional tensions at Davis and Gore length ratio calculated as (for example) $T_p^* = \frac{T_p}{T_{T0}}$, with $T_{T0} = 10.13\ mmHg\,mm$ (at $l = 1$).

length ratio l	Passive Data T_p^*	Active Data T_a^*
0.55	0	0.15
0.60	0	0.33
0.65	0.01	0.46
0.70	0.02	0.54
0.75	0.02	0.61
0.80	0.04	0.67
0.85	0.06	0.74
0.90	0.06	0.79
0.95	0.07	0.85
1.00	0.12	0.88
1.05	0.30	0.81
1.10	0.67	0.59
1.15	1.07	not shown
1.20	1.47	not shown

Table 5.20: *Passive and Active data from Figure 2.10 non-dimensionalised with the total tension at $L = L_0$.*

5.4.2 Non-dimensional Model parameters

For each of the pressure limit scenarios, there is a different set of parameters that can be found by optimising the non-dimensional data in the same way as for the dimensional parameters. For different values of a, the L/L_0 values are shifted and the basal state tension is found by interpolating the data at new $L_0 = 1$. The results of these calculations are given in Table 5.21.

a	0.9904	0.8194	0.7087
$T_{p,0}$	1.16	0.45	0.20
$T_{a,0}$	8.83	7.04	5.61
T_0	9.98	7.49	5.81
d_p	1.02	1.24	1.43
d_a	1.00	1.21	1.40
C^*_{p1} ($\times 10^{-4}$)	2.36	3.17	3.82
C_{dp1}	6.21	5.11	4.40
m^*_p	6.94	7.66	8.57
c^*_p	-6.90	-9.29	-12.04
C^*_{t1}	-23.52	-105.88	-141.58
C^*_{a1}	24.40	107.07	143.12
C_{da1}	0.11	0.02	0.02
C_{ea1}	1.07	1.30	1.51
C^*_{a2}	0.88	1.18	1.52
C_{da2}	47.34	31.49	23.55
C_{ea2}	1.01	1.23	1.43

Table 5.21: *The parameters calculated for varying reference diameter for non-dimensional tension.*

5.4.3 Non-dimensional Model Results

The resulting passive and active tension calculated using the $a = 0.8194$ parameters from Table 5.21 are given in Table 5.22 and shown in Figure 5.10.

d	Passive Data	Passive Model	Error	Active Data	Active Model	Error
0.67	0	0.01		0.2	0.35	0.15
0.73	0	0.01		0.45	0.5	0.05
0.79	0.01	0.02	0.01	0.63	0.64	0.02
0.85	0.03	0.02	0	0.73	0.77	0.03
0.92	0.03	0.03	0	0.82	0.87	0.06
0.98	0.05	0.05	0	0.9	0.97	0.06
1.04	0.08	0.06	-0.01	1	1.04	0.04
1.1	0.08	0.09	0	1.07	1.1	0.03
1.16	0.1	0.12	0.02	1.15	1.15	0
1.22	0.17	0.16	-0.01	1.18	1.18	-0.01
1.28	0.4	0.53	0.13	1.1	1.09	-0.02
1.34	0.9	0.99	0.09	0.8	0.79	-0.01
1.4	1.45	1.46	0.01	not shown	0.46	
1.46	1.99	1.93	-0.06	not shown	0.21	
RMSE	-	-	0.05			0.05

Table 5.22: *Passive and active data from Figure 2.10 non-dimensionalised and modelled as described*

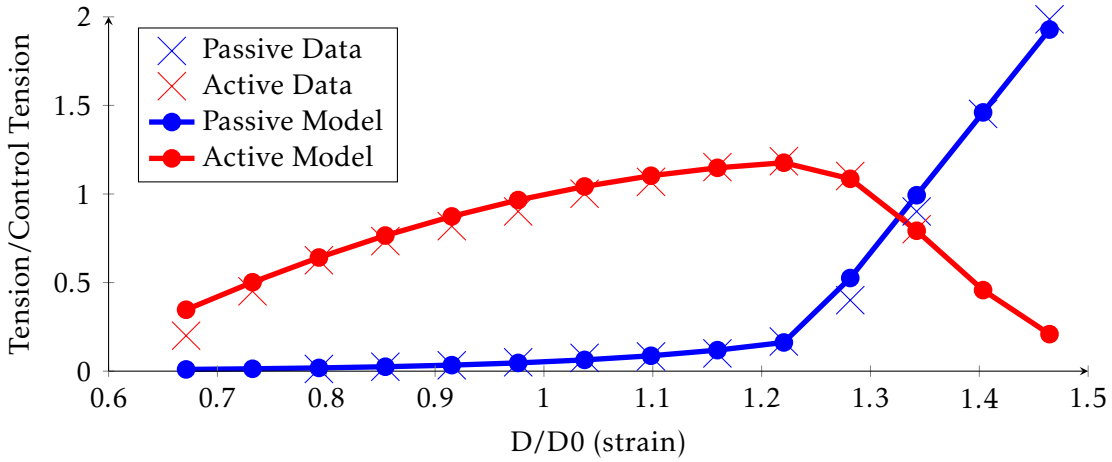

Figure 5.10: *The Davis and Gore tension data modelled non-dimensionally for* $D_0 = 0.8194L_0$.

The errors are reduced compared with the previous results (Tables 5.8 and 5.14) due to the reduced magnitude of non-dimensional tension. Multiplying by T_{T0} gives an error for both passive and active tension of 0.3745 which is higher than found previously. However, the usefulness of a non-dimensional model for all the vessels outweighs the slightly increased error. The maximum and minimum diameter ratios for a ±50 % pressure regulation are 1.32 and 0.86; Figure 5.10 shows that the highest active tension is towards the top of this diameter range.

Summary

In chapter 5, a continuous model is proposed for passive and active tension related to diameter strain, based on a data set from Davis and Gore. This data set is non-dimensionalised for basal tension so that it can be used for a vessel of any size. This non-dimensionalised model relies on assumption that vessels act similarly when stretched regardless of location and size. The basal diameter is investigated and a method proposed which uses autoregulation pressure limits to establish the diameters which conserve flow at high and low pressure. By finding the tension at these limits in the Lucas model, and comparing (along with the basal tension) with the data, the graph is shifted by a parameter a which relates the Lucas basal diameter D_0 with the data basal diameter L_0. The shifting of the data is done by interpolation and the model parameters which mimic the shifted data are found by trust-region optimisation. Both of these methods are subject to error but the overall results show a good fit compared to previous attempts. The approach of the method is empirical, the experimental data being fit to strain and the model optimised to fulfil the known pressure limits based on the concept of smooth muscle activation. The resulting equations are therefore based upon a physiological set of parameters related to the mechanics of the vessels and activation of the muscle cells. The next chapter uses these equations, along with the concept of activation, to stimulate the myogenic response to pressure in the network.

CHAPTER 6

The Myogenic Response

In this chapter, the elastic and active responses to changes in perfusion pressure are investigated and an expression for activation described which reproduces the autoregulation curve. This incorporates a weighted signal depending on the shear and hoop stress which determines the proportion of muscle cells which are active in the vessel, and therefore the vessel diameter. A method to calculate the weights is described which follows the calculations presented in chapter 5.

Section 6:1 Passive Pressure Response

Without autoregulation, the arterioles and venules undergo a passive elastic response to changes in pressure due to the length-tension characteristics determined in chapter 5. Capillaries lack elastin and therefore do not expand to accommodate flow.

6.1.1 Diameter Change

The steady-state elastic diameter response to a pressure change is a balance between hoop stress (Equation 2.30), and total passive and active tension, described by Equation 2.55. At basal state, the hoop stress is equal to;

$$T_{h,0} = \frac{P_0 D_0}{2}, \tag{6.1}$$

which is equal to T_{T0}. Therefore, the non-dimensional values for passive (Equation 5.33) and active (Equation 5.34) tension can be found by dividing by basal hoop stress $T_{h,0}$:

$$T^*_{\text{pass}} = \frac{T_{\text{pass}}}{T_{h,0}} \tag{6.2}$$

$$T^*_{\text{act}} = \frac{T_{\text{act}}}{T_{h,0}}, \tag{6.3}$$

and, by rearranging Equation 2.55, hoop stress is equal to:

$$\frac{PD}{2} = \frac{P_0 D_0}{2}(T^*_{\text{pass}} + A_0 T^*_{\text{act}}) = T_T. \tag{6.4}$$

The activation for the elastic response remains at A_0, calculated as described in subsection 5.3.4 where $A_0 = 0.6909$ for arterioles and $A_0 = 0$ for other vessels.

Following a change in pressure, the diameter changes dynamically until equilibrium between T_T and T_h is reached [77]. The elastic dynamics are assumed first order of the form:

$$\tau_D \frac{dD}{dt} = \frac{2}{P_0}\left(\frac{PD}{2} - T_T\right), \tag{6.5}$$

where τ_D is the time constant of the system and P_0 is the basal state pressure. This equation can be divided by T_{T0} to write in terms of non-dimensional tension:

$$\tau_D \frac{1}{D_0}\frac{dD}{dt} = \frac{PD}{P_0 D_0} - (T^*_{\text{pass}} + A_0 T^*_{\text{act}}). \tag{6.6}$$

Note that τ_D only affects the speed of the response where a smaller value increases the speed of the response. An initial value of 1 s is chosen since the elastic response is close to instantaneous.

6.1.2 A Passive Network

Simulations in the network of vessels are first performed with elastic vessels (so that the activation does not change). The steady state results of the passive response to varying perfusing pressure for vessel $A1$ are shown in Figure 6.1. Since the flow in vessel $A1$ is equal to the total flow in the network, Figure 6.1 (b) also shows the passive network flow change with pressure. The diameter has a nonlinear dependence on driving pressure which affects flow. A 40% increase in pressure causes a 100% increase in flow when the diameter is subject only to elasticity. For high pressure ($> 1.4\Delta P_{tot,0}$) the relationship between pressure and flow becomes approximately linear.

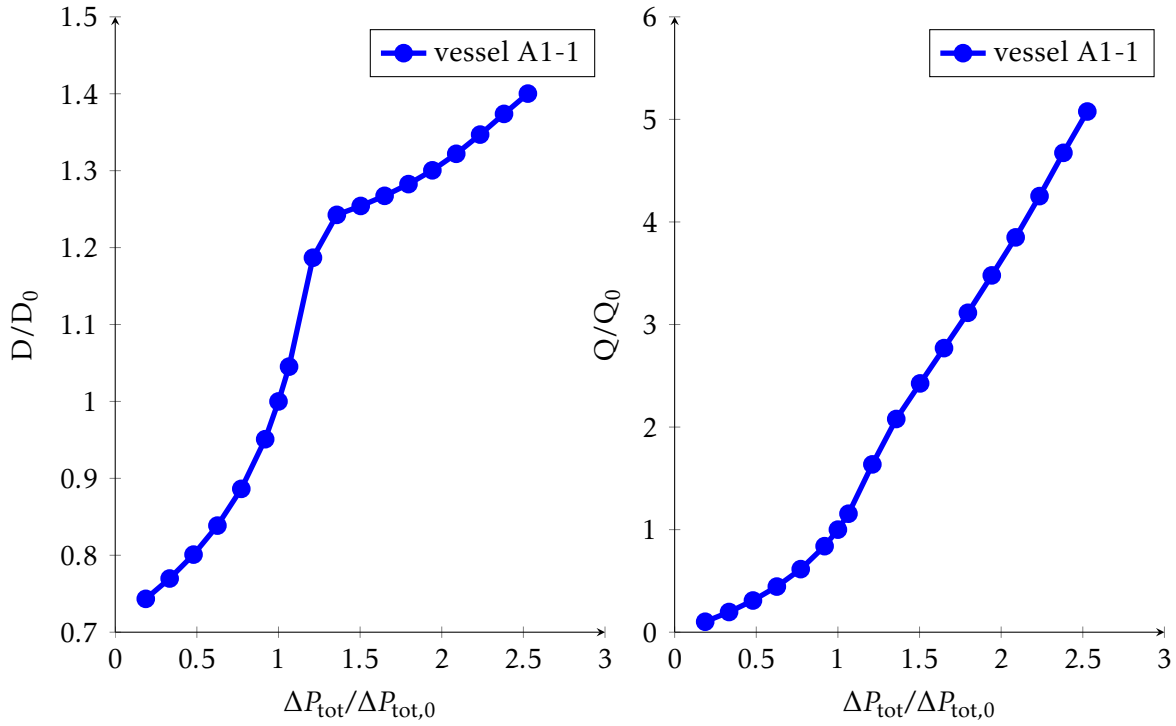

(a) Diameter (b) Flow

Figure 6.1: *Flow and diameter at steady state following arterial pressure perturbation .*

Section 6:2 Active Response

The activation of smooth muscle affects the contribution of passive and active vessel tension to the total tension (Equation 2.55) and the amount of activation is determined by certain physiological conditions. The myogenic response potentially involves both hoop stress, T_h, and shear stress, τ_w (see discussion in section 2.6).

6.2.1 Activation

The activation is described by Carlson as being sigmoidally dependent on an input signal S [42]. At basal state, activation $A_0 = 0.6909$ and the activation saturates at $A_u = 1$ and $A_l = 0$. Therefore, activation can be written in the form:

$$A = \frac{m}{m + e^{-S}}. \tag{6.7}$$

It is assumed that the basal state input signal is 0, but it could be the sum of absolute physical parameters. Carlson sets A_0 to be 0.5, but the basal activation for the network calculated in subsection 5.3.4 is 0.6909. For $S_0 = 0$ and $A_0 = 0.5$, $m = 1$ which reduces Equation 6.7 to Equation 2.58. Otherwise m is calculated as:

$$m = \frac{A_0}{1 - A_0}, \tag{6.8}$$

for $A_0 = 0.6909$, $m = 2.24$.

6.2.2 Constricted and Dilated Results

If the simulation is run with activation held at 0 and at 1, the resulting fully dilated and fully constricted pathways can be calculated and are given in Figure 6.2. Fully constricted, the flow is equal to basal flow at $\Delta P_{tot}/\Delta P_{tot,0} \approx 1.4$ (where $D/D_0 \approx 0.88$). When dilated, the flow is equal to basal flow at $\Delta P_{tot}/\Delta P_{tot,0} \approx 0.6$ (where $D/D_0 \approx 1.29$). The potential of the vessels is therefore for autoregulation (conserved flow) between ±40% of basal driving pressure. However, the length-tension characteristics were calculated for ±50% in chapter 5. The disparity is due to the varying approximations in finding the length-tension characteristics and the basal activation. At $0.5P_0$ with $A = 1$, the flow is $0.8Q_0$, and at $1.5\Delta P_{tot,0}$, the flow is $1.2Q_0$ with activation 0.

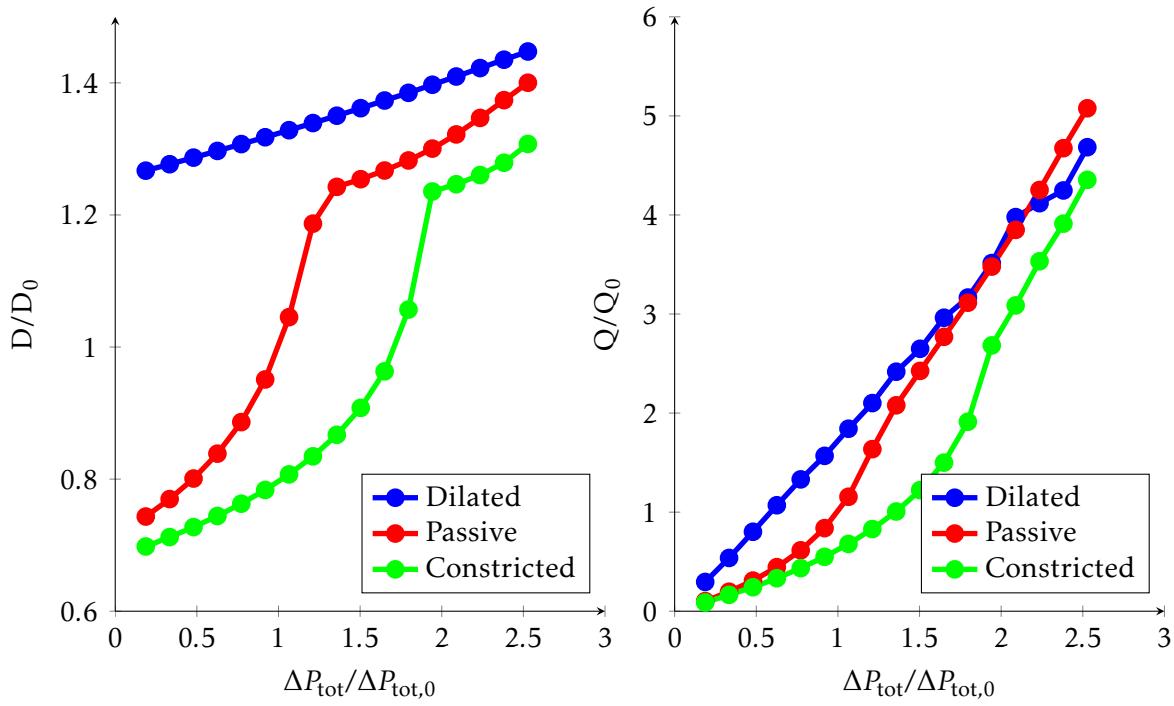

(a) Diameter

(b) Flow

Figure 6.2: *Flow and diameter at steady state following arterial pressure perturbation with $A = 1$ (constricted) $A = 0$ (dilated) and $A = A_0$ (passive) .*

6.2.3 Necessary Activation

By running simulations at varying fixed activation and interpolating the pressure-flow results, the steady-state pressure-activation curve can be found for which flow is conserved at basal state (Table B.1). Although it is therefore assumed that $Q = Q_0$, the flow does actually increase slightly. The required activation for conservation of flow is linear above $0.64\Delta P_{tot,0}$ (see Figure 6.3) with a steep drop below this pressure; this can be compared with the model of Feldberg [76] where there is linear dependence of activation on pressure between two pressure boundaries (Equation 2.56). For ±40% $\Delta P_{tot,0}$, the relationship between driving pressure and diameter is very slightly non-linear (see Figure 6.4) with the diameter being $1.3D_0$ at the lower pressure limit and $0.86D_0$ at the higher.

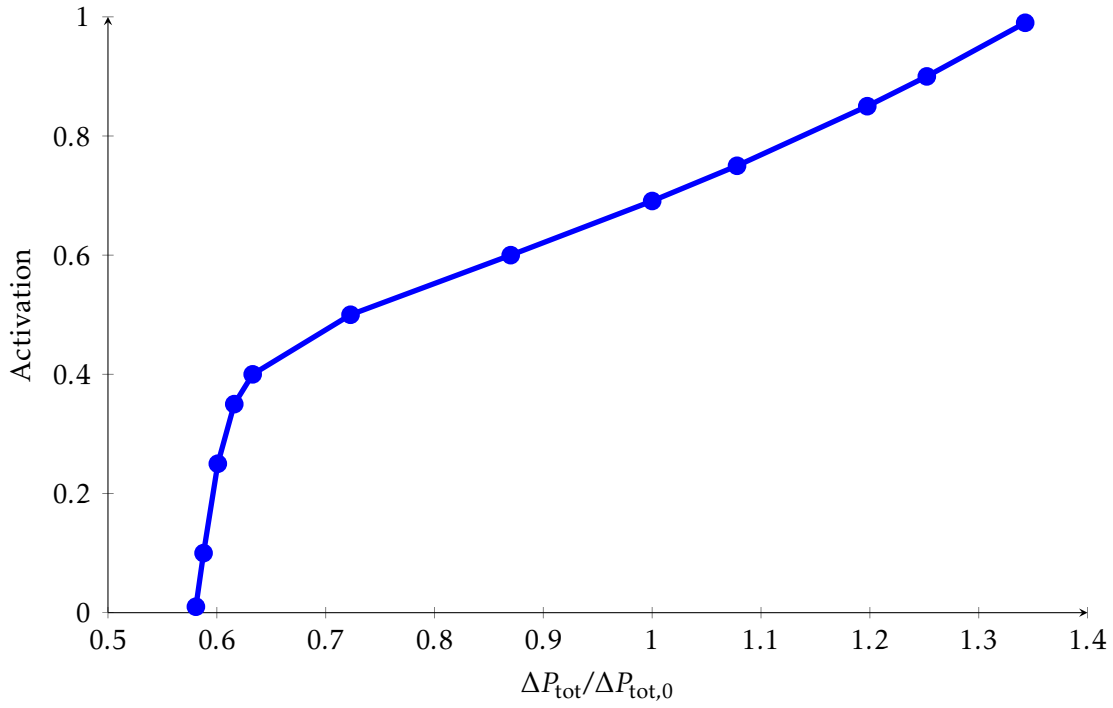

Figure 6.3: *Activation necessary for autoregulation of flow.*

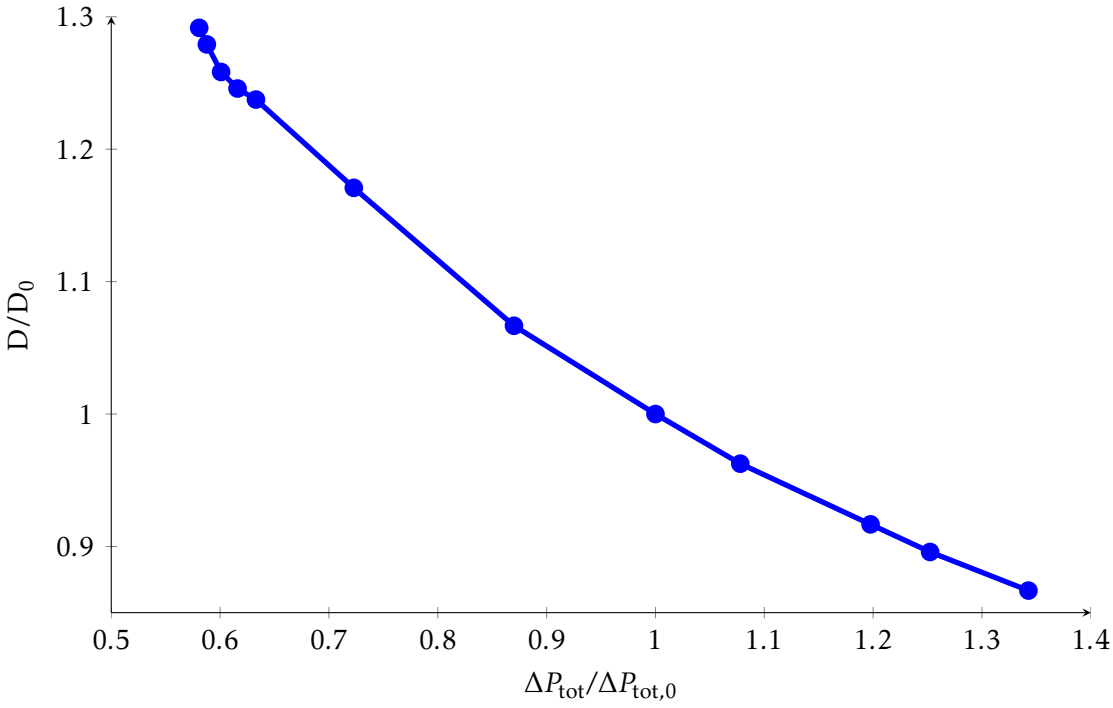

Figure 6.4: *Diameter required for autoregulation of flow.*

6.2.4 Signal

Equation 6.8 can be rearranged for signal:

$$S = -ln\left(\frac{m(1-A)}{A}\right). \tag{6.9}$$

The necessary signal to conserve flow is calculated from Table B.1 using Equation 6.9. At maximum activation, $A = 1$, but this cannot be solved with Equation 6.9 and so instead $A = 0.99$, $S = 3.7908$ are used as approximations. Similarly, for $A = 0$, $A = 0.01$ gives $S = -5.3995$. Note that the resulting signal (see Figure 6.5) is not symmetrical with respect to the driving pressure fraction. The relationship between signal and driving pressure fraction is approximately linear between 0.625 and $1.25\Delta P_0$ with a steep low-pressure and high-pressure curve, this is in line with the function for activation proposed by Feldberg Equation 2.56 [76].

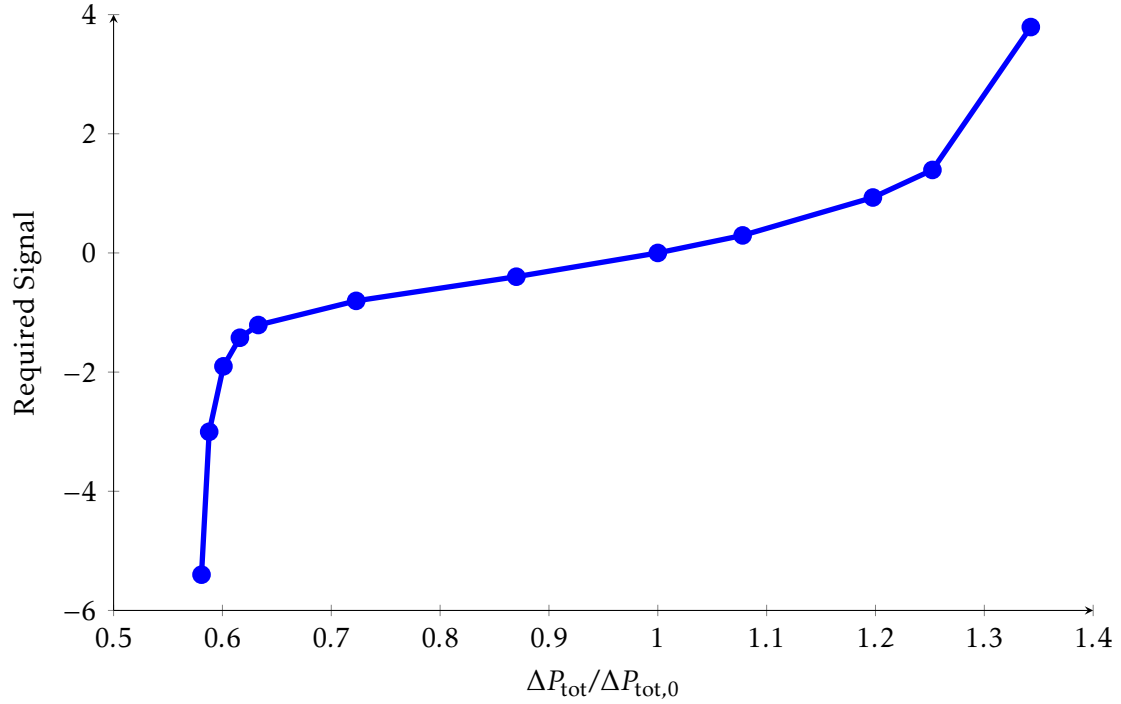

Figure 6.5: *Signal required for varying pressure levels in order to maintain flow.*

For non-dimensional signal S, the following function is now proposed (giving $S = 0$ at steady state):

$$S = k_p(T_h - T_{h,0}) + k_w(T_w - T_{w,0}). \tag{6.10}$$

Equation 6.10 gives positive and negative signal S for increases and decreases respectively in hoop stress T_h and shear stress T_w which correlates with diameter constriction and dilation, reducing and increasing the hoop stress where necessary.

6.2.5 Signal Weight

By running a simulation with A fixed at the known desired activation for each pressure change (from Table B.1), the parameters of the network can be determined as they would be at each pressure change, and at any point in time. k_p ($/mm\,mmHg$) and k_w ($/mmHg$) can then be found by solving equations 2.30, 2.46 and 6.10 at these points.

Following a step increase in pressure, there is no immediate effect on activation and so the vessel diameter stays the same and flow increases due to a larger pressure difference. The initial time step parameters immediately following a step-change in flow are given in Table 6.1 with the second column giving the desired signal for each pressure change.

If these are formed into a set of simultaneous equations (Equation 6.11 for each row of Table 6.1), then k_p and k_w can be solved for the immediate step change by minimising the RMS error between S calculated from Equation 6.11 and the desired S for autoregulation given in the second column of Table 6.1.

$$\begin{bmatrix} T_h - T_{h0} & T_w - T_{w0} \end{bmatrix} \times \begin{bmatrix} k_p \\ k_w \end{bmatrix} = S \tag{6.11}$$

Over the entire range of Table 6.1, the weights are solved giving $k_p = 411.80$ $/mm\,mmHg$ and $k_w = -3024.20$ $/mmHg$. If the non-linear signal part of the signal-

Pressure $\frac{\Delta P_{tot}}{\Delta P_{tot,0}}$	Signal	Flow $(10^{-3} mm^3/s)$	Diameter (μm)	Hoop Stress $(10^{-2}\ mm\,mmHg)$	Shear Stress $(10^{-2} mmHg)$
0.58	-5.40	2.15	23.97	49.66	2.78
0.59	-3.00	2.17	23.97	49.92	2.82
0.60	-1.91	2.22	23.97	50.40	2.88
0.62	-1.43	2.28	23.97	50.96	2.95
0.63	-1.21	2.34	23.97	51.58	3.03
0.72	-0.81	2.71	23.97	55.26	3.51
0.87	-0.40	3.22	23.97	60.31	4.17
1.00	0	3.70	23.97	65.09	4.79
1.08	0.29	3.99	23.97	67.96	5.17
1.20	0.93	4.43	23.97	72.36	5.74
1.25	1.39	4.63	23.97	74.38	6.00
1.34	3.79	4.97	23.97	77.70	6.43

Table 6.1: *Initial time step parameters following a step pressure change with activation set to the required value for autoregulation.*

pressure curve (see Figure 6.5) is ignored, the weights are calculated to be $k_p = 901.83\ /mm\,mmHg$ and $k_w = -6831.10\ /mmHg$.

The process of simulations at fixed activation can be repeated with the steady-state hoop stress and shear stress recorded once the flow has returned to the basal level. These parameters are given in Table 6.2.

Pressure $\frac{\Delta P_{tot}}{\Delta P_{tot,0}}$	Signal	Flow $(10^{-3} mm^3/s)$	Diameter (μm)	Hoop Stress $(10^{-2}\ mm\,mmHg)$	Shear Stress $(10^{-2}\ mmHg)$
0.58	-5.40	3.70	31.02	65.32	2.40
0.59	-3.00	3.70	30.73	65.01	2.46
0.60	-1.91	3.70	30.21	64.44	2.57
0.62	-1.43	3.70	29.85	64.37	2.65
0.63	-1.21	3.70	29.70	64.84	2.69
0.72	-0.81	3.70	28.12	63.35	3.11
0.87	-0.40	3.70	25.71	65.21	3.95
1.00	0	3.70	23.97	65.09	4.79
1.08	0.29	3.70	23.09	65.16	5.35
1.20	0.93	3.70	21.96	65.47	6.23
1.25	1.39	3.70	21.51	65.70	6.62
1.34	3.79	4.00	20.85	66.12	7.28

Table 6.2: *Parameters at steady state with activation fixed at required value for flow conservation following a pressure change.*

Once again, these can be formed into a set of simultaneous equations and the weights solved which would give the required signal for autoregulation. Over the whole pressure range, the weights are calculated as $k_p = -106.24\ /mm\,mmHg$ and $k_w = 137.61\ mm/mmHg$. Ignoring the non-linear extreme pressure changes, the weights are calculated to be $k_p = -49.63\ /mm\,mmHg$ and $k_w = 93.06\ /mmHg$. These weights have opposite signs to those calculated following the initial step change in pressure. Since it is assumed that the weights cannot change dynamically, there must be a different dominant parameter which sets the activation signal at the start and end of the autoregulation process.

Noticeably, at steady state (see Table 6.2) the hoop stress is almost back to the basal value ($T_{h,0} = 0.65\ mmHg\,mm$). Therefore, the myogenic signal is very small at steady state since the diameter changes reduce or increase hoop stress where necessary. The shear stress, however, changes compared to the basal state ($T_{w,0} = 4.79^{-2}\ mmHg$). Initially then, the myogenic signal sets the activation but, at steady state, it is the shear signal which maintains activation.

The magnitude of activation can saturate in response to the step-change in hoop stress, before returning to a steady state value. The initial signal can be larger than required as long as it returns to the desired steady state value, which is determined by k_w since the myogenic signal is so small.

Solving at steady state for $S = k_w(T_w - T_{w,0})$, the error is minimised over the entire pressure range when $k_w = 110.77\ /mmHg$ ($RMSE = 1.4722$). Solved over the linear portion of Figure 6.5 (corresponding to rows 5-10 of Table 6.2) results in a value of $k_w = 60.55\ /mmHg$ ($RMSE = 0.1569$, see Table B.2).

With $k_w = 60.55\ /mmHg$, k_p is then solved at the initial state (see Table 6.1) where activation is set by the change in hoop stress. Minimising the error between calculated and required signal gives a value of $k_p = 10.31\ /mm\,mmHg$ over the whole range ($RMSE = 1.1256$) and $k_p = 2.50\ /mm\,mmHg$ over the linear pressure

range ($RMSE = 0.2158$).

At the initial state, the signal can be higher than necessary as long as it returns to the required steady state signal and so the absolute calculated signal can be greater than the absolute desired signal. Table 6.3 shows the resulting signal error at the initial time-state for fixed $k_w = 60.55\ /mmHg$ and varying k_p.

S (required)	$k_p = 2.5$		$k_p = 10.31$		$k_p = 20$		$k_p = 27.11$	
	S	error	S	error	S	error	S	error
-5.40	-1.60	3.80	-2.81	2.59	-4.30	1.10	-5.40	0.00
-3.00	-1.57	1.43	-2.76	0.24	-4.23	-1.23	-5.31	-2.31
-1.91	-1.52	0.39	-2.67	-0.76	-4.09	-2.18	-5.14	-3.23
-1.43	-1.47	-0.04	-2.57	-1.14	-3.94	-2.51	-4.94	-3.51
-1.21	-1.4	-0.19	-2.46	-1.25	-3.77	-2.56	-4.73	-3.52
-0.81	-1.02	-0.21	-1.79	-0.98	-2.74	-1.93	-3.44	-2.63
-0.40	-0.49	-0.09	-0.87	-0.47	-1.33	-0.93	-1.67	-1.27
0.29	0.30	0.01	0.53	0.24	0.80	0.51	1.01	0.72
0.93	0.76	-0.17	1.32	0.39	2.03	1.10	2.55	1.62
1.39	0.96	-0.43	1.69	0.30	2.59	1.20	3.25	1.86
3.79	1.31	-2.48	2.29	-1.50	3.52	-0.27	4.41	0.62

Table 6.3: *Initial time step signal calculated with $k_w = 60.55\ /mmHg$ and varying k_p compared with the required signal.*

A larger value of k_p ($27.11\ /mm\,mmHg$) is better for ensuring that the absolute signal is greater than required over the range of autoregulation. However, over-activation is physiologically costly since muscles require oxygen for activation. The linear portion of the desired signal curve is from rows 5 to 10 of Table 6.3, corresponding to pressure fractions of $0.63 : 1.2$, for this range $k_p = 10.31\ /mm\,mmHg$ is sufficient to ensure that the absolute signal is greater than required.

With $k_p \geq 10.31\ /mm\,mmHg$, the steady state signal error must be minimised. Instead of the absolute signal error, the fractional error ($S_{\text{calc}}/S_{\text{req}} - 1$) can be used to normalise.Signal errors for varying k_p are calculated and the fractional overall and linear-range error are given in Table 6.4.

There is therefore a compromise between the initial activation and steady-state solution. $k_p = 10.31\ /mm\,mmHg$ is a good compromise on the steady state error

k_p $(/mm\,mmHg)$	$k_p = 10.31$	$k_p = 20$	$k_p = 27.11$
Overall			
RMSE	0.3787	0.4011	0.4241
Linear			
RMSE	0.2449	0.3149	0.3719

Table 6.4: *Steady state fraction error for differing values of k_p with $k_w = 60.55$ $mm/mmHg$.*

and on the initial state signal but $k_p = 20$ $/mm\,mmHg$ is worth considering for the better initial state signal.

With varying values of k_p and $k_w = 60.55$ $/mmHg$, the resulting flow ratio error at steady state (after 60 seconds of simulation) are given in Table 6.5.

k_p $(/mm\,mmHg)$	k_w $(/mmHg)$	RMSE (overall)	RMSE (linear)
2.5	60.55	0.3952	0.0581
10.31	60.55	0.3363	0.0572
20	60.55	0.3305	0.0636
27.11	60.55	0.3291	0.0649

Table 6.5: *Root mean squared error of flow as a fraction of basal state following 60 second simulations with varying k_p.*

A value of $k_p = 10.31$ $/mm\,mmHg$ results in the lowest linear flow error. It has a higher overall error though since autoregulation over the entire range requires a higher value for k_p. Therefore, the value $k_p = 10.31$ $/mm\,mmHg$ is high enough that the initial signal saturates, and together with $k_w = 60.55$ $/mmHg$, results in the best autoregulation since the steady state depends on k_w, and a low value of k_p.

Section 6:3 Active Autoregulation Curve

The results obtained for values of $k_p = 10.31$ $/mm\,mmHg$ and $k_w = 60.55$ $/mmHg$ are shown in Figures 6.6, 6.7 and 6.8 (with results given in Table B.3).

The gradient of the autoregulation curve between 0.6 and 1.36 ΔP_0 is approximately linear at 0.3553. The 'corner' of flow regulation around $\Delta P_{tot}/\Delta P_{tot,0} = 0.6$ does not correspond to the corner of diameter regulation. This is the steepest part of the activation curve where the diameter is reaching a maximum value. As found experimentally by Hayashi [96], the diameter does not change below a certain

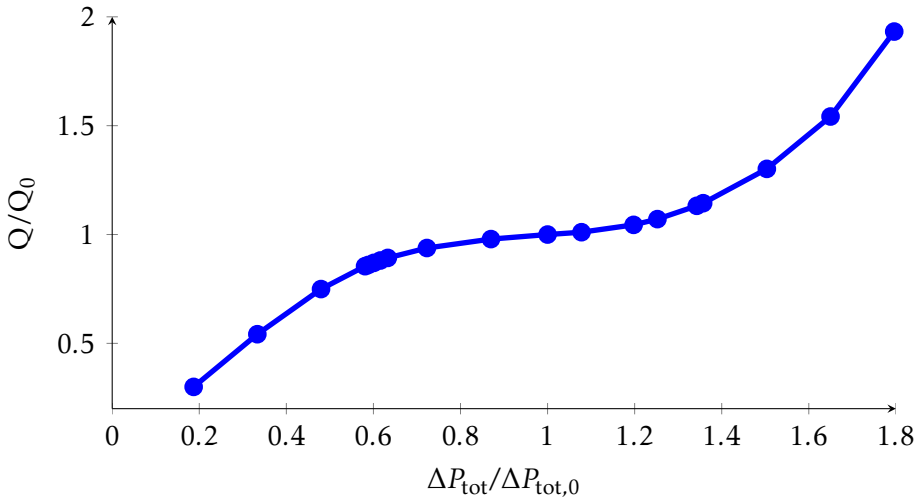

Figure 6.6: *Autoregulation curve with weighting $k_p = 10.31$ /mm mmHg and $k_w = 60.55$ /mmHg.*

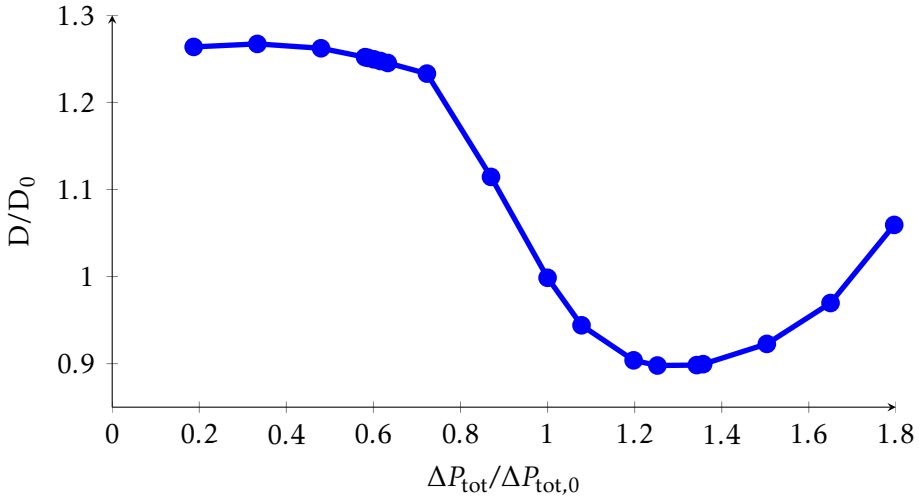

Figure 6.7: *Diameter ratio curve with weighting $k_p = 10.31$ /mm mmHg and $k_w = 60.55$ /mmHg.*

pressure. At +20% ΔP_0, the desired activation is 0.85 and diameter $0.92D_0$. The resulting diameter ratio is 0.90 and activation 0.86 and so the signal is slightly too high, since the weightings k_p and k_w ensure a high signal over the autoregulation pressure range. For pressure drops, though, the activation is not high enough as a result of the compromise for the weighting of k_p and k_w.

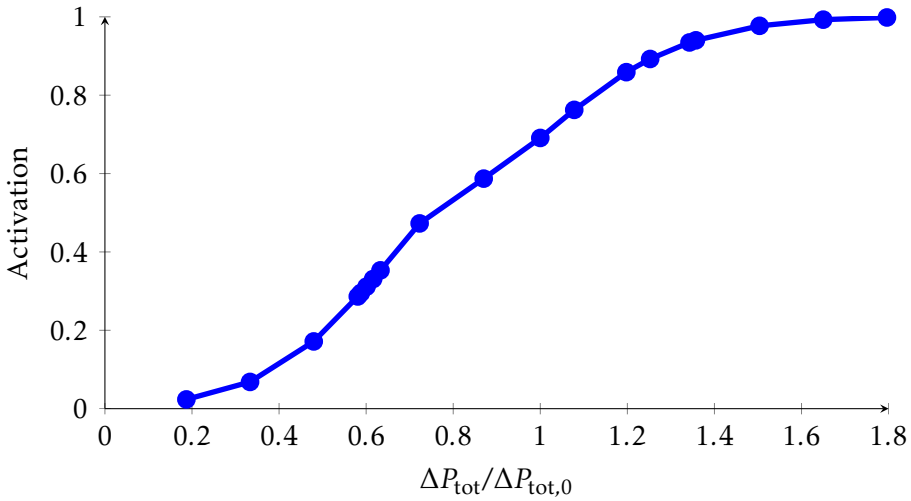

Figure 6.8: *Activation curve with weighting* $k_p = 10.31\ /mm\,mmHg$ *and* $k_w = 60.55\ /mmHg$.

6.3.1 Dynamic Results

For ±20% pressure change, the dynamics of activation and the resulting diameter and flow ratios can be calculated. The speed of the myogenic response is set by τ_d and the steady state results are not affected by this value. A value of $\tau_d = 6\ s$ is chosen to match the dynamics described by Panerai [188].

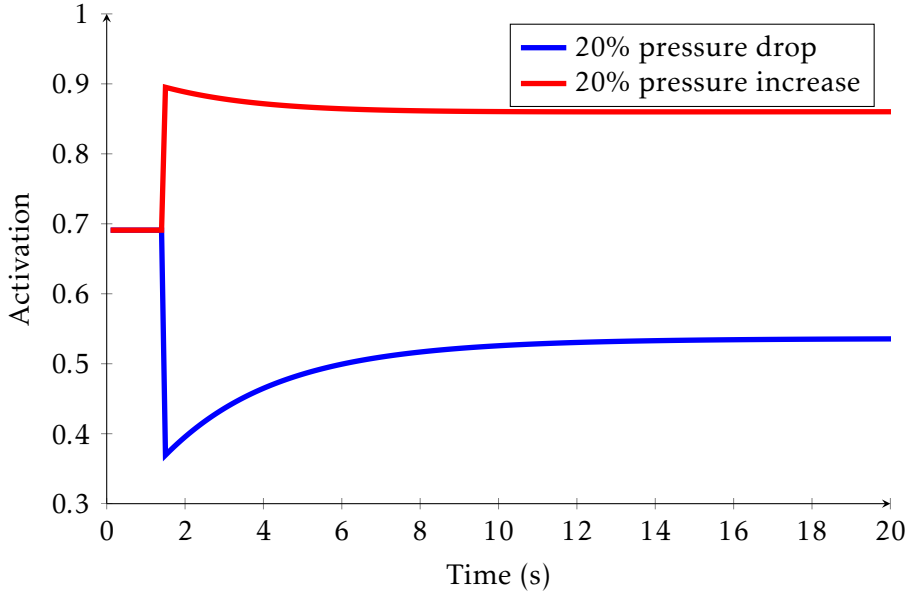

Figure 6.9: *Activation dynamics over a 60 second simulation following a* ±20% *driving pressure increase.*

The activation (Figure 6.9) initially saturates, with a pressure increase having a smaller step change than a pressure decrease. The steady state activation following a pressure drop is equal to 0.54. Following a pressure increase, the steady state activation is 0.86.

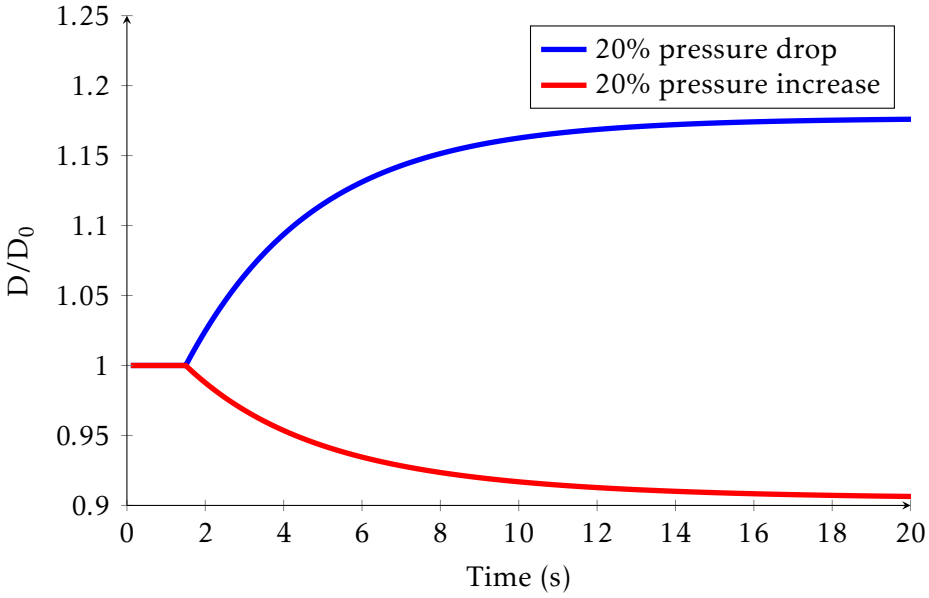

Figure 6.10: *Diameter over a 60 second simulation following a ±20% driving pressure increase.*

The diameter does not have the same step change and the dynamics are delayed compared with the activation taking longer to reach steady state (see Figure 6.10). The dilated diameter ratio following a 20 % pressure decrease is 1.18 and the constricted ratio 0.90. Therefore, the diameter response is non-symmetrical with a larger dilation required for autoregulation than constriction.

The resulting flow dynamics (Figure 6.11) are a large initial step change followed by a fast return towards the basal flow. The flow ratio initially matches the pressure change (±20 %) but, following a pressure decreases, reaches 0.96 and, in response to a pressure increase, reaches 1.05. The flow ratio is therefore approximately symmetrical for the same increase and decrease in pressure.

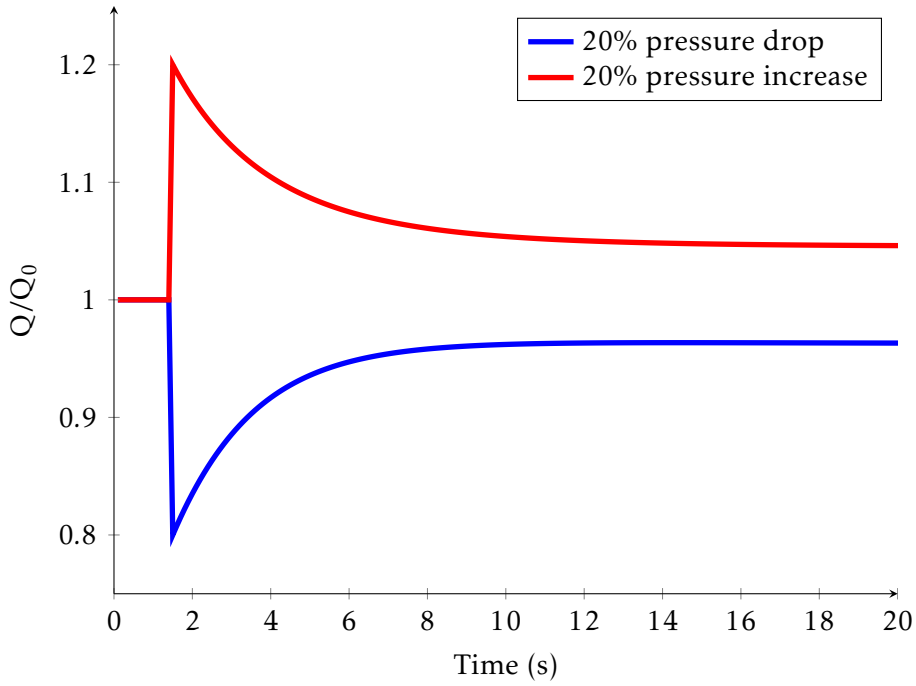

Figure 6.11: *Flow over a 60 second simulation following a ±20% driving pressure increase.*

Summary

In this chapter, two contributors to the myogenic response are identified, and the weighting of them in the overall signal determined. These are calculated from the desired signal, solved from the condition of maintained flow. Simulations in the network show good autoregulation in the ±40% driving pressure range. There are other signal components described in the literature which influence metabolic control. These are explored in the next chapter.

CHAPTER 7

The Metabolic Response

In chapter 7, the metabolic response is investigated, first under suppressed flow conditions and then with an added conducted response. Input signals related to oxygen availability and demand are proposed to add to those calculated in chapter 6 and their weights calculated. The time constants for diameter and oxygen are varied and the effect on the magnitude and dynamics of the overall response described.

Section 7:1 Control-State Demand

At steady state, the rate of flux of oxygen out of the vessel, J_{O_2}, (Equation 2.21) is assumed to be equal to the sum of the demands of the tissue and components of the vessel wall (the consumption). For the node concentrations presented in Table 4.15, basal demand M_0 ($\mu M/s$) is calculated as:

$$M_0 = J_{O_2} = (C_{in} - C_{out})Q, \tag{7.1}$$

where C_{in} and C_{out} are the vessel inlet and outlet oxygen concentration and Q is the flow. Tissue demand across generations is therefore not uniform (see Table 7.1 where the molar demand is converted to volume by Equation 2.16).

Generation	Molar Demand M_0 ($\times 10^{-3} \mu M/s$)	Volume Demand M_0 ($\times 10^{-4}\ ml O_2/s$)
A1	27.14	6.08
A2	14.22	3.18
A3	5.51	1.23
A4	2.09	0.47
A5	0.78	0.18
A6	0.54	0.12
C	1.60	0.36
V6	0.49	0.11
V5	0.40	0.90
V4	0.91	0.20
V3	1.94	0.43
V2	3.73	0.84
V1	6.19	1.39

Table 7.1: *The basal tissue demand in generations calculated with Equation 7.1.*

The values of consumption for the larger vessels are comparable in magnitude to the tissue consumption values collected in Table 2.6, though smaller vessels have less demand, since they have less tissue volume.

Section 7:2 Tissue Dynamics

If demand increases, the tissue oxygen concentration initially reduces which, in turn, increases the extracted oxygen due to the increased oxygen concentration gradient across the vessel wall. The change in tissue concentration is due to the imbalance between the oxygen extracted J_{O_2} and demand M:

$$V_T \frac{\partial C_T}{\partial t} = J_{O_2} - M, \tag{7.2}$$

where V_T is the tissue compartment volume and C_T is the tissue oxygen concentration.

V_T can be redefined in terms of basal flow Q_0 as $\tau_O \times Q_0$, so that the oxygen time-constant τ_O is:

$$\tau_O = \frac{V_T}{Q_0}. \tag{7.3}$$

Using the gradient $(\Delta C_T/\Delta t)$ of tissue oxygen concentration from the data, τ_O can be calculated using Equation 7.4:

$$\tau_O = \frac{\left(J_{O_2} - M\right)}{Q_0} \frac{\Delta t}{\Delta C_T}. \tag{7.4}$$

The dynamics of a 12.5% demand increase in a non-regulating arteriole are reproduced from experiments by Vazquez et al. [264] in Figure 2.12 where $dP_T/dt = -0.5\ mmHg/s$ (−1.52%) or $dC_t/dt = -0.6757\ \mu M/mm^3/s$. In the initial period before flow change (where the vessel can be approximated as non-regulating), Ances et al. [4] found $dP_T/dt = -0.42 \pm 0.24\ mmHg/s$ (−1.82%) or $-0.5672\ \mu M/mm^3 s$ implying a similar demand to that investigated by Vazquez.

The flux out of the vessel changes with tissue concentration so that, by equations 2.21, 4.2 and 7.1:

$$\tau_O = \frac{\left(-Q_0(e^{-\frac{D_w \pi DL}{wQ}} - 1)(C_{in} - C_T) - M\right)}{Q_0} \frac{\Delta t}{\Delta C_T}. \tag{7.5}$$

Using the percentage rate of tissue concentration change calculated from the Vazquez result (−1.52%), the time constant is calculated separately for each generation of vessel and the results are given in Table 7.2. The tissue radius is calculated from the tissue volume V_T, vessel radius R_V and vessel length L:

$$R_T = \sqrt{\left(\frac{V_T}{\pi L} + R_V^2\right)}. \tag{7.6}$$

Generation	Time Constant $\tau_o(s)$	Tissue Radius $R_T(\mu m)$
A1	0.134	18.05
A2	0.118	14.24
A3	0.077	11.07
A4	0.046	8.49
A5	0.299	15.75
A6	0.580	15.74
C	3.196	28.76
V6	0.028	6.05
V5	0.017	7.74
V4	0.007	9.10
V3	0.014	11.18
V2	0.020	13.61
V1	0.020	16.54

Table 7.2: *Oxygen time constant calculated from the rate of percentage change of tissue concentration in experiments.*

For capillaries then, the resulting time constant is 3.20 s so that $R_T = 28.76\mu m$ (smaller than the assumed $40\mu m$ but close to the value of $32\mu m$ set by Mintun [163]). The capillary tissue radius is much larger than for other vessels where the tissue oxygen gradient is calculated over the vessel wall. The size of the tissue compartment in other vessels is variable, increasing with vessel diameter in the venules but with a larger radius in the pre-capillary arterioles.

Section 7:3 Steady State Calculations

At steady state, Equation 7.2 becomes:

$$C_{in} - C_{out} = \frac{M}{Q}. \tag{7.7}$$

For $M = 1.125M_0$ (the Vazquez demand increase [264]) and $Q = 1.488Q_0$ (the flow increase found by Vazquez), $C_{in} - C_{out} = 0.756\Delta C_{v,0}$ by Equation 7.7. For the capillaries, with no dilation, Equation 4.2 is rearranged to include this $0.756\Delta C_v$ and the flow increase so that:

$$C_{in} - C_T = \frac{0.756\Delta C_{v,0}}{1 - e^{-\frac{D_w \pi D_0 L_0}{w_0 1.488 Q_0}}}. \tag{7.8}$$

Using Equation 7.8, $C_{in} - C_T$ is calculated to be 46.98 $\mu M/mm^3$. The basal value of $C_{in,0} - C_{T,0} = 44.14$ $\mu M/mm^3$. There are three options for how this increase happens: an increase in both tissue and inlet concentration, or a separate inlet or tissue concentration increase. For the first option, the gradient implies a 6 % increase in tissue concentration and inlet concentration which is slightly higher than the 2% found at steady state by Ances, for a steady-state flow ratio of 1.1. In order to achieve the 27.7 % increase in tissue concentration found by Vazquez (with no inlet increase), the demand must increase by 34.96 %, or flow decrease by 44 % (solved by rearranging Equation 7.8). A further option is that the oxygen concentration at the inlet of the vessel increases: a value of $C_{in} = 83.87$ $\mu M/mm^3$ ($\Delta C_v = 1.125\Delta C_{v,0}$) would reproduce the experimental results .

7.3.1 Steady-state suppressed flow

Under suppressed flow conditions where $Q = Q_0$ and $\Delta C_v = 1.125\Delta C_{v,0}$; $C_{in} - C_T = 49.68$ $\mu M/mm^3$ which requires a 17.7 % decrease in tissue concentration (with no other inputs the inlet concentration is assumed to stay the same), higher than the value of 11.7 % found by Vazquez et al. [264]. With the proposed time

constant for the capillaries, the time taken for flux to equal the new demand ($J_{O_2} = 1.125M_0$) is 56 s and an 11.7% decrease in tissue concentration takes 10 s.

For other generations, the steady state tissue concentration reduction is calculated and given in Table 7.3.

Generation	Tissue Concentration Reduction $\frac{C_T - C_{T,0}}{C_{T0}}$ (%)
A1	2.5
A2	2.3
A3	2.1
A4	1.9
A5	2.3
A6	2.8
C	17.7

Table 7.3: *The steady state tissue concentration reduction in vessels following a demand increase of* 12.5 % *and assuming suppressed flow.*

These decreases are small, apart from in the capillary vessels. In order to achieve tissue concentration decreases of 11.7 %, the required demand percentage increase is calculated and given in Table 7.4.

Generation	Demand Increase $\frac{M}{M_0}$ (%)
A1	58.6
A2	64.3
A3	70.8
A4	77.3
A5	62.4
A6	52.1
C	8.2

Table 7.4: *The demand increase required for a* 11.7 % *tissue concentration decrease at steady state.*

It is assumed that Vazquez calculated the tissue concentration reduction to steady-state, though this is unclear. However, for the Lucas network, the high tissue concentration at basal state allows for adaption so that large demand increases are required for arteriolar tissue concentration reduction. It is possible that the ex-

periment of Vazquez did not reach steady state, so that although the tissue concentration rate reduction is reproduced here, the time-constant must actually be recalculated using the time taken for the vessel to reach steady-state and the steady state concentration (in order to use Equation 7.4, the flux must equal the demand).

Section 7:4 Metabolic Signals

The proposed signals described in the literature review are a conducted signal related to oxygen demand, and a local signal determined by the tissue concentration. The myogenic response described in chapter 6 means that although local flow increases, the overall network flow remains tightly controlled. The extra flow is achieved by upstream pathway dilation, and constriction of surrounding vessels. This extra flow also achieves the inlet node concentration increase necessary to replicate the experimental results, as described on page 183.

7.4.1 Conducted Signal

If it is assumed that the metabolism matches the demand via the redundancy in the tissue compartment, it is possible that any chemical released as a result of the metabolism could form the basis of a metabolic signal. Carbon dioxide is an especially potent vasodilator and also a product of metabolism. Therefore, increased demand would lead to an increase of carbon dioxide which could potentially be propagated upstream (the mechanics of how are less important here). A signal S_m is proposed here which is proportional (with weight k_s) to the change in demand:

$$S_m = k_s(M - M_0). \tag{7.9}$$

S_m is conducted upstream from the capillaries, integrated along vessels and summed at converging nodes. The signal is also assumed to decay exponentially along vessel length so that at distance z from the end of the vessel:

$$S_m(z) = S_m e^{-z/L}. \tag{7.10}$$

This follows the same decay and accumulation assumption as used by Arciero, and by Pries and Secomb (described in section 2.8).

7.4.2 Tissue Concentration Signal

The local tissue concentration could also be a direct local signal for dilation or constriction. Extra oxygen availability would cause an increase in the tissue concentration by Equation 7.2 and a proportional signal could counteract this increase via vessel constriction. The proposed signal S_o is weighted by a factor k_o:

$$S_o = k_o(C_T - C_{T,0}). \tag{7.11}$$

7.4.3 Overall Signal

The overall signal is therefore:

$$S = k_p(T_h - T_{h,0}) + k_w(\tau_w - \tau_{w,0}) + k_s(S_m - S_{m,0}) + k_o(C_T - C_{T,0}), \tag{7.12}$$

where k_p and k_w have been initially calculated as 10.31 $/mmHg\,mm$ and 60.55 $/mmHg$ in subsection 6.2.5.

Section 7:5 Tissue signal weight

When the perfusing pressure changes, there is no effect on the conducted signal but the resulting changes in flow and diameter affect the tissue concentration. Referring to subsection 6.2.5, k_o is calculated by finding ΔC_T at steady state after running a simulation at fixed inlet pressure, and (known) activation required for pressure autoregulation (calculated in subsection 6.2.3). Table 7.5 gives the required total activation signal for autoregulation (calculated with Equation 6.9)

along with the hoop and shear stress and tissue concentration found in vessel $A1$ at steady state.

Signal S_{stst}	Flow Q $(10^{-3} mm^3/s)$	Hoop Stress T_h $(10^{-2}\ mmHg\, mm)$	Shear Stress τ_w $(10^{-2} mmHg)$	Tissue Concentration C_T $(\mu M/mm^3)$
-5.40	3.70	65.33	2.40	95.41
-3.00	3.70	65.02	2.46	95.24
-1.91	3.70	64.45	2.57	94.91
-1.43	3.70	64.38	2.65	94.68
-1.21	3.70	64.85	2.69	94.58
-0.81	3.70	63.41	3.10	93.45
-0.40	3.70	65.21	3.95	91.32
0	3.70	65.09	4.79	89.39
0.29	3.70	65.14	5.36	88.27
0.93	3.70	65.45	6.23	86.65
1.39	3.70	65.67	6.63	85.94
3.79	3.70	66.09	7.28	84.81

Table 7.5: *Table giving parameters to solve Equation 7.12 to find signal weights at steady state.*

Table 7.6 shows the changes in tissue concentration, hoop and shear stress where basal state tissue concentration is 89.39 $\mu M/mm^3$, hoop stress 65.09 $mm\, mmHg$ and shear stress 4.79 $mmHg$. The tissue concentration change is large compared with the hoop and shear stress.

Total Signal S	Tissue ΔC_T $(\mu M/mm^3)$	Hoop $100\Delta T_h$ $(mmHg\, mm)$	Shear $100\Delta\tau_w$ $(mmHg)$
-5.40	6.02	-6.43	0.23
-3.00	5.85	-0.87	-0.08
-1.91	5.52	6.04	-0.65
-1.43	5.29	7.20	-0.72
-1.21	5.13	2.54	-0.25
-0.81	4.06	-1.68	-1.74
-0.40	1.93	-1.13	0.12
0.29	-0.69	-0.57	0.07
0.93	-2.74	-3.65	0.38
1.39	-3.45	-5.70	0.61
3.79	-4.58	-8.03	1.03

Table 7.6: *The signals due to hoop stress, shear stress and tissue concentration calculated at steady state.*

With $k_w = 60.55\ /mm\, mmHg$ and $k_p = 10.31\ /mmHg$, k_o is solved by minimis-

ing the steady-state signal error (Equation 7.13). The the root mean squared error between the required activation signal, and the signal calculated from the parameters and weights is minimised using a trust-region dogleg algorithm (see subsubsection 5.2.1.1).

$$k_o = \frac{S_{stst} - \left(k_w(\tau_w - \tau_{w,0}) + k_p(T_h - T_{h,0})\right)}{(C_T - C_{T,0})}, \tag{7.13}$$

giving $k_o = 0.0216\ mm^3/\mu M$ for the linear portion (see Figure 6.5). k_o therefore has to be small compared with k_p and k_w in order to maintain myogenic autoregulation.

With $k_o = 0.0216$	Without k_o
-4.11	-3.98
-1.71	-1.58
-0.61	-0.49
-0.17	-0.05
-0.02	0.09
0.30	0.39
0.06	0.10
-0.02	-0.04
0.08	0.02
0.30	0.22
2.28	2.18

Table 7.7: *Error in signal calculated with k_o, k_p and k_w at steady state following autoregulation.*

Table 7.7 gives the error between the required and calculated activation signals and shows that a small value of k_o slightly improves the autoregulation steady state signal for small pressure changes but reduces the effectiveness of autoregulation for larger pressure changes. In practice, the overall effect is very small (see Figure 7.1) but autoregulation is reduced at lower pressure.

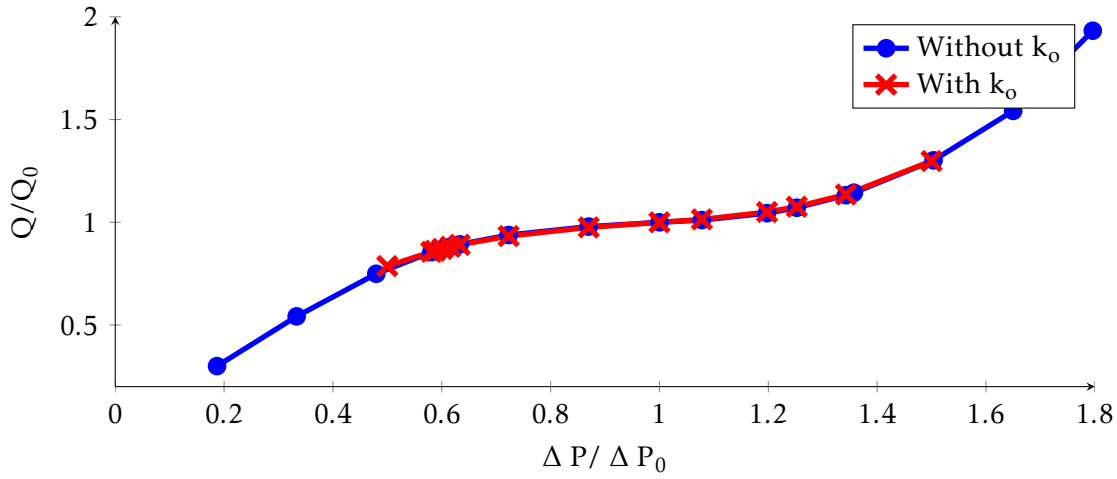

Figure 7.1: *The autoregulation curve with and without k_o.*

Section 7:6 Dynamic Response

Under non-suppressed flow with a 12.5% demand increase, Vazquez found a 27.7% increase in tissue concentration (from 32.8 $mmHg$) and a 48.8% increase in flow at peak. Ances found a larger peak flow increase of 55.8% with a smaller, 20.7% increase in tissue concentration (from 23.1 $mmHg$) after an initial decrease in tissue concentration (to 98.2 %). Vazquez' tissue concentration is high compared with the tissue concentration of the Lucas network (31.11 $\mu M/mm^3$ or 23.04 $mmHg$), but this value is very similar to that of Ances. Therefore, the results of Ances are preferred as a reference.

7.6.1 Weighting of conducted signal

The magnitude of conducted signal in the capillaries at basal state is 0.1529 and a change of 12.5% demand in the tissue surrounding the vessel results in an absolute signal change of 0.0191. Since signals over the range of activation are between −5.4 and 3.79, initially k_s is set to −100 $s/\mu M$.

Following a demand increase of 12.5% in a capillary (simulated with vessel 74, between nodes 43 and 75), the resulting maximum flow ratio is 1.33 with a maximum tissue ratio of 1.14. The magnitude of k_s is increased and the maximum flow

ratio, and maximum and minimum tissue ratios reached are recorded in Table 7.8.

k_s	flow ratio $\frac{\Delta Q}{Q_0}$ (%)	min tissue $\frac{\Delta C_T}{C_{T,0}}$ (%)	max tissue $\frac{\Delta C_T}{C_{T,0}}$ (%)
-100	32.9	98.3	13.9
-135	49.3	98.5	23.4
-145	55.6	98.5	26.3
-145.5	56.0	98.6	26.6
-146	56.4	98.6	26.9
-146.5	56.8	98.6	27.4
-147	57.2	98.6	28.1
-150	59.8	98.6	29.7

Table 7.8: *The diameter and flow ratio reached at steady state in vessel 74 after a 12.5% demand increase with* $k_p = 10.31\ /mm\,mmHg$, $k_w = 60.55\ /mmHg$ *and* $k_o = 0.0216\ mm^3/\mu M$.

$k_s = 135$ gives a value close the flow ratio found by Vazquez, with a 23.4% increase in tissue concentration. $k_s = 145.5$ gives the larger flow increase found by Ances and $k_s = 147$ the tissue increase found by Vazquez. Although the Ances basal tissue concentration is approximately the same as the Lucas capillary concentration, $k_s = 147$ is chosen in order to establish the maximum tissue concentration response.

7.6.2 Time to steady-state

With τ_o calculated from suppressed-flow results and $k_s = 147$, the dynamic response is slow. It takes 38.5 seconds for the tissue concentration to reach maximum (see Figure 7.2), this is much longer than 5 seconds found by Ances or 6.8 seconds found by Vazquez. The flow response (to maximum) with $\tau_d = 6\ s$ takes 17.1 s compared with 10.8 found by Vazquez and 4 s found by Ances. There is also a 21.4 s delay between the flow and tissue response (compared with a 1.0 s delay found by Ances) due to the difference between the diameter and oxygen time constants.

Vazquez found that it took 3.2 s for the flow to reach +48.8 % of the basal value and 33 s for the tissue concentration to reach +27.7 % of the basal value. Ances

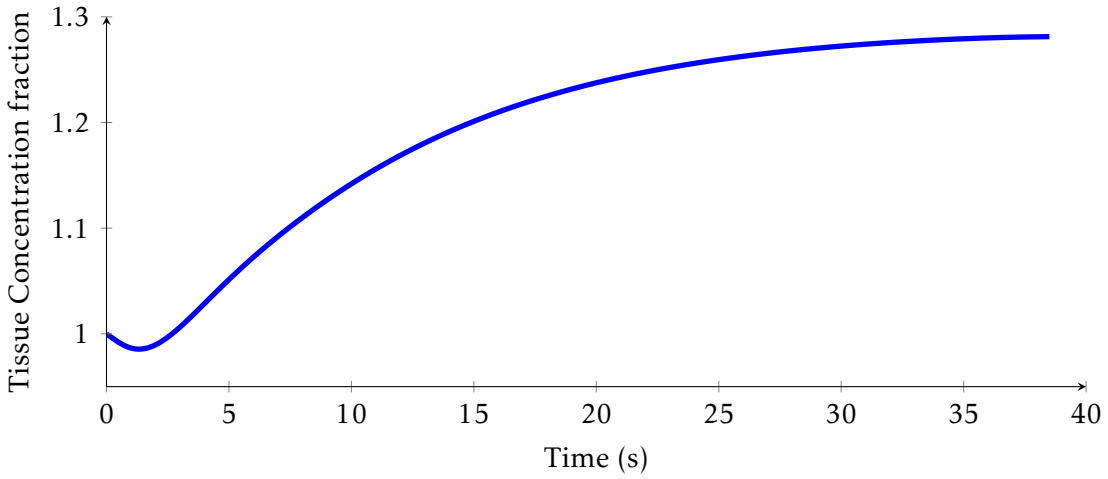

Figure 7.2: *The resulting dynamic flow with τ_o = 3.20 s in the capillary.*

found that it took 15.7 *s* for the tissue to reach +20.7 % of the basal concentration and 9 *s* for the flow to reach +55.8 % of the basal flow. To replicate the results of Ances, the maximum tissue concentration need not be as high, and the time to reach it will therefore be reduced.

The time taken to reach steady-state is set by the interaction between the diameter time constant τ_d, and the oxygen concentration time constant τ_o. If oxygen time constants are reduced in all vessels by the same factor, the second set of results in Table 7.9 are found. The top half is for a change only in the capillary vessel time constants. Table 7.10 then gives the time taken to replicate both the Ances and Vazquez tissue and flow results with varying oxygen time constant.

Reducing the time constant in all vessels affects the speed and magnitude of the flow response whereas reducing only the capillary constant decreases the time taken for the peak tissue response without affecting flow. With the capillary oxygen time constant at 0.64 (R_T = 13.4μm), the time taken to reach 20.7 % is 4.9 seconds and the flow takes 9.0 *s* to reach +55.8 %. The flow response time can be reduced by decreasing τ_d. However, this also affects the speed of the myogenic response. Tables 7.11 and 7.12 give the result of changing the myogenic time constant on the maximum ratios, and on the time taken to replicate the experimental

Time Constant τ_o (s)	max flow ratio $\frac{\Delta Q}{Q_0}$ (%)	time (s)	min tissue ratio $\frac{\Delta C_T}{C_{T,0}}$ (%)	time (s)	max tissue ratio $\frac{\Delta C_T}{C_{T,0}}$ (%)	time (s)
Capillary Time Constant						
3.20 ($\tau_{o,0}$)	57.2	17.1	98.6	1.3	28.1	38.5
1.60 ($0.5\tau_{o,0}$)	57.2	17.1	97.3	1.3	29.1	30.7
0.64 ($0.2\tau_{o,0}$)	57.2	17.1	94.4	1.1	29.3	20.7
0.48 ($0.15\tau_{o,0}$)	57.2	17.1	93.1	1.1	29.3	19.4
All Time Constants						
$0.5\tau_{o,0}$	57.2	16.5	97.5	1.1	29.0	29.2
$0.2\tau_{o,0}$	53.3	12.4	95.0	0.9	40.2	15.8

Table 7.9: *The effect of the oxygen time constant on the maximum tissue ratio, and the time taken to reach maximum.*

	Tissue Ratio		Flow Ratio	
Time Constant τ_o (s)	time to +20.7 % (s)	time to +27.7 % (s)	time to +55.8 % (s)	time to +48.8 % (s)
Capillary Time Constant				
3.20 ($\tau_{o,0}$)	15.7	33.0	9.0	3.2
1.60 ($0.5\tau_{o,0}$)	9.6	18.0	9.0	3.2
0.64 ($0.2\tau_{o,0}$)	5.6	10.2	9.0	3.2
0.48 ($0.15\tau_{o,0}$)	4.9	9.0	9.0	3.2
All Time Constants				
$0.5\tau_{o,0}$	9.4	17.8	9.0	3.3
$0.2\tau_{o,0}$	4.1	5.1	-	3.6
Data	Ances (5 s)	Vazquez (9.8 s)	Ances (4 s)	Vazquez (6.8 s)

Table 7.10: *The effect of the tissue time constant on the rate of change of flow and tissue concentration.*

results. Reducing τ_d to 3 s moves the simulation towards the Ances result.

Time Constant τ_d (s)	max flow ratio $\frac{\Delta Q}{Q_0}$ (%)	time (s)	min tissue ratio $\frac{\Delta C_T}{C_{T,0}}$ (%)	time (s)	max tissue ratio $\frac{\Delta C_T}{C_{T,0}}$ (%)	time (s)
4	58.1	15.1	94.9	1.0	29.8	38.5
3	58.2	8.2	95.3	0.9	29.9	38.5

Table 7.11: *The effect of the diameter time constant τ_d on the magnitude and speed of the maximum flow and tissue response.*

	Tissue Ratio		Flow Ratio	
Time Constant τ_d (s)	time to +20.7 % (s)	time to +27.7 % (s)	time to +55.8 % (s)	time to +48.8 % (s)
4	4.9	8.5	5.8	2.1
3	4.6	7.7	4.2	1.6
Data	Ances (5 s)	Vazquez (9.8 s)	Ances (4 s)	Vazquez (6.8 s)

Table 7.12: *The effect of the diameter time constant τ_d on the rate of the tissue and flow response.*

Section 7:7 Results

7.7.1 Results: Capillary Flow and Tissue Concentration

With $\tau_d = 3$ s, there is an initial flow peak of +55.8 % before a second slower increase to +58.2 % (see Figure 7.3). The capillaries do not display the reduction in flow and tissue concentration after the maximum has been reached because the demand signal being conducted to the feeding vessels is still large, and there is no local diameter change in the capillaries. Figure 7.4 shows the initial reduction in capillary tissue concentration with a slower time to reach maximum than for flow.

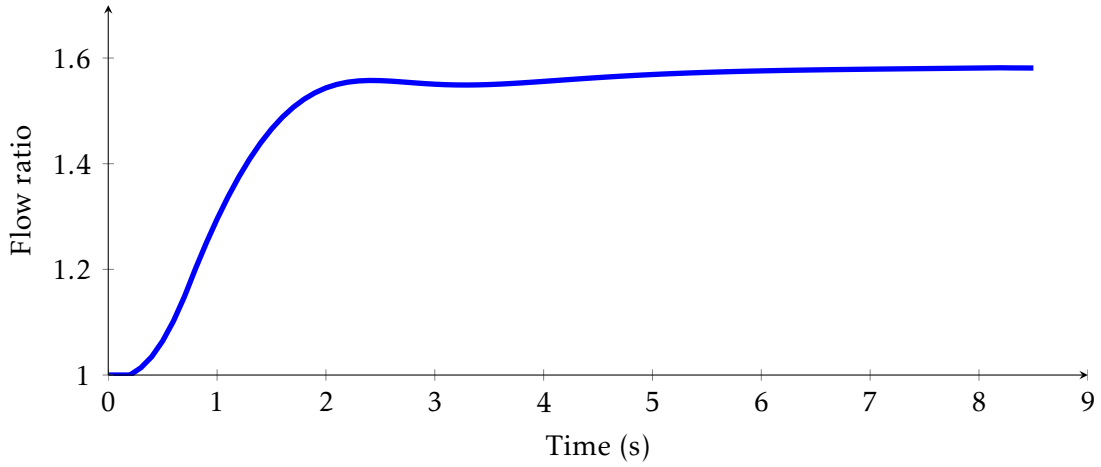

Figure 7.3: *The dynamics of flow in the capillary following a 12.5 % demand increase.*

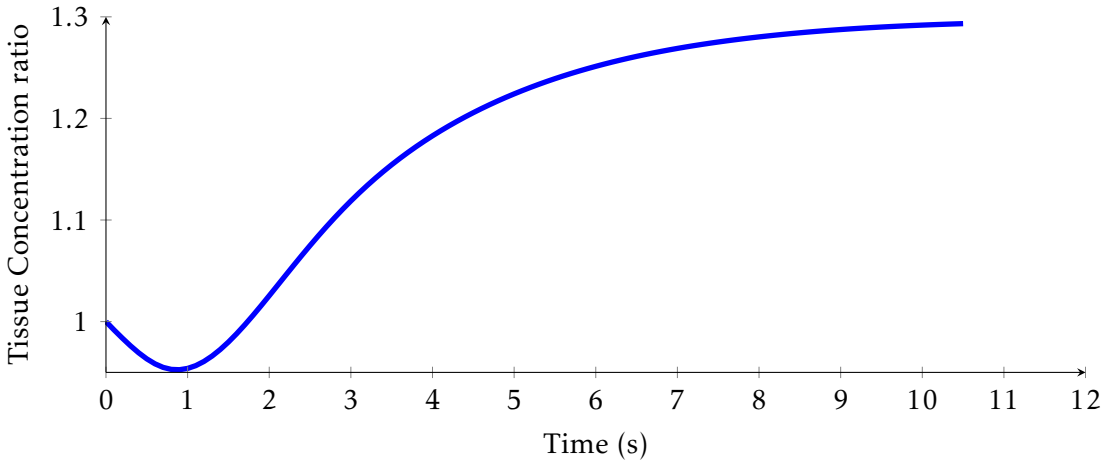

Figure 7.4: *The dynamics of the tissue concentration in the capillary following a* 12.5 % *demand increase.*

7.7.2 Results: Network Diameter Response

For vessel 74 (nodes 43 to 75), the vessel pathway is shown in Figure 7.5. Vessels which should constrict are shaded with a thick black dashed line, dilating vessels with a thick red line and surrounding vessels are thin blue dotted lines.

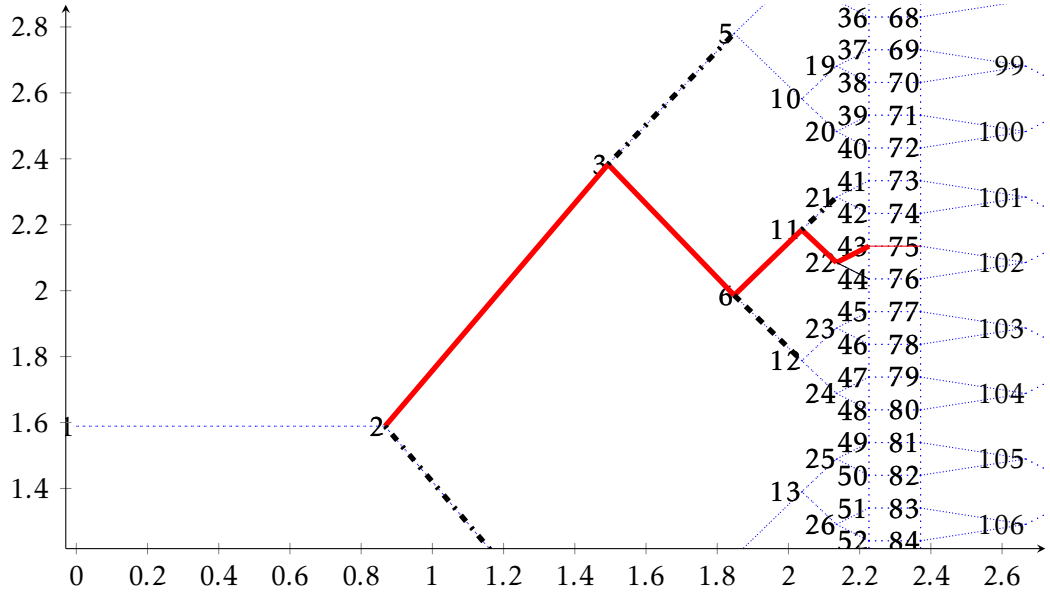

Figure 7.5: *The vessel pathway which feeds vessel* 74 *(between nodes* 43 *and* 75*).*

Following a 10 *s* 12.5% demand increase in the capillary, the conditions in the network at 4.2 *s* (when the flow in vessel 74 is at +55.8 %) are recorded and given

in Table 7.13.

Vessel	Response	Start node	End node	Flow Ratio $\frac{Q}{Q_0}$	Tissue Ratio $\frac{C_T}{C_{T,0}}$	Diameter Ratio $\frac{D}{D_0}$
2	Dilate	2	3	1.25	1.04	1.14
3	Constrict	2	4	1.03	1.00	0.98
4	Constrict	3	5	1.10	1.01	0.97
5	Dilate	3	6	1.41	1.05	1.17
11	Constrict	6	12	1.22	1.02	0.97
20	Constrict	11	21	1.41	1.05	0.97
21	Dilate	11	22	1.78	1.10	1.21
42	Dilate	22	43	1.84	1.14	1.01
43	Constrict	22	44	1.71	1.12	0.98
74	-	43	75	1.56	1.19	1.00

Table 7.13: *The flow, tissue concentration and diameter ratio in vessels in the pathway of vessel* 74.

The tissue ratio does not decrease in vessels outside the pathway due to the local tissue signal which prevents further contraction of these vessels. The dynamics of the diameter response in these vessels is given in Figure 7.6. Vessels in the same generation have been given the same colour, vessels which should constrict are dashed and those which should dilate are solid.

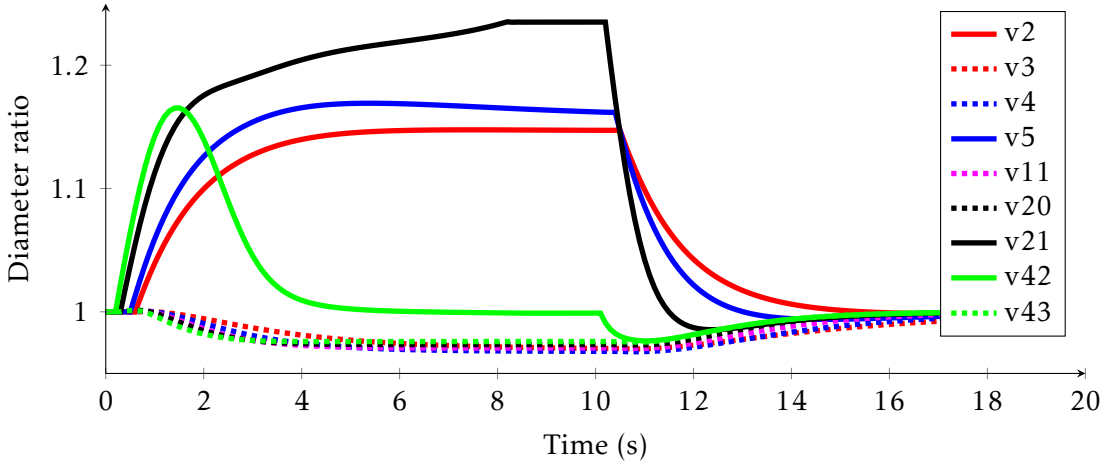

Figure 7.6: *The dynamic diameter response of vessels in the pathway which feeds vessel* 74.

Due to the increased tissue concentration ratio in vessel 42 (immediately feeding the capillary) the diameter decreases again. Vessel 42 also has the largest

undershoot post demand offset. This pre-capillary arteriole is subject to a large change in flow ratio and tissue concentration (other than the capillaries) and so has the biggest diameter response (since the capillaries do not regulate). Similarly, vessel 43 adjacent to 42 has the largest initial contraction. Vessel 21 saturates since the conducted signal overrides the smaller increase in flow and tissue concentration. The vessel response is delayed through the network as the signal is conducted and this is the reason for the secondary response seen in vessel 74 in Figure 7.3 earlier.

7.7.3 Results: Collateral Circulation

Vessel 105 is between nodes 42 and 43 and is the collateral capillary serving vessel 74. Vessel 106 is between nodes 43 and 44 and is the collateral draining capillary for vessel 74. Initially nodes 42, 43 and 44 have the same pressure and so the flow in these vessels is 0. During the demand increase, the pressure at node 43 increases more than 42 and 44 so that flow is drained, hence the large increase in the feeding vessel. It is desired that the flow in these vessels would feed the capillary, but this requires an increase in pressure in these nodes which is achieved by an increase in flow in the feeding vessels (i.e. the opposite of what is shown in Figure 7.6). Therefore, the collateral capillaries in the Lucas network are part of the response to flow, preventing large increases in shear stress in the capillaries and ensuring sufficient flow to capillary tissue regardless of the feeding vessel.

Summary

The response to increased oxygen demand in the capillary generation has been investigated in this chapter. It is shown that a large flow and tissue response can be achieved with a conducted upstream signal, and a local tissue concentration signal. The tissue signal is shown to have only a small, but beneficial, effect on the myogenic response. The tissue signal prevents a decrease of tissue concentration in the vessels outside of the direct pathway during the metabolic response. The metabolic response depends on the interaction of two time constants, as well as the magnitude of the conducted signal. Here, the experimental result of Ances is modelled, but the process could be followed to replicate an alternative experimental result. The dynamic diameter response in the network enables flow to be directed towards a vessel with increased demand without compromising the demand of these vessels. The collateral circulation does not aid this response, but instead prevents an increased shear stress in the capillary vessels which cannot dilate to accommodate extra flow.

CHAPTER 8

Conclusions and Future Work

The thesis describes the development of an anatomical model of the cerebral vasculature which has accurate geometry, flow and oxygen concentration and is able to autoregulate over a perfusing pressure range of ±40% of the basal level. The dynamics of flow and tissue concentration following a demand increase in a capillary vessel are replicated by a pathway diameter response. This response is governed by an activation factor set by a weighted sum of physiological signals which controls to the proportion of muscle cells activated in the vessel wall. This muscle tone in turn contributes to the total tension in the vessel wall, along with the passive tension due to collagen and elastin fibres. The vessel diameter regulates until equilibrium is reached between the circumferential tension (due to transmural pressure and vessel diameter) and this total wall tension.

Section 8:1 Summary of Results

In chapter 3, the geometry of the basal model was established which gave the vessel resistance necessary for experimentally validated pressure and flow. The method proposed here to calculate vessel length and diameter can be repeated for a network of any number of generations based solely on the experimental capillary diameter and flow velocity. A process is also described by which, using the vessel geometry and an inlet and outlet network pressure, the nodal pressures and flows

can be calculated for all vessels. Capillary flow is extracted here from the experimental results of Zweifach [281] and multiplied by the number of capillaries to get the total network flow. The number of capillaries chosen sets the number of vessel generations in the network since a branching approximation is assumed. The small total network flow ($3.7 \times 10^{-3} mm^3/s$) is therefore a consequence of the size of the capillary generation, flow being calculated from the velocity and cross-sectional area which are validated by the data.

The concentration of oxygen in the vessels and in surrounding tissue was calculated in chapter 4 using Fick's law for oxygen flux. Reference concentrations in tissue and vessels were used to investigate the assumption that wall and tissue radial gradients are different. The assumption made by previous models of uniform radial tissue concentration gradient throughout the network has here been superseded by separate gradients across the wall and radially through tissue. The diffusion coefficient was redefined in terms of wall permeability which was approximated as being proportional to wall volume (and therefore vessel diameter) with different proportionality constants for large and small vessels reflecting the varying proportion of smooth muscle present. In capillaries, however, the vessel wall was approximated as being so thin that it can be lumped with surrounding tissue and so capillaries have a large flux for their size since a large tissue volume is taken into account. The findings related to oxygen exchange show that there must be consumption in the wall which is proportional to wall volume and requires a separate wall permeability rather than diffusion coefficient is very useful in settling debate within the literature and providing new physiological insight.

A basal tissue concentration was then calculated from reference vessel concentration and permeability. These values were used to determine nodal oxygen concentrations in the network using only the overall inlet concentration and the parameters of Fick's law. The resulting values approximate the reference values in-

terpolated from the data, though arteriole concentrations are higher, probably due to the separation into large and small vessels for wall permeability which could be separated further.

A new set of mathematical functions describing the passive and active length-tension relationships were proposed in chapter 5, which are more accurate than those proposed previously. The equations are based on existing exponential functions but split into two phases for high and low strain. The point of transition between phases for passive and active tension was found to be close to the point of maximum active tension. For high strain, passive tension was found to be well approximated by a linear relationship with strain. Active tension was shown to have a set tension for low strain. The resulting active strain-tension curve is non-symmetrical, as found experimentally.

These functions were applied to the new network model by calculating the basal passive and active tension which enable autoregulation of flow over ±50% of the basal pressure gradient. The equations were then non-dimensionalised so that they can be applied to other vessels of any size. The resulting basal activation (proportion of activated muscle cells) is more than half so that the activation over the pressure range is non-symmetrical due to the low-strain active tension. The basal activation and tension can be calculated for any autoregulation limits, or alternatively the potential autoregulation limits calculated from the basal activation by the method proposed here with a resulting shift on the strain axis. For example, for ±50% autoregulation, the basal condition is found to be below the point of maximum active tension. If it is instead assumed that the basal network is at the point of maximum active tension, the autoregulation limit is reduced to ±30% with a large proportion of muscle cells activated at basal conditions. The relationship between length and tension is linked to the autoregulation state of the network in this model and therefore provides new insight onto the extent of activation (and

therefore diameter compensation) possible over a range of pressure.

Simulation of myogenic autoregulation was performed in chapter 6. A sigmoidal activation signal was proposed with components proportional to shear and hoop stress. The weight of these signals was determined by minimising the error with the signal required for conservation of basal flow at varying pressure within the autoregulation range. The necessary signal for autoregulation was found to be linear with pressure for ±40% of the driving pressure gradient with steep changes beyond these limits, this is in agreement with the equation proposed by Feldberg Equation 2.56 [76] which has activation as a linear function of pressure between two limits and is based on experimental results. The dynamic analysis of autoregulation implied that the signal due to hoop stress sets the initial activation and the steady-state activation is maintained by the shear stress signal. The result of autoregulation occurring is that hoop tension almost returns to its basal value and so this shear signal is necessary. A potential physiological mechanism for shear-stress maintained activation is that the endothelial layer releases chemicals in response to shear which affect muscle tone.

The combination of assumptions made in chapter 5 and the compromise between low and high pressure activation means that the resulting model is able to autoregulate only between ±40%, rather than ±50%. The autoregulation curve was thus reproduced for a pressure change of ±40% with a non-symmetrical flow increase of +17% and −13% change in flow over this range. Beyond these limits the relationship between pressure and flow was similarly non-symmetrical: a 30% increase in flow was found following a 50% increase in pressure with a smaller 23% decrease in flow after a 50% decrease in pressure.

The response to capillary oxygen demand was investigated in chapter 7 where further contributions to the activation signal were identified as a local tissue concentration signal and a conducted oxygen demand signal. This conducted signal is

assumed to sum at bifurcations between vessels and to decay along vessel length. Inclusion of these signals has a very small effect on the myogenic curve, but the ability to autoregulate is slightly reduced at low pressure. The tissue compartment was found experimentally to give some redundancy after increased demand with the flow response overcompensating for the reduced tissue concentration, causing an overall increase. The metabolic signals proposed here enable the model to replicate this feature, along with the upstream pathway response to increased tissue demand in the capillaries.

An initial flow peak in the capillaries was found during simulation of capillary demand increase which was followed by a secondary flow increase due to a delay in the conducted signal which affected individual vessels in the network. The tissue concentration signal ensures that surrounding vessels only contract by a small amount with the tissue compartment compensating for reduced flux. The diameter of the immediately feeding vessel decreased following an initial dilation so that the increased oxygen is directed to the area of demand. In the preceding generation to the feeding arteriole, the diameter response was found to saturate since the conducted demand overrides the increase in flow and tissue concentration. The collateral capillaries were found to respond primarily to flow by draining the demanding capillary to prevent large increases in shear stress since the capillary vessels were assumed not to dilate.

Section 8:2 Discussion

8.2.1 Method Repeatability

Existing models of the vasculature have been mostly compartmental: grouping vessels together. The model established here is a vasculature model, based on branching physiology. This yields an improvement to existing compartmental model since vessels are represented individually. The activation signal in in-

dividual vessels is set by local conditions of stress and tissue concentration yet the collection of arterial diameter responses to global pressure ensures that flow is maintained over a pressure range. Vessels are also co-ordinated by a conducted signal proportional to oxygen demand which enables simulations of the effect of localised oxygen demand increases on the rest of the network to be performed.

The parameters in the model have been calculated to reproduce reference values of pressure, flow and oxygen concentration, where the reference values were found by interpolating data. In similar calculations for other networks, all that is required is the number of generations, the inlet and outlet pressure and the inlet oxygen concentration and tissue concentration. Therefore this model can easily be linked with other models which provide these boundary conditions (such as capillary or tissue models) or with data derived from MRI. Alternatively, the length-tension relationships or, indeed, any other parameters calculated in this thesis could be incorporated into other models of the vasculature and of autoregulation.

To make the model more relevant to MRI data, the results of the whole network need to be related to *mm* voxel size. For example, a 3 $mm \times 3$ *mm* voxel contains 6 generations of arterioles with a branching layout. Therefore the volume and flow of blood contained in a voxel can be used as the reference total flow in this model from which the number of vessels is derived. Since the network is specified by the number of capillaries, with experimentally verified diameter and velocity, the model can easily be re-scaled for any network. Similarly, the permeability of the vessel wall to oxygen is proportional to vessel diameter and reference tissue concentrations can be calculated for any vessel size. The length-tension characteristics of the vessels are found from a non-dimensional set of equations which can be scaled for any vessel diameter and the basal vessel tension is derived from the desired autoregulation curve. The method proposed is thus entirely data-driven

and therefore repeatable and scaleable for other network sizes.

8.2.2 Use of the model

The geometry and parameters used in the model are derived from experimental data with reference to physiology and are therefore an improvement on models which reproduce the data without physiological relevance. The use of the branching order to calculate geometry from the capillaries outwards (rather than the largest vessels) mean that networks of any size can be created which continue to mimic the data. Branching order, rather than vessel size, is important when considering the use of data from larger networks since these can include several vessel generations of this model within only two data points. The ability to recreate networks with very small vessels is aided by the use of non-dimensionalised expressions for length-tension and by including wall permeability as a function of the wall volume. Since the model is branching rather than compartmental, the effect of individual vessels on the branch, or network, resistance can be modelled which means that the network can be used to simulate specific experiments.

The review of the literature highlighted the ongoing physiological question of the inclusion of oxygen consumption in the wall when considering oxygen exchange in the cerebral vasculature. The forming of the model showed that oxygen consumption in the vessel wall was necessary to reproduce the flux and tissue concentration found experimentally. This oxygen consumption correlated with the vessel wall volume though not linearly. The conclusion was that the amount of oxygen consumption in the wall was therefore related to the amount of vascular smooth muscle and endothelial cells present, which depended on the vessel branching order. The model can therefore be used in support of the usage of permeability instead of a diffusion coefficient when calculating oxygen flux.

The autoregulating model could be used to simulate ischaemic stroke whereby a vessel diameter is reduced and the effect on oxygen delivery to tissue noted.

By linking with a model which incorporates tissue death, the consequences of ischaemia could be studied. The action of surrounding vessels to maintain oxygen supply in this situation could also be simulated with this model since the individual vessels are able to respond to a signal conducted due to tissue oxygen concentration. The degree of compensation that the pathway response in the network is able to provide can also be better understood using the model together with increased demand, or impaired reactions in specific vessels as well as for simulating stroke.

The model is able to autoregulate with four signals: tissue oxygen concentration, oxygen demand, hoop stress and shear stress. There is no neural control or relationship with blood oxygen or carbon dioxide concentration as described in the literature, though the method used to determine the contribution of the four signals could be repeated to include other reactions. The ability of vessels to regulate when compromised could also be investigated by reducing the weighting of specific signals in individual vessels since all arterioles currently have an identically weighted response to the same signal.

By having individual vessels at the smallest physiological scales the model contributes towards further understanding of autoregulation at a local scale. This localised and pathway activation is helpful in interpreting the change in blood flow data in, for example, the blood oxygen level dependent (BOLD) response found using functional MRI (fMRI). The modelling of flow in local vessels is also valuable for the analysis of data found by other imaging techniques which are based on perfusion and oxygen transport: for example, arterial spin labelling (ASL) and positron emission tomography (PET).

The ability to reproduce images by simulation of physiological events could aid the understanding of the relationship between the image and the activity. modelling the brain as a localised, active network of vessels is particularly valuable as

part of a large scale model of brain flow and metabolism.

8.2.3 Model limitations

The model has fulfilled the requirements laid out in section 1.2; of having individual vessels, with appropriate geometry, which display a co-ordinated active diameter response to both pressure changes and oxygen demand governed by physiologically relevant parameters. However, the model parameters were established by making sets of assumptions in order to simplify calculations (in some cases) or be able to calculate parameters (in others).

An underlying approximation of the model is that vessels branch into two equal daughter vessels (or that two equal vessels combine in the venules). In particular, capillaries have a more web-like than tree-like structure [44] (for example Figure 2.1 shows a capillary bed which connects an arteriole and venule).

Although there are some data available for the microcirculation, the length-tension characteristics derived in chapter 5 were scaled from larger vessels ($100-200\mu m$ diameter). The scaleability for these vessels of length-tension characteristics depends on the proportion of the vessel wall taken up by smooth muscle which is considered to vary between vessels when calculating oxygen permeability. Experimental data for the fraction in different vessels would improve the model, especially with investigation of the length-tension characteristics of small vessels. If smaller vessels have a higher proportion of smooth muscle this will affect the both active and elastic curves. In the mathematical relationship proposed here the negative strain function utilises a shift so that a basal tension exists at low strain. Whilst this enables more accurate modelling of the data, the result is that the function is invalid below a strain of 0.48.

The activation and diameter ratios during autoregulation were calculated for vessel $A1$ but assumed to be the same for all vessels. Along with the smooth muscle fraction, this assumption is necessary since the resistance required to reproduce

autoregulation at varying pressure can only be calculated for the whole network. Considering the underlying assumption of uniform diameter ratio response to pressure, the resulting ability to autoregulate locally, globally and in co-ordinated pathways to both global pressure and local oxygen demand is a great achievement. Data for different vessel orders during autoregulation would enable more accurate determination of activation and tension at basal state throughout the network. The transmural oxygen gradients are also affected by the basal activation of the vessel since this affects the vessel wall thickness by stretch and affects the amount of consumption in the wall because of the increased smooth muscle tone. Therefore, transmural concentration cannot necessarily be scaled by diameter, even with the separation into large and small vessels proposed in chapter 4. More experimental data will be needed to clarify this.

Autoregulation is assumed to be achieved by the alteration of diameter in order to satisfy equilibrium between circumferential tension due to transmural pressure and the tension in the material within the vessel wall, due to the elastic material and vascular smooth muscle. An activation factor sets the contribution of muscle tension to this total tension and the translation between signal and activation is approximated by a sigmoidal relationship. However, this does not relate to any physiological mechanisms, for the conducted signal this too is important because interference with the vessel pathways will also affect the signalling pathway.

The dynamics of the adaption of the diameter and oxygen concentration are assumed first order. There are no considerations of long-term adaption of wall thickness (for example) or the differing speeds of chemical pathways. Whilst the signals are based on physiological inputs, the proportionality is assumed linear whereas the individual signals may saturate. The weights are also assumed to be uniform in all vessels and proportional to the absolute value. Although this makes for untidy dimensions, it is physiologically relevant since absolute chemical concentrations

are related to the metabolism of smooth muscle. With reference to the uniformity of signal weights, it is possible that larger vessels react more to, for example, shear stress because of the larger volume fraction of the endothelial layer. Much more experimental data will be required to disentangle these different effects.

8.2.4 Data limitations

Ultimately the model proposed is based upon previous models relating to geometry, oxygen exchange and activation which are then improved with reference to data, and in controlling the signal for the desired response. A fundamental assumption which underlies the model is that the branching order of the vessels relates to diameter, which in turn relates to flow velocity, pressure and oxygen concentration. The available data have been invaluable and enabled an approximation of individual vessel response but the progression and accuracy of the model are limited by the lack of small-vessel, human cerebral data: both at basal state and during autoregulation.

The data are taken to be the average for the vessel but for pressure and oxygen concentration (which have longitudinal gradients along the vessel), data which are measured at a known point along the vessel would be very useful in improving the model. This is evident in the results for pressure where the resulting pressure curve in chapter 3 is not as smooth as in the graph presented by Zweifach. The (assumed) mid-vessel pressures are interpolated to find the nodal pressure, assuming constant pressure gradient along a vessel length. Finding the vessel length relies on the pressure values and flow calculated since the length is determined from the vessel resistance, which is in turn derived from the relationship between the pressure difference across a vessel and the flow. The calculated capillary length in the model proposed here is 144.87 μm for an 8 μm diameter vessel. This compares with an average length of 258 μm in capillaries of the same diameter extracted by Vovenko [265]. The venules in particular have a resulting variation in length,

compared with the arterioles in which diameter is related to length. If the relationship between diameter and velocity, and diameter and pressure can be calculated more accurately, and in particularly the point in the vessel length where pressure is recorded is known, the method described could be used to specify a network of any size with greater accuracy.

In chapter 4, reference oxygen concentrations are found at the model diameters by interpolating the data. As with pressure, the longitudinal gradient of oxygen concentration along the vessel affects the result if the measurement of concentration is not recorded mid-vessel. The sparseness of the data set for oxygen concentration (whereby several vessel diameters are contained within a range of the data) also reduces the accuracy of the interpolation for small vessels. The result is that some of the concentrations found by interpolation of data have to be altered so that the nodal concentrations make physiological sense. The longitudinal gradients are therefore found to be variable, with no clear relationship between vessel size and gradient. The oxygen concentration data are affected by the accuracy of the experimental technique such as the physical limitation of probe tip size, as discussed in subsubsection 2.3.5.7. The consistency of the relationship between vessel size and gradient is improved by taking into account the standard deviation of the experimental data. Therefore, even small errors in the data can have an effect on the model unless they are smoothed before use in the model.

The geometry, pressure and flow determined in chapter 3 are derived from data related to the cat mesentery. Wall thickness is taken from cerebral vessels, but these are for rats rather than humans. Similarly, the oxygen concentration data are taken from rat brains. The vessels analysed by Vovenko in rat brain (Table 2.4) and Duling in cat cerebral vessels show some equivalence between the oxygen concentrations in these species but the relationship between flow in mesentery and in the brain is unknown. Figure 2.7 shows that cerebral vessels have higher oxygen

concentrations but tissue gradients from other vascular beds (such as skeletal muscle) are also used in this model. The combination of data from different species and different organs limits the accuracy of the model for analysis of the cerebral microcirculation in humans. Even within humans there is individual variation in wall mechanics and geometry and so a model incorporating all of these data has to be treated with some caution.

There are discrepancies between data sets due to experimental technique, species and vascular bed as described above. However, outside of these considerations there is variance between experimental results. For example, the dynamics of the metabolic response were evaluated from two data sets which gave different flow and tissue ratios. The data from Ances were chosen as a reference due to the similarity in tissue concentration values to the model but it was found that replicating the high flow increase also resulted in a high tissue concentration ratio, as found by Vazquez.

It is evident that although there is sometimes a lot of data on particular aspects of network behaviour, it is often confusing and contradictory. The method proposed here is a first approach to modelling this complex interacting system. The major limitation to this is the lack of available data and much more data will be required before a definitive model can be produced. However, this approach does provide a framework within which further experimental data can be incorporated.

Section 8:3 Future Work

The method set out for deriving geometry, flow and pressure given a number of capillaries can be extended to networks of different sizes, and to other organs given an applicable data-set. The model could now be used to investigate what happens when a vessel is blocked, wall stiffness increased or conducted responses impaired which may be useful for those investigating vascular dementia and stroke. The

model could also be extended by linking with both imaging data, and other models.

The geometric model is two-dimensional with straight vessels, laminar flow and no turbulence at junctions. The scope of including more realistic tapering and twisting geometry, three-dimensional layout and non-laminar flow has been beyond the scope of the thesis considering the overall aims of the model. It would be interesting therefore to include the regulating parts of this model with a more accurate geometry. A statistical approach could be used in future to recreate vessel geometry and connectivity based on morphometric data with known frequency distribution of vessel diameter, length, vessel density and connectivity (number of branches at each junction). As well as connecting this model with a more accurate tissue compartment or capillary network, this network could also be placed within a larger scale brain model (i.e. multiscale modelling).

The current model uses uniform signal weights for all vessels whereas previous investigators have shown that small and large vessels respond differently to shear and circumferential stress. The calculation of vessel weights was based on all vessels contracting or dilating to the same diameter ratio at the limits of autoregulation and so experimental data which provides information about vessel response would be very useful in investigating the differing signal weights. A control theory approach to the interaction of signals would enable the inclusion of more complex signals and communication. The weights could be optimised to reproduce the data so that they might be found to be non-uniform and non-constant.

In Arterial Spin Labelling measurements of perfusion there is a residue function which represents the amount of blood in the vessel and is modelled as a function of transit time. The input is evaluated from the signal by a statistical model. By using data from multiple imaging modalities with linked model approximations probabilistic and statistical models can be improved. This model could therefore

be linked directly with modelling data to improve image analysis.

Bibliography

[1] Aaslid, R., Lindegaard, K., Sorteberg, W., and Nornes, H. Cerebral autoregulation dynamics in humans. *Stroke*, 20(1):45–52, 1989.

[2] Alastruey, J., Parker, K., Peiró, J., Byrd, S., and Sherwin, S. Modelling the circle of willis to assess the effects of anatomical variations and occlusions on cerebral flows. *Journal of Biomechanics*, 40(8):1794–1805, 2007.

[3] Alzaidi, S. *Computational Models of Cerebral Hemodynamics*. PhD thesis, University of Cantebury, NZ, 2009.

[4] Ances, B., Buerk, D., Greenberg, J., and Detre, J. Temporal dynamics of the partial pressure of brain tissue oxygen during functional forepaw stimulation in rats. *Neuroscience letters*, 306(1-2):106–110, 2001.

[5] Andersen, K., Olsen, T., Dehlendorff, C., and Kammersgaard, L. Hemorrhagic and ischemic strokes compared: stroke severity, mortality, and risk factors. *Stroke*, 40(6):2068, 2009.

[6] Arciero, J., Carlson, B., and Secomb, T. Theoretical model of metabolic blood flow regulation: roles of *atp* release by red blood cells and conducted responses. *American Journal of Physiology- Heart and Circulatory Physiology*, 295(4):H1562, 2008.

[7] Assad, F., Sciultheiss, R., Leniger-Follert, E., and Wullenweber, R. Measurement of local oxygen partial pressure (po_2) of the brain cortex in cases of tumors. *Adv Neurosurg*, 12:263–266, 1984.

[8] Baldwin, A., Thurston, G., et al. Mechanics of endothelial cell architecture and vascular permeability. *Critical reviews in biomedical engineering*, 29(2):247, 2001.

[9] Banaji, M., Tachtsidis, I., Delpy, D., and Baigent, S. A physiological model of cerebral blood flow control. *Mathematical biosciences*, 194(2):125–173, 2005.

[10] Bartlett, K., Saka, M., and Jones, M. Polarographic electrode measures of cerebral tissue oxygenation: Implications for functional brain imaging. *Sensors*, 8(12):7649–7670, 2008.

[11] Bauersachs, J., Popp, R., Hecker, M., Sauer, E., Fleming, I., and Busse, R. Nitric oxide attenuates the release of endothelium-derived hyperpolarizing factor. *Circulation*, 94(12):3341–3347, 1996.

[12] Baumgartl, H. and Lubbers, D. Microcoaxial needle sensor for polarographic measurement of local o_2 pressure in the cellular range of living tissue. its construction and properties. *Polarographic oxygen sensors: aquatic and physiological applications. Springer, Berlin Heidelberg New York*, pages 37–65, 1983.

[13] Bayliss, W. On the local reactions of the arterial wall to changes of internal pressure. *The Journal of physiology*, 28(3):220, 1902. ISSN 0022-3751.

[14] Beach, J., McGahren, E., and Duling, B. Capillaries and arterioles are electrically coupled in hamster cheek pouch. *American Journal of Physiology-Heart and Circulatory Physiology*, 275(4):H1489, 1998. ISSN 0363-6135.

[15] Becker, R. *Textbook of Coronary Thrombosis and Thrombolysis*. Developments in Cardiovascular Medicine. Kluwer Academic Publishers, 1997. ISBN 9780792399230.

[16] Behzadi, Y. and Liu, T. An arteriolar compliance model of the cerebral blood flow response to neural stimulus. *Neuroimage*, 25(4):1100–1111, 2005.

[17] Bereczki, D., Wei, L., Otsuka, T., Acuff, V., Pettigrew, K., et al. Hypoxia increases velocity of blood flow through parenchymal microvascular systems in rat brain. *Journal of Cerebral Blood Flow & Metabolism*, 13(3):475–486, 1993.

[18] Bergel, D. The static elastic properties of the arterial wall. *The Journal of physiology*, 156(3): 445, 1961. ISSN 0022-3751.

[19] Berger, S. and Jou, L. Flows in stenotic vessels. *Annual Review of Fluid Mechanics*, 32(1): 347, 2003.

[20] Bergfeld, G. and Forrester, T. Release of atp from human erythrocytes in response to a brief period of hypoxia and hypercapnia. *Cardiovascular research*, 26(1):40, 1992. ISSN 0008-6363.

[21] Bergman, R., Afifi, A., and Miyauchi, R. Circle of willis. *Illustrated Encyclopedia of Human Anatomic Variation, URL: http://www. anatomyatlases. org/AnatomicVariants/Cardiovascular/Text/Arteries/CircleofWillis. shtml. Accessed on November*, 6, 2005.

[22] Berne, R. and Levy, M. *Cardiovascular Physiology*. CV Mosby, 1997.

[23] Bevan, J. and Osher, J. A direct method for recording tension changes in the wall of small blood vessels in vitro. *Inflammation Research*, 2 (5):257–260, 1972.

[24] Bhagavan, N. *Medical biochemistry*. Harcourt/Academic Press, San Diego, 2002. ISBN 0120954400.

[25] Birch, A., Neil-Dwyer, G., and Murrills, A. The repeatability of cerebral autoregulation assessment using sinusoidal lower body negative pressure. *Physiological measurement*, 23:73, 2002.

[26] Bishop, C., Powell, S., and Rutt, D. Transcranial Doppler measurement of middle cerebral artery blood flow velocity: a validation study. *Stroke*, 17(5):913, 1986.

[27] Boas, D., Jones, S., Devor, A., Huppert, T., and Dale, A. A vascular anatomical network model of the spatio-temporal response to brain activation. *NeuroImage*, 40(3):1116–1129, 2008.

[28] Bohlen, H. and Harper, S. Evidence of myogenic vascular control in the rat cerebral cortex. *Circulation research*, 55(4):554–559, 1984.

[29] Bondar, R., Kassam, M., Stein, F., Dunphy, P., and Riedesel, M. Simultaneous transcranial doppler and arterial blood pressure response to lower body negative pressure. *The Journal of Clinical Pharmacology*, 34(6):584–589, 1994.

[30] Borgström, P. and Gestrelius, S. Integrated myogenic and metabolic control of vascular tone in skeletal muscle during autoregulation of blood flow. *Microvascular research*, 33(3): 353–376, 1987.

[31] Borgström, P. and Grände, P. Myogenic microvascular responses to change of transmural pressure a mathematical approach. *Acta Physiologica Scandinavica*, 106(4):411–423, 1979.

[32] Borgström, P., Grände, P., and Mellander, S. A mathematical description of the myogenic response in the microcirculation. *Acta Physiologica Scandinavica*, 116(4):363–376, 1982.

[33] Bouskela, E. and Wiederhielm, C. Microvascular myogenic reaction in the wing of the intact unanesthetized bat. *American Journal of Physiology-Heart and Circulatory Physiology*, 237(1):H59, 1979. ISSN 0363-6135.

[34] Bradley, P., Harding, S., Coles, J., Chatfield, D., Pickard, J., and Menon, D. Blood flow and oxygen extraction fraction in regions of oedema following head injury. *Critical Care*, 8 (Suppl 1):P311, 2004.

[35] Bronzino, J. *The Biomedical Engineering Handbook*. The electrical engineering handbook series. CRC Press, 2000. ISBN 9783540663515.

[36] Brozovich, F. and Morgan, K. Stimulus-specific changes in mechanical properties of vascular smooth muscle. *American Journal of Physiology-Heart and Circulatory Physiology*, 257(5):H1573–H1580, 1989.

[37] Burnstock, G. Release of vasoactive substances from endothelial cells by shear stress and purinergic mechanosensory transduction. *Journal of anatomy*, 194(3):335–342, 1999.

[38] Butcher Jr, H. and Newton, W. The influence of age, arteriosclerosis and homotransplantation upon the elastic properties of major human arteries. *Annals of Surgery*, 148(1):1, 1958.

[39] Buxton, R. and Frank, L. A model for the coupling between cerebral blood flow and oxygen metabolism during neural stimulation. *Journal of Cerebral Blood Flow and Metabolism*, 17 (1):64–72, 1997.

[40] Byar, D., Fiddian, R., Quereau, M., Hobbs, J., and Edwards, E. The fallacy of applying the poiseuille equation to segmental arterial stenosis. *American heart journal*, 70(2):216–224, 1965.

[41] Carlson, B., Arciero, J., and Secomb, T. Theoretical model of blood flow autoregulation: roles of myogenic, shear-dependent, and metabolic responses. *American Journal of*

Physiology- Heart and Circulatory Physiology, 295(4):H1572, 2008.

[42] Carlson, B. and Secomb, T. A theoretical model for the myogenic response based on the length–tension characteristics of vascular smooth muscle. *Microcirculation*, 12(4):327–338, 2005.

[43] Casellas, D. and Moore, L. Autoregulation of intravascular pressure in preglomerular juxtamedullary vessels. *American Journal of Physiology-Renal Physiology*, 264(2):F315–F321, 1993.

[44] Cassot, F., Lauwers, F., Fouard, C., Prohaska, S., and Lauwers-Cances, V. A novel three-dimensional computer-assisted method for a quantitative study of microvascular networks of the human cerebral cortex. *Microcirculation*, 13(1):1–18, 2010.

[45] Chiras, D. *Human biology*. Jones and Bartlett Learning, Sudbury, MA, 2012. ISBN 9780763783457.

[46] Clark, D., Erdmann, W., Halsey, J., and Strong, E. Oxygen diffusion, conductivity and solubility coefficients in the microarea of the brain.(measurements with noble metal microelectrodes). *Advances in experimental medicine and biology*, 94:697, 1977.

[47] Clark Jr, L. and Lyons, C. Electrode systems for continuous monitoring in cardiovascular surgery. *Annals of the New York Academy of Sciences*, 102(Automated and Semi-Automated Systems in Clinical Chemistry):29–45, 1962.

[48] Clarke, D., Sokoloff, L., et al. Circulation and energy metabolism of the brain. *Basic neurochemistry*, 5:645–680, 1999.

[49] Collins, D., McCullough, W., and Ellsworth, M. Conducted vascular responses: communication across the capillary bed. *Microvascular research*, 56(1):43–53, 1998. ISSN 0026-2862.

[50] Consortium, T. S. S. G. What's a stroke? *http://www.genestroke.com/?p=168*.

[51] Cope, M. *The development of a near infrared spectroscopy system and its application for non invasive monitoring of cerebral blood and tissue oxygenation in the newborn infants*. PhD thesis, University College London (University of London), 1991.

[52] Cornelissen, A., Dankelman, J., VanBavel, E., and Spaan, J. Balance between myogenic, flow-dependent, and metabolic flow control in coronary arterial tree: a model study. *American Journal of Physiology-Heart and Circulatory Physiology*, 282(6):H2224, 2002. ISSN 0363-6135.

[53] Cusack, S. and Miller, A. Determination of the elastic constants of collagen by brillouin light scattering. *Journal of molecular biology*, 135(1):39–51, 1979.

[54] Dacey Jr, R. and Duling, B. A study of rat intracerebral arterioles: methods, morphology, and reactivity. *American Journal of Physiology-Heart and Circulatory Physiology*, 243(4):H598–H606, 1982.

[55] Damage, R. Faster access to better stroke care. *National Audit Office*, 2005.

[56] Davis, M., Donovitz, J., and Hood, J. Stretch-activated single-channel and whole cell currents in vascular smooth muscle cells. *American Journal of Physiology-Cell Physiology*, 262 (4):C1083, 1992. ISSN 0363-6143.

[57] Davis, M. and Gore, R. Length-tension relationship of vascular smooth muscle in single arterioles. *American Journal of Physiology-Heart and Circulatory Physiology*, 256(3):H630, 1989. ISSN 0363-6135.

[58] Davis, M. and Hill, M. Signaling mechanisms underlying the vascular myogenic response. *Physiological reviews*, 79(2):387, 1999. ISSN 0031-9333.

[59] Davis, M., Wu, X., Nurkiewicz, T., Kawasaki, J., Davis, G., Hill, M., and Meininger, G. Integrins and mechanotransduction of the vascular myogenic response. *American Journal of Physiology-Heart and Circulatory Physiology*, 280(4):H1427–H1433, 2001.

[60] Dintenfass, L. Inversion of the Fahraeus–Lindqvist phenomenon in blood flow through capillaries of diminishing radius. 1967.

[61] Donegan, J., Traystman, R., Koehler, R., Jones, M., and Rogers, M. Cerebrovascular hypoxic and autoregulatory responses during reduced brain metabolism. *American Journal of Physiology-Heart and Circulatory Physiology*, 249(2):H421, 1985. ISSN 0363-6135.

[62] Doppenberg, E., Watson, J., Broaddus, W., Holloway, K., Young, H., and Bullock, R. Intraoperative monitoring of substrate delivery during aneurysm and hematoma surgery: initial experience in 16 patients. *Journal of neurosurgery*, 87(6):809–816, 1997.

[63] Drachman, D. Aging of the brain, entropy, and alzheimer disease. *Neurology*, 67(8):1340–1352, 2006.

[64] Dulin, B. and Berne, R. Longitudinal gradients in periarteriolar oxygen tension: a possible mechanism for the participation of oxygen in local regulation of blood flow. *Circulation research*, 27(5):669, 1970.

[65] Duling, B. Microvascular responses to alterations in oxygen tension. *Circulation research*, 31(4):481, 1972.

[66] Duling, B., Gore, R., Dacey Jr, R., and Damon, D. Methods for isolation, cannulation, and in vitro study of single microvessels. *American Journal of Physiology-Heart and Circulatory Physiology*, 241(1):H108–H116, 1981.

[67] Duling, B., Hogan, R., Langille, B., Lelkes, P., Segal, S., Vatner, S., Weigelt, H., Young, M., et al. Vasomotor control: functional hyperemia and beyond. In *Federation proceedings*, volume 46, page 251, 1987.

[68] Duling, B., Kuschinsky, W., and Wahl, M. Measurements of the perivascular po_2 in the vicinity of the pial vessels of the cat. *Pflügers Archiv European Journal of Physiology*, 383(1): 29–34, 1979.

[69] Duvernoy, H., Delon, S., and Vannson, J. Cortical blood vessels of the human brain. *Brain research bulletin*, 7(5):519–579, 1981.

[70] Easton, J. Cerebral embolism and Doppler ultrasound. *Cerebrovascular Diseases*, 9(3):188–192, 2000.

[71] Edvinsson, L., MacKenzie, E., and McCulloch, J. *Cerebral blood flow and metabolism*. Lippincott Williams & Wilkins Philadelphia, PA, 2002.

[72] Ellsworth, M. The red blood cell as an oxygen sensor: what is the evidence? *Acta physiologica scandinavica*, 168(4):551–559, 2000.

[73] Ellsworth, M., Forrester, T., Ellis, C., and Dietrich, H. The erythrocyte as a regulator of vascular tone. *American Journal of Physiology-Heart and Circulatory Physiology*, 269(6):H2155–H2161, 1995.

[74] Ellsworth, M., Popel, A., and Pittman, R. Assessment and impact of heterogeneities of convective oxygen transport parameters in capillaries of striated muscle: experimental and theoretical. *Microvascular research*, 35(3):341–362, 1988.

[75] Faraci, F. and Heistad, D. Regulation of large cerebral arteries and cerebral microvascular pressure. *Circulation research*, 66(1):8–17, 1990.

[76] Feldberg, R., Colding-Jorgensen, M., and Holstein-Rathlou, N. Analysis of interaction between tgf and the myogenic response in renal blood flow autoregulation. *American Journal of Physiology-Renal Physiology*, 269(4):F581, 1995. ISSN 0363-6127.

[77] Fry, B. Time-dependent myogenic behavior of arterioles. 2009.

[78] Fung, Y. *Biomechanics: mechanical properties of living tissues*. Springer, 1993. ISBN 0387979476.

[79] Furchgott, R. and Vanhoutte, P. Endothelium-derived relaxing and contracting factors. *The FASEB journal*, 3(9): 2007–2018, 1989.

[80] Garcia-Roldan, J. and Bevan, J. Flow-induced constriction and dilation of cerebral resistance arteries. *Circulation research*, 66(5):1445–1448, 1990.

[81] Gaskill-Shipley, M. Routine CT evaluation of acute stroke. *Neuroimaging clinics of North America*, 9(3):411, 1999.

[82] Gaw, A. and Bevan, J. Flow-induced relaxation of the rabbit middle cerebral artery is composed of both endothelium-dependent and-independent components. *Stroke*, 24(1):105–109, 1993.

[83] Giller, C., Bowman, G., Dyer, H., Mootz, L., and Krippner, W. Cerebral arterial diameters during changes in blood pressure and carbon dioxide during craniotomy. *Neurosurgery*, 32 (5):737, 1993.

[84] Ginsberg, M., Dietrich, W., and Busto, R. Coupled forebrain increases of local cerebral glucose utilization and blood flow during physiologic stimulation of a somatosensory pathway in the rat. *Neurology*, 37(1):11–11, 1987.

[85] Golub, A., Barker, M., and Pittman, R. po_2 profiles near arterioles and tissue oxygen consumption in rat mesentery. *American Journal of Physiology-Heart and Circulatory Physiology*, 293(2):H1097–H1106, 2007.

[86] Granger, H., Goodman, A., and Granger, D. Role of resistance and exchange vessels in local microvascular control of skeletal muscle oxygenation in the dog. *Circulation Research*, 38 (5):379, 1976.

[87] Groebe, K. Precapillary servo control of blood pressure and postcapillary adjustment of flow to tissue metabolic status: a new paradigm for local perfusion regulation. *Circulation*, 94(8): 1876, 1996.

[88] Günther, M. Magnetic resonance techniques to measure distribution of cerebral blood flow. *Applied Cardiopulmonary Pathophysiology*, 13: 212–218, 2009.

[89] Haas, J., Granger, J., and Knox, F. Effect of renal perfusion pressure on sodium reabsorption from proximal tubules of superficial and deep nephrons. *American Journal of Physiology-Renal Physiology*, 250(3):F425–F429, 1986.

[90] Hademenos, G. and Massoud, T. Biophysical mechanisms of stroke. *Stroke*, 28(10):2067, 1997.

[91] Harder, D. Pressure-dependent membrane depolarization in cat middle cerebral artery. *Circulation research*, 55(2):197, 1984.

[92] Harder, D., Sanchez-Ferrer, C., Kauser, K., Stekiel, W., and Rubanyi, G. Pressure releases a transferable endothelial contractile factor in cat cerebral arteries. *Circulation research*, 65(1): 193, 1989.

[93] Harper, S. and Bohlen, H. Microvascular adaptation in the cerebral cortex of adult spontaneously hypertensive rats. *Hypertension*, 6(3): 408–419, 1984.

[94] Harris, D. and Warshaw, D. Smooth and skeletal muscle actin are mechanically indistinguishable in the in vitro motility assay. *Circulation research*, 72(1):219–224, 1993.

[95] Hathaway, D., March, K., Lash, J., Adam, L., and Wilensky, R. Vascular smooth muscle. a review of the molecular basis of contractility. *Circulation*, 83(2):382–390, 1991.

[96] Hayashi, K., Handa, H., Nagasawa, S., Okumura, A., and Moritake, K. Stiffness and elastic behavior of human intracranial and extracranial arteries. *Journal of biomechanics*, 13 (2):175–179, 1980. ISSN 0021-9290.

[97] Haywood, J., Shaffer, R., Fastenow, C., Fink, G., and Brody, M. Regional blood flow measurement with pulsed Doppler flowmeter in conscious rat. *American Journal of Physiology-Heart and Circulatory Physiology*, 241(2):H273, 1981.

[98] Heistad, D., Kontos, H., Shepherd, J., and Abboud, F. Handbook of Physiology, section 2, The Cardiovascular System. *Bethesda, MD, USA: American Physiological Society*, pages 137–182, 1983.

[99] Hematol, C., Dev, C., Arch, P., and Res, C. 2. popel as: Theory of oxygen transport to tissue. *Crit Rev Biomed Eng*, 17:257–321, 1989.

[100] Hendrikse, J., van der Grond, J., Lu, H., van Zijl, P., and Golay, X. Flow territory mapping of the cerebral arteries with regional perfusion MRI. *Stroke*, 35(4):882, 2004.

[101] Hennerici, H. *Imaging in Stroke*. Remedica Publishing Limited, 2003. ISBN 9781901346251.

[102] Herlihy, J. and Murphy, R. Length-tension relationship of smooth muscle of the hog carotid artery. *Circulation research*, 33(3):275–283, 1973.

[103] Hesselink, J. Imaging of stroke and cerebral ischemia. *http://spinwarp.ucsd.edu/NeuroWeb/Text/br-710.htm*.

[104] Heymann, M., Payne, B., Hoffman, J., and Rudolph, A. Blood flow measurements with radionuclide-labeled particles. *Progress in cardiovascular diseases*, 20(1):55–79, 1977.

[105] Hudetz, A. Regulation of oxygen supply in the cerebral circulation. *Advances in experimental medicine and biology*, 428:513, 1997.

[106] Hudetz, A. Mathematical model of oxygen transport in the cerebral cortex. *Brain research*, 817(1-2):75–83, 1999.

[107] Hughes, J. and Bund, S. Arterial myogenic properties of the spontaneously hypertensive rat. *Experimental physiology*, 87(5):527–534, 2002. ISSN 1469-445X.

[108] Hyman, W., Grounds, D., and Newell Jr, P. Oxygen tension in a capillary-tissue system subject to periodic occlusion. *Microvascular Research*, 9(1):49–63, 1975.

[109] Ibayashi, S., Ngai, A., Meno, J., and Winn, H. Effects of topical adenosine analogs and forskolin on rat pial arterioles in vivo. *Journal of cerebral blood flow and metabolism: official journal of the International Society of Cerebral Blood Flow and Metabolism*, 11(1):72, 1991.

[110] Iida, N. Physical properties of resistance vessel wall in peripheral blood flow regulation–i. mathematical model. *Journal of biomechanics*, 22(2):109–117, 1989.

[111] Intaglietta, M., Johnson, P., and Winslow, R. Microvascular and tissue oxygen distribution. *Cardiovascular research*, 32(4):632–643, 1996.

[112] Jacobsen, J., Mulvany, M., and Holstein-Rathlou, N. A mechanism for arteriolar remodeling based on maintenance of smooth muscle cell activation. *American Journal of Physiology-Regulatory, Integrative and Comparative Physiology*, 294(4):R1379, 2008. ISSN 0363-6119.

[113] Johansson, B. and Mellander, S. Static and dynamic components in the vascular myogenic response to passive changes in length as revealed by electrical and mechanical recordings from the rat portal vein. *Circulation Research*, 36(1):76, 1975.

[114] Johnson, P. Autoregulation of blood flow. *Circulation research*, 59(5):483, 1986.

[115] Johnson, P. The myogenic response in the microcirculation and its interaction with other control systems. *Journal of hypertension. Supplement: official journal of the International Society of Hypertension*, 7(4):S33, 1989. ISSN 0952-1178.

[116] Johnson, P., University, I., and Service, U. S. P. H. *Autoregulation of Blood Flow; Proceedings of an International Symposium Held June 10, 11, 12, 1963, in Indianapolis. Edited by Paul C. Johnson*. American Heart Assn., 1964.

[117] Johnson, P. and Wayland, H. Regulation of blood flow in single capillaries. *American Journal of Physiology–Legacy Content*, 212(6):1405, 1967. ISSN 0002-9513.

[118] Johnston, A., Steiner, L., Gupta, A., and Menon, D. Cerebral oxygen vasoreactivity and cerebral tissue oxygen reactivity†. *British journal of anaesthesia*, 90(6):774–786, 2003.

[119] Jørgensen, L., Perko, M., Perko, G., and Secher, N. Middle cerebral artery velocity during head-up tilt induced hypovolemic shock in humans. *Clinical Physiology*, 13(4):323–336, 1993.

[120] Kassissia, I., Goresky, C., Rose, C., Schwab, A., Simard, A., Huet, P., and Bach, G. Tracer oxygen distribution is barrier-limited in the cerebral microcirculation. *Circulation research*, 77 (6):1201, 1995.

[121] Kato, H. and Kogure, K. Biochemical and molecular characteristics of the brain with developing cerebral infarction. *Cellular and molecular neurobiology*, 19(1):93–108, 1999.

[122] Kaufman, K., An, K., and Chao, E. Incorporation of muscle architecture into the muscle length-tension relationship. *Journal of biomechanics*, 22(8-9):943–948, 1989.

[123] Kellie, G. Appearances observed in the dissection of two individuals; death from cold and congestion of the brain. *Trans Med-Chir Soc Edinburgh*, 1:84, 1824.

[124] Kelman, G. Digital computer subroutine for the conversion of oxygen tension into saturation. *Journal of Applied Physiology*, 21(4):1375–1376, 1966.

[125] Kenney, W. *Physiology of sport and exercise*. Human Kinetics, Champaign, IL, 2012. ISBN 0736094091.

[126] Kety, S. and Schmidt, C. The determination of cerebral blood flow in man by the use of nitrous oxide in low concentrations. *American Journal of Physiology*, 143(1):53, 1945.

[127] Kirkham, F., Padayachee, T., Parsons, S., Seargeant, L., House, F., and Gosling, R. Transcranial measurement of blood velocities in the basal cerebral arteries using pulsed Doppler ultrasound: velocity as an index of flow. *Ultrasound in medicine & biology*, 12(1): 15–21, 1986.

[128] Klabunde, R. Autoregulation of organ blood flow. *http://www.cvphysiology.com/Blood20Flow/BF004.htm*, March 2009.

[129] Klitzman, B., Damon, D., Gorczynski, R., and Duling, B. Augmented tissue oxygen supply during striated muscle contraction in the hamster. relative contributions of capillary recruitment, functional dilation, and reduced tissue po_2. *Circulation Research*, 51(6):711, 1982.

[130] Knot, H. and Nelson, M. Regulation of membrane potential and diameter by voltage-dependent k^+ channels in rabbit myogenic cerebral arteries. *American Journal of Physiology-Heart and Circulatory Physiology*, 269(1):H348, 1995. ISSN 0363-6135.

[131] Knot, H. and Nelson, M. Regulation of arterial diameter and wall $[ca^{2+}]$ in cerebral arteries of rat by membrane potential and intravascular pressure. *The Journal of physiology*, 508 (1):199, 1998. ISSN 0022-3751.

[132] Koch, A. Some mathematical forms of autoregulatory models. *Circulation research*, 15: SUPPL–269, 1964. ISSN 0009-7330.

[133] Koeppen BM, S. B. *Berne & Levy Physiology*. Philadelphia: Mosby Elsevier, 2008.

[134] Kontos, H., Wei, E., Raper, A., Rosenblum, W., Navari, R., and Patterson, J. Role of tissue hypoxia in local regulation of cerebral microcirculation. *American Journal of Physiology-Heart and Circulatory Physiology*, 234(5):H582, 1978. ISSN 0363-6135.

[135] Krogh, A. The number and distribution of capillaries in muscles with calculations of the oxygen pressure head necessary for supplying the tissue. *The Journal of Physiology*, 52(6):409, 1919.

[136] Kuo, L., Chilian, W., and Davis, M. Coronary arteriolar myogenic response is independent of endothelium. *Circulation research*, 66(3):860, 1990.

[137] Kuo, L., Davis, M., and Chilian, W. Myogenic activity in isolated subepicardial and subendocardial coronary arterioles. *American Journal of Physiology-Heart and Circulatory Physiology*, 255(6):H1558, 1988. ISSN 0363-6135.

[138] Kuo, L., Davis, M., and Chilian, W. Endothelium-dependent, flow-induced dilation of isolated coronary arterioles. *American Journal of Physiology-Heart and Circulatory Physiology*, 259(4):H1063, 1990. ISSN 0363-6135.

[139] Kuo, L. and Pittman, R. Effect of hemodilution on oxygen transport in arteriolar networks of hamster striated muscle. *American Journal of Physiology-Heart and Circulatory Physiology*, 254(2):H331–H339, 1988.

[140] Kuo, L. and Pittman, R. Influence of hemoconcentration on arteriolar oxygen transport in hamster striated muscle. *American Journal of Physiology-Heart and Circulatory Physiology*, 259(6):H1694–H1702, 1990.

[141] Lassen, N. Control of cerebral circulation in health and disease. *Circulation Research*, 34(6): 749, 1974.

[142] Learoyd, B. and Taylor, M. Alterations with age in the viscoelastic properties of human arterial walls. *Circulation Research*, 18(3):278–292, 1966.

[143] Lee, S. and Schmid-Schönbein, G. Biomechanical model for the myogenic response ... *Journal of biomechanical engineering*, 118:145, 1996.

[144] Lin, A., Fox, P., Hardies, J., Duong, T., and Gao, J. Nonlinear coupling between cerebral blood flow, oxygen consumption, and atp production in human visual cortex. *Proceedings of the National Academy of Sciences*, 107(18):8446, 2010.

[145] Lübbers, D., Baumgärtl, H., et al. Heterogeneities and profiles of oxygen pressure in brain and kidney as examples of the po_2 distribution in the living tissue. *Kidney international*, 51(2):372, 1997.

[146] Lucas, C. and Payne, S. An anatomical model of the cerebral vasculature and the autoregulation of cerebral blood flow. In *6th World Congress of Biomechanics (WCB 2010). August 1-6, 2010 Singapore*, pages 446–449. Springer, 2010.

[147] Maas, A., Fleckenstein, W., De Jong, D., Van Santbrink, H., et al. Monitoring cerebral oxygenation: experimental studies and preliminary clinical results of continuous monitoring of cerebrospinal fluid and brain tissue oxygen tension. *Acta neurochirurgica. Supplementum*, 59:50, 1993.

[148] Malek, A. and Izumo, S. Mechanism of endothelial cell shape change and cytoskeletal remodeling in response to fluid shear stress. *Journal of Cell Science*, 109(4):713–726, 1996.

[149] Mandeville, J., Marota, J., Ayata, C., Zaharchuk, G., Moskowitz, M., Rosen, B., and Weisskoff, R. Evidence of a cerebrovascular postarteriole windkessel with delayed compliance. *Journal of Cerebral Blood Flow & Metabolism*, 19(6):679–689, 1999.

[150] Martinez-Lemus, L., Hill, M., and Meininger, G. The plastic nature of the vascular wall: a continuum of remodeling events contributing to control of arteriolar diameter and structure. *Physiology*, 24(1):45, 2009. ISSN 1548-9213.

[151] Masamoto, K. and Tanishita, K. Oxygen transport in brain tissue. *Journal of biomechanical engineering*, 131:074002, 2009.

[152] Matsumoto, T. and Hayashi, K. Mechanical and dimensional adaptation of rat aorta to hypertension. *Journal of biomechanical engineering*, 116:278, 1994.

[153] Mayhew, J., Johnston, D., Berwick, J., Jones, M., Coffey, P., and Zheng, Y. Spectroscopic analysis of neural activity in brain: increased oxygen consumption following activation of barrel cortex. *Neuroimage*, 12(6):664–675, 2000.

[154] McCarron, J., Crichton, C., Langton, P., MacKenzie, A., and Smith, G. Myogenic contraction by modulation of voltage-dependent calcium currents in isolated rat cerebral arteries. *The Journal of Physiology*, 498(Pt 2):371, 1997. ISSN 0022-3751.

[155] McCullough, W., Collins, D., and Ellsworth, M. Arteriolar responses to extracellular atp in striated muscle. *American Journal of Physiology-Heart and Circulatory Physiology*, 272(4):H1886–H1891, 1997.

[156] McGuire, B. and Secomb, T. A theoretical model for oxygen transport in skeletal muscle under conditions of high oxygen demand. *Journal of Applied Physiology*, 91(5):2255–2265, 2001.

[157] Meininger, G. and Davis, M. Cellular mechanisms involved in the vascular myogenic response. *American Journal of Physiology-Heart and Circulatory Physiology*, 263(3):H647, 1992. ISSN 0363-6135.

[158] Metzger, H. and Heuber, S. Local oxygen tension and spike activity of the cerebral grey matter of the rat and its response to short intervals of o_2 deficiency or co_2 excess. *Pflügers Archiv European Journal of Physiology*, 370(2):201–209, 1977.

[159] Meyer, J., Yoshida, K., and Sakamoto, K. Autonomic control of cerebral blood flow measured by electromagnetic flowmeters. *Neurology*, 17 (7):638, 1967.

[160] Michiels, C. Endothelial cell functions. *Journal of cellular physiology*, 196(3):430–443, 2003.

[161] Middleman, S. *Transport phenomena in the cardiovascular system*. Wiley-Interscience New York, 1972.

[162] Miller, F., Dellsperger, K., and Gutterman, D. Myogenic constriction of human coronary arterioles. *American Journal of Physiology-Heart and Circulatory Physiology*, 273(1):H257, 1997. ISSN 0363-6135.

[163] Mintun, M., Lundstrom, B., Snyder, A., Vlassenko, A., Shulman, G., and Raichle, M. Blood flow and oxygen delivery to human brain during functional activity: theoretical modeling and experimental data. *Proceedings of the National Academy of Sciences*, 98(12): 6859, 2001.

[164] Mishra, L. Cerebral blood flow and anaesthesia: a review. *Indian Journal of anesthesia*, 46(2): 87–95, 2002.

[165] Moffett, D., Moffett, S., and Schauf, C. *Human physiology: foundations & frontiers*. Mosby, 1993. ISBN 9780801669033.

[166] Monro, A. Observations on the Structure and Functions of the Nervous System. 1783.

[167] Monson, K., Goldsmith, W., Barbaro, N., and Manley, G. Significance of source and size in the mechanical response of human cerebral blood vessels. *Journal of biomechanics*, 38(4): 737–744, 2005. ISSN 0021-9290.

[168] Monson, K., Goldsmith, W., Barbaro, N., Manley, G., et al. Axial mechanical properties of fresh human cerebral blood vessels. *Journal of biomechanical engineering*, 125(2):288, 2003.

[169] Moore, S., Moorhead, K., Chase, J., David, T., and Fink, J. One-dimensional and three-dimensional models of cerebrovascular flow.

Journal of biomechanical engineering, 127:440, 2005.

[170] Muhl, Z. Active length-tension relation and the effect of muscle pinnation on fiber lengthening. *Journal of morphology*, 173(3):285–292, 1982.

[171] Muller, J., Chilian, W., and Davis, M. Integrin signaling transduces shear stress–dependent vasodilation of coronary arterioles. *Circulation research*, 80(3):320, 1997.

[172] Mulvany, M. and Warshaw, D. The active tension-length curve of vascular smooth muscle related to its cellular components. *The Journal of general physiology*, 74(1):85–104, 1979.

[173] Murphy, R. What is special about smooth muscle? the significance of covalent crossbridge regulation. *The FASEB journal*, 8(3):311–318, 1994.

[174] Ndubuizu, O. and LaManna, J. Brain tissue oxygen concentration measurements. *Antioxidants & redox signaling*, 9(8):1207–1220, 2007.

[175] Nelson, R., Czosnyka, M., Pickard, J., Maksymowicz, W., Perry, S., and Lovick, A. Experimental aspects of cerebrospinal hemodynamics: the relationship between blood flow velocity waveform and cerebral autoregulation. *Neurosurgery*, 31(4):705, 1992. ISSN 0148-396X.

[176] Ngai, A. and Winn, H. Modulation of cerebral arteriolar diameter by intraluminal flow and pressure. *Circulation research*, 77(4):832–840, 1995.

[177] Nocedal, J. and Wright, S. *Numerical optimization*. Springer verlag, 1999.

[178] Novak, V., Novak, P., Spies, J., and Low, P. Autoregulation of cerebral blood flow in orthostatic hypotension. *Stroke*, 29(1):104, 1998.

[179] Nyborg, N., Baandrup, U., Mikkelsen, E., and Mulvany, M. Active, passive and myogenic characteristics of isolated rat intramural coronary resistance arteries. *Pflügers Archiv European Journal of Physiology*, 410(6):664–670, 1987.

[180] Nyborg, N., Korsgaard, N., and Nielsen, P. Active wall tension–length curve and morphology of isolated bovine retinal small arteries: important feature for pharmacodynamic studies. *Experimental eye research*, 51(2):217–224, 1990.

[181] Olsen, T. Regional cerebral blood flow after occlusion of the middle cerebral artery. *Acta Neurologica Scandinavica*, 73(4):321–337, 1986.

[182] Olufsen, M. and Nadim, A. On deriving lumped models for blood flow and pressure in the systemic arteries. *Math Biosci Eng*, 1(1):61–80, 2004.

[183] Osol, G., Brekke, J., McElroy-Yaggy, K., and Gokina, N. Myogenic tone, reactivity, and forced dilatation: a three-phase model of in vitro arterial myogenic behavior. *American Journal of Physiology-Heart and Circulatory Physiology*, 283(6):H2260–H2267, 2002.

[184] Osol, G., Laher, I., and Cipolla, M. Protein kinase c modulates basal myogenic tone in resistance arteries from the cerebral circulation. *Circulation research*, 68(2):359, 1991.

[185] Otten, E. A myocybernetic model of the jaw system of the rat. *Journal of neuroscience methods*, 21(2):287–302, 1987.

[186] Palmer, R., Ferrige, A., Moncada, S., et al. Nitric oxide release accounts for the biological activity of endothelium-derived relaxing factor. *Nature*, 327(6122):524–526, 1987.

[187] Panerai, R. Assessment of cerebral pressure autoregulation in humans-a review of measurement methods. *Physiological measurement*, 19:305, 1998.

[188] Panerai, R., Dawson, S., Eames, P., and Potter, J. Cerebral blood flow velocity response to induced and spontaneous sudden changes in arterial blood pressure. *American Journal of Physiology-Heart and Circulatory Physiology*, 280(5):H2162–H2174, 2001.

[189] Park, C. and Payne, S. A generalized mathematical framework for estimating the residue function for arbitrary vascular networks. *Interface Focus*, In Press 2013.

[190] Paul, R. Smooth muscle mechanochemical energy conversion: relations between metabolism and contractility. *Physiology of the gastrointestinal tract*, 1:483–506, 1987.

[191] Paulson, O., Olesen, J., and Christensen, M. Restoration of autoregulation of cerebral blood flow by hypocapnia. *Neurology*, 22(3):286–286, 1972.

[192] Pittman, R., Golub, A., and Schleicher, W. Rate of decrease of *po2* from an arteriole with arrested flow. *Oxygen transport to tissue XXVI*, pages 257–262, 2005.

[193] Popel, A., Pittman, R., and Ellsworth, M. Rate of oxygen loss from arterioles is an order of magnitude higher than expected. *American Journal of Physiology-Heart and Circulatory Physiology*, 256(3):H921–H924, 1989.

[194] Pries, A., Neuhaus, D., and Gaehtgens, P. Blood viscosity in tube flow: dependence on diameter and hematocrit. *American Journal of Physiology- Heart and Circulatory Physiology*, 263(6):1770–1778, 1992.

[195] Pries, A., Reglin, B., and Secomb, T. Structural response of microcirculatory networks to changes in demand: information transfer by shear stress. *American Journal of Physiology-Heart and Circulatory Physiology*, 284(6):2204–2212, 2003.

[196] Pries, A., Reglin, B., and Secomb, T. Remodeling of blood vessels responses of diameter and wall thickness to hemodynamic and metabolic stimuli, 2005.

[197] Pries, A. and Secomb, T. Control of blood vessel structure: insights from theoretical models. *American Journal of Physiology- Heart and Circulatory Physiology*, 288(3):1010–1015, 2005.

[198] Pries, A., Secomb, T., and Gaehtgens, P. Structural autoregulation of terminal vascular beds: vascular adaptation and development of hypertension. *Hypertension*, 33(1):153, 1999.

[199] Qin, K., Xu, Z., Zhang, H., Xiang, C., Ge, S., and Jiang, Z. Dynamic modeling for modulation of atp concentration at the endothelial surface by viscous shear flow. In *Computer Aided Control System Design, 2006 IEEE International Conference on Control Applications, 2006 IEEE International Symposium on Intelligent Control, 2006 IEEE*, pages 1270–1275. IEEE, 2006.

[200] Quick, C., Young, W., Leonard, E., Joshi, S., Gao, E., and Hashimoto, T. Model of structural and functional adaptation of small conductance vessels to arterial hypotension. *American Journal of Physiology- Heart and Circulatory Physiology*, 279(4):1645–1653, 2000.

[201] Rein, H. Vasomotorische regulationen. *Ergebnisse der Physiologie, biologischen Chemie und experimentellen Pharmakologie*, 32(1):28–72, 1931. ISSN 0080-2042.

[202] Reinhart, W. Shear-dependence of endothelial functions. *Cellular and Molecular Life Sciences*, 50(2):87–93, 1994.

[203] Rhodin, J. Architecture of the vessel wall. *Comprehensive Physiology*, 1980.

[204] Roggendorf, W., Cervos-Navarro, J., and Lazaro-Lacalle, M. Ultrastructure of venules in the cat brain. *Cell and Tissue Research*, 192 (3):461–474, 1978.

[205] Rolett, E., Azzawi, A., Liu, K., Yongbi, M., Swartz, H., and Dunn, J. Critical oxygen tension in rat brain: a combined 31p-nmr and epr oximetry study. *American Journal of Physiology-Regulatory, Integrative and Comparative Physiology*, 279(1):R9–R16, 2000.

[206] Román, G., Tatemichi, T., Erkinjuntti, T., Cummings, J., Masdeu, J., Garcia, J., Amaducci, L., Orgogozo, J., Brun, A., Hofman, A., et al. Vascular dementia. *Neurology*, 43(2): 250–250, 1993.

[207] Royal College of Physicians. National clinical guidelines for stroke: 3rd edition. *http://www.rcplondon.ac.uk/pubs/books*.

[208] Rubio, R. and Berne, R. Regulation of coronary blood flow. *Progress in cardiovascular diseases*, 18(2):105–122, 1975. ISSN 0033-0620.

[209] Sabatini, U., Celsis, P., Viallard, G., Rascol, A., and Marc-Vergnes, J. Quantitative assessment of cerebral blood volume by single-photon emission computed tomography. *Stroke*, 22(3):324–330, 1991.

[210] Santilli, S., Stevens, R., Anderson, J., Payne, W., and Caldwell, M. Transarterial wall oxygen gradients at the dog carotid bifurcation. *American Journal of Physiology-Heart and Circulatory Physiology*, 268(1):H155–H161, 1995.

[211] Saver, J. Time is brain–quantified. *Stroke*, 37 (1):263, 2006.

[212] Schneider, J., Arvanitakis, Z., Bang, W., and Bennett, D. Mixed brain pathologies account for most dementia cases in community-dwelling older persons. *Neurology*, 69(24): 2197–2204, 2007.

[213] Schubert, R. and Mulvany, M. The myogenic response: established facts and attractive hypotheses. *Clinical Science*, 96:313–326, 1999. ISSN 0143-5221.

[214] Secomb, T., Beard, D., Frisbee, J., Smith, N., and Pries, A. The role of theoretical modeling in microcirculation research. *Microcirculation*, 15(8):693–698, 2008.

[215] Secomb, T. and Pries, A. 13. the blood vasculature as an adaptive system: Role of mechanical sensing. *Sensors and Sensing in Biology and Engineering*, page 187, 2003.

[216] Seiyama, A., Chen, S., Imai, T., Kosaka, H., and Shiga, T. Assessment of rate of o_2 release from single hepatic sinusoids of rats. *American Journal of Physiology-Heart and Circulatory Physiology*, 267(3):H944–H951, 1994.

[217] Seiyama, A., Tanaka, S., Kosaka, H., and Shiga, T. o_2 transfer from single microvessels to acinar cells in secretin-stimulated pancreas of rat. *American Journal of Physiology-Heart and Circulatory Physiology*, 270(5):H1704–H1711, 1996.

[218] Serway, R. and Jewett, J. *Principles of Physics: Calculus*. Number v. 1. Cengage Learning, 2012. ISBN 9781133110279.

[219] Severinghaus, J. Simple, accurate equations for human blood o_2 dissociation computations. *Journal of Applied Physiology*, 46(3):599–602, 1979.

[220] Sharan, M. and Popel, A. A mathematical model of countercurrent exchange of oxygen between paired arterioles and venules. *Mathematical biosciences*, 91(1):17–34, 1988.

[221] Sharan, M., Vovenko, E., Vadapalli, A., Popel, A., and Pittman, R. Experimental and theoretical studies of oxygen gradients in rat pial microvessels. *Journal of Cerebral Blood Flow & Metabolism*, 28(9):1597–1604, 2008.

[222] Shaver, S., Sposito, N., and Gross, P. Quantitative fine structure of capillaries in subregions of the rat subfornical organ. *The Journal of comparative neurology*, 294(1):145–152, 1990.

[223] Sherwood, L. *Human Physiology: From Cells to Systems*. Cengage Learning, 2012. ISBN 9781133108931.

[224] Shibata, M., Ichioka, S., Ando, J., and Kamiya, A. Microvascular and interstitial po_2 measurements in rat skeletal muscle by phosphorescence quenching. *Journal of Applied Physiology*, 91(1):321–327, 2001.

[225] Shibuki, K., Hishida, R., Murakami, H., Kudoh, M., Kawaguchi, T., Watanabe, M., Watanabe, S., Kouuchi, T., and Tanaka, R. Dynamic imaging of somatosensory cortical activity in the rat visualized by flavoprotein autofluorescence. *The Journal of physiology*, 549(3): 919–927, 2003.

[226] Shonat, R., Richmond, K., and Johnson, P. Phosphorescence quenching and the microcirculation: an automated, multipoint oxygen tension measuring instrument. *Review of scientific instruments*, 66(10):5075–5084, 1995.

[227] Smith, J., Kampine, J., et al. *Circulatory physiology: The essentials*. Williams & Wilkins Baltimore, 1990.

[228] Sokoloff, L. et al. Relationships among local functional activity, energy metabolism, and blood flow in the central nervous system. In *Federation proceedings*, volume 40, page 2311, 1981.

[229] Sokoloff, L., Reivich, M., Kennedy, C., Des Rosiers, M., Patlak, C., Pettigrew, K., Sakurada, O., and Shinohara, M. The [14C] deoxyglucose method for the measurement of local cerebral glucose utilization: theory, procedure, and normal values in the conscious and anesthetized albino rat1. *Journal of Neurochemistry*, 28(5):897–916, 1977.

[230] Stefanovic, B., Hutchinson, E., Yakovleva, V., Schram, V., Russell, J., Belluscio, L., Koretsky, A., and Silva, A. Functional reactivity of cerebral capillaries. *Journal of Cerebral Blood Flow & Metabolism*, 28(5):961–972, 2007.

[231] Stein, J. and Ellsworth, M. Microvascular oxygen transport: impact of a left-shifted dissociation curve. *American Journal of Physiology-Heart and Circulatory Physiology*, 262(2):H517–H522, 1992.

[232] Strub, R. Vascular dementia. *The Ochsner Journal*, 5(1):40–43, 2003.

[233] Swain, D. and Pittman, R. Oxygen mass balance in arterioles of hamster retractor muscle. *Int. J. Microcirc. Clin. Exp*, 3:379, 1984.

[234] Swain, D. and Pittman, R. Oxygen exchange in the microcirculation of hamster retractor muscle. *American Journal of Physiology-Heart and Circulatory Physiology*, 256(1):H247–H255, 1989.

[235] Takayasu, M. and Dacey Jr, R. Calcium dependence of intracerebral arteriolar vasomotor tone and constrictor responses in rats. *Stroke*, 20(6):778–782, 1989.

[236] The Internet Stroke Centre. Stroke diagnosis. *http://www.strokecenter.org/prof/guidelines.htm#Diagnosis*.

[237] The University Hospital. Anatomy of the Brain. *http://www.theuniversityhospital.com/stroke/anatomy.htm*.

[238] Torres Filho, I. and Intaglietta, M. Microvessel po_2 measurements by phosphorescence decay method. *American Journal of Physiology-Heart and Circulatory Physiology*, 265(4):H1434–H1438, 1993.

[239] Torres Filho, I., Kerger, H., and Intaglietta, M. po_2 measurements in arteriolar networks. *Microvasc Res*, 51(2):202–212, 1996.

[240] Tremper, K. Pulse oximetry. *Chest*, 95(4):713, 1989.

[241] Tsai, A., Friesenecker, B., Cabrales, P., Hangai-Hoger, N., and Intaglietta, M. The vascular wall as a regulator of tissue oxygenation. *Current opinion in nephrology and hypertension*, 15(1):67, 2006.

[242] Tsai, A., Friesenecker, B., Mazzoni, M., Kerger, H., Buerk, D., Johnson, P., and Intaglietta, M. Microvascular and tissue oxygen gradients in the rat mesentery. *Proceedings of the National Academy of Sciences*, 95(12):6590, 1998.

[243] Tsai, A., Johnson, P., and Intaglietta, M. Oxygen gradients in the microcirculation. *Physiological reviews*, 83(3):933, 2003.

[244] Tsai, A., Kerger, H., and Intaglietta, M. Microcirculatory consequences of blood substitution with hemoglobin. *Blood substitutes. Physiological basis of efficacy, edited by RM Winslow, KD Vandegriff, and M. Intaglietta. Boston: Birkhäuser*, pages 155–174, 1995.

[245] Tsukada, K., Sekizuka, E., Oshio, C., Tsujioka, K., and Minamitani, H. Red blood cell velocity and oxygen tension measurement in cerebral microvessels by double-wavelength photoexcitation. *Journal of Applied Physiology*, 96 (4):1561–1568, 2004.

[246] Tuma, R., Durán, W., and Ley, K. *Microcirculation*. Handbook of physiology (Bethesda, Md.).: Cardiovascular system. Elsevier/Academic Press, 2008. ISBN 9780123745309.

[247] ulbring, E. B. Correlation between membrane potential, spike discharge and tension in smooth muscle. *The Journal of physiology*, 128 (1):200, 1955. ISSN 0022-3751.

[248] University of Pittsburgh Medical Centre. Stroke surgical treatment. *www.upmc.com/HealthAtoZ/patienteducation/Documents/StrokeSurgical.pdf*.

[249] Ursino, M., Colantuoni, A., and Bertuglia, S. Vasomotion and blood flow regulation in hamster skeletal muscle microcirculation: a theoretical and experimental study. *Microvascular research*, 56(3):233–252, 1998.

[250] Ursino, M., Di Giammarco, P., and Belardinelli, E. A mathematical model of cerebral blood flow chemical regulation. i. diffusion processes. *Biomedical Engineering, IEEE Transactions on*, 36(2):183–191, 1989.

[251] Ursino, M. and Fabbri, G. Role of the myogenic mechanism in the genesis of microvascular oscillations (vasomotion): analysis with a mathematical model. *Microvascular research*, 43(2):156–177, 1992. ISSN 0026-2862.

[252] Ursino, M. and Lodi, C. A simple mathematical model of the interaction between intracranial pressure and cerebral hemodynamics. *Journal of Applied Physiology*, 82(4):1256, 1997.

[253] Ursino, M. and Lodi, C. Interaction among autoregulation, co_2 reactivity, and intracranial pressure: a mathematical model. *American Journal of Physiology-Heart and Circulatory Physiology*, 274(5):H1715, 1998. ISSN 0363-6135.

[254] Ursino, M., Ter Minassian, A., Lodi, C., and Beydon, L. Cerebral hemodynamics during arterial and co_2 pressure changes: in vivo prediction by a mathematical model. *American Journal of Physiology-Heart and Circulatory Physiology*, 279(5):H2439, 2000.

[255] Vadapalli, A., Pittman, R., and Popel, A. Estimating oxygen transport resistance of the microvascular wall. *American Journal of Physiology-Heart and Circulatory Physiology*, 279(2):H657–H671, 2000.

[256] Valabrègue, R., Aubert, A., Burger, J., Bittoun, J., and Costalat, R. Relation between cerebral blood flow and metabolism explained by a model of oxygen exchange. *Journal of Cerebral Blood Flow & Metabolism*, 23(5):536–545, 2003.

[257] VanBavel, E. and Mulvany, M. Role of wall tension in the vasoconstrictor response of cannulated rat mesenteric small arteries. *The Journal of Physiology*, 477(Pt 1):103–115, 1994.

[258] Vander, A., Sherman, J., and Luciano, D. *Human physiology : the mechanisms of body function*. McGraw-Hill, Boston, 2001. ISBN 0072908017.

[259] Vanderkooi, J., Maniara, G., Green, T., and Wilson, D. An optical method for measurement of dioxygen concentration based upon quenching of phosphorescence. *Journal of Biological Chemistry*, 262(12):5476, 1987.

[260] VanDijk, A., Wieringa, P., van der Meer, M., and Laird, J. Mechanics of resting isolated single vascular smooth muscle cells from bovine coronary artery. *American Journal of Physiology-Cell Physiology*, 246(3):C277–C287, 1984.

[261] Vanhoutte, P., Rubanyi, G., Miller, V., and Houston, D. Modulation of vascular smooth muscle contraction by the endothelium. *Annual review of physiology*, 48(1):307–320, 1986.

[262] Vanzetta, I. and Grinvald, A. Increased cortical oxidative metabolism due to sensory stimulation: implications for functional brain imaging. *Science*, 286(5444):1555, 1999.

[263] Varjavand, N., Kaye, J., Wang, S., and Primiano, F. The interactive oxyhemoglobin dissociation curve, 2002.

[264] Vazquez, A., Masamoto, K., and Kim, S. Dynamics of oxygen delivery and consumption during evoked neural stimulation using a compartment model and cbf and tissue po_2 measurements. *Neuroimage*, 42(1):49–59, 2008.

[265] Vovenko, E. Distribution of oxygen tension on the surface of arterioles, capillaries and venules of brain cortex and in tissue in normoxia: an experimental study on rats. *Pflügers Archiv European Journal of Physiology*, 437(4): 617–623, 1999.

[266] Vovenko, E. Transmural oxygen tension gradients in rat cerebral cortex arterioles. *Neuroscience and behavioral physiology*, 39(4):363–370, 2009.

[267] Wei, E., Christman, C., Kontos, H., and Povlishock, J. Effects of oxygen radicals on cerebral arterioles. *American Journal of Physiology-Heart and Circulatory Physiology*, 248(2):H157–H162, 1985.

[268] Winn, H., Welsh, J., Rubio, R., and Berne, R. Brain adenosine production in rat during sustained alteration in systemic blood pressure. *American Journal of Physiology-Heart and Circulatory Physiology*, 239(5):H636, 1980. ISSN 0363-6135.

[269] Wolf, P., Clagett, G., Easton, J., Goldstein, L., Gorelick, P., Kelly-Hayes, M., Sacco, R., and Whisnant, J. Preventing ischemic stroke in patients with prior stroke and transient ischemic attack: a statement for healthcare professionals from the Stroke Council of the American Heart Association. *Stroke*, 30(9): 1991, 1999.

[270] Wuyts, F., Vanhuyse, V., Langewouters, G., Decraemer, W., Raman, E., and Buyle, S. Elastic properties of human aortas in relation to age and atherosclerosis: a structural model. *Physics in medicine and biology*, 40:1577, 1995.

[271] Yanagisawa, M., Kurihara, H., Kimura, S., Tomobe, Y., Kobayashi, M., Mitsui, Y., Yazaki, Y., Goto, K., Masaki, T., et al. A novel potent vasoconstrictor peptide produced by vascular endothelial cells. *Nature*, 332(6163):411–415, 1988.

[272] Yang, J., Clark, J., et al. The myogenic response in isolated rat cerebrovascular arteries: smooth muscle cell model. *Medical engineering & physics*, 25(8):691–709, 2003. ISSN 1350-4533.

[273] Yang, J., Clark, J., et al. The myogenic response in isolated rat cerebrovascular arteries: vessel model. *Medical engineering & physics*, 25 (8):711–717, 2003. ISSN 1350-4533.

[274] Zauner, A., Daugherty, W., Bullock, M., and Warner, D. Brain oxygenation and energy metabolism: part i-biological function and pathophysiology. *Neurosurgery*, 51(2):289, 2002.

[275] Zauner, A. and Muizelaar, J. Brain metabolism and cerebral blood flow. *Head Injury*, pages 89–99, 1997.

[276] Zheng, Y., Johnston, D., Berwick, J., Chen, D., Billings, S., and Mayhew, J. A three-compartment model of the hemodynamic response and oxygen delivery to brain. *Neuroimage*, 28(4):925–939, 2005.

[277] Zieve, D. and Dugdale, D. Stroke from medline plus. *http://www.nlm.nih.gov/medlineplus/ency/article/000726.htm*.

[278] Zimmermann, P., Knot, H., Stevenson, A., and Nelson, M. Increased myogenic tone and diminished responsiveness to atp-sensitive k+ channel openers in cerebral arteries from diabetic rats. *Circulation research*, 81(6):996, 1997.

[279] Zou, H., Ratz, P., and Hill, M. Role of myosin phosphorylation and $[ca^{2+}]$ in myogenic reactivity and arteriolar tone. *American Journal of Physiology-Heart and Circulatory Physiology*, 269(5):H1590, 1995. ISSN 0363-6135.

[280] Zulliger, M., Fridez, P., Hayashi, K., and Stergiopulos, N. A strain energy function for arteries accounting for wall composition and structure. *Journal of biomechanics*, 37(7):989–1000, 2004.

[281] Zweifach, B. and Lipowsky, H. Quantitative studies of microcirculatory structure and function. iii. microvascular hemodynamics of cat mesentery and rabbit omentum. *Circulation research*, 41(3):380–390, 1977.

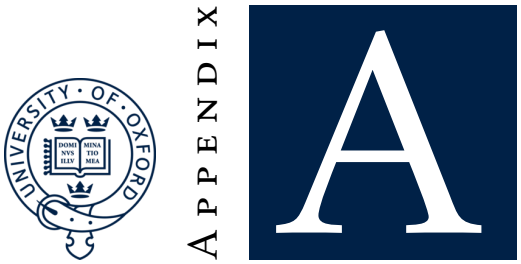

Appendix A

Section 1:1 Polynomial Fitting of Zweifach Data

A.1.1 Velocity Fit

For all data points:

With D in μm, velocity v is calculated with a cubic fit as:

$$v = p_1 D^3 + p_2 D^2 + p_3 D + p_4, \tag{A.1}$$

with polynomial coefficients given in Table A.1.

A fourth-order fit has form:

$$v = p_1 D^4 + p_2 D^3 + p_3 D^2 + p_4 D + p_5. \tag{A.2}$$

A fifth-order fit is given in Equation A.3 with coefficients in Table A.1.

$$v = p_1 D^5 + p_2 D^4 + p_3 D^3 + p_4 D^2 + p_5 D + p_6 \tag{A.3}$$

Coefficient	Cubic Fit	Fourth-order fit	Fifth-order fit
p1	$3.46 \times 10^{-2}/\mu m^2$ s	-1.41 $\times 10^{-3}/\mu m^3$ s	-2.88 $\times 10^{-6}/\mu m^4 s$
p2	$4.16/\mu ms$	$2.85 \times 10^{-2}/\mu m^2 s$	$-1.44 \times 10^{-3}/\mu m^3 s$
p3	$-125.42s$	$7.91/\mu ms$	$3.78 \times 10^{-2}/\mu m^2 s$
p4	$2.85 \times 10^3 \mu m/s$	$-119.58s$	$7.97/\mu ms$
p5	n/a	$1.53 \times 10^3 \mu m/s$	$-125.09s$
p6	n/a	n/a	$1.51 \times 10^3 \mu m/s$

Table A.1: *Polynomial coefficients for velocity fits over all data points.*

Vessel Type	Diameter (μm)	Velocity (mm/s)	Cubic Fit (mm/s)	Fourth-order fit (mm/s)	Fifth-order fit (mm/s)
A	54.6	15.0	16.46 (+1.46)	14.48 (-0.52)	14.6 (-0.41)
A	50.7	14.7	15.39 (+0.69)	14.90 (+0.20)	14.9 (+0.19)
A	47.3	14.4	14.42 (+0.02)	14.81 (+0.41)	14.8 (+0.36)
A	43.4	13.8	13.30 (-0.50)	14.29 (+0.49)	14.2 (+0.41)
A	40.3	13.3	12.39 (-0.91)	13.61 (+0.31)	13.5 (+0.24)
A	36.1	12.7	11.17 (-1.53)	12.42 (-0.28)	12.4 (-0.33)
A1	30.5	11	9.56 (-1.44)	10.51 (-0.49)	10.5 (-0.50)
A	26.2	9.4	8.37 (-1.03)	8.91 (-0.49)	8.94 (-0.46)
A2	24.4	8.7	7.88 (-0.79)	8.24 (-0.43)	8.3 (-0.40)
A	22.9	8.0	7.49 (-0.51)	7.69 (-0.31)	7.7 (-0.28)
A3	19.5	6.7	6.62 (-0.08)	6.45 (-0.25)	6.5 (-0.20)
A4	15.6	5	5.69 (+0.69)	5.13 (+0.13)	5.2 (+0.17)
A5	12.5	3.2	5.00 (+1.80)	4.17 (+0.97)	4.2 (+1.01)
A	11.6	3.4	4.81 (+1.41)	3.91 (+0.51)	4.0 (+0.55)
A6	10	2.8	4.48 (+1.68)	3.47 (+0.67)	3.5 (+0.71)
C	8	2.3	2.85 (+0.55)	1.53 (-0.77)	1.5 (-0.79)
V6	12	1.7	2.00 (+0.30)	1.25 (-0.45)	1.2 (-0.51)
V5	15	1.8	2.02 (+0.22)	1.54 (-0.26)	1.5 (-0.32)
V	16.8	1.8	2.08 (+0.28)	1.78 (-0.02)	1.7 (-0.08)
V4	18.7	1.9	2.18 (+0.28)	2.07 (+0.17)	2.00 (+0.12)
V	21.1	2.3	2.38 (+0.08)	2.52 (+0.22)	2.5 (+0.18)
V3	23.4	3.0	2.63 (-0.37)	3.00 (=)	2.99 (-0.02)
V	26.0	3.4	3.01 (-0.39)	3.62 (+0.22)	3.9 (+0.22)
V2	29.3	4.5	3.61 (-0.89)	4.49 (-0.01)	4.5 (+0.02)
V	31.6	5.0	4.13 (-0.87)	5.14 (+0.14)	5.2 (+0.19)
V1	36.6	6.3	5.52 (+0.78)	6.61 (+0.31)	6.70 (+0.40)
V	41.0	8.5	7.08 (-1.42)	7.90 (-0.60)	7.99 (-0.51)
V	46.1	9.3	9.29 (-0.01)	9.25 (-0.05)	9.30 (=)
V	51.7	10.2	12.25 (+2.05)	10.36 (+0.16)	10.25 (+0.05)
RMS error			0.9806	0.4103	0.4066

Table A.2: *Comparison of third, fourth and fifth order fits of the velocity with root mean squared error.*

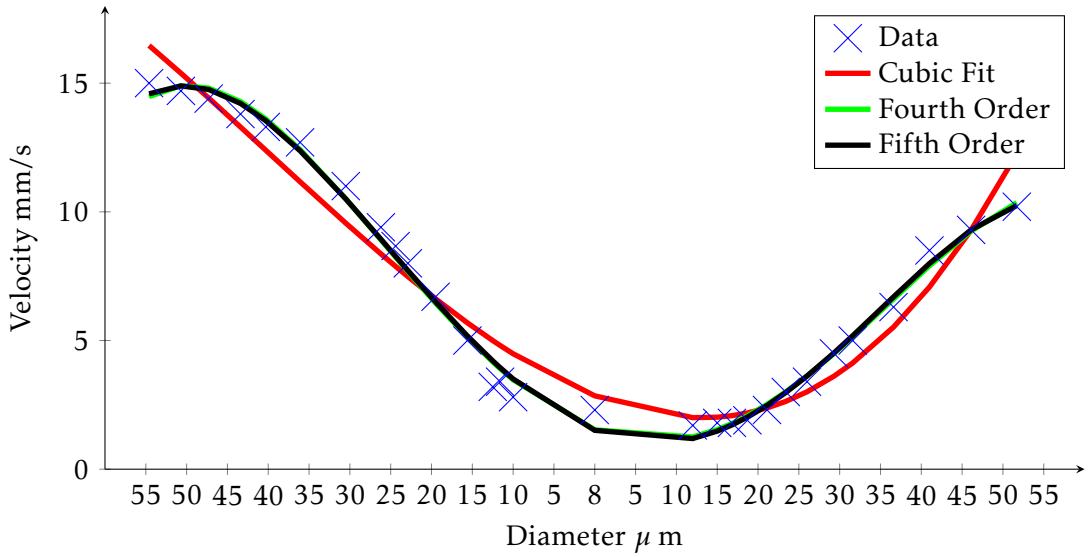

Figure A.1: *Showing the polynomial fit for velocity as a function of diameter of selected data-points from Zweifach Figure 2.4.*

For small vessels:

Fit for vessels $\leq 41\mu m$ are Equations A.4 (cubic), A.5 (fourth-order) and A.6 (fifth-order) with coefficients given in Table A.3:

$$v = p_1 D^3 + p_2 D^2 + p_3 D + p_4. \tag{A.4}$$

$$v = p_1 D^4 + p_2 D^3 + p_3 D^2 + p_4 D + p_5. \tag{A.5}$$

$$v = p_1 D^5 + p_2 D^4 + p_3 D^3 + p_4 D^2 + p_5 D + p_6. \tag{A.6}$$

Coefficient	Cubic Fit	Fourth-order fit	Fifth-order fit
p1	$2.78 \times 10^{-2}/\mu m^2 s$	$-1.57 \times 10^{-3}/\mu m^3 s$	$-5.89 \times 10^{-5}/\mu m^4 s$
p2	$5.74/\mu ms$	$3.13 \times 10^{-2}/\mu m^2 s$	$-1.62 \times 10^{-3}/\mu m^3 s$
p3	$-119.97s$	$8.31/\mu ms$	$8.51 \times 10^{-2}/\mu m^2 s$
p4	$2.04 \times 10^3 \mu m/s$	$-123.71s$	$8.33/\mu ms$
p5	n/a	$1.41 \times 10^3 \mu m/s$	$-80.43s$
p6	n/a	n/a	$1.45 \times 10^3 \mu m/s$

Table A.3: *Polynomial coefficients for velocity fits over small vessel data points.*

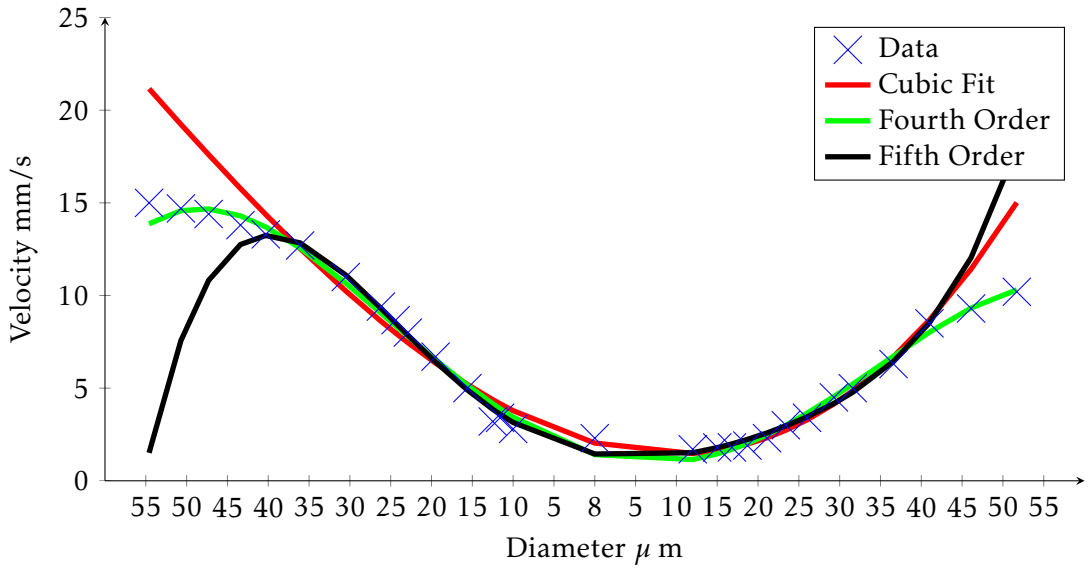

Figure A.2: *Showing the polynomial fit for velocity as a function of diameter of selected data-points from Zweifach Figure 2.4 where fit is for diameters smaller than* $40\mu m$.

Vessel Type	Diameter (μm)	Velocity (mm/s)	Cubic Fit (mm/s)	Fourth-order fit (mm/s)	Fifth-order fit (mm/s)
A	54.6	15.0	21.16 (+6.16)	13.87 (-1.13)	1.51 (-13.49)
A	50.7	14.7	19.24 (+4.54)	14.58 (-0.12)	7.57 (-7.14)
A	47.3	14.4	17.60 (+3.20)	14.67 (+0.27)	10.82 (-3.58)
A	43.4	13.8	15.77 (+1.97)	14.30 (+0.50)	12.75 (-1.05)
A	40.3	13.3	14.37 (+1.07)	13.70 (+0.40)	13.24 (-0.06)
A	36.1	12.7	12.53 (-0.17)	12.56 (-0.14)	12.84 (+0.14)
A1	30.5	11	10.24 (-0.76)	10.67 (-0.33)	11.10 (+0.10)
A	26.2	9.4	8.62 (-0.78)	9.05 (-0.35)	9.31 (-0.09)
A2	24.4	8.67	7.98 (-0.69)	8.37 (-0.30)	8.52 (-0.15)
A	22.9	8.0	7.46 (-0.54)	7.80 (-0.20)	7.86 (-0.14)
A3	19.5	6.7	6.35 (-0.35)	6.53 (-0.17)	6.41 (-0.29)
A4	15.6	5	5.20 (+0.20)	5.15 (+0.15)	4.90 (-0.10)
A5	12.5	3.2	4.38 (+1.18)	4.16 (+0.96)	3.86 (+0.66)
A	11.6	3.4	4.16 (+0.76)	3.89 (+0.49)	3.59 (+0.19)
A6	10	2.8	3.78 (+0.98)	3.43 (+0.63)	3.15 (+0.35)
C	8	2.3	2.04 (-0.26)	1.41 (-0.89)	1.45 (-0.85)
V6	12	1.7	1.47 (-0.23)	1.15 (-0.55)	1.51 (-0.19)
V5	15	1.8	1.62 (-0.18)	1.45 (-0.35)	1.79 (-0.01)
V	16.8	1.8	1.77 (-0.03)	1.70 (-0.10)	1.99 (+0.19)
V4	18.7	1.9	1.98 (+0.08)	2.02 (+0.12)	2.23 (+0.33)
V	21.1	2.3	2.32 (+0.02)	2.48 (+0.18)	2.58 (+0.28)
V3	23.4	3.0	2.73 (-0.27)	3.00 (=)	2.96 (-0.04)
V	26.0	3.4	3.29 (-0.11)	3.64 (+0.24)	3.45 (+0.05)
V2	29.3	4.5	4.15 (-0.35)	4.55 (+0.05)	4.18 (-0.32)
V	31.6	5.0	4.85 (-0.15)	5.22 (+0.22)	4.78 (-0.22)
V1	36.6	6.3	6.70 (+0.40)	6.72 (+0.42)	6.45 (+0.15)
V	41.0	8.5	8.68 (+0.18)	8.02 (-0.48)	8.53 (+0.03)
V	46.1	9.3	11.43 (+2.13)	9.32 (+0.02)	12.04 (+2.74)
V	51.7	10.2	15.02 (+4.82)	10.31 (+0.11)	17.96 (+7.76)
RMS error			0.979	0.4174	0.4140

Table A.4: *Comparison of third, fourth and fifth order fits of the velocity with root mean squared error.*

A.1.2 Pressure Fit

For all data points.

Cubic:

$$P = p_1 D^3 + p_2 D^2 + p_3 D + p_4. \tag{A.7}$$

Fourth order:

$$P = p_1 D^4 + p_2 D^3 + p_3 D^2 + p_4 D + p_5. \tag{A.8}$$

Fifth order:

$$P = p_1 D^5 + p_2 D^4 + p_3 D^3 + p_4 D^2 + p_5 D + p_6. \tag{A.9}$$

with coefficients in Table A.5.

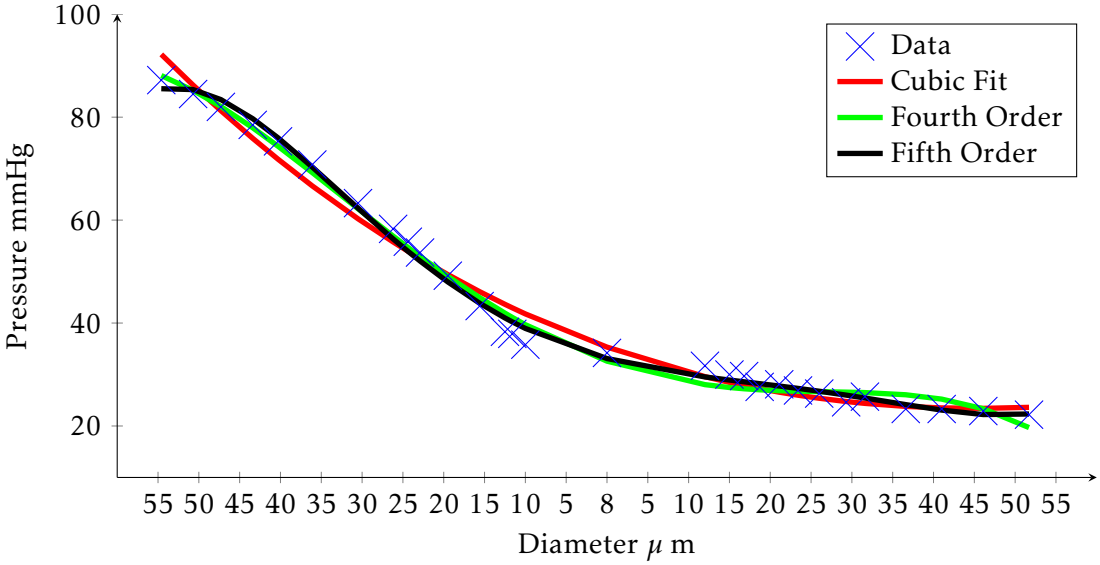

Figure A.3: *Showing the polynomial fit for mean vessel pressure as a function of diameter of selected data-points from Zweifach Figure 2.4.*

Coefficient	Cubic Fit	Fourth-order fit	Fifth-order fit
p1	$-1.99\times10^{-5} mmHg/\mu m^3$	$-2.92\times10^{-6} mmHg/\mu m^4$	$6.79\times10^{-8} mmHg/\mu m^5$
p2	$7.61\times10^{-3} mmHg/\mu m^2$	$-3.25\times10^{-5} mmHg/\mu m^3$	$-2.25\times10^{-6} mmHg/\mu m^4$
p3	$-0.57 mmHg/\mu m$	$1.54\times10^{-2} mmHg/\mu m^2$	$-2.52\times10^{-4} mmHg/\mu m^3$
p4	$35.33 mmHg$	$-0.55 mmHg/\mu m$	$1.38\times10^{-2} mmHg/\mu m^2$
p5	n/a	$32.59 mmHg$	$-0.42 mmHg/\mu m$
p6	n/a	n/a	$33.10 mmHg$

Table A.5: *Polynomial coefficients for pressure fits over all vessel data points.*

Vessel Type	Diameter (μm)	Pressure ($mmHg$)	Cubic Fit ($mmHg$)	Fourth-order fit ($mmHg$)	Fifth-order fit ($mmHg$)
A	54.6	87.2	92.20 (+5.00)	88.09 (+0.89)	85.53 (-1.67)
A	50.7	84.5	86.22 (+1.72)	85.20 (+0.70)	85.36 (+0.86)
A	47.3	82.0	81.27 (-0.73)	82.07 (+0.07)	83.42 (+1.42)
A	43.4	78.5	75.89 (-2.61)	77.94 (-0.56)	79.71 (+1.21)
A	40.3	75.3	71.83 (-3.47)	74.36 (-0.94)	75.99 (+0.69)
A	36.1	70.8	66.64 (-4.16)	69.23 (-1.57)	70.30 (-0.50)
A1	30.5	63.3	60.26 (-3.04)	62.22 (-1.08)	62.32 (-0.98)
A	26.2	58.3	55.76 (-2.54)	56.89 (-1.41)	56.35 (-1.95)
A2	24.4	55.8	53.98 (-1.82)	54.72 (-1.08)	53.97 (-1.83)
A	22.9	53.7	52.54 (-1.16)	52.95 (-0.75)	52.05 (-1.65)
A3	19.5	49.2	49.42 (+0.22)	49.08 (-0.12)	47.99 (-1.21)
A4	15.6	43.3	46.10 (+2.80)	44.94 (+1.64)	43.85 (+0.55)
A5	12.5	38.3	43.64 (+5.34)	41.92 (+3.62)	40.99 (+2.69)
A	11.6	37.9	42.96 (+5.06)	41.09 (+3.19)	40.23(+2.33)
A6	10	35.8	41.78(+5.98)	39.68 (+3.88)	38.95 (+3.15)
C	8	34.2	35.33 (+1.13)	32.59 (-1.61)	33.10 (-1.10)
V6	12	31.7	29.59 (-2.11)	28.03 (-3.67)	29.53 (-2.17)
V5	15	30.0	28.47 (-1.53)	27.48 (-2.52)	28.93 (-1.07)
V	16.8	29.7	27.86 (-1.84)	27.23 (-2.47)	28.58 (-1.12)
V4	18.7	27.6	27.26 (-0.34)	27.03 (-0.57)	28.22 (+0.62)
V	21.1	28.1	26.57 (-1.53)	26.85 (-1.25)	27.76 (-0.34)
V3	23.4	26.9	25.98 (-0.92)	26.74 (-0.16)	27.30 (+0.40)
V	26.0	26.3	25.39 (-0.91)	26.66 (+0.36)	26.75 (+0.45)
V2	29.3	24.6	24.75 (+0.15)	26.58 (+1.98)	26.00 (+1.40)
V	31.6	25.7	24.39 (-1.31)	26.49 (+0.79)	25.43 (-0.27)
V1	36.6	23.3	23.80 (+0.50)	26.07 (+2.77)	24.15 (+0.85)
V	41.0	23.3	23.51 (+0.21)	25.22 (+1.92)	23.09 (-0.21)
V	46.1	22.9	23.43 (+0.53)	23.35 (+0.45)	22.22 (-0.68)
V	51.7	22.2	23.62 (+1.42)	19.69 (-2.51)	22.33 (+0.13)
RMS error			2.6433	1.8921	1.3821

Table A.6: *Comparison of third, fourth and fifth order fits of the pressure with root mean squared error.*

For small vessels.

Fit for vessels $\leq 41 \mu m$, coefficients given in Table A.7.

$$P = p_1 D^3 + p_2 D^2 + p_3 D + p_4 \tag{A.10}$$

$$P = p_1 D^4 + p_2 D^3 + p_3 D^2 + p_4 D + p_5 \tag{A.11}$$

Coefficient	Cubic Fit	Fourth-order fit	Fifth-order fit
p1	$-1.35\times10^{-4} mmHg/\mu m^3$	$-3.87\times10^{-6} mmHg/\mu m^4$	$2.57\times10^{-7} mmHg/\mu m^5$
p2	$1.04\times10^{-2} mmHg/\mu m^2$	$-1.26\times10^{-3} mmHg/\mu m^3$	$-4.09\times10^{-6} mmHg/\mu m^4$
p3	$-0.46 mmHg/\mu m$	$1.67\times10^{-2} mmHg/\mu m^2$	$-6.34\times10^{-4} mmHg/\mu m^3$
p4	$33.89 mmHg$	$-0.47 mmHg/\mu m$	$1.68\times10^{-2} mmHg/\mu m^2$
p5	n/a	$32.59 mmHg$	$-0.28 mmHg/\mu m$
p6	n/a	n/a	$32.50 mmHg$

Table A.7: *Polynomial coefficients for pressure fits over small vessel data points.*

$$P = p_1 D^5 + p_2 D^4 + p_3 D^3 + p_4 D^2 + p_5 D + p_6 \tag{A.12}$$

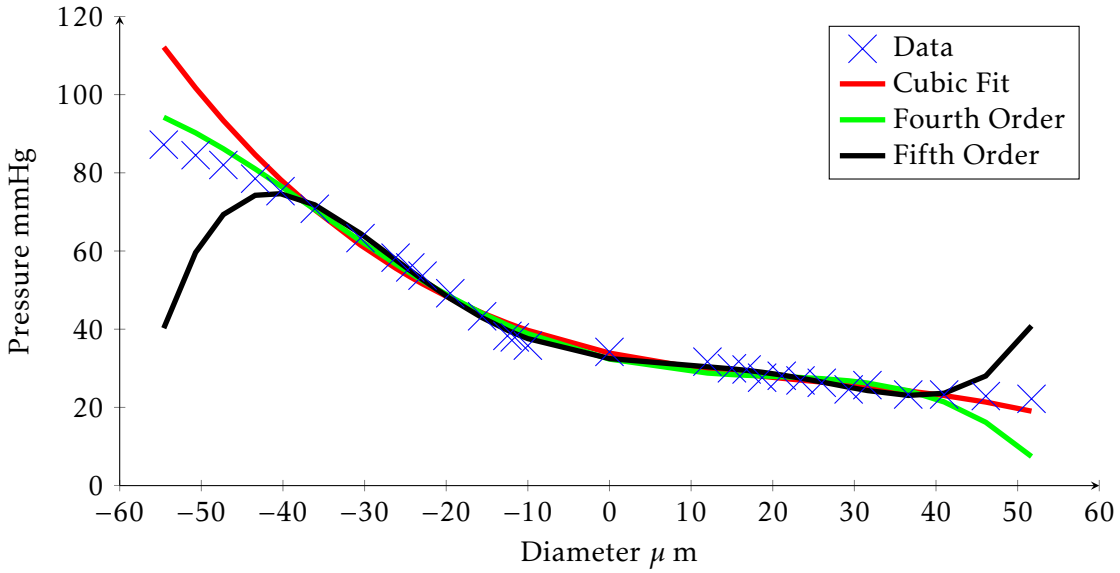

Figure A.4: *Showing the polynomial fit for mean vessel pressure as a function of diameter of selected data-points from Zweifach Figure 2.4.*

Vessel Type	Diameter (μm)	Pressure ($mmHg$)	Cubic Fit ($mmHg$)	Fourth-order fit ($mmHg$)	Fifth-order fit ($mmHg$)
A	54.6	87.2	112.14 (+24.94)	94.21 (+7.01)	40.26 (-46.94)
A	50.7	84.5	101.69 (+17.19)	90.22 (+5.72)	59.62 (-24.88)
A	47.3	82.0	93.35 (+11.35)	86.15 (+4.15)	69.32 (-12.68)
A	43.4	78.5	84.62 (+6.12)	80.99 (+2.49)	74.25 (-4.25)
A	40.3	75.3	78.29 (+2.99)	76.64 (+1.34)	74.65 (-0.65)
A	36.1	70.8	70.53 (-0.27)	70.60 (-0.20)	71.80 (+1.00)
A1	30.5	63.3	61.54 (-1.76)	62.58 (-0.72)	64.48 (+1.18)
A	26.2	58.3	55.61 (-2.69)	56.68 (-1.62)	57.79 (-0.51)
A2	24.4	55.8	53.36 (-2.44)	54.32 (-1.48)	54.99 (-0.81)
A	22.9	53.7	51.59 (-2.11)	52.42 (-1.28)	52.70 (-1.00)
A3	19.5	49.2	47.89 (-1.31)	48.32 (-0.88)	47.82 (-1.38)
A4	15.6	43.3	44.17 (+0.87)	44.06 (+0.76)	42.95 (-0.35)
A5	12.5	38.3	41.58 (+3.28)	41.04 (+2.74)	39.74 (+1.44)
A	11.6	37.9	40.88 (+2.98)	40.22 (+2.32)	38.92 (+1.02)
A6	10	35.8	39.71 (+3.91)	38.85 (+3.05)	37.59 (+1.79)
C	8	34.2	33.89 (-0.31)	32.35 (-1.85)	32.50 (-1.70)
V6	12	31.7	29.58 (-2.12)	28.78 (-2.92)	30.39 (-1.31)
V5	15	30.0	28.81 (-1.19)	28.39 (-1.61)	29.86 (-0.14)
V	16.8	29.7	28.38 (-1.32)	28.21 (-1.49)	29.47 (-0.23)
V4	18.7	27.6	27.96 (+0.36)	28.05 (+0.45)	29.00 (+1.40)
V	21.1	28.1	27.45 (-0.65)	27.85 (-0.25)	28.29 (+0.19)
V3	23.4	26.9	26.99 (+0.09)	27.65 (+0.75)	27.50 (+0.60)
V	26.0	26.3	26.48 (+0.18)	27.36 (+1.06)	26.51 (+0.21)
V2	29.3	24.6	25.82 (+1.22)	26.80 (+2.20)	25.18 (+0.58)
V	31.6	25.7	25.34 (-0.36)	26.24 (+0.54)	24.31 (-1.39)
V1	36.6	23.3	24.21 (+0.91)	24.28 (+0.98)	23.06 (-0.24)
V	41.0	23.3	23.03 (-0.27)	21.40 (-1.90)	23.62 (+0.32)
V	46.1	22.9	21.37 (-1.53)	16.19 (-6.71)	28.04 (+5.14)
V	51.7	22.2	19.04 (-3.16)	7.44 (-14.76)	40.84 (+18.64)
RMS error			6.3640	3.8446	10.8244

Table A.8: *Comparison of third, fourth and fifth order fits of the pressure for $D \leq 41 \mu m$ with root mean squared error.*

APPENDIX B

Appendix B

Section 2:1 Appendix B

B.1.1 Necessary Activation For Conserved Flow

Inlet Pressure P_a $(mmHg)$	Pressure change $\frac{\Delta P}{\Delta P_0}$	Activation A	Diameter fraction D/D0
43.46	0.58	0.01	1.29
43.70	0.59	0.10	1.28
44.15	0.60	0.25	1.26
44.66	0.62	0.35	1.25
45.24	0.63	0.40	1.24
48.31	0.72	0.50	1.17
53.34	0.87	0.60	1.07
57.79	1.00	0.69	1.00
60.45	1.08	0.75	0.96
64.54	1.20	0.85	0.92
66.41	1.25	0.90	0.90
69.50	1.34	0.99	0.87

Table B.1: *Diameter and activation required to maintain flow for varying pressure changes.*

B.1.2 Shear Signal Error

Shear Signal $100\ T_w - T_{w,0}$	Required Signal S	Calculated Signal $k_w(T_w - T_{w,0})$	Error
-2.39	-5.4	-1.45	3.95
-2.33	-3	-1.41	1.59
-2.22	-1.9	-1.34	0.56
-2.14	-1.42	-1.3	0.13
-2.1	-1.21	-1.27	-0.06
-1.68	-0.8	-1.02	-0.21
-0.84	-0.4	-0.51	-0.11
0.56	0.29	0.34	0.04
1.44	0.93	0.87	-0.06
1.83	1.39	1.11	-0.28
2.49	3.79	1.51	-2.28

Table B.2: *Error in calculated steady state shear signal using* $k_w = 60.55\ /mmHg$.

B.1.3 Autoregulation Results

Pressure Fraction $\frac{\Delta P}{\Delta P_0}$	Flow Fraction Q/Q_0	Diameter Fraction (required) D/D_0	Activation (required) A
0.19	0.30	1.26	0.02
0.33	0.54	1.27	0.07
0.48	0.75	1.26	0.17
0.58	0.85	1.25 (1.29)	0.29 (0.01)
0.59	0.86	1.25 (1.28)	0.30 (0.10)
0.60	0.87	1.25 (1.26)	0.31 (0.25)
0.62	0.88	1.25 (1.25)	0.33 (0.35)
0.63	0.89	1.25 (1.24)	0.35 (0.40)
0.72	0.94	1.23 (1.17)	0.47 (0.50)
0.87	0.98	1.11 (1.07)	0.59 (0.60)
1.08	1.01	0.94 (0.96)	0.76 (0.75)
1.2	1.04	0.90 (0.92)	0.86 (0.85)
1.25	1.07	0.90 (0.90)	0.89 (0.90)
1.34	1.13	0.90 (0.87)	0.93 (0.99)
1.36	1.14	0.90	0.94
1.5	1.30	0.92	0.98
1.65	1.54	0.97	0.99
1.8	1.93	1.06	1.00
RMSE	0.3359		
RMSE (linear)	0.0572		

Table B.3: *Flow, diameter and activation results for varying pressure changes. Where known, the (parenthesised) values are those for which the required diameter and autoregulation have been calculated (see Table B.1).*

APPENDIX C

Appendix C

Section 3:1 Conversion Factors

	Unit	Unit
Tension	1×10^2 $dyne/cm$	0.75006 $mmHg$ mm
Tension	1 N/m	7.5006 $mmHgmm$
Pressure	1 $mmHg$	133 Pa
Molar volume	1 $\mu M/mm^3$	22.39 $ml O_2/ml$

Table C.1: *Conversion between units.*